Advanced Gas Turbine Cooling: Double-Wall Turbine Cooling Technologies in Turbine NGV/Blade Applications

Alexander Vesale Murray

Wadham College



A thesis submitted for the degree of

Doctor of Philosophy

Hilary Term, 2019

Oxford Thermofluids Institute, University of Oxford

Advanced Gas Turbine Cooling: Double-Wall Turbine Cooling Technologies in Turbine NGV/Blade Applications

Alexander Vesale Murray, Wadham College, University of Oxford

A thesis submitted for the degree of *Doctor of Philosophy*, Hilary Term 2019

Under the Supervision of Professor Peter T. Ireland

Abstract

The drive to increase the thermal efficiency and specific power output of the gas turbine results in increasing turbine temperatures which necessitate active cooling of the turbine blades. High performance cooling systems are required which achieve the necessary blade life requirements whilst minimising coolant consumption. This thesis explores one potential turbine cooling system advancement termed the double-wall, effusion cooled system which is envisaged to find application in areas where high cooling performance is required.

Single wall effusion cooling performance is initially investigated given its importance in the double-wall system. An experimental investigation is performed and used to validate a computational model. A two-dimensional superposition method for predicting effusion cooling performance is presented and validated based upon the experimental and computational data.

The superposition method was used as part of a computationally light, decoupled conjugate method which was developed to predict the cooling performance of double-wall geometries. This decoupled method was used to assess several developed double-wall geometries. Those geometries which exhibited preferable cooling characteristic were manufactured for testing in a novel experimental facility, designed and commissioned as part of the thesis work. The facility incorporates several features to improve the quality of data obtained and matches several relevant non-dimensional parameters. The facility was used to obtain both overall effectiveness and film effectiveness results for five flat plate, double-wall geometries. This data was then used to infer the convective cooling performance of each geometry at varying coolant flow rates, with preferable cooling features identified. The results indicate the high cooling performance achieved in double-wall, effusion cooled geometries.

Two computational methods were used to replicate the experimental setup utilising boundary conditions obtained from the facility. The first was a fully conjugate solver, and the second was a modified form of the developed decoupled method. The results from both sets of simulations compared favourably with the experimental data. The decoupled conjugate method was particularly encouraging given the vast reduction in simulation time required when compared to the fully conjugate solver.

Thermomechanical analyses were performed to identify how various geometric features influence the stress field developed under thermal load, which has direct implication on blade lifespan. The work was successful in indicating certain double-wall configurations which could reduce the magnitude of the stresses.

Acknowledgements

Firstly, I must express my gratitude to my supervisor Prof Peter Ireland. From my days as a final year undergraduate student to my present studies, Peter has always provided great enthusiasm, support and incredible knowledge which has helped make these past few years such a brilliant experience and one in which I feel my engineering ability has much advanced. His faith in my ability – faith which I scarcely had in myself – has been, and continues to be, a source of real encouragement.

I would also like to thank all the staff and technicians at the Oxford Thermofluids Institute for their guidance, friendship and support with the project work. I would particularly like to thank Jason McCluskey for his friendship and incredible ingenuity with getting the experimental facility up and running. In the workshop I'd particularly like to thank David O'Dell, Gerald Walker and Dave Mountain, along with Duncan Blake whom I'm sure will be quite glad to not have to drill anymore 30^{o} angled holes for me (hopefully…). I'd also like to thank the many postdocs and students who have been a great sounding board for my often ludicrous (and probably more often than not non-engineering related) ramblings. Amongst others, Marios Kapsis, Nicholas Holgate, Daniel Fahy, Alexander Bucknell and Olufemi Awe have proved particularly tolerant and so this must be noted.

Thanks also to Rolls-Royce PLC for their technical and financial support with the project. Eduardo Romero and Anton Rawlinson have provided great guidance along the way and have always demonstrated a genuine interest in the work. The work would also not have been possible without the EPSRC CDT in Gas Turbine Aerodynamics.

And thanks to all those friends who have encouraged me along the way, and who are too numerous to mention individually, but who have been of huge support over the last few years.

Finally, but most importantly, I'd like to thank my parents and my sister who have shown endless love and support which words cannot truly convey.

Contents

Abstract i

Acknowledgements iii

Nomenclature viii

1 Introduction 1

1.1 The Gas Turbine Cycle and the Necessity of Advancements in Turbine Cooling 1

1.2 Research Aims 6

1.3 Thesis Outline 7

1.4 Publications 9

2 Literature Review 11

2.1 Chapter Overview 11

2.2 Turbine Cooling Performance Metrics 11

2.3 Current Turbine Cooling Technologies 13

2.3.1 Internal Cooling Technologies 13

2.3.2 External Cooling Technologies – Film Cooling 15

2.3.3 Performance of Current Cooling Technologies 18

2.4 Double-Wall, Effusion Cooling Systems 19

2.4.1 Effusion Cooling 21

2.4.2 Literature on Double-Wall, Effusion Cooled Systems 23

2.5 Summary 27

3 Methods of Modelling Multiple Row Effusion Cooling Performance 28

3.1 Chapter Overview 28

3.2 Experimental Setup 28

3.2.1 Pressure Sensitive Paint Methodology 30

3.2.2 Study of Parametric Variations of Geometry 34

3.2.3 Experimental Operating Conditions and Measurement Uncertainties 35

3.3 Single Wall Effusion Cooling Computational Investigations....35
3.3.1 Passive Scalar Concentration Methodology....36
3.3.2 Multiple Row Effusion Cooling CFD Domain and Setup....37
3.3.3 Single Film Hole CFD Domain and Superposition Method for Multiple Ejection Modelling....38
3.4 Results....39
3.4.1 Further Investigation of Superposition in Effusion Cooling Performance Modelling....50
3.5 Summary....53
4 Geometrical Design Study....55
4.1 Chapter Overview....55
4.2 Diamond Pedestal Designs....55
4.3 Circular Pedestal Designs....57
4.4 Crenulation Concept Design....58
4.5 Summary....58
5 Decoupled Conjugate Method for Predicting Double-Wall, Effusion Cooling Performance....62
5.1 Chapter Overview....62
5.2 Internal Convective Cooling Model....62
5.2.1 Boundary Conditions....63
5.2.2 Mesh Independence Study and Turbulence Model Selection....63
5.3 External Film Model....66
5.4 Coupling of the Internal and External Cooling Models....67
5.5 Aerothermal Results....70
5.5.1 Film Effectiveness....70
5.5.2 Overall Effectiveness....72
5.5.3 Effective Porosity....79
5.6 Summary....82

6 Steady-State Thermomechanical Analyses 83
6.1 Chapter Overview 83
6.2 Thermomechanical Simulations of the Developed Double-Wall Geometries 84
6.2.1 FEA Domain and Setup 84
6.2.2 Results 85
6.3 Summary 92
7 Double-Wall Experimental Facility: Design and Commissioning 94
7.1 Chapter Overview 94
7.1.1 Facility Characteristics 94
7.2 Experimental Facility Design 97
7.2.1 Tunnel Fan Selection 97
7.2.2 Mainstream Heating Method and Flow Recirculation 99
7.2.3 Coolant Supply System 103
7.2.4 Facility Instrumentation 104
7.3 Commissioning Data for the Facility 113
7.4 Experimental Uncertainties 117
7.5 Summary 118
8 Results – Overall Effectiveness Measurements 119
8.1 Chapter Overview 119
8.2 Processing 119
8.3 Results 121
8.3.1 Overall Effectiveness Data 122
8.3.2 Pressure Ratio and Discharge Coefficient 139
8.3.3 Summary of Overall Effectiveness Performance 144
8.3.4 Experimental Uncertainties 146
8.4 Summary 147
9 Results – Film Effectiveness and Internal Convective Cooling Measurements 151
9.1 Chapter Overview 151

9.2 Processing 151
9.3 Results 152
9.3.1 Film Effectiveness 153
9.3.2 Convective Efficiency 162
9.3.3 Idealised Overall Effectiveness Trajectory 166
9.4 Experimental Uncertainties 168
9.5 Summary 168
10 Computational Methods to Simulate the Experimental Setup 171
10.1 Chapter Overview 171
10.2 Conjugate CFD of the Experimental Domain 171
10.3 Adapted Decoupled Conjugate Method 174
10.4 Results – Flow Aerodynamics and Heat Transfer 175
10.4.1 Effect of Varying Temperature Ratio and Biot Number 188
10.5 Summary 191
11 Summary and Concluding Remarks 192
11.1 Summary of the Experimental Work 192
11.2 Summary of the Aerothermal Computational Work 193
11.3 Summary of the Thermomechanical Computational Work 195
11.4 Suggestions for Future Work 196
11.4.1 Developments to the Experimental Facility 196
11.4.2 Developments to the Aerothermal Computational Work 197
11.4.3 Developments to the Thermomechanical Computational Work 198
12 Bibliography 199
Appendix A: Simple Cooling Analysis of an Isothermal Blade 208
Appendix B: Double-Wall Geometrical Investigation Range 209
Appendix C: Axisymmetric Double-Wall Thermomechanical Analyses 210
Appendix D: Manufacturing Methods 227

Nomenclature

Symbols

A	Area (m^2)
a	Speed of sound (m/s)
B	Bias uncertainty
$Bi\ (=hL/k_{sd})$	Biot number
C	Precision uncertainty or Mass fraction
C_d	Discharge coefficient
c_p	Specific heat capacity (constant pressure, $J/K.kg$)
C_R	Raw camera count
D	Diameter (m)
D_m	Mass diffusivity (m^2/s)
E	Young's modulus (Pa)
$h\ (or\ htc)$	Heat transfer coefficient ($W/m^2.K$)
k	Thermal conductivity ($W/m.K$)
K_D	Darcy Coefficient
K_F	Forchheimer Coefficient
K_{loss}	Loss coefficient
K_σ	Stress concentration factor
I	Current (A) or Image intensity
L	Length (m)
$Le\ (=\alpha/D_m)$	Lewis number
M	Blowing ratio
$\dot{M}$	Molecular flow rate ($kmol/s$)
$\dot{m}$	Mass flow (kg/s)
m^*	Non-dimensional mass flow
$Ma\ (=v/a)$	Mach number
MW	Molecular weight ($kg/kmol$)

n	Mole fraction
$Nu\ (=hL/k_{fl})$	Nusselt number
$\dot{Q}$	Heat flow (W)
$\dot{q}$	Heat flux (W/m^2)
q^*	Reflecting radiance ($W/m^2.Sr$)
q_{cam}	Camera incident radiance ($W/m^2.Sr$)
p	Pressure (Pa)
P	Non-dimensional pitch
PR	Pressure ratio
$Pr\ (= c_p\mu/k_{fl})$	Prandtl number
R	Specific gas constant ($J/kg.K$)
R_p	Pedestal fillet radius (m)
r	Radius (m)
$Re\ (= \rho vL/\mu)$	Reynolds number
S	Pitch (m)
s_ϕ	Source term
T	Temperature (K)
t	Time (s)
TKE	Turbulent kinetic energy (J/kg)
U	Total absolute uncertainty
V	Volume (m^3) or Volts (V)
v	Velocity (m/s)
$\dot{W}$	Power (W)
x	Streamwise direction (m)
y	Vertical direction (m)
z	Spanwise direction (m)
$z_{1/2}$	Spanwise distance at which film effectiveness halves (m)

Greek Characters

α	Thermal diffusivity (m^2/s)
β	Coefficient of thermal expansion

Γ	Diffusivity (m^2/s)
γ	Ratio of specific heat capacities
ε_o	Overall effectiveness
η	Efficiency
η_c	Convective efficiency
η_f	Film effectiveness
Θ	Dimensionless temperature ratio
θ	Circumferential direction
λ	Wavelength (m)
μ	Dynamic viscosity ($Pa.s$)
ν	Poisson's ratio
ξ	Emissivity
ρ	Density (kg/m^3)
σ	Stress (Pa)
$\bar{\sigma}$	Nominal stress (Pa)
σ_b	Stefan-Boltzmann constant ($W/m^2.K^4$)
σ_{VM}	Equivalent (Von Mises) stress (Pa)
σ_y	Yield Stress (Pa)
τ	Transmissivity
ϕ	Scalar quantity
ϕ_f	Geometric porosity of external surface
ϕ_{eff}	Effective porosity
ψ	Phase angle (^{o})

Subscripts

0	Total or Initial
amb	Ambient
actual	Actual property
atm	Atmospheric
ave	Average
aw	Adiabatic wall

b	Distance between pedestals
bb	Blackbody
c	Coolant property
cam	Camera property
c,e	Coolant at film hole exit
c,i	Coolant at inlet
comp	Compressor property
cond	Conduction
cycle	Thermodynamic cycle property
decay	Film decay variable
engine	Engine property
ext	External
f	Film property
fl	Fluid property
h	Hydraulic
i	Impingement property
ideal	Ideal property
in	Inlet
int	Internal
l	Laminar
local	Local property
m	Metal property
max	Maximum
mesh	Mesh property
min	Minimum
mix	Mixture
nt	Nozzle throat
opt	Optical property
out	Outlet
p (or ped)	Pedestal property
ref	Reference

rig	Rig property
s	Static
sd	Solid property
surf	Surface
t	Turbulent
th	Thermal
thermo	Thermocouple property
turb	Turbine property
vol	Volume
w	Wall property
∞	Mainstream gas property

Abbreviations

CFD	Computational fluid dynamics
CFVN	Critical flow Venturi nozzle
CPU	Central processing unit
DCM	Decoupled conjugate method
DoE	Design of experiments
EDM	Electrical discharge machining
FEA	Finite element analysis
FoV	Field of view
HP	High pressure
IR	Infrared
LE	Leading edge
LES	Large eddy simulation
NaN	Not a number
NGV	Nozzle guide vane
PSP	Pressure sensitive paint
TBC	Thermal barrier coating
TET	Turbine entry temperatures
UV	Ultraviolet

1 Introduction

The modern era of aviation propulsion has been significantly influenced by an increasing public awareness of the environmental damage attributed to industrialisation. The result has been the tightening of regulations in the aviation industry with a drive to reduce specific fuel consumption and carbon dioxide emissions. Flightpath 2050 [1] (developed by the Advisory Council for Aviation research and Innovation in Europe, *ACARE*) provides an example of this with a target reduction in CO_2 emissions of 75% by the year 2050 (among other environmental targets). Increasing the efficiency of the gas turbine cycle provides one means by which this can be achieved, and this is discussed in the following section, along with the implications for turbine cooling.

1.1 The Gas Turbine Cycle and the Necessity of Advancements in Turbine Cooling

The necessity of advancements in gas turbine cooling can be explained with reference to the thermodynamic cycle occurring within a gas turbine – a cycle often termed the Joule cycle. In its simplest form, the cycle can be described by three stages which are visually depicted in the upper left corner of Figure 1.1:

1 – 2s: *Isentropic compression of the gas*

2s – 3: *Isobaric heat addition*

3 – 4s: *Isentropic expansion of the gas*

Figure 1.1 also demonstrates the temperature-entropy plot that results from these three stages.

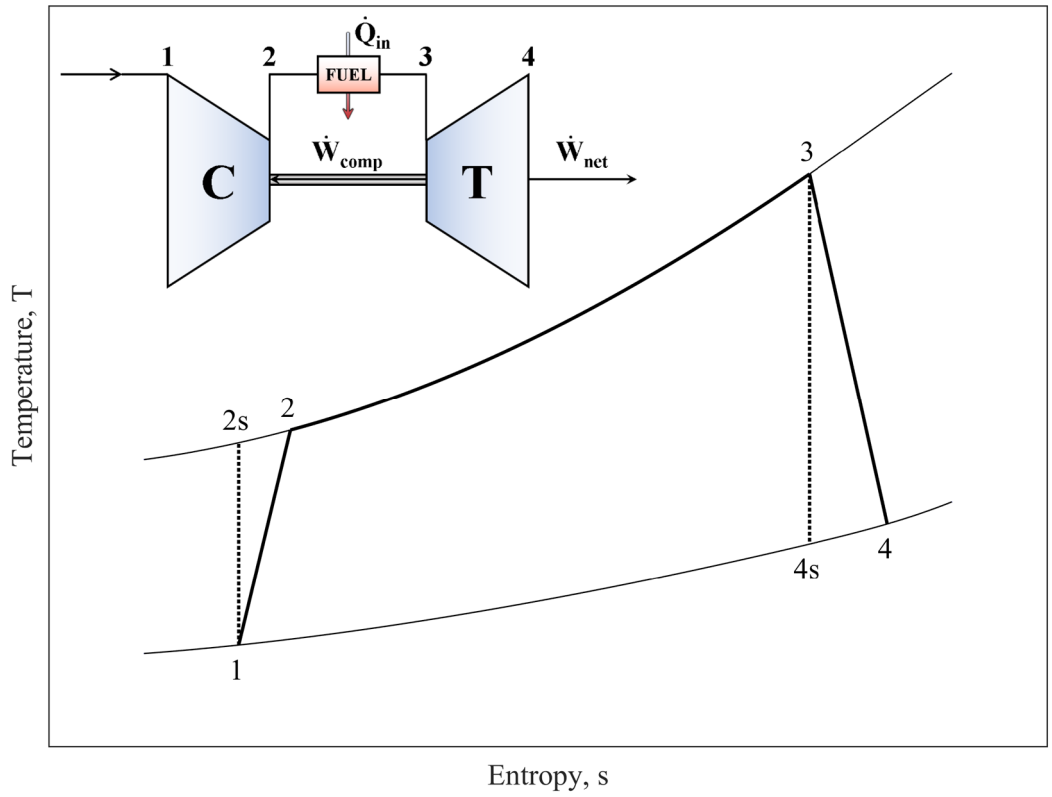


Figure 1.1 - Temperature-entropy plot for the gas turbine thermodynamic cycle showing ideal (denoted by isentropic stations 2s and 4s), and non-ideal stations arising due to entropy creation during compression and expansion of the gas. A simple gas turbine schematic showing the respective stations is also demonstrated

In an idealised model of the gas turbine cycle, the compression process between 1-2, and the expansion process between 3-4 can be considered isentropic (i.e. both adiabatic and reversible). In reality, whilst it is reasonable to consider these processes to be adiabatic, an increase in entropy means they cannot be considered reversible. Therefore, isentropic efficiencies are introduced for these processes as defined in equations 1.1.

$$\eta_{comp} = \frac{T_{02s} - T_{01}}{T_{02} - T_{01}} \qquad \text{and} \qquad \eta_{turb} = \frac{T_{03} - T_{04}}{T_{03} - T_{04s}} \tag{1.1}$$

Consequently, during compression of the gas, there is an increase in entropy and a resulting larger increase in temperature, whilst during expansion, there is a smaller decrease in gas temperature and an increase in entropy. With knowledge of the pressure ratio within the turbine (where the combustor is assumed to incur no pressure drop), the isentropic temperature ratios can simply be obtained based on polytropic relations.

The compressor power requirement and turbine power output for the non-isentropic components can be calculated as in equations 1.2 and 1.3, where the pressure ratio is denoted as $p_{02}/p_{01} = p_{03}/p_{01} = PR$.

$$\dot{W}_{comp} = \dot{m}c_p(T_{02} - T_{01}) = \frac{\dot{m}c_p(T_{02s} - T_{01})}{\eta_{comp}} = \frac{\dot{m}c_p T_{01}\left(\mathrm{PR}^{\gamma-1/\gamma} - 1\right)}{\eta_{comp}} \tag{1.2}$$

$$\dot{W}_{turb} = \dot{m}c_p(T_{03} - T_{04}) = \eta_{turb}\dot{m}c_p(T_{03} - T_{04s}) = \eta_{turb}\dot{m}c_p T_{03}\left(1 - \frac{1}{\mathrm{PR}^{\gamma-1/\gamma}}\right) \tag{1.3}$$

The net work available is calculated as the difference between the turbine power output and compressor power requirement as in equation 1.4.

$$\dot{W}_{net} = \dot{W}_{turb} - \dot{W}_{comp} = \dot{m}c_p T_{01}\left(\eta_{turb}\frac{T_{03}}{T_{01}}\left(1 - \frac{1}{\mathrm{PR}^{\gamma-1/\gamma}}\right) - \frac{\left(\mathrm{PR}^{\gamma-1/\gamma} - 1\right)}{\eta_{comp}}\right) \tag{1.4}$$

The thermal efficiency of the cycle can be obtained by evaluating the net work output from the cycle, to the heat addition arising from fuel combustion (stages 2 – 3) as per equation 1.5.

$$\begin{aligned}\eta_{cycle} = \frac{\dot{W}_{net}}{\dot{Q}_{in}} &= \frac{T_{01}\left(\eta_{turb}\frac{T_{03}}{T_{01}}\left(1 - \frac{1}{\mathrm{PR}^{\gamma-1/\gamma}}\right) - \frac{\left(\mathrm{PR}^{\gamma-1/\gamma} - 1\right)}{\eta_{comp}}\right)}{(T_{03} - T_{02})} \\ &= \frac{\left(\eta_{turb}\frac{T_{03}}{T_{01}}\left(1 - \frac{1}{\mathrm{PR}^{\gamma-1/\gamma}}\right) - \frac{\left(\mathrm{PR}^{\gamma-1/\gamma} - 1\right)}{\eta_{comp}}\right)}{\frac{T_{03}}{T_{01}} - \frac{\left(\mathrm{PR}^{\gamma-1/\gamma} - 1\right)}{\eta_{comp}} - 1}\end{aligned} \tag{1.5}$$

The result of the above analysis is graphically demonstrated in Figure 1.2, where both the cycle efficiency (based on equation 1.5) and dimensionless net power output (equation 1.4) at various pressure ratios (*PR*) are shown for four different temperature ratios. In the plots, the isentropic efficiencies of the compressor and turbine are equal and set to 0.9 whilst the ratio of

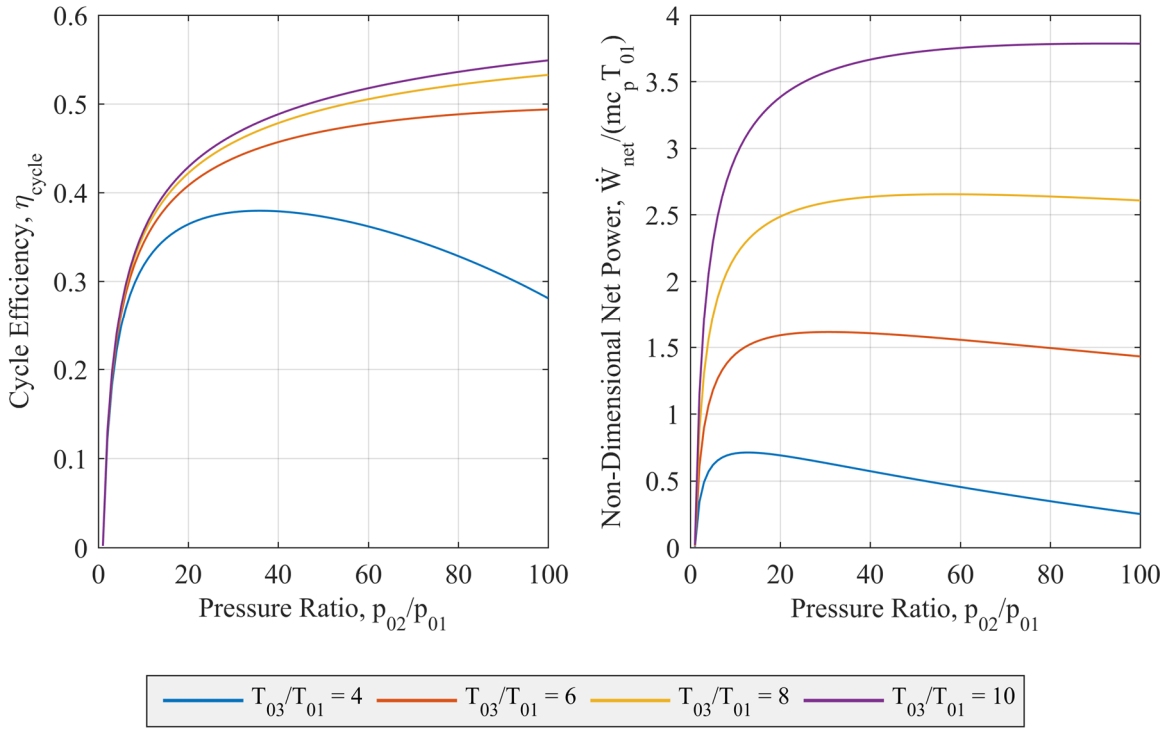


Figure 1.2 - Pressure ratio against Left) cycle thermal efficiency (based on equation 1.5) and Right) net power output (based on equation 1.4) at various temperature ratios

specific heat capacities is taken to be 1.4 [2]. It is noted that a modern gas turbine has an approximate pressure ratio of 40 and temperature ratio of 6.

The above discussion pertaining to the thermodynamic cycle occurring within the gas turbine demonstrates the dependence of cycle efficiency and specific power output on both the pressure ratio achieved, and the temperature ratio T_{03}/T_{01}. It is apparent from Figure 1.2 that increasing pressure ratio and temperature ratio are means by which the both the efficiency of the gas turbine and specific power output can be raised. Indeed, elevation of the specific power output of the turbine permits turbine core sizes to be reduced resulting in lower engine weight, whilst increasing cycle efficiency directly reduces specific fuel consumption. Further characterisation of total engine efficiency considers the propulsive efficiency. Turbofan engines, typically featured on commercial aircraft, feature high bypass ratios. For a given nacelle size, a reduction in core size – which can be achieved through increasing core specific power output – results in greater engine bypass ratios; consequently, propulsive efficiency is observed to increase.

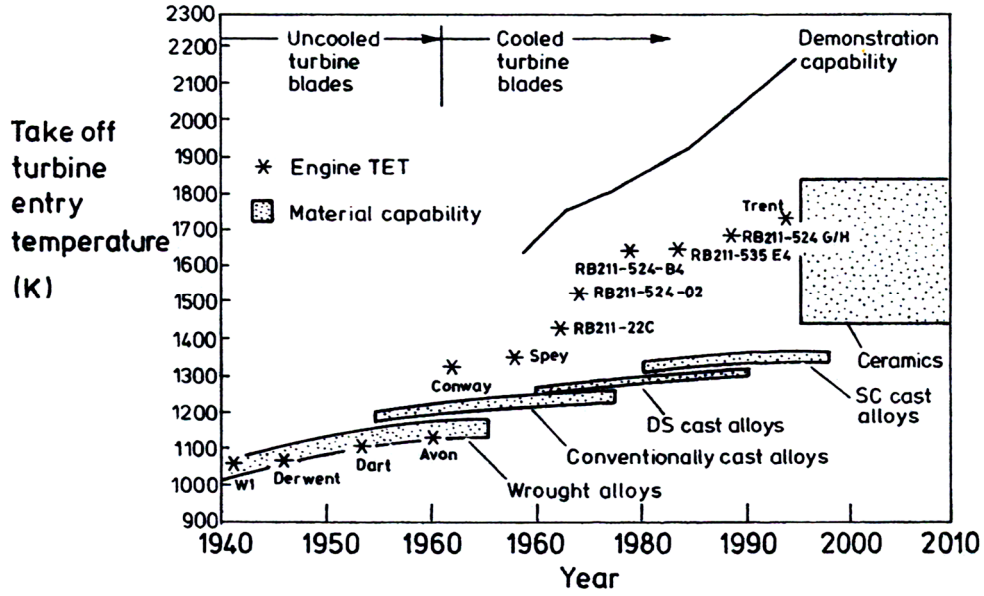


Figure 1.3 - Turbine entry temperatures (TET) for Rolls-Royce PLC engines (figure from 1993) [2]

The consequence of the above analysis is the increasing temperature (and pressure) ratios in commercial gas turbines. Indeed, Figure 1.3 demonstrates how turbine entry temperatures (*TET*, here demonstrated by T_{03}) have increased over the years. The figure is interesting in identifying several developments that have helped make these temperature increases possible.

The advancement in material capabilities is apparent in the figure which demonstrates approximate temperature limits for the various types of materials. Early turbine blades relied simply on wrought alloys before moving on to conventional cast materials. Current technologies rely on directionally grown single crystal cast superalloys (typically nickel based superalloys) which exhibit good creep resistance. The figure also demonstrates the impressive temperature capabilities of ceramics, although other ceramic properties currently mean their use for blade construction is not feasible. However, ceramic coatings (termed thermal barrier coatings or *TBCs*) are often applied to the external surface of turbine blades (typically yttria-stablised zirconia). These TBCs coat the blade with a thickness of between 100 – 400 μm [3]. The low thermal conductivity of the coating results in an increased thermal resistance and reduction in temperature seen by the underlying metal blade.

The figure also demonstrates the necessity of blade cooling. Early turbine blades were uncooled as the material capabilities were sufficiently high to withstand the core gas temperatures. However, the increase in TETs quickly exceeded the developments in the material technologies. Consequently, active cooling of the components became necessary.

The coolant supply is air typically syphoned off from the latter stages of the compressor prior to the core gas entering the combustion chamber. This coolant air is therefore itself at temperatures of approximately 1000 K in a modern gas turbine. However, as the coolant is extracted from the compressed core air and does not produce any useful work, it represents a source of loss. As a result, advancements in turbine blade cooling are generally characterised by systems featuring higher convective efficiency and cooling effectiveness, whilst simultaneously reducing the quantity of percentage coolant airflow extracted from the core compressed gas.

1.2 Research Aims

Below are detailed some of the primary aims of the research presented in this thesis:

- Perform a design study to obtain a range of double-wall geometries which can be used to assess how varying the geometric parameters influences both aerothermal and thermomechanical performance.

- Develop a computational method which can be used to predict the cooling performance of a double-wall geometry at the early design stages.

- Design and commission an experimental facility to be used to obtain overall cooling effectiveness and film effectiveness measurements from flat plate, double-wall cooling geometries.

- Develop a computational model of the experimental setup allowing simulations to be performed permitting the flow features occurring within the double-wall geometry to be ascertained.

- Begin to develop an understanding of the thermomechanical stress field developed in double-wall systems under thermal load.

1.3 Thesis Outline

A chapter-by-chapter outline of the thesis is provided below:

- Chapter 2 provides an overview of existing gas turbine cooling technologies and a literature review pertaining to studies performed which investigate double-wall type cooling systems.

- Chapter 3 presents an experimental and computational study used to assess single wall effusion cooling performance. The results of the study are used in the validation of an additive superposition model applied to model two-dimensional streamwise film development from multiple film holes.

- Chapter 4 presents an overview of the double-wall geometries investigated in this thesis which can be separated into three general forms: those incorporating diamond pedestals, those with circular pedestals, and a crenulation concept geometry.

- Chapter 5 discusses the development of a *decoupled conjugate* method for assessing the aerothermal cooling performance of double-wall geometries at a relatively light computational cost. Simulations are performed on all the geometries presented in Chapter 4 with the results of the simulations used in a preliminary assessment of those geometric features which display preferable aerothermal characteristics.

- Chapter 6 presents thermomechanical work performed to inform how the various geometric parameters influence the stress field developed under thermal load. The work considers three-dimensional geometries where solid temperature profiles are based on the results of Chapter 5. A further study which considers a simplified axisymmetric model is presented in Appendix C. For this analysis, a code was developed to predict the temperature profile.

- Chapter 7 discusses the development of a new, novel experimental facility used to measure the cooling performance of flat plate, double-wall geometries. The facility attempts to match a number of relevant dimensionless parameters to those seen at engine conditions. Commissioning data from the facility is provided.

- Chapters 8 and 9 present experimental data obtained from the facility which includes overall effectiveness and film effectiveness data. This data is then used to infer the total cooling contributions arising in each geometry from internal convective cooling, and the external film cooling. Various other relevant aerothermal measurements are provided along with the calculated uncertainty in the measured and derived quantities.

- Chapter 10 presents computational simulations performed to mimic the experimental setup based on experimentally obtained boundary conditions. These include fully conjugate CFD simulations of the experimental domain along with a modified version of the decoupled conjugate method presented in Chapter 5. The results of the simulations are encouraging, particularly with regards to the decoupled method which required approximately one-hundredth of the computational processing time.

1.4 Publications

Journal Papers

A. V. Murray, P. T. Ireland, and E. Romero, 'Development of a Steady-State Experimental Facility for the Analysis of Double-Wall Effusion Cooling Geometries', *J. Turbomach.*, Oct. 2018.

A. V. Murray, P. T. Ireland, T. H. Wong, S. W. Tang, and A. J. Rawlinson, 'High Resolution Experimental and Computational Methods for Modelling Multiple Row Effusion Cooling Performance', *Int. J. Turbomach. Propuls. Power*, vol. 3, no. 1, p. 4, Jan. 2018.

G. C. Ngetich, P. T. Ireland, A. V. Murray, and E. Romero, 'A 3D Conjugate Approach for Analysing a Double-Walled Effusion-Cooled Turbine Blade', *J. Turbomach.*, Sep. 2018.

Conference Papers

A. V. Murray, P. T. Ireland, and E. Romero, 'Experimental and Computational Methods for the Evaluation of Double-Wall, Effusion Cooling Systems', in *ASME Turbo Expo 2019: Turbomachinery Technical Conference and Exposition*, Phoenix, AZ, USA, 2019

A. V. Murray, P. T. Ireland, and E. Romero, 'Development of a Steady-State Experimental Facility for the Analysis of Double-Wall Effusion Cooling Geometries', in *ASME Turbo Expo 2018: Turbomachinery Technical Conference and Exposition*, Oslo, Norway, 2018

A. V. Murray, P. T. Ireland, and A. J. Rawlinson, 'An Integrated Conjugate Computational Approach for Evaluating the Aerothermal and Thermomechanical Performance of Double-Wall Effusion Cooled Systems', in *ASME Turbo Expo 2017: Turbomachinery Technical Conference and Exposition*, Charlotte, NC, USA, 2017

A. V. Murray, P. T. Ireland, T. H. Wong, S. Tang, and A. J. Rawlinson, 'High Resolution Experimental and Computational Methods for Modelling Multiple Row Effusion Cooling Performance', in *12th European Conference on Turbomachinery Fluid Dynamics & Thermodynamics*, Stockholm, Sweden, 2017.

Y. Jiang, A. V. Murray, P. T. Ireland, and L. di Mare, 'Jets Interaction in Effusion Cooling, Part I: Experimental and Numerical Study', in *ASME Turbo Expo 2019: Turbomachinery Technical Conference and Exposition*, Phoenix, AZ, USA, 2019

G. C. Ngetich, P. T. Ireland, A. V. Murray, and E. Romero, 'A 3D Conjugate Approach for Analysing a Double-Walled Effusion-Cooled Turbine Blade', in *ASME Turbo Expo 2018: Turbomachinery Technical Conference and Exposition*, Oslo, Norway, 2018

Under Review

A. V. Murray, P. T. Ireland, and E. Romero, 'Experimental and Computational Methods for the Evaluation of Double-Wall, Effusion Cooling Systems', *J. Turbomach.*

E. Elmukashfi, A. V. Murray, P. T. Ireland, and A. C. F. Cocks, 'Analysis of the thermo-mechanical Stresses in Double-Wall Effusion Cooled Systems", *J. Turbomach.*

Y. Jiang, A. V. Murray, P. T. Ireland, and L. di Mare, 'Jets Interaction in Effusion Cooling, Part I: Experimental and Numerical Study', *J. Turbomach.*

***Patents** (Submitted Applications)*

A. V. Murray, P. T. Ireland, E. Romero and A. J. Rawlinson, 'A Double-Wall Geometry'

N. Ashton, P. T. Ireland, A. V. Murray and E. Romero, 'Novel Pedestal shape to increase HTC and reduce pressure drop'

2 Literature Review

2.1 Chapter Overview

This chapter provides a further insight into the context for the current research. The chapter begins by introducing various metrics used in assessing the aerothermal performance of turbine cooling systems which are used throughout the thesis. Following this is provided a summary of some current turbine cooling technologies, which is by no means exhaustive, but rather suffices to permit the reader to ascertain how the technology under investigation in this thesis relates to currently implemented cooling systems. Finally, the chapter discusses literature more directly pertaining to double-wall type systems, or systems which incorporate effusion cooling type technology.

2.2 Turbine Cooling Performance Metrics

In the early stages of cooling system design, several metrics are used in assessing the potential cooling benefits of a particular system. Several of these, which will be used throughout this thesis, are defined here for reference.

The cooling benefit achieved by a system is typically presented as a non-dimensional temperature ratio termed the overall effectiveness (ε_o) defined in equation 2.1. A value of unity indicates a perfectly cooled system in which the metal temperature is equal to that of the incoming coolant. It can therefore be considered to provide an overall assessment of the cooling scheme being utilised.

$$\varepsilon_o = \frac{(T_\infty - T_m)}{(T_\infty - T_{c,i})} \qquad (2.1)$$

The efficiency of the heat exchanger is characterised by the convective efficiency (η_c) and is demonstrated in equation 2.2 from which it is apparent that a value of unity indicates that the cooling medium has reached the metal temperature. Performance heat exchangers are characterised by high convective efficiencies.

$$\eta_c = \frac{(T_{c,e} - T_{c,i})}{(T_m - T_{c,i})} \tag{2.2}$$

The non-dimensional mass flow rate, *m** (sometimes termed the heat load parameter [4], [5]) is defined in equation 2.3 and describes the ratio of internal heat fluxes to those external to the blade. It is useful in allowing the comparison of various cooling systems with varying absolute coolant mass flow rates.

$$m^* = \frac{\dot{m}_c c_p}{\bar{h} A_{ext}} \tag{2.3}$$

Note, equations 2.1 – 2.3 can be related via a simplified analysis of an isothermal blade with a uniform external temperature field subject to internal convective cooling. The result of the analysis is shown in equation 2.4 with the derivation provided in Appendix A.

$$\varepsilon_o = \frac{\eta_c m^*}{1 + \eta_c m^*} \tag{2.4}$$

The result of this simplified analysis is plotted in Figure 2.1. The figure demonstrates the significant increase in overall cooling effectiveness at equivalent mass flows as convective efficiency is increased. The figure also shows a strong dependence on coolant flow rate.

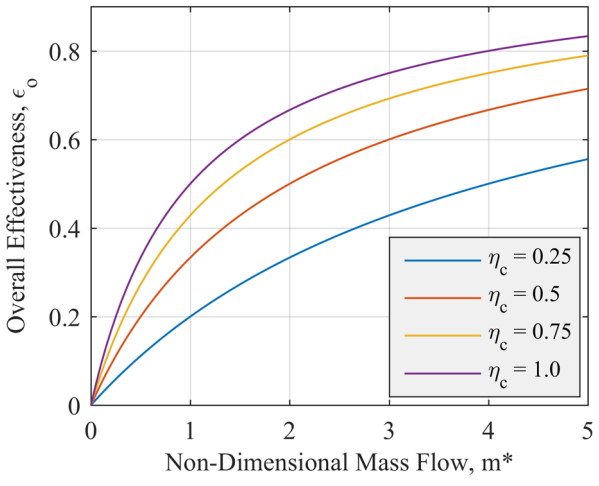


Figure 2.1 - Relation between ε_o, m and η_c*

2.3 Current Turbine Cooling Technologies

Below follows a succinct overview of current technologies implemented in turbine cooling systems. These have been separated into those cooling system features implemented either internally or externally on a turbine blade. Several of these cooling features are demonstrated in Figure 2.2 (adapted from [6]). It is noted that a number of these current technologies feature heavily in the double-wall cooling systems to which this work pertains.

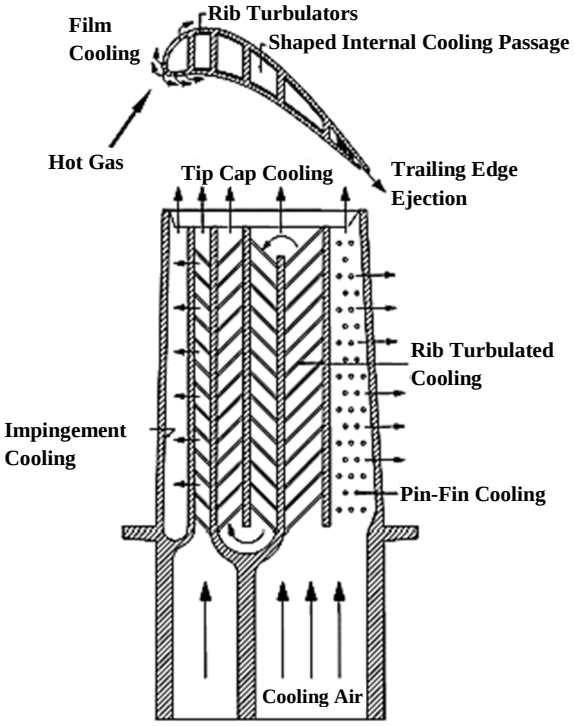


Figure 2.2 - Diagram showing several conventional cooling schemes implemented on HP turbine blades [6]

2.3.1 Internal Cooling Technologies

- *Straight Duct Passages* – Among the simpler cooling mechanisms is the internal cooling passage which provides a path via which coolant can flow through the blade. More advanced forms exhibit a "serpentine" pathway where the coolant makes multiple passes along the blade span prior to being expelled into the external flow [7]. These systems typically exhibit convective efficiencies of 15-30%, although higher values are possible with multi-pass pathways [4].

- *Pedestals/Pin-Fins* – Pedestals typically find application towards the trailing edge of a blade (as demonstrated in Figure 2.2). They act to increase heat transfer, help control trailing edge exit pressures and provide a mechanical support between the two external blade walls. By mechanically connecting these walls, pedestals also permit conduction to occur between them alleviating thermal stresses that arise as a result of the temperature gradient between

the two walls. The pedestals are shaped to provide suitable heat transfer characteristics whilst also considering the incurred pressure losses. Typically, circular pedestals featured at the trailing edge demonstrate a small height-to-diameter ratio (y/D_p between 0.5 – 4 [8]). Pedestal arrays are normally of two forms: inline configurations and staggered configurations. Area-averaged heat transfer coefficients are generally observed to be higher for staggered configurations [9]–[11] with maximum heat transfer typically occurring later (normally one row later) [10]–[12]. Generally, the cooling effect of the pedestals is shown to be related to the pedestal aspect ratio, shape, configuration, flow Reynolds number and fillet size [10], [13]. Pedestals form an integral part of the double-wall, effusion system and further discussion on their incorporation in such systems is presented later.

- *Impingement Cooling* – Impingement cooling is the term applied to the impingement of a high velocity coolant jet – typically through pores on an internal wall – onto the target wall on which a high cooling effect is desired. The impact of the high velocity jet on the target surface causes a large local increase in heat transfer coefficients – an increase suggested to be the greatest among all heat transfer enhancement methods [6], [14]. Impingement cooling is most commonly found at the leading edge of HP turbine rotor blades, a region typically subjected to the greatest thermal load. The heat transfer achieved by impingement cooling is found to depend on a range of factors. Among the most significant of these include the jet Reynolds number (Re_i), the spacing of the impingement hole to the target surface (y/D_i), hole geometry/inclination and internal crossflow effects. Highest heat transfer rates are typically observed around the stagnation point. Moving radially outwards from the stagnation point, heat transfer rates decrease. For closely positioned target walls ($y/D_i < 2$), secondary peaks in heat transfer are observed outside of the stagnation region and are thought to result from heat transfer enhancement attributed to vortex rings in the shear layer [15], and for low Re_i a third peak has been observed [16]

which has been attributed to boundary layer transition. Crossflow has also been shown to be detrimental to impingement cooling. Rhee et al. [17] demonstrated that for crossflow velocities equal or greater than those of the impinging jets, stagnation point Nusselt numbers were notably reduced due to the effect of impingement jet sweeping. Indeed, even small crossflows have been shown to be detrimental to the impingement heat transfer effect [18]. Prediction of impingement zone heat transfer rates are typically based upon empirical correlations. CFD simulations are also frequently used, however, prediction of impingement heat transfer is relatively inaccurate using less computationally intensive turbulence models, and large eddy simulations (*LES*), whilst providing good accuracy, have high computational resource requirements [19].

- *Rib-Turbulators* – Ribs typically feature along the mid-chord region of the blade and are integrated along the serpentine duct passage. The basic function of the rib is to disrupt the boundary layer. The rib causes a separation region. Downstream of the rib, the boundary layer restarts with a corresponding increase in heat transfer rates. The ribs can also be angled to the oncoming flow or incorporate a chevron form. The angling of the ribs introduces secondary flow features within that of the main cooling flow direction resulting in an enhancement in heat transfer [6], [20], [21]. The heat transfer enhancement is observed to be a function of rib geometry including the height, pitch, inclination angle and oncoming flow Reynolds number [22].

2.3.2 External Cooling Technologies – Film Cooling

Thermal barrier coatings, briefly mentioned in the introduction, provide one method whereby the surface temperature of the metal blade can be reduced via an increase in the thermal resistance between this surface and the mainstream core gas. Film cooling is another commonly implemented method whereby cooling of the external blade surface is achieved.

Film cooling is the term applied to the process in-which the internal coolant is discharged through discrete film holes located in the blade surface forming a protective film of cooler air over the outer surface of the blade; a process demonstrated in Figure 2.3. The cooling benefit attributed to film cooling can be separated into two processes. The first is the effective reduction in the temperature driving heat transfer from the mainstream flow to the blade surface. The second is the internal convective cooling effect within the discrete film holes. These are further elaborated upon below.

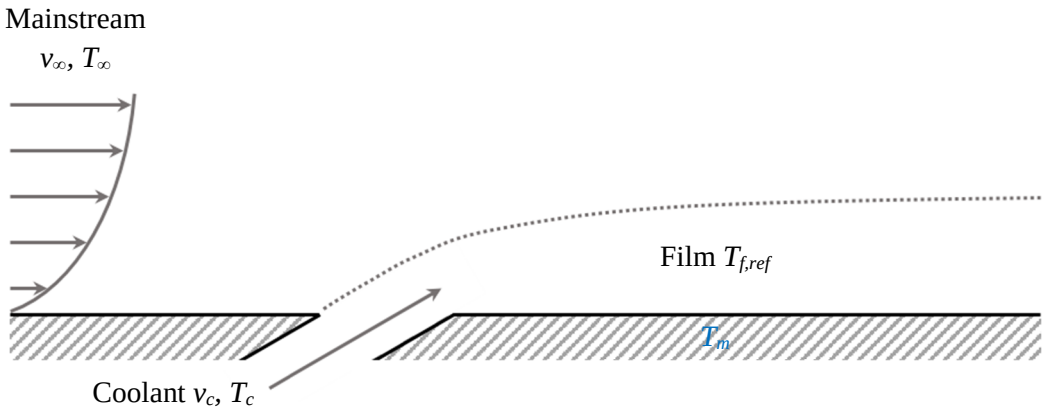


Figure 2.3 - Diagram demonstrating the discharge of coolant through a film hole and into the mainstream flow forming a protective film of spent coolant over the blade surface

The heat flux to the surface of the blade can be expressed as per equation 2.5.

$$\dot{q} = h(T_{f,ref} - T_m) \tag{2.5}$$

As noted in [23], for the heat transfer coefficient to be independent of the coolant temperature, the adiabatic wall temperature is typically taken as the film reference temperature and is representative of the fluid temperature immediately above the surface (or the surface temperature of a perfectly insulated solid). The heat transfer coefficient in the presence of cooling films is thus characterised by equation 2.6, whilst the heat transfer coefficient that occurs when there are no cooling films is shown in equation 2.7.

$$\dot{q}_f = h_f(T_{aw} - T_m) \qquad (2.6)$$

$$\dot{q}_\infty = h_\infty(T_\infty - T_m) \qquad (2.7)$$

Consequently, the reduction in heat flux due to the presence of the cooling film can be derived as in equation 2.8.

$$\frac{\Delta\dot{q}}{\dot{q}_\infty} = 1 - \frac{\dot{q}_f}{\dot{q}_\infty} = 1 - \frac{h_f(T_{aw} - T_m)}{h_\infty(T_\infty - T_m)} = 1 - \frac{h_f}{h_\infty}\left(1 - \frac{\eta_f}{\varepsilon_o}\right) \qquad (2.8)$$

Equation 2.8 demonstrates that the reduction in heat flux to the blade surface in the presence of films can be presented as a function of the *h* ratio with and without film cooling, the overall cooling effectiveness defined in equation 2.1, and the adiabatic film effectiveness, η_f, a parameter defined in equation 2.9 that is used to quantify the film cooling performance.

$$\eta_f = \frac{T_\infty - T_{aw}}{T_\infty - T_{c,e}} \qquad (2.9)$$

The ejection of coolant films into the mainstream flow often causes a heat transfer augmentation effect [24] due to the increased turbulence that results (due to the formation of a counter rotating vortex pair and potential flow separations occurring for film jets with high momentum [25]). Therefore, as demonstrated in equation 2.8, both the adiabatic film cooling effectiveness and heat transfer augmentation with films needs to be considered to fully quantify the film cooling benefit in a particular application.

Film effectiveness is observed to be a strong function of the film blowing ratio. Blowing ratio is the term used to describe the ratio of coolant to mainstream mass flux and is demonstrated in equation 2.10.

$$M = \frac{\rho_c v_c}{\rho_\infty v_\infty} \qquad (2.10)$$

For cylindrical holes, optimal films are typically formed between blowing ratios of approximately 0.3 – 0.7 [26]–[28]. Similar observations are made for fanned holes although

improved film performance can be achieved at higher blowing ratios by further shaping of the holes [29] and incorporating compound angles. Films operating at higher than optimal blowing ratios typically experience film jet lift-off where films demonstrate poor adhesion to the blade surface, although reattachment may occur downstream of the injection site. At high blowing ratios, heat transfer coefficient augmentation is also observed to increase [30]. Other significant parameters in film cooling include the pitching of the holes, the coolant-to-mainstream density ratio, mainstream turbulence, blade surface curvature and roughness.

Film cooling forms a significant part of the double-wall system (in the form of effusion cooling) and this will be further discussed below.

2.3.3 Performance of Current Cooling Technologies

The cooling systems presented above demonstrate varying aerothermal performance. Often the technologies are combined in a turbine cooling geometry with various systems implemented in different sections of the blade depending on the required cooling effectiveness, or the integral strength of a blade region. Figure 2.4 [31] demonstrates the cooling effectiveness achieved for various cooling systems at a range of coolant flow rates (as a percentage of core flow).

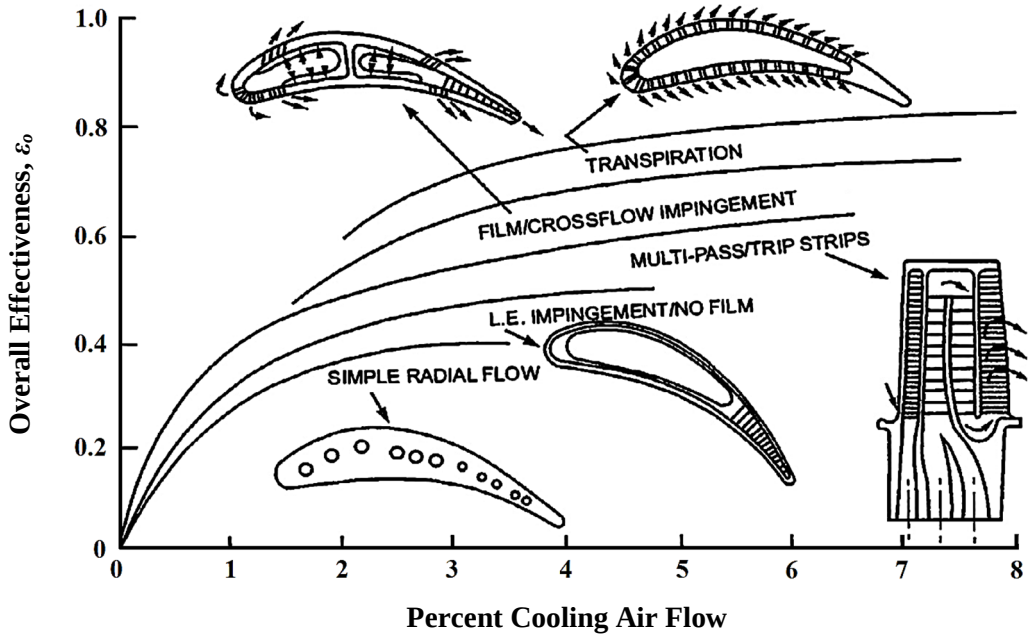


Figure 2.4 – Overall cooling effectiveness achieved for various turbine cooling systems at varying coolant air flows [31]

The graph neatly demonstrates how increasingly complex internal cooling configurations demonstrate higher overall cooling effectiveness at similar coolant flow rates; a phenomenon indicative of higher convective efficiencies. It is also observed that the rate of increasing overall effectiveness diminishes as coolant volume is further increased. For blades requiring high cooling effectiveness, this therefore necessitates the use of copious coolant quantities at the detriment of cycle efficiency. Thus exists the drive for more complex cooling systems which demonstrate both high internal convective and external film cooling performance such as transpiration cooling systems (characterised by an intrinsic material porosity), or, as in the case of the current research, quasi-transpiration systems.

2.4 Double-Wall, Effusion Cooling Systems

The present work investigates a novel turbine cooling technology termed the double-wall, effusion cooling system. Due to the high manufactured porosity, the system can be considered to be a quasi-transpiration type technology. It incorporates elements of conventional turbine cooling systems in a more optimal configuration. The double-wall, effusion cooled system is characterised by two walls, one with impingement holes through which coolant enters, impinging on the second outer wall, with film holes embedded in a regular, closely packed array commonly associated with effusion cooling. The two walls are mechanically connected via an array of pedestals which increase coolant wetted area relative to conventional multi-pass systems, and promote flow mixing between the walls. Additionally, the pedestals provide a conduction pathway between the two walls, potentially reducing temperature gradients that could lead to thermal fatigue. Figure 2.5 demonstrates a flat plate model of a double-wall, effusion cooled system incorporating circular pedestals, whilst the same double-wall configuration is applied (in a non-optimal manner) to a turbine blade type geometry in Figure 2.6.

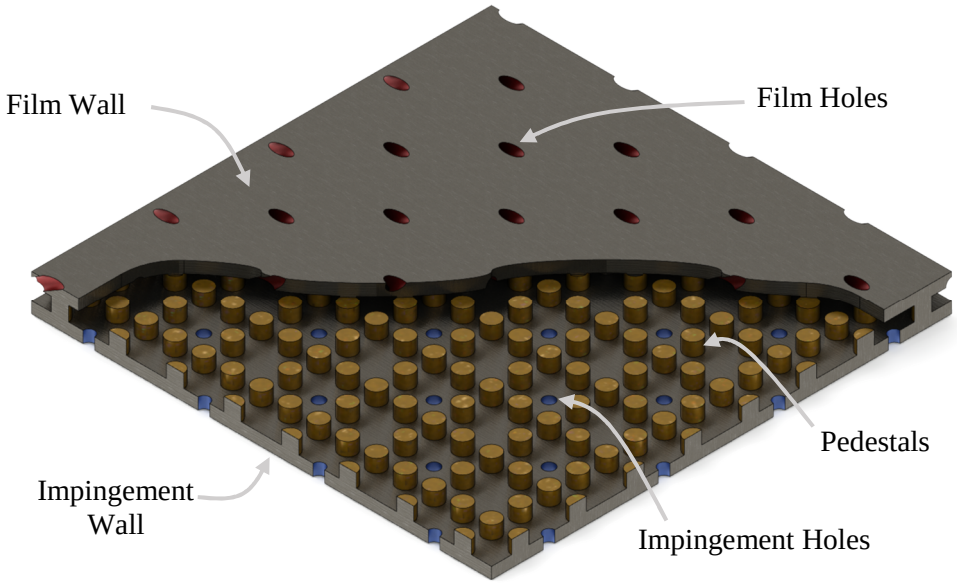


Figure 2.5 – Section-view flat plate diagram demonstrating the various elements of a double-wall, effusion cooled system incorporating circular pedestals

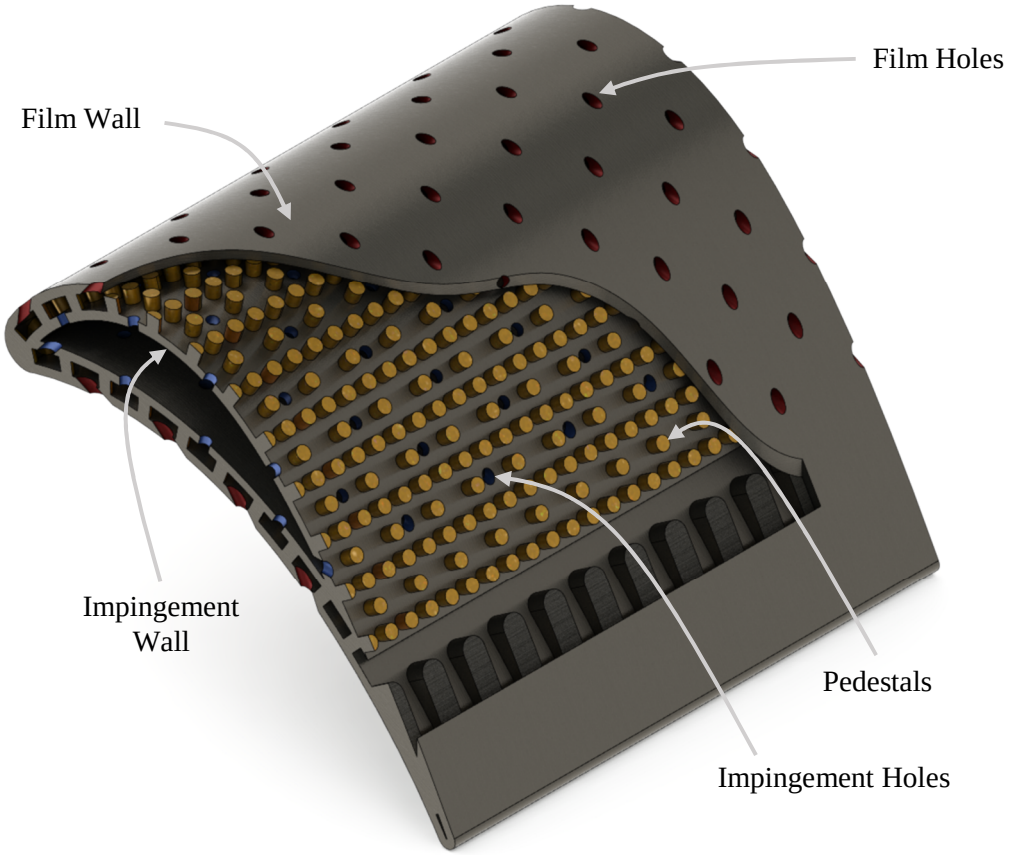


Figure 2.6 – Section-view turbine blade concept incorporating double-wall, effusion cooling (in a non-optimised form)

Effusion cooling – sometimes termed full coverage film cooling – forms a key element in the double-wall system and so, prior to a literature survey on double-wall systems, a brief discussion follows on single wall effusion cooling and key considerations in such systems.

2.4.1 Effusion Cooling

Effusion cooling can be considered a more optimal form of film cooling with the cooling principles largely unchanged. Effusion cooling differs from film cooling then only in the arrangement of the films holes. In effusion cooling systems, the film holes are typically arranged in a regular array at relatively low non-dimensional pitches (*P*). This results in a greater surface porosity which, in turn, results in correspondingly low blowing ratios. Consequently, effusion systems in turbine applications scarcely suffer the effect of jet lift-off associated with high blowing ratios. These closely pitched holes operating at lower blowing ratios result in more complete films being developed [32]–[35] over the external surface. Accordingly, there are much reduced variations in surface temperature which would otherwise contribute to reduced blade life. Additionally, this close pitching of typically small film holes results in a large convective cooling effect as the coolant flows through the holes prior to exiting into the mainstream flow field [32]. It has been shown that a number of rows of film holes are required in effusion systems before a complete film is formed [35], [36], although how many rows is dependent on the specific effusion hole configuration, with the author of [35] suggesting seven rows may be necessary.

Research into effusion cooling has been primarily focused on the aerothermal aspects of the technology. Some of the important considerations and findings are briefly discussed below. It is noted that many of the findings and parameters share similarities with those for film cooling.

- *Effect of Hole Pitching and Hole Geometry* – As for the more general case of film cooling, variations in the form and density of cooling holes significantly impacts the cooling performance achieved. Reducing the size of the film holes whilst simultaneously increasing their density can provide a significant increase in cooling effectiveness [34], [37]. This is typically characterised by the film hole non-dimensional pitch ($P=S/D_f$) where experiments on effusion systems have investigated hole pitches in the range of 2 – 15 [34], [35], [37]–[42]. However, non-dimensional pitch doesn't capture all potential benefits attributed to reducing the physical film hole size (whilst maintaining P). A reduction in hole size whilst increasing the number of holes results in a greater internal wetted area for convective cooling whilst also increasing the hole roughness relative to hole diameter which has been suggested to improve film effectiveness [35]. Jets from smaller holes are also suggested to experience reduced interaction with the mainstream flow boundary layer improving film cooling performance [43]. As with more conventional film cooling, hole geometry also plays a large role in the film effectiveness achieved. Diffuser-shaped outlet holes can help in reducing flow exit velocity whilst increasing film coverage [35], [44]. For similar reasons, film holes are often inclined to the blade surface direction, typically at around 30-35^o [26]. Some studies investigating hole inclination angle for effusion cooled systems demonstrate little variation in film effectiveness for film hole inclinations of 30^o and 60^o [45], however, the 30^o holes demonstrate increased convective cooling performance due to the additional hole length.

- *Mach Number and Reynolds Number Effects* – Several studies have been performed in which mainstream Mach and Reynolds numbers have been varied to ascertain the resulting effect on effusion cooling performance. In one study [33], two crossflow Mach numbers (0.15 and 0.4) were investigated at various film blowing ratios. Minimal variation in spatially averaged adiabatic film effectiveness was observed for blowing ratios lower than

unity, although a greater difference was observed as blowing ratio was further increased. However, the findings of the study indicate that effusion cooling performance is largely insensitive to the crossflow Mach number. These findings are supported by an earlier study [46] conducted on an effusion cooled NGV in which exit Mach numbers were varied from 0.4 – 0.95 with little variation in cooling performance observed.

- *Mainstream-to-Coolant Temperature/Density/Velocity Ratio Effects* – In engine applications, mainstream-to-coolant temperature ratios are typically observed to be between 1.8 – 2.0 (based on the TET). Many studies therefore attempt to replicate this ratio due to the impact it has on factors such as the density ratio. One study [29] investigated the effect of density ratio on the film effectiveness achieved with density ratios of 1.0 and 1.4 assessed for three different hole geometries. In general, the effect of density ratio was a relatively small one when compared to varying blowing ratio. The authors observed that an increased density ratio reduced centreline film effectiveness but improved jet spreading with an observable increase in spanwise averaged film effectiveness. Only a handful of studies have been conducted nearer engine representative temperatures due to the challenges associated with high temperature setups. A 1985 study [37] attempted to quantify how the absolute temperature influenced results whilst investigating the effect of varying film hole size. Radiative effects were found to become significant at temperatures greater than 500 K resulting in a slight overprediction in cooling performance. A separate study quantified the effect of velocity ratio at various temperature ratios concluding that as velocity ratio was increased, film effectiveness became increasingly insensitive to the density ratio [34].

2.4.2 Literature on Double-Wall, Effusion Cooled Systems

As eluded to, the double-wall system is an amalgamation of more conventional cooling techniques for which there exists a wealth of literature. However, understanding into the

combined effect of these conventional systems – as in the double-wall, effusion cooled system – is somewhat lacking with relatively little literature available on such technologies in the public domain. Of the studies that have been performed, even fewer are experimental in nature. The following section provides an overview of some of the relevant literature that is available.

It is noted that single wall effusion systems, and double-wall type systems which share *some* similarities to those being discussed here, have found application in gas turbine combustor cooling where, typically, heat fluxes are much lower and the necessary material/mechanical properties reduced when compared to the turbine cooling applications being considered here. Furthermore, flow properties in the combustor vary significantly from turbine cooling applications with highly turbulent combustor mainstream flow [47] necessary for adequate mixing of the fuel and air, and films typically operating at much higher blowing ratios [48]. Several papers focusing on such combustor systems are briefly summarised here. Wassell and Bhangu [49] discuss an industry driven investigation into a double-wall type cooling geometry primarily focusing on combustor cooling applications in a paper from 1980. They discuss the general construction of the technology, and provide data pertaining to the pressure losses incurred in the system as well as some of the heat transfer characteristics whilst also commenting on the long-term durability. Chua et al. [50] present a study of a double-wall combustor tile in which coolant flow enters via feed holes in the internal wall, then navigates through a collection of pedestals prior to being ejected via either a short bank of effusion holes (comprised of two rows of holes), or through a slot at the trailing edge (*TE*) of the tile. The authors demonstrate the significant effect of the highly turbulent mainstream flow field on the performance of the cooling films for the case of TE flow ejection where degeneration of the films appears to be accelerated. The incorporation of effusion holes reduces the effect of this film deterioration in highly turbulent flow fields. A second paper from the same institution authored by Denman et al.[51], analysed similar tile systems but in the absence of effusion holes. The study predominantly focused on the effect of changing pedestal height/configuration

and discussed how varying these influenced the distribution of coolant flow. Further studies on combustor systems have analysed impingement/pedestal systems, but in the absence of film cooling, and attempted to quantify both the heat transfer enhancement and reduction in impingement jet crossflow sweep attributed to the presence of the pedestals [52], [53].

Several further studies are presented below for systems in which the target application appears to be turbine cooling, as is the case for the current research.

A study conducted by Sweeney and Rhodes [54], experimentally investigated double-wall systems akin to those discussed above, utilising an array of pedestals comprised of alternating square and hexagonal elements. Four flat plate geometries were tested in which two pitches were investigated ($P = 10.5$ and 14.8), and two film injection angles (30^o and 90^o). The experiments were steady-state and utilised infrared thermography to evaluate overall cooling effectiveness. The facility provided a close match on both mainstream-to-coolant temperature ratio and Biot number. The study concluded that the shallower film injection angle of 30^o coupled with the lower hole pitching produced improved cooling performance, a consequence of the increased convection in the longer film holes and more regular jet impingement, along with the more complete films developed on the outer wall.

Manzhao et al. [55] also conducted experimental work on double-wall geometries incorporating an array of circular pedestals. The study was predominantly focused on the impact of impingement hole spacing on h. The authors observed local increases in h around both the film and impingement holes due to accelerating flow. They also noted that pedestals had the general effect of increasing average internal h.

A 2005 study by Nakamata et al. [56] experimentally investigated six double-wall geometries incorporating various forms including only impingement cooling, impingement and film cooling, and three further systems incorporating circular pedestal elements. Impingement hole to target plate spacing was maintained at $y/D_i = 1.5$ for all geometries. The authors demonstrated that the presence of pedestals increased overall cooling effectiveness and this

effect was particularly pronounced at higher coolant flow rates. The authors also indicate that – whilst not explicitly studied – internal pedestal configuration has some effect on the film cooling performance achieved when compared to a no pedestal case operating at the same blowing ratio. The study demonstrated the potential benefit of staggering pedestal elements at lower coolant flow rates whilst also commenting that positioning of pedestals too close to impingement holes can have a detrimental effect on cooling performance. It is noted, however, specimens were manufactured from two different materials with no comment on Biot number effects which may be different between the materials.

The aforementioned study by Rhee et al. [17] which investigated the effect of internal crossflow in an impingement/effusion system was furthered in 2007 by Hong et al. [57] who introduced variously shaped pedestal elements between the two walls thereby mimicking the double-wall system. The study demonstrated the reduced effect of jet-sweep from crossflow in the presence of pedestals and this was particularly apparent in the case of rectangular pedestals. All rectangular pedestal geometries also demonstrated higher heat transfer characteristics than both the circular pedestals and baseline test case with no pedestals. Heat transfer coefficients were increased by as much as 45% for rectangular pedestals in the case of high crossflow blowing ratios with geometric variations becoming more significant as blowing ratio was elevated. Similarly, a study by Chyu et al. [11] investigated the effect of pedestal shape in a channel crossflow situation with square pedestals rotated at 45^{o} to the oncoming flow demonstrating higher pressure losses when compared to square and circular pedestals, along with a delay in the row for which maximum heat transfer coefficients were observed.

Both Bunker [58] and Chyu and Siw [59] comment on two commercial double-wall technologies, one of which is formed via a bonding process whilst the other is investment cast.

In [32], [35], [58] the authors comment on the issue of mechanical integrity that arise in double-wall, effusion type systems. This is an area on which information is particularly sparse in the public domain. Indeed, only one computational study from 2018 was identified [60]. The

study investigates the creep performance of double-wall systems akin to those described here featuring an inline configuration of circular pedestals. Seven geometries were investigated in which the proximity of impingement and film cooling holes to pedestals was varied. The results indicated the more significant effect of impingement hole proximity to pedestals compared to film hole proximity. The study also demonstrated stress relaxation effects and stress redistribution with increasing creep time. However, the impact of the study is somewhat limited with the main conclusion of the authors pertaining to the detrimental effect of position cooling holes too closely to pedestals which is likely simply a result of the interacting stress concentration effects surrounding these two features.

A number of patents also exist in the public domain which predominantly focus on manufacturing methods for double-wall type geometries, the majority of which have an industrial affiliation [61]–[67].

2.5 Summary

The above summary of existing literature on double-wall, effusion systems demonstrates that data on these cooling technologies is somewhat lacking. The present work, therefore, attempts to develop the existing knowledge and data on double-wall systems in multiple ways. This thesis presents an experimental study into the cooling performance of double-wall systems with the data used to validate a computationally inexpensive conjugate method developed by the author specifically designed for modelling the aerothermal performance of these systems. A thermomechanical investigation is also performed to ascertain how varying geometric parameters effects the magnitude of the developed stress field.

3 Methods of Modelling Multiple Row Effusion Cooling Performance

3.1 Chapter Overview

The present chapter discusses an experimental and computational study conducted to assess the performance of single wall effusion geometries. Effusion cooling represents an important aspect of the double-wall cooling technology being studied. Consequently, isolating the effusion cooling performance from the rest of the double-wall system was deemed an important step in understanding the overall cooling performance achieved, and indeed, in assessing potential computational methods for modelling effusion cooling performance which could be used in the analyses of double-wall systems.

This chapter discusses a pressure sensitive paint (PSP) method implemented on a low speed wind tunnel facility to obtain adiabatic film cooling effectiveness measurements for two, single wall, effusion cooled, flat plate geometries. These results are then used in the validation of a scalar particle tracking CFD method used to capture adiabatic film effectiveness, as well as the validation of a superposition model which was to be used in the computational method developed to assess double-wall systems presented in a later chapter.

3.2 Experimental Setup

A pre-existing low speed wind tunnel facility was extensively modified to perform this experimental, single wall effusion cooling study. A schematic of the setup is shown below in Figure 3.1 with some of the key features elaborated upon in the following.

The mainstream airflow was comprised of ambient air that was drawn-in through a filtered open intake by a water ring vacuum pump. The cross-sectional dimensions of this mainstream

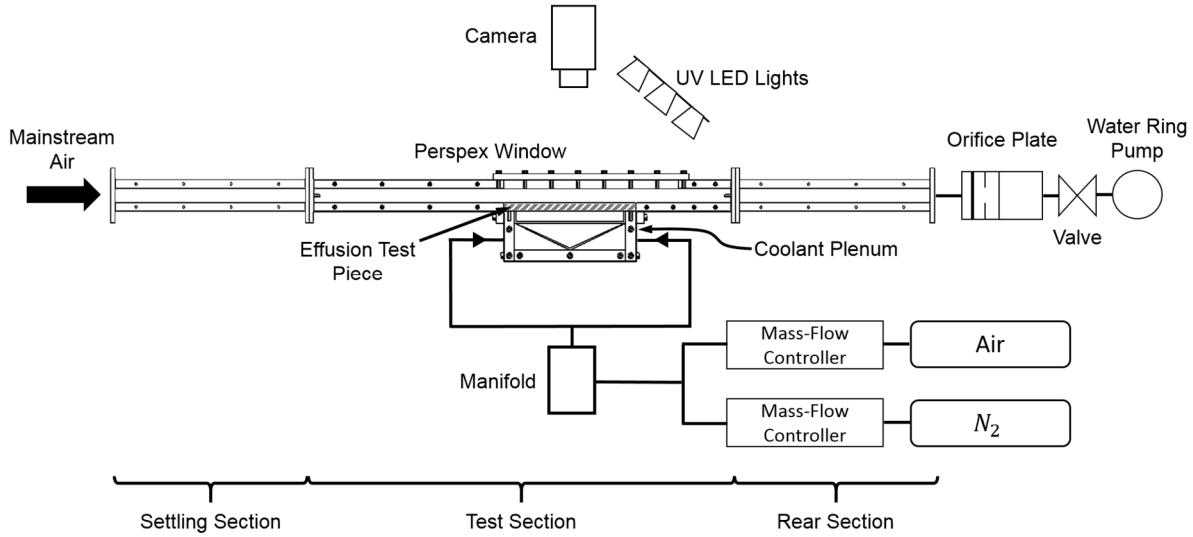


Figure 3.1 - Schematic of the experimental setup

channel measured 192 × 24 mm. A settling section was positioned upstream of the test section and was of sufficient length (ten hydraulic diameters) to allow for flow development thereby helping to ensure a uniform, symmetrical velocity profile. All sections comprising the wind tunnel were constructed from Perspex allowing for easy optical access.

Coolant flow comprised a mixture of air and nitrogen. The respective mass flows of each were controlled by the use of two automated mass flow controllers. The nitrogen source was a compressed bottle whilst that of the coolant air was the laboratory compressed air supply. Mixing of the two gas streams occurred via a manifold system. The mixed streams were then fed from the manifold to the coolant plenum through four hoses (of equal length and diameter). These jets were fed into the plenum in a symmetrical manner and passed through a two-layer perforated plate system to help dissipate the jets in an effort to ensure an even feed of coolant to the film holes.

The flat plate test geometries were manufactured from aluminium and painted, first in a matt black paint, followed by a coating of the pressure sensitive paint used to obtain the film effectiveness measurements (see section 3.2.1). The film holes were fed coolant from the plenum and vented into the mainstream flow. The painted surface of the geometry was

illuminated by a bank of eight 5 W ultraviolet LED lights. The response of the pressure sensitive painted surface was captured during experimental runs using a 1928 × 1452 resolution, monochromatic CCD camera with a 610 nm long pass filter.

3.2.1 Pressure Sensitive Paint Methodology

The use of pressure sensitive paint (*PSP*) has become a well-established method to obtain adiabatic film cooling effectiveness measurements via heat-mass transfer analogy. In the present study, the PSP used was UniFIB PSP which is comprised of a mixture of fluoro isopropyl butyl polymer (FIB), platinum tetra(pentafluorophenyl) porphine (PtTFPP) and a white pigment. PtTFPP is a luminophore that, when excited by blue light (around a 400 nm wavelength), emits a higher wavelength light in the red spectrum (around 600 nm) [6], [68] as the comprising, excited electrons, return to their unexcited state. An alternative method whereby the electrons are able to return to their unexcited state is via interaction with oxygen molecules. The light emitted by the PSP is found to be inversely proportional to the partial pressure of oxygen in contact with the surface, i.e. as the partial pressure increases, the emitted light intensity decreases – a process known as oxygen quenching [69]. Via a carefully performed calibration method (described below), the partial pressure of oxygen can be related to the intensity of the emitted red light. With knowledge of the concentration of oxygen in the working fluid, the absolute pressure on the painted surface can be determined.

3.2.1.1 PSP Calibration Method

Calibration is best performed in-situ to minimise variations between the calibration and experimental setup (for example variations in temperature which, as demonstrated by Mhretras et al. effect the intensity of emitted light [70]).

For the current study, the PSP was calibrated in-situ prior to each set of experimental runs. During the calibration process, fifteen known partial pressures of oxygen were used to obtain

fifteen images of light intensity from the surface of the paint. To set the partial pressure of oxygen, two mass flow controllers were used to control the respective flow rates of nitrogen and air, where the assumed mole fraction of oxygen in air is n_{air} = 20.95%. Knowing the molecular weights of both air (MW_{air}= 28.97 kg/kmol) and nitrogen (MW_{N_2}= 28.01 kg/kmol), the mass flow rate of the two streams could be used to calculate the molecular flow rates via equation 3.1. The two streams were fully mixed prior to entering the coolant plenum via a manifold system, and the mole fraction of oxygen in the combined mixture determined using equation 3.2.

$$\dot{M} = \frac{\dot{m}}{MW} \tag{3.1}$$

$$n_{mix} = n_{air} \times \frac{\dot{M}_{air}}{\dot{M}_{air} + \dot{M}_{N_2}} \tag{3.2}$$

The partial pressure of a component of a gas mixture can be calculated by multiplying the mole fraction of the component by the pressure of the fluid. To obtain the partial pressure of oxygen in the coolant mixture, the absolute pressure on the PSP painted surface ($p_{s,surf}$) was obtained via a static pressure tapping. The partial pressure of oxygen under ambient conditions (used for the reference condition) was obtained using a mercury barometer. These calculations are shown in equation 3.3.

$$p_{O_2,surf} = n_{mix} \times p_{s,surf} \quad | \quad p_{O_2,ref} = n_{air} \times p_{atm} \tag{3.3}$$

At each of the fifteen calibration partial pressure conditions, the image intensity ratio was calculated as per equation 3.4, where I_{dark} denotes an adjustment for the background noise captured by the camera in dark conditions. In calculating the intensity ratio, a 200 × 200 pixel area surrounding the pressure tapping was used; it is noted that other work performed in the lab had shown this area to be representative of the entire painted surface [71], [72].

$$I_{ratio} = \frac{I_{ref} - I_{dark}}{I_{mix} - I_{dark}} \tag{3.4}$$

An example of the calibration curve obtained during the calibration process is demonstrated below in Figure 3.2.

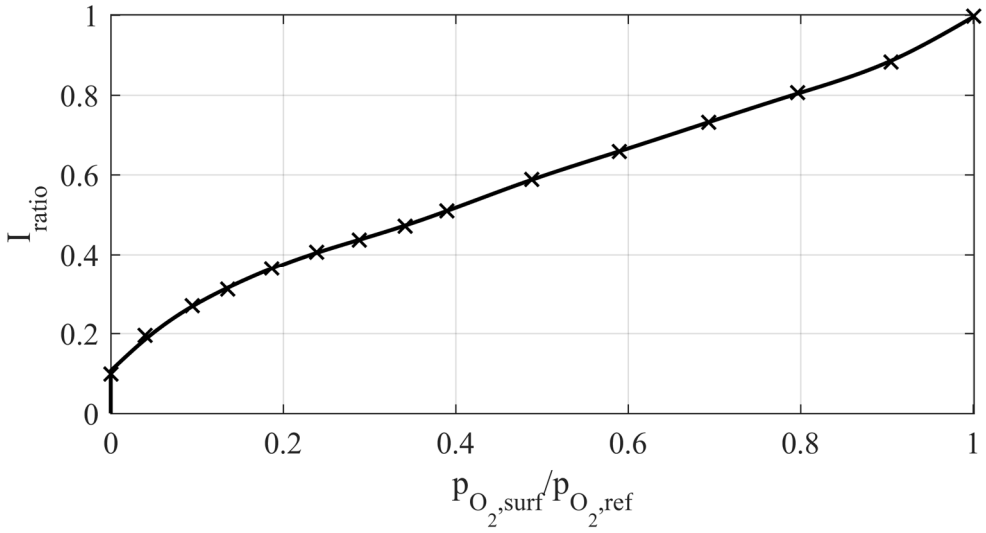


Figure 3.2 - Example of the PSP calibration curve showing the pressure ratio to image intensity ratio

3.2.1.2 Using the PSP Method to Calculate Film Cooling Effectiveness

To calculate film cooling effectiveness for a geometry operating at a particular blowing ratio, four images were required. For experiments on the same geometry conducted in the same set of runs, two of these images could be used for tests at different blowing ratios; these were the reference image where an image was taken of the surface under ambient conditions but with the excitation lights (i.e. the ultraviolet LEDs) on, and the dark image where the lights were off. At each blowing ratio a further two tests were required, both in the presence of the mainstream flow. The first of these used pure nitrogen as the coolant, the second used air. The intensity images captured during the tests could be converted to the equivalent partial pressure of oxygen over the painted surface via the calibration. It is noted that the second run using air as the coolant is performed to account for any local perturbations in the surface partial pressure of oxygen cause by the test geometry and flow field rather than as a result of nitrogen mixing. To minimise

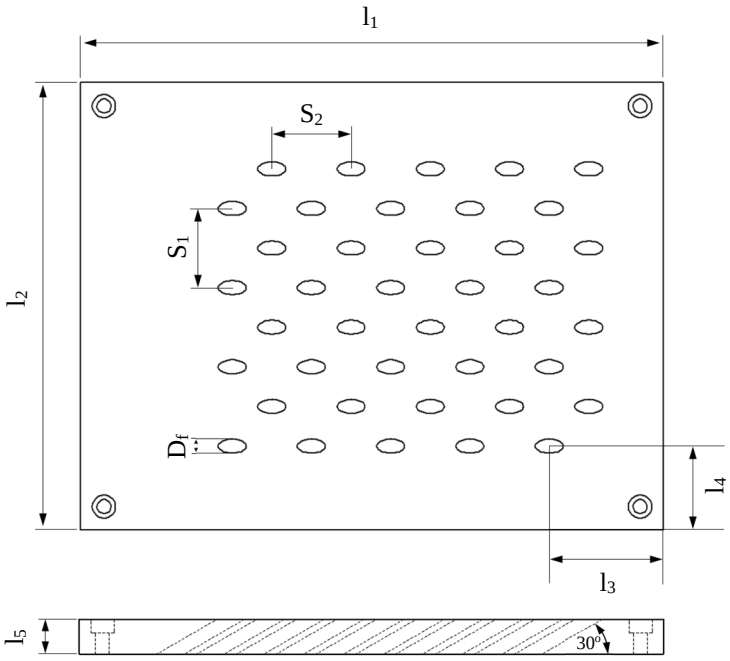
temperature effects, a thermocouple was used to monitor the temperature of the coolant in the plenum, prior to entering the cooling holes, to ensure it did not significantly deviate from that observed during the calibration process (within ±2 K). To further reduce temperature effects, reference images were taken immediately after the main test images (rather than using the same reference image across all blowing ratios investigated). For each experimental condition, 30 frames were captured and averaged to create the image used in calculating the film effectiveness.

As demonstrated by Han and Rallabandi [68], the boundary conditions and governing equations for heat and mass transfer in two-dimensional turbulent boundary layers can be demonstrated to have a very similar form. In the case that both the turbulent thermal diffusivity and turbulent mass diffusivity are approximately equal (i.e. the turbulent Lewis number, Le_T, is unity), then non-dimensional solutions to the governing equations - i.e. temperatures or mass concentrations – will be equal. In the case of turbulent gas flows this can be assumed valid [73]. Consequently, the mainstream gas field was turbulent across all experimental blowing ratios investigated. Equation 3.5 demonstrates the experimental measurements of oxygen partial pressure required to allow for an estimation of film effectiveness by heat-mass transfer analogy [68]. Given the similar molecular weights of air and nitrogen, the mass fraction ratio is approximately equivalent to the mole fraction ratio and consequently the partial pressure ratio. It is also noted that in equation 3.5, $C_{O_2,c}$ is zero, as pure nitrogen was used as the coolant in the experiments.

$$\eta_f = \frac{(T_\infty - T_{aw})}{(T_\infty - T_{c,e})} \approx \frac{(C_\infty - C_w)}{(C_\infty - C_c)} = \frac{(C_{O_2,air} - C_{O_2,N_2})}{(C_{O_2,air} - C_{O_2,c})} = 1 - \frac{C_{O_2,N_2}}{C_{O_2,air}} = 1 - \frac{p_{O_2,N_2}}{p_{O_2,air}} = 1 - \frac{p_{O_2,N_2}/p_{O_2,ref}}{p_{O_2,air}/p_{O_2,ref}} \tag{3.5}$$

3.2.2 Study of Parametric Variations of Geometry

The dimensions of the two experimentally investigated geometries are provided below in Figure 3.3. The test pieces were manufactured from a plate of aluminium measuring 280 × 192 × 15 mm. Both geometries exhibited a staggered configuration of circular film holes inclined at 30^o to the plate surface. Two non-dimensional hole pitches (based on the primary holes) were tested with geometry 1 (referred to hereon in as E1) exhibiting a pitch of P = 3.0, and geometry 2 (E2) a pitch of P = 5.66. E1 exhibited an array of 7 × 8 primary holes with a total of 112 holes including the staggered elements, whilst E2 had an array of 4 × 5 primary holes with a total of 40 holes including the staggered holes. O-ring seals were placed at the base of the plates to minimise flow leakage during the experiments with the plate secured via bolts placed in each corner. Two static pressure tappings required for the calibration process, were placed on each geometry towards the trailing edge of the plate.



	E1	E2
D_f	6.0 mm	
S_1	3.0D_f	5.66D_f
S_2	3.0D_f	5.66D_f
l_1	41.67D_f	
l_2	32.0D_f	
l_3	6.17D_f	6.0D_f
l_4	9.83D_f	8.17D_f
l_5	2.5D_f	

Figure 3.3 - Schematic showing the dimensions of the two flat plate test geometries as a function of the film hole diameter

3.2.3 Experimental Operating Conditions and Measurement Uncertainties

For both geometries, experiments were performed at blowing ratios ranging from 0.2 – 1.2 at increments of approximately 0.1. Additionally, a blowing ratio of 0.1 could be tested for the more porous geometry (i.e. E1), a blowing ratio not possible in the larger pitched geometry due to the larger uncertainty in coolant mass flow it would introduce. Indeed, the uncertainty in coolant mass flow ranged from a maximum of 17% (for E2 with a blowing ratio of 0.2) to 1.8% (for E1 at a blowing ratio of 1.2). It is also noted that the uncertainty in coolant mass flow quickly reduced as blowing ratio was increased. Uncertainty in film effectiveness was calculated via the perturbation method discussed by Moffat [74] and further elaborated upon in Chapter 7. The measurement uncertainty in image intensity was that calculated for the facility by Wong [72]. Uncertainty in film effectiveness was calculated as 3.1% for effectiveness values lower than 0.14, reducing to 1.4% for effectiveness values in excess of 0.8.

For the heat-mass transfer analogy to be valid for the PSP method, the mainstream flow field needs to be turbulent throughout all experiments for Le_T to be approximately unity; for pipe flow, this was taken as being above Re_D = 4000. Indeed, mainstream *Re* (based on duct hydraulic diameter) prior to the test piece varied between 15000 – 25000 for the two geometries. Coolant and mainstream conditions were both at ambient temperature providing a density ratio of unity. Coolant *Re* varied between 400 – 3800 based on the diameter of the film holes (with corresponding velocities of 1.0 – 7.0 m/s for E1 and 1.0 – 10 m/s for E2).

3.3 Single Wall Effusion Cooling Computational Investigations

The modelling of film cooling performance by computational means provides a significant engineering challenge due to the difficulties associated with capturing the innately complex flow features associated with film ejection and downstream flow-mixing [22], [75]. To accurately resolve such features typically requires the use of dense meshes and computationally intensive turbulence models. Alternative methods for modelling film cooling are therefore

further considered later in this chapter and in Chapter 5. The method of modelling film performance via CFD used here that was particularly suited to the validation of the PSP experimental results utilised a mass transfer method in which the concentrations of an introduced passive species were obtained throughout the flow domain. By careful setup of the boundary conditions, and under certain assumptions, this species concentration can be shown to be analogous to the film effectiveness as discussed below.

3.3.1 Passive Scalar Concentration Methodology

The scalar concentration CFD method passively calculates the motion of introduced scalar particles in the fluid medium. The motion of these particles is described via the general convection-diffusion equation repeated in equation 3.6.

$$\frac{\partial \phi}{\partial t} = \nabla \bullet (\Gamma \nabla \phi) - \nabla \bullet (v\phi) + s_\phi \qquad \textit{(3.6)}$$

For the current simulations it is noted that there are no source terms ($s_\phi = 0$). The simulations are also steady-state and consequently $\partial\phi/\partial t = 0$ leading to the simplification shown in equation 3.7.

$$\nabla \bullet (v\phi) = \nabla \bullet (\Gamma \nabla \phi) \qquad \Rightarrow \qquad \frac{\partial (v_n \phi)}{\partial x_n} = \frac{\partial}{\partial x_n}\left(\Gamma \frac{\partial \phi}{\partial x_n}\right) \qquad \textit{(3.7)}$$

The flow is also assumed to be incompressible given both the ambient temperature and low speed of the rig being validated, along with a further assumption of constant c_p. To reproduce the mixing behaviour observed in the thermal field, the diffusivity of the introduced scalar is set to that of the effective thermal diffusivity and this is shown in *equation 3.8* where the turbulent Prandtl number has a value of approximately 0.85. Note that, as with the experiments, Le_T is near unity and therefore the result of equation 3.8 is near equal to the mass diffusivity.

$$\Gamma = \frac{1}{\rho c_p}\left(k_{l,fl} + \left(\frac{c_p \mu_t}{Pr_t}\right)\right) = \alpha \qquad \textit{(3.8)}$$

As noted in [76], by setting the scalar concentrations at the inlet of the cooling holes to 1, and that at the inlet of the mainstream to 0, the scalar concentration in the mixed flow can be calculated as a fraction of the coolant-to-mixed mass flow rate. This, in combination with the continuity and energy equations, has been shown [76], [77] to be analogous to the adiabatic film effectiveness as described in equation 3.9.

$$\Sigma\phi = \frac{(T_\infty - T_{aw})}{(T_\infty - T_{c,e})} = \eta_f \tag{3.9}$$

3.3.2 Multiple Row Effusion Cooling CFD Domain and Setup

The multiple row effusion cooling simulations modelled the test section used in the experimental setup. The mainstream flow domain commenced at the leading edge of the flat plate with the exit of the simulated domain at the trailing edge of the plate. Viscous walls were situated at locations corresponding to the walls of the wind tunnel. Coolant was fed to the inlet of the effusion cooling holes via a plenum that was of identical cross-sectional area to that used in the experimental setup. A velocity boundary condition was specified at the inlet of the mainstream flow with the velocity profile obtained from separate simulations that modelled flow development along the inlet settling section of the experimental rig up until the leading edge of the flat plate test piece. The coolant inlet boundary condition was a specified mass flow rate. Both the mainstream and coolant boundary conditions were based on the same values tested in the experiments. Turbulence intensities were estimated using an empirical correlation for pipe flow and based upon the inlet mainstream and coolant Reynolds numbers (with duct hydraulic diameter as the relevant length scale). Additional boundary conditions were required for the introduced species at both flow inlets, as well as the outlet (as described in section 3.3.1).

The meshes used in the study were unstructured in nature and comprised tetrahedral elements with prism layers at the solid/fluid interfaces and refinements around the film hole locations. A mesh independence study was performed with the selected meshes demonstrating

a good balance between simulation times and solution veracity. The meshes for both test geometries were approximately 6 million elements in size and with y^+ values less than 5. The simulations employed the realisable k-ε turbulence model (using enhanced wall treatment) and were performed in *ANSYS Fluent v16.2*.

3.3.3 Single Film Hole CFD Domain and Superposition Method for Multiple Ejection Modelling

An additional way of effusion cooling modelling was considered which extended the additive superposition method proposed by Sellers [78]. The use of a superposition model allows for the manipulation of data from a single film ejection to develop data for multiple row film performance. The Sellers model treats each ejected film as being an independent and confined layer and is described in equation 3.10. The basis of the method is that the freestream temperature for the single film cooling hole is replaced by the adiabatic wall temperature which results from the upstream films. Use of the method when applied to spanwise average one-dimensional data can be found throughout the open literature. However, the current work is – to the best of the author's knowledge – the first use of the method for two-dimensional distributions of film effectiveness.

$$\eta_f = 1 - \prod_{i=1}^{n} \left(1 - \eta_{f_i}(x)\right) \qquad (3.10)$$

To make the method as comparable as feasibly possible to the experimental work and multiple hole CFD simulations, the CFD domain once again modelled the experimental setup; however, in this case, the flat plate simulated had only a single film hole. Mesh parameters and the CFD solver setup remained the same as for the multiple hole simulations. After running the solution, the resulting film effectiveness distribution and node location information was imported into a *MATLAB* script which replicated the film effectiveness data in the spanwise

direction based on a specified hole pitch, whilst in the streamwise direction, Sellers' superposition method was used to model film development. For simplification, the non-dimensional pitching tested via this method was 5.66 (i.e. that in geometry E2), given that there is little spanwise interaction between the individual film jets at this pitch. A graphical demonstration of the method is shown below in Figure 3.4 where the mainstream gas temperature for the second, downstream film block, is taken to be the adiabatic wall temperature at the exit of the upstream film block.

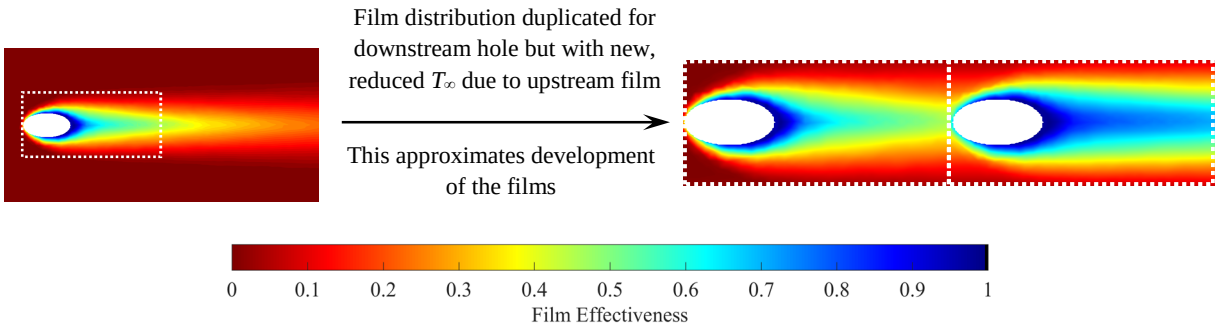


Figure 3.4 - Graphical demonstration of the developed two-dimensional superposition method

3.4 Results

In the processing of all results, it is noted that data at the location of the film holes were set to NaNs (not a number) and thus contained no data at these pixels. Additionally, all methods of effusion modelling presented were for a density ratio of approximately unity. Figure 3.5 and Figure 3.6 depict two-dimensional adiabatic film effectiveness contours obtained from both the PSP experimental method and multiple row CFD simulations at a range of blowing ratios for both geometries. Measurements were taken at blowing ratio increments of approximately 0.1 between the range of 0.1–1.2, but for brevity, only a selection of the results are presented here.

Perhaps most striking are the highly effective films developed in the $3.0D_f$ pitch geometry. Given the close proximity of the holes, near continuous films are developed in which variations in spanwise effectiveness quickly diminish as blowing ratios are increased above 0.5, an effect that is captured in both the experiments and multi-hole CFD simulations. The results for this

geometry also indicate that the number of rows of holes required for fully developed films is a strong function of the blowing ratio. Spanwise averaged results for the multi-hole CFD simulations (not shown here) indicate that for blowing ratios greater than 0.5, approximately seven rows of primary holes are required for fully-developed films, a value in keeping with observations made by Krewinkel [35]. Indeed, for blowing ratios between 0.5 and 1.2, little variation was observed in the spanwise averaged film effectiveness absolute values and trends.

The performance of the multiple row, heat-mass transfer analogy CFD model for the $3.0D_f$ pitch geometry was reasonably satisfactory. Many of the trends captured in the experiments were evident in the CFD. At lower blowing ratios, there is a noticeable variation in film effectiveness across the spanwise holes in each row, and this was observed in both the CFD and PSP experiments. This is believed to result from variations in the blowing ratio across the width of the test plate. Towards the edges of the plate, the development of the side-wall boundary layers act to reduce mainstream flow velocity; as a consequence, the blowing ratio is increased at these edge film holes, and the extent of the film cooling increased. The CFD over-predicts the performance of the films across all blowing ratios. The mixing of the jets observed in the CFD appears to be less than that shown by the experiments, and this is evidenced by the reduced spreading of the films along with a slower rate of film decay. It is anticipated that the highly complex spanwise interactions between films ejected at the same row are not fully resolved in the simulations, and this accounts for some of the variations observed between the CFD and experiments. It is also hypothesised that turbulent viscosity may be under-predicted in the simulations. The results for the $3.0D_f$ pitch geometry also appear to indicate no film development over the first couple of rows of film holes for the lowest blowing ratio shown (M = 0.19) for both the experiments and multi-hole CFD. Pressure contours in the CFD simulations indicate that, to a small extent, at the lowest mass flows, coolant is not evenly fed to all the holes, with the middle and latter holes being favoured. This is confirmed via velocity vectors,

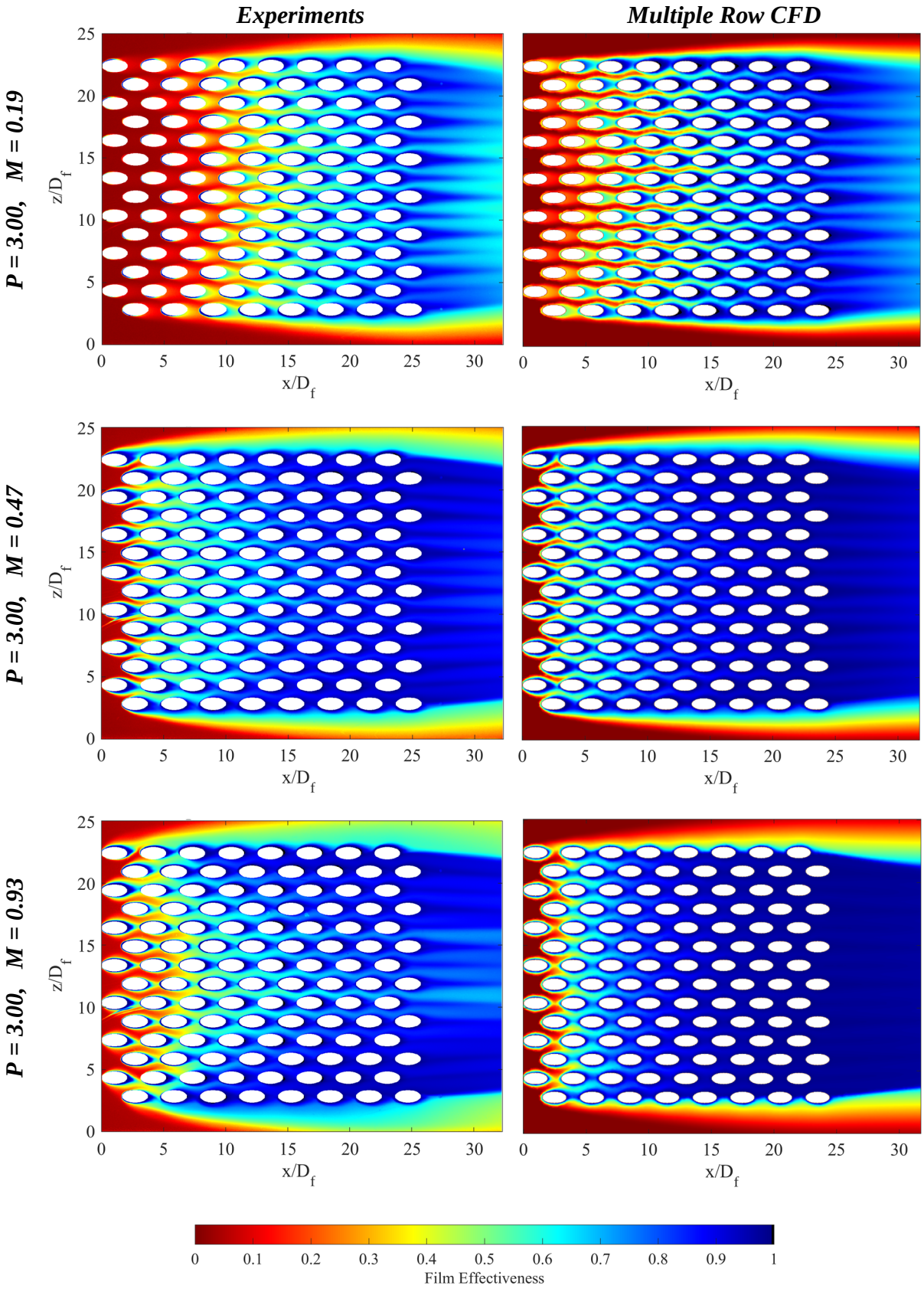


Figure 3.5 - PSP experimental and multiple row CFD film effectiveness contours for three of the tested blowing ratios for the non-dimensional hole pitch of 3.00

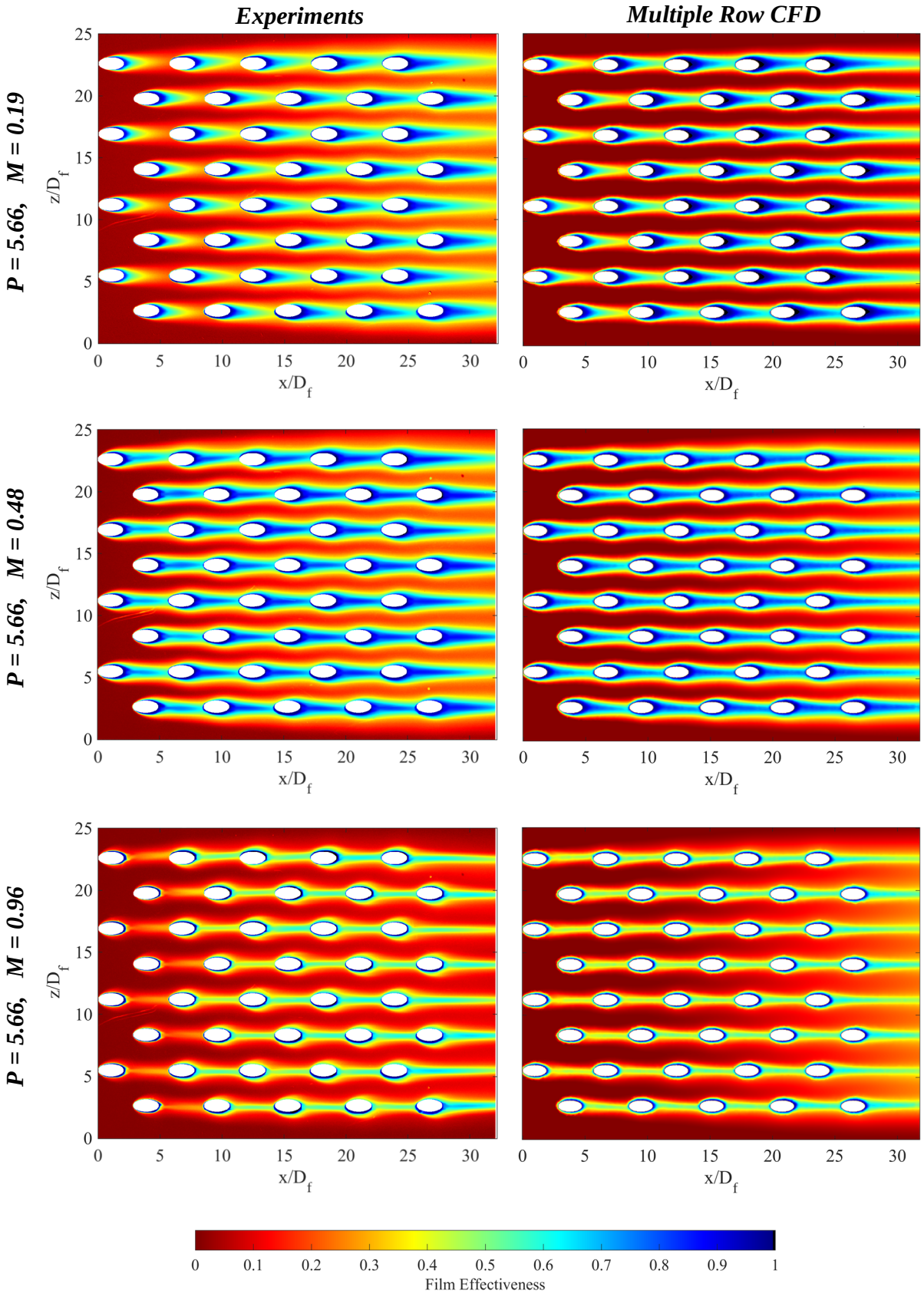


Figure 3.6 - PSP experimental and multiple row CFD film effectiveness contours for three of the tested blowing ratios for the non-dimensional hole pitch of 5.66

which demonstrate that some ingestion occurs in the first row of film holes. At higher blowing ratios, where coolant total inlet pressure is increased, this behaviour is not observed.

Good agreement was observed between the multi-hole CFD simulations and experimental results for the hole pitch of $5.66D_f$, and this is, in-part, expected to result from the reduced lateral jet interactions. The multi-hole CFD simulations capture the trends observed in the experiments particularly well with a steadily increasing film effectiveness up until a blowing ratio of approximately 0.5, after which the effect of jet lift-off is observed. Indeed, particularly over the first few rows of holes, the difference between the multi-hole CFD and experiments is well within the experimental uncertainty. As with the closer pitch geometry, the CFD does slightly under-predict mixing of the jets, although this effect is relatively minimal. The number of primary hole rows required for fully-developed films also appears to be reduced when compared to the $3.0D_f$ geometry, with around five rows of holes being required (similar to observations made by Ling et al. [79]), although once again this is a function of the blowing ratio. Furthermore, the multi-hole CFD model does appear to estimate that a greater number of holes are required for fully-developed films, and this effect increases with blowing ratios greater than unity (see Figure 3.7 which shows spanwise averaged film effectiveness from both the experimental and computational methods). Indeed, the figure shows that, at all five blowing ratios, films in the multi-hole CFD have not reached a fully-developed state by the end of the test piece. However, at the higher blowing ratios of 0.96 and 1.15, the experimental results do seem to indicate fully-developed films at an x/D_f of around 20.

To allow for further benchmarking of the results, the findings were compared to data obtained in a previous study by Ling et al. [79], who attempted to quantify effusion cooling performance via a liquid crystal thermography method. Ling et al. investigated two flat plate geometries with hole pitches of $10D_f$ and $16D_f$ and presented the average film effectiveness achieved in the fully-developed film region as a function of normalised coolant mass flow. The data obtained by Ling et al. have been adapted and are presented along with the data from the

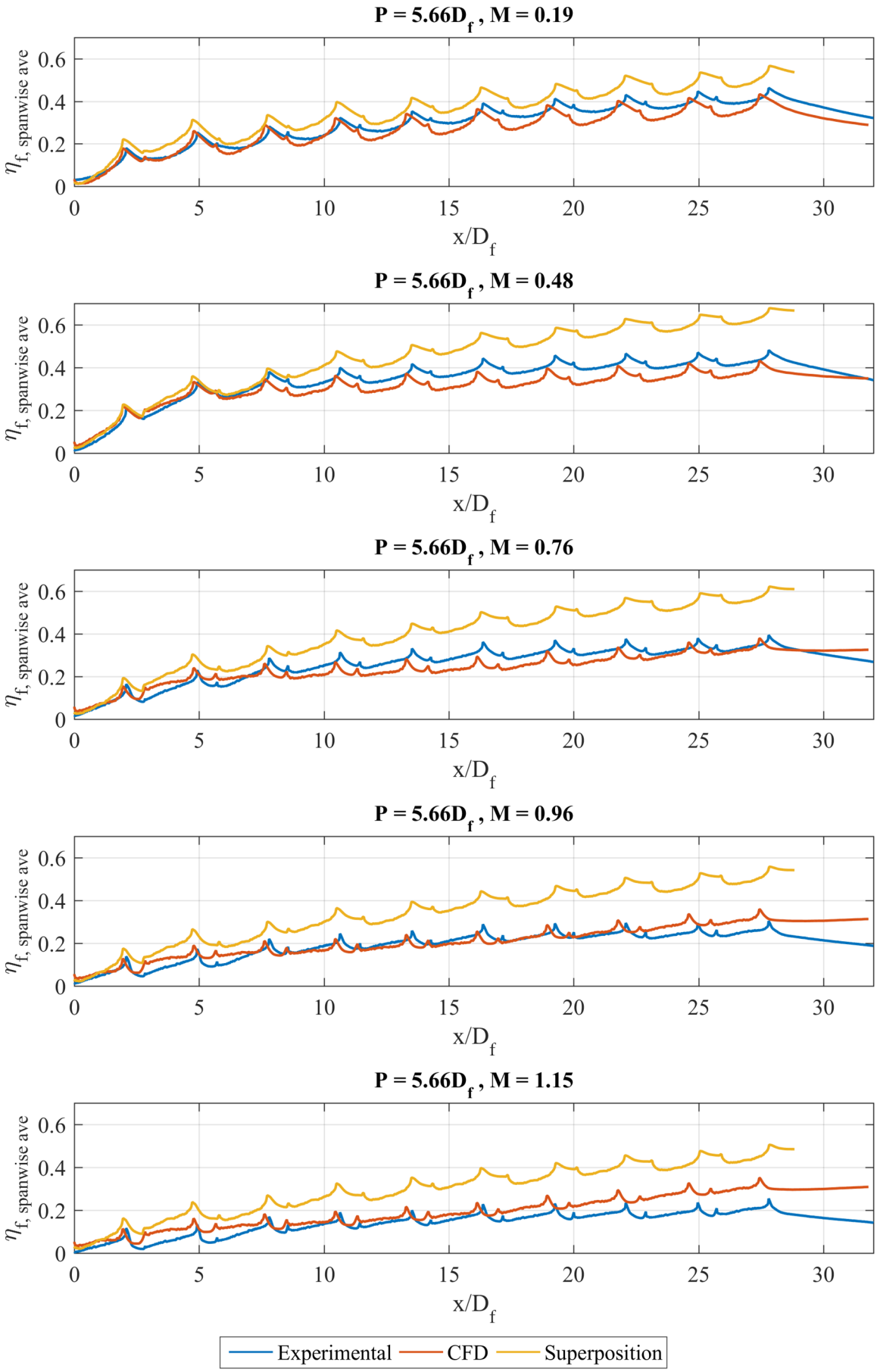


Figure 3.7 - Comparison of the spanwise averaged film effectiveness results for the PSP experiment, multiple row CFD and single hole superposition CFD model at five blowing ratios

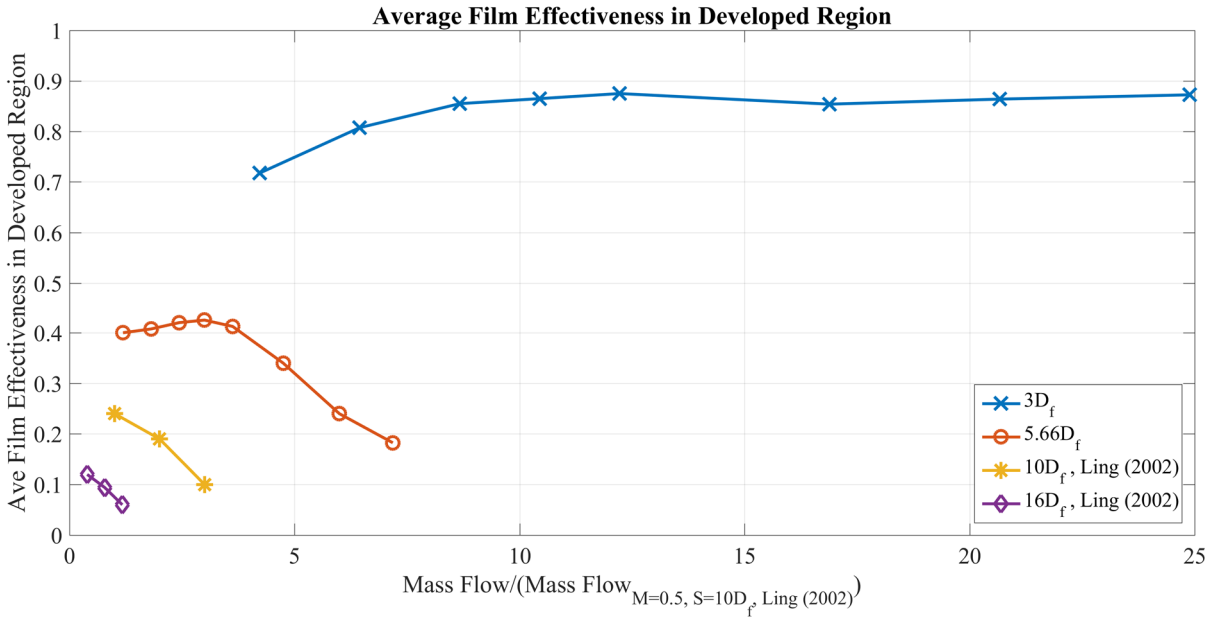


Figure 3.8 - Average film effectiveness in the developed film region against normalised mass flow for both the $3D_f$ and $5.66D_f$ pitch geometries, along with a comparison against data obtained by Ling et al. [70] for pitches of $10D_f$ and $16D_f$

current study in Figure 3.8. The graph demonstrates the considerable increase in film effectiveness achieved with the closer pitched holes, with average film effectiveness in the fully-developed region of the $3.0D_f$ pitch geometry between 0.8 – 0.9 across almost all blowing ratios investigated. At normalised mass flows of around unity, the figure shows how, as the film hole pitch decreases from $16D_f$ to $5.66D_f$, effectiveness increases by around a factor of four. Similarly, at normalised mass flows of around five, average film effectiveness values for the $3D_f$ pitch are almost twice that of the $5.66D_f$ pitch. The results therefore clearly demonstrate the potential of effusion cooling and the significant increases in cooling performance achieved at very low hole pitches at similar levels of coolant mass flow. This benefit can be explained with reference to the relatively low values of blowing ratio exhibited across a wide range of coolant mass flows in effusion systems with correspondingly well adhered films.

Experimental and multiple row local spanwise film effectiveness distributions are compared in Figure 3.9 for E2 at two blowing ratios ($M = 0.19$ and 0.96). For both blowing ratios spanwise effectiveness is shown at streamwise locations which are depicted at the top of the figure. For the lower blowing ratio, at the first position, the CFD and experimental results compare

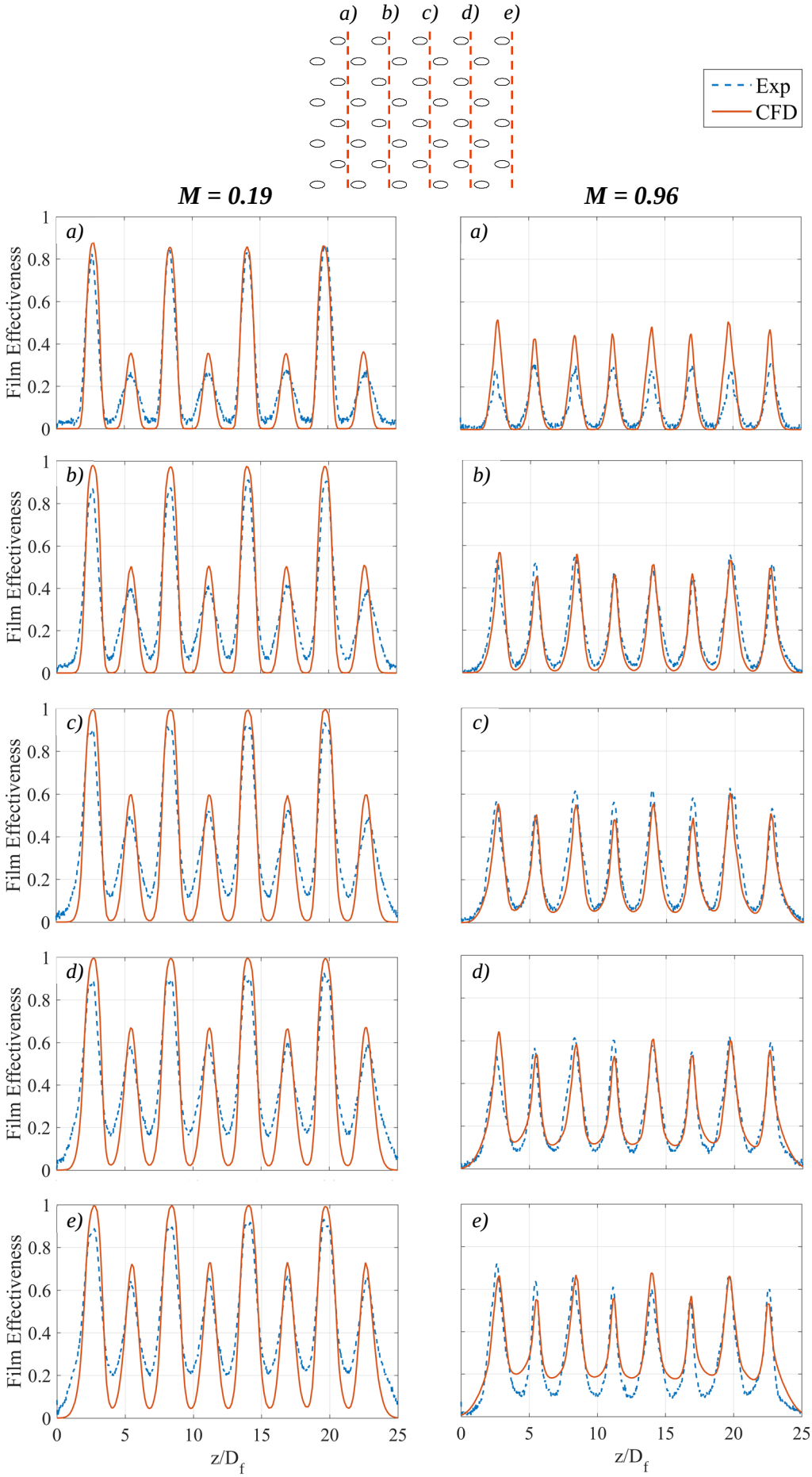


Figure 3.9 – Local spanwise film effectiveness from both the experiments and multiple row CFD at five different streamwise positions in geometry E2 (P=5.66) at two blowing ratios

favourably. As the films move downstream and develop, peak effectiveness values are slightly over-predicted by the CFD, whilst the troughs are slightly under-predicted. The implication of this is that the diffusivity predicted by the scalar tracking CFD method is being under-predicted resulting in more defined peaks and troughs in the CFD when compared with experiments.

At the higher blowing ratio, the performance of the CFD is encouraging. Whilst at the first position there is a clear overprediction of peak effectiveness, development of the films in the streamwise direction appears to be more accurately captured. It is also observed that, when compared to the lower blowing ratio, the peaks are much sharper with less lateral spreading of the films and this is attributed to the effect of jet lift-off occurring at this higher blowing ratio. It can also be seen that the peaks of the primary and staggered holes are very similar at the downstream locations indicating the films don't decay as quickly as at the lower blowing ratio, although general film effectiveness coverage is worse (as confirmed by Figure 3.6).

Some of the features in the Figure 3.9 may also be explained with reference to the experimental uncertainties. As noted above, the performance of the CFD in capturing local spanwise film effectiveness appears to be improved at the higher blowing ratio where uncertainty in coolant mass flow rate was 4%, a significant reduction compared to the 17% for the lower blowing ratio. Additionally, the difference between the experimental results and CFD generally appear to be greater in the troughs than the peaks; this may again be the result of the increased experimental uncertainty at lower values of film effectiveness.

Figure 3.10 demonstrates normalised velocity contours (where the reference velocity is the bulk average of the mainstream at the inlet) for the E2 geometry at 5 streamwise locations – each midway downstream of the primary film holes – for blowing ratios of both 0.19 and 0.96. Whilst it is appreciated that a finer, structured grid would capture more boundary layer flow features, some interesting observations can still be made. For the lower blowing ratio case, the coolant jet velocity is significantly slower than that of the mainstream and consequently, the ejection of the jet into the mainstream causes a local reduction in mainstream flow speed with

a general migration of the mainstream flow away from the effusion wall. This results in local variations in blowing ratio where each successive hole will experience a slightly higher blowing ratio, until after many rows, a fully developed flow state is reached. For the case of the higher blowing ratio of 0.96 the coolant jet velocity is roughly equal to that of the mainstream flow. The ejection of this coolant into the mainstream causes a local increase in the near wall mainstream boundary layer flow velocity, which, after several rows of cooling holes results in multiple peaks in the mainstream velocity profile (a trend neatly demonstrated by the finer mesh used in the study by [80]).

Sellers' superposition method applied to a single hole CFD model displayed greater discrepancy when compared to the PSP experimental results, and this is highlighted in Figure 3.11. The figure displays two-dimensional film effectiveness data obtained from experiments and both the multi-hole and single hole superposition CFD simulations at a blowing ratio of 0.48 on the $5.66D_f$ pitch geometry. Apparent is the considerable over-prediction in film

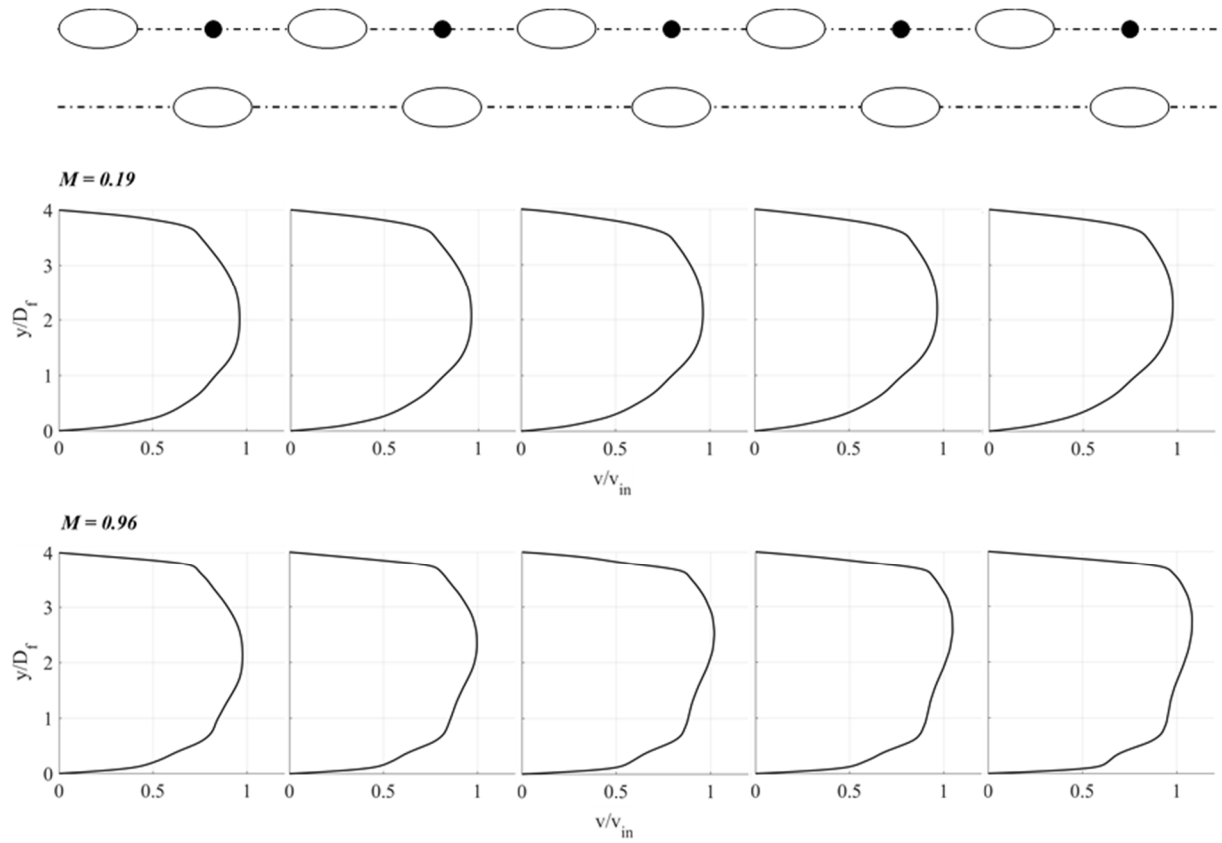


Figure 3.10 - Normalised velocity against normalised height at five streamwise locations (denoted by the black dots) for blowing ratios of 0.19 and 0.96 in the E2 geometry (P = 5.66)

development using the superposition method, with much wider and more effective films being developed by the second row of holes. This trend was observed across all blowing ratios tested with the deviation in effectiveness becoming more prominent as the blowing ratio was elevated. This is well shown by Figure 3.7, which displays spanwise averaged film effectiveness for three of the blowing ratios investigated using the experimental data, along with the results from both computational methods.

Figure 3.7 demonstrates that, by a blowing ratio of approximately unity, spanwise averaged film effectiveness values via the superposition method were around twice those displayed by the multi-hole CFD simulations and PSP experiments. Several reasons are hypothesised for this discrepancy. As already established, the blowing ratio across the tested multi-hole plate was not constant, and this is inherently disregarded in the superposition method. The effects of uneven flow turning in the coolant plenum that feeds the effusion holes were also evident in the multi-hole CFD model. This will once again affect both the blowing ratio and flow field in each individual hole and is not accounted for in the superposition method. The multi-hole CFD simulations also demonstrated how the upstream jets significantly impact the flow characteristics downstream with notable variations in both the velocity and turbulence profiles at downstream film holes. To further explore this hypothesis, further investigations were performed and are discussed below.

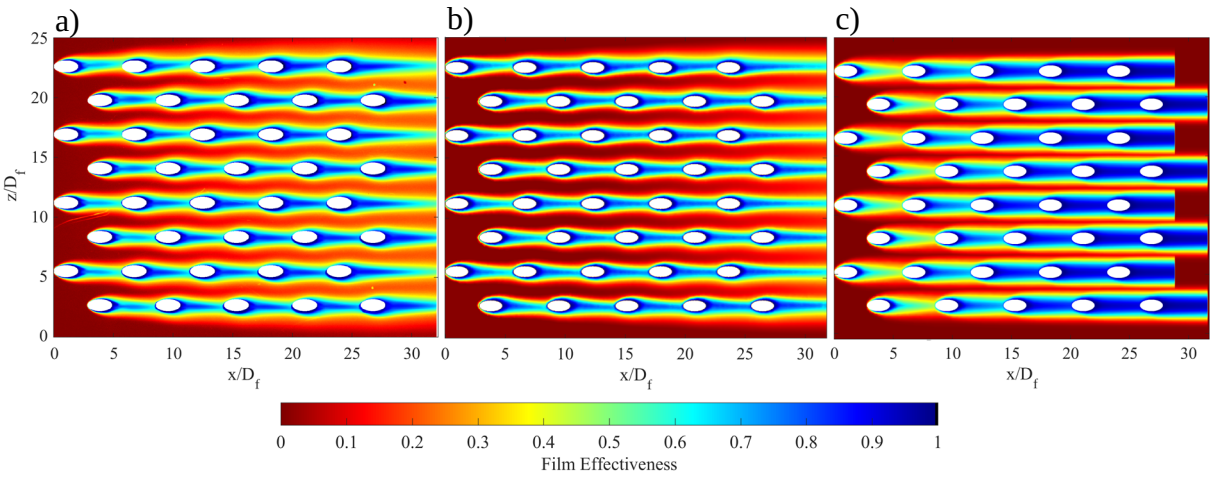


*Figure 3.11 - Film effectiveness contours for a pitch of 5.66D_f and an average blowing ratio of 0.48 from: **a**) the PSP experimental rig; **b**) multiple row CFD simulation; and **c**) Sellers' superposition method applied to a single hole CFD simulation using the two-dimensional film data.*

3.4.1 Further Investigation of Superposition in Effusion Cooling Performance Modelling

To further investigate the cause of the deviation exhibited by Sellers' superposition method in the above analysis and to establish the applicability of the superposition method to effusion cooling, a further geometry was examined via the above multi-hole CFD method. Spanwise hole pitching in the geometry was maintained at $5.66D_f$. To test the hypothesis that it is indeed the variations in the flow characteristics at downstream film holes caused by the upstream film jets that are responsible for this deviation, streamwise hole pitching was increased by a factor of three to $16.98D_f$. It was anticipated, based on the previous results, that this hole pitching would allow for the re-establishment of the downstream flow field and consequently minimise the effect of flow variations due to upstream jets. It is noted that the CFD domain was extended to allow for three rows of primary holes to be simulated. In addition to the multi-hole CFD simulation, the superposition model was applied to the results from a single hole ejection and a comparison made. It is noted that for both methods of analysis, a blowing ratio of 0.48 was investigated. For the multi-hole CFD model the coolant plenum domain was adjusted so that each film hole inlet was fed separately thereby ensuring each hole received the same coolant mass flux and consequently helping to reduce the variation in blowing ratio from each hole.

Figure 3.12 shows the resulting spanwise averaged film effectiveness plots for the increased hole pitch geometry for both the multi-hole CFD simulation and superposition method, along with the contour plots for each case. Apparent is the considerable improvement in the performance of the superposition method at increased streamwise hole pitching with peak spanwise averaged effectiveness values showing a less than 10% discrepancy by the third row of holes. The contour plots demonstrate that the superposition method still develops slightly stronger stripes of effectiveness; however, it is anticipated that this deviation would reduce as hole pitch is further increased. The results do indicate that at the low values of hole pitching that characterise effusion cooling, there are significant interactions between the film jets that

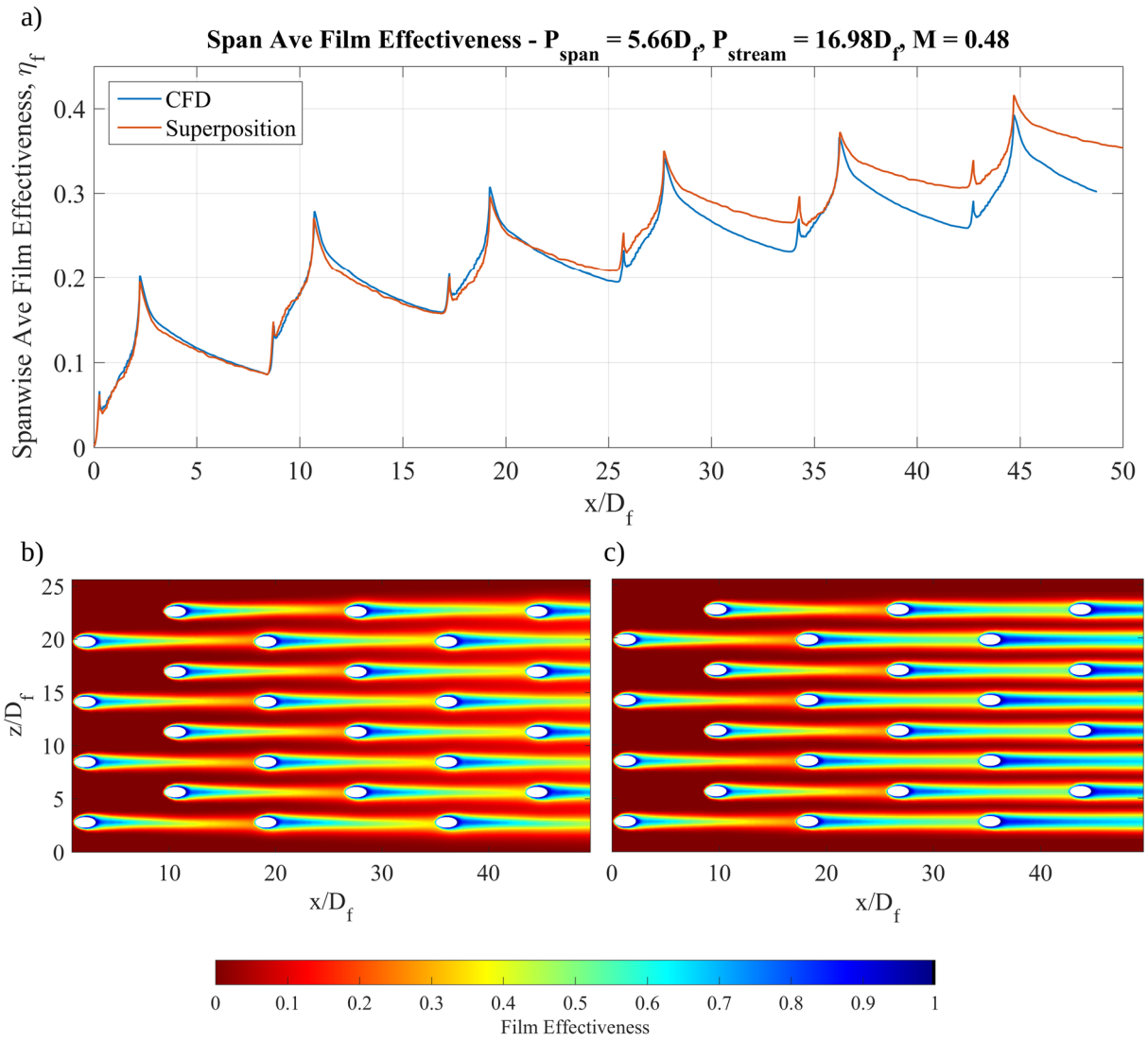


*Figure 3.12 - **a)** Comparison of the spanwise averaged film effectiveness results from both the multi-hole CFD simulations and superposition method for the increased streamwise hole pitching of 16.98D_f (and spanwise pitching of 5.66D_f) at a blowing ratio of 0.48, along with contour plots showing the film effectiveness trends from the **b)** multiple row CFD simulation and **c)** superposition model*

effect the resulting film effectiveness, and these need to be accounted for in any superposition method.

To further demonstrate the effect of upstream jet interactions, flow characteristics were compared for both the *5.66D_f* and *16.98D_f* streamwise hole pitch geometries for the case of a constant blowing ratio of 0.48 using the results of the multi-hole CFD simulations. Contour plots depicting normalised streamwise velocity and turbulent kinetic energy (*TKE*) at a height of *0.33D_f* from the plate surface are demonstrated for both geometries in Figure 3.13 and Figure 3.14, respectively. For the case of the *5.66D_f* pitch geometry, there are notable interactions

between upstream and downstream jets, and these are clearly demonstrated in both the trends for velocity and TKE. Whilst the increased hole pitch still displays some interaction between jets, the effect is significantly reduced, and the flow conditions prior to each hole are approximately the same. Thus, the cooling effect achieved from each hole is similar with little reduction in effectiveness being caused by increased turbulence and flow mixing from upstream jets. Consequently, it is suggested that, without alteration to the superposition method to account for variations in the flow field, care must be taken when applying the method to effusion cooling performance prediction where closely pitched streamwise holes are featured.

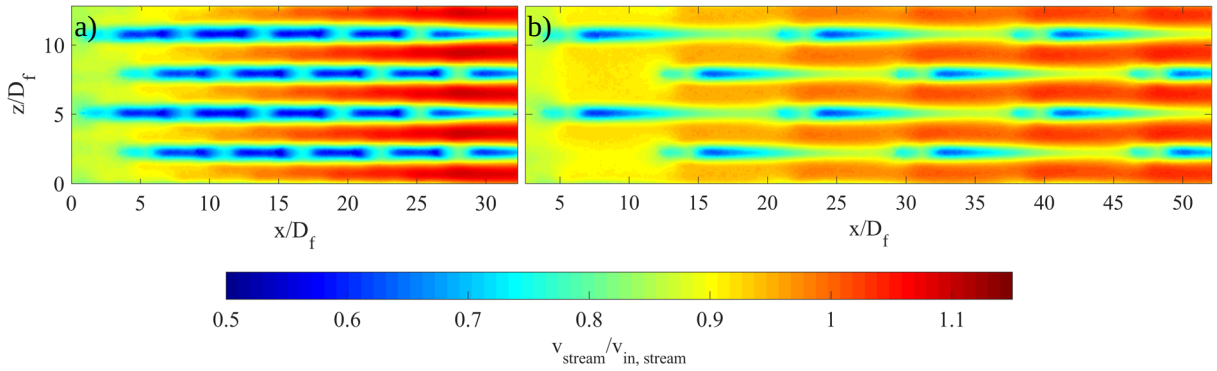


*Figure 3.13 - Normalised streamwise velocity contours at a height of 0.33D_f from the plate surface for the streamwise hole pitches of **a)** 5.66D_f and **b)** 16.98D_f based on the results of the multiple row CFD simulations*

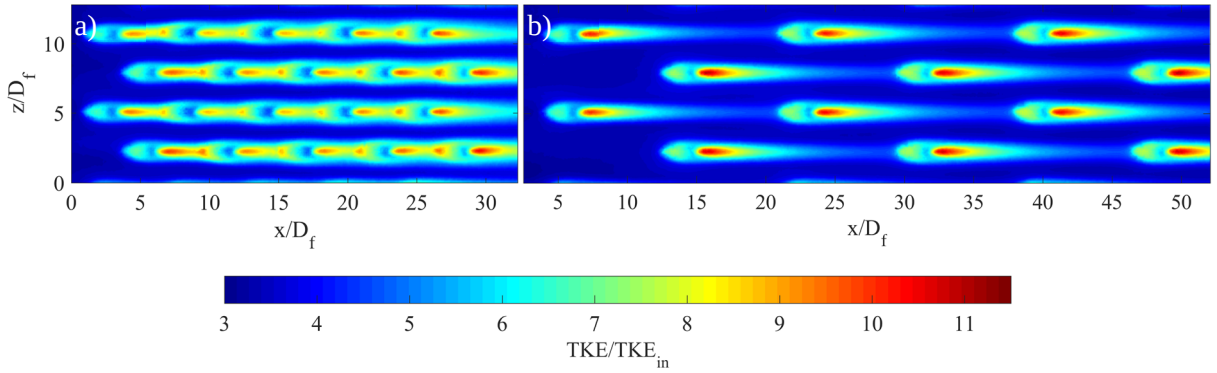


*Figure 3.14 - Normalised turbulent kinetic energy contours at a height of 0.33D_f from the plate surface for the streamwise hole pitches of **a)** 5.66D_f and **b)** 16.98D_f based on the results of the multiple row CFD simulations*

3.5 Summary

The work presented in this chapter has discussed several experimental and computational methods investigated for the modelling of multiple, staggered-row, effusion cooling performance. Two flat plate effusion cooling geometries were investigated with primary hole pitches of $3.0D_f$ and $5.66D_f$, at blowing ratios of between 0.1 and 1.2.

The experimental PSP method developed has provided very high resolution film effectiveness data that have permitted benchmarking of the computational methods. The experimental data have also demonstrated the very high levels of film effectiveness that can be achieved at relatively low blowing ratios when utilising closely-pitched, effusion cooling hole geometries. The $3.0D_f$ pitched hole geometry displayed strong spanwise jet interactions with near complete spanwise films being developed at blowing ratios as low as 0.3. Whilst with the $5.66D_f$ pitch geometry, complete films were not developed at any of the investigated blowing ratios, the experimental results displayed strong film build-up in the streamwise direction.

The multi-hole, heat-mass transfer analogy CFD method has displayed promising results, particularly at the larger of the two pitches investigated in which both the trends observed and absolute film effectiveness values were very similar to those witnessed in the experiments. It is noted that the jet mixing displayed by the CFD does appear to under-predict those seen in the experiments, although this effect is less prominent at the larger pitching.

The results of the superposition model when applied to two-dimensional film effectiveness distributions obtained from a single hole CFD simulation showed greater discrepancy with the experiments. This was primarily expected to result from the increased interactions between the jets in the streamwise direction. Given the much closer hole pitching that characterises effusion cooling, these interactions are more significant. To test this hypothesis, a further geometry was analysed, which maintained a spanwise pitch of $5.66D_f$, but increased the streamwise hole pitch by a factor of three to $16.98D_f$. The superposition method displayed much improved performance at this increased streamwise pitch. Indeed, the multi-hole CFD simulations

demonstrated that, at this greater hole pitch, the general flow field prior to each hole was approximately the same given the increased length over which the flow was able to re-establish after an upstream film ejection. This was displayed via streamwise velocity and turbulent kinetic energy contours that demonstrated the significant reduction in streamwise jet interactions when pitching was increased. Consequently, it is suggested that, for optimal performance prediction in effusion cooling geometries, superposition methods should consider the complex jet interactions that result from the upstream film holes. The potential of the method in significantly reducing simulation times, however, is apparent, and indeed, this is demonstrated in some of the following chapters.

4 Geometrical Design Study

4.1 Chapter Overview

The following chapter discusses the double-wall geometries investigated in this work. Three categories of geometry were investigated featuring a basic repeating unit, termed the *unit cell*. For each of these three categories of geometry, a range of geometric parameters were investigated including pedestal height, spacing and size, along with impingement and film hole non-dimensional pitch. The three basic types of geometry studied were:

- A diamond pedestal geometry where the basic repeating unit comprised two quarter film holes, two quarter impingement holes, five complete pedestals and four half pedestals. Thirteen such geometries were designed using a *Design of Experiments* approach.
- A circular pedestal geometry where the basic repeating unit comprised two quarter film holes, two quarter impingement holes, one complete pedestal and four half pedestals. This geometry was largely investigated for comparison purposes. A total of seven geometries were designed via a Design of Experiments approach.
- A geometry termed the *crenulation concept*. The design of the geometry occurred after the diamond and circular pedestal geometries and was, in-part, informed by analyses of these simpler geometries. The basic design of this geometry has formed the basis of a patent application. One geometry of this form was investigated in the present work.

4.2 Diamond Pedestal Designs

The initial design study was based upon the use of square pedestals oriented at 45^{o} to the streamwise direction, which from this point on will be referred to as diamond pedestals. Several reasons are presented for the selection of diamond pedestals:

- At this early stage of research into double-wall, effusion cooling systems, it was preferable that a relatively simple pedestal geometry be selected to limit the broad design space. A pedestal geometry for which some heat transfer and flow data exists, albeit in alternative cooling systems, was highly desirable – a criterion which diamond pedestals fulfil (see for example [6], [11]). Additionally, diamond pedestals (or variants thereof) have been depicted on similar systems [64], [67].
- With manufacturing methods for double-wall systems providing one of the challenges in the adoption of these cooling technologies, a pedestal design was desirable that would be *relatively* simple to manufacture (see Appendix D).
- The high film effectiveness associated with effusion systems is the result of both the relatively high film hole density (i.e. high outer wall porosity) and low blowing ratios resulting in good film adhesion to the external surface. Whilst clearly the porosity of the outer wall plays a large role in achieving low film blowing ratios, increasing the pressure losses inside the double-wall geometry (thereby decreasing the discharge coefficient) provides another method to reduce film blowing ratio for a given pressure drop across the two walls. Diamond pedestals have, when compared to circular and square pedestals, demonstrated increased pressure losses. The staggering of the pedestals elements has further increased pressure losses whilst increasing convective heat transfer levels [11].

As informed by previous work, a range of parameters were selected for the pedestal sizing, impingement and film hole diameters and wall thicknesses based on industry experience and manufacturing capabilities. This range is demonstrated in Appendix B where there are a total of seven variable geometric parameters. To reduce the size of the design space, both the inner and outer wall thicknesses were equal and constant throughout all the geometries considered (i.e. $L_{w,i} = L_{w,f} = L_w$). Indeed, to further reduce the design space, a basic repeating unit building block – hereon termed the *unit cell* – was proposed and is demonstrated on the right-hand side

of Figure 4.1. The left-hand side of the figure demonstrates the manner in which the unit cell is replicated along with the three different layers of the geometry. It is noted that, for simplicity (and further discussed in Chapter 5), the unit cell enlargement shows normally inclined film holes, whereas the figures on the left demonstrate 30^o inclined film holes.

The effect of the various geometric parameters will be strongly coupled and consequently this needed to be considered during development of the test geometries. Consequently, a *Design of Experiments* (*DoE*) approach was utilised. In such a method, a fully factorial design would require $2^{\text{No. of Parameters}}$ to fully assess every possible configuration (where only the maximum and minimum possible value of each parameter was considered); clearly an unfeasible proposition. Instead then, a fractional factorial approach was undertaken on the understanding that certain effects would be confounded. However, care was taken in selecting the test geometries to allow for the benefits of each parameter to be assessed. The result was twelve geometries where the values for each parameter took either the maximum or minimum of the specified range, with a thirteenth geometry in which the intermediate value was specified for each variable geometric parameter. The specific dimensions for each design are provided in Table 4.1 where it is noted that $P_{primary}$ refers to the non-dimensional pitch between primary, inlined film holes and is calculated by dividing the absolute hole pitch ($S_{primary}$) by the film hole diameter (D_f). A further staggered film hole is positioned at half the non-dimensional pitch in both the stream- and span-wise directions as apparent on the left of Figure 4.1.

4.3 Circular Pedestal Designs

In addition to the thirteen, diamond pedestal double-wall geometries discussed above, a further seven circular pedestal geometries were created, predominantly for comparison purposes. A similar DoE approach was undertaken in their development. The general arrangement of the geometry is demonstrated in Figure 4.2 with respective dimensions for the seven geometries provided in Table 4.2.

4.4 Crenulation Concept Design

A further geometry was designed for both computational and experimental analyses with the basic design demonstrated in Figure 4.3. The design features were, in-part, informed by the analyses of both the diamond and circular pedestal geometries. Several key features are discussed below along with the reasoning behind them:

- An increased pedestal layer height (with a total of 3 mm) provides a greater coolant wetted area for heat transfer to occur.
- Increased impingement hole-to-target wall spacing can be to the detriment of impingement cooling with a potential reduction in impingement zone heat transfer coefficients. Consequently, to maintain the impingement hole-to-target wall spacing, raised protrusions (termed from hereon as crenulations) were created in which the impingement holes were placed.
- The crenulations also have the added effect of further increasing surface area (on both surfaces of the impingement wall) whilst potentially increasing flow mixing and turbulent flow features to further enhance heat transfer in the pedestal layer.
- The arrangement of the pedestal and crenulations were as such to form channels for the flow in the pedestal layer to further increase convective heat transfer.

4.5 Summary

This chapter has presented the double-wall, effusion cooling geometries developed and analysed in this thesis. The geometries can be split into three basic categories, those incorporating diamond pedestals, those incorporating circular pedestals, and a more novel crenulation concept. The latter of these was developed based on analyses of the diamond and circular pedestals and a patent has been filed covering some of the advantageous features of this double-wall cooling iteration.

Diamond Pedestal Geometries

Table 4.1 – Parametric values for the thirteen diamond pedestal geometries selected based on a fractional factorial Design of Experiments methodology

	L_w (*mm*)	L_p (*mm*)	L_3 (*mm*)	L_4 (*mm*)	D_i (*mm*)	D_f (*mm*)	$P_{primary}$	Outer Wall Porosity, ϕ_f
D1	1.0	0.5	0.5	0.5	0.5	0.5	11.32	2.45%
D2	1.0	0.5	1.5	1.5	1.0	1.0	16.96	1.09%
D3	1.0	0.5	0.5	0.5	1.0	1.0	5.66	9.82%
D4	1.0	0.5	1.5	1.5	0.5	0.5	33.92	0.27%
D5	1.0	1.5	0.5	0.5	1.0	0.5	11.32	2.45%
D6	1.0	1.5	0.5	0.5	0.5	1.0	5.66	9.82%
D7	1.0	1.5	0.5	1.5	1.0	0.5	22.64	0.61%
D8	1.0	1.5	0.5	1.5	0.5	1.0	11.32	2.45%
D9	1.0	1.5	1.5	0.5	0.5	0.5	22.64	0.61%
D10	1.0	1.5	1.5	0.5	1.0	1.0	11.32	2.45%
D11	1.0	1.5	1.5	1.5	0.5	0.5	33.92	0.27%
D12	1.0	1.5	1.5	1.5	1.0	1.0	16.96	1.09%
D13	1.0	1.0	1.0	1.0	0.75	0.75	15.09	1.38%

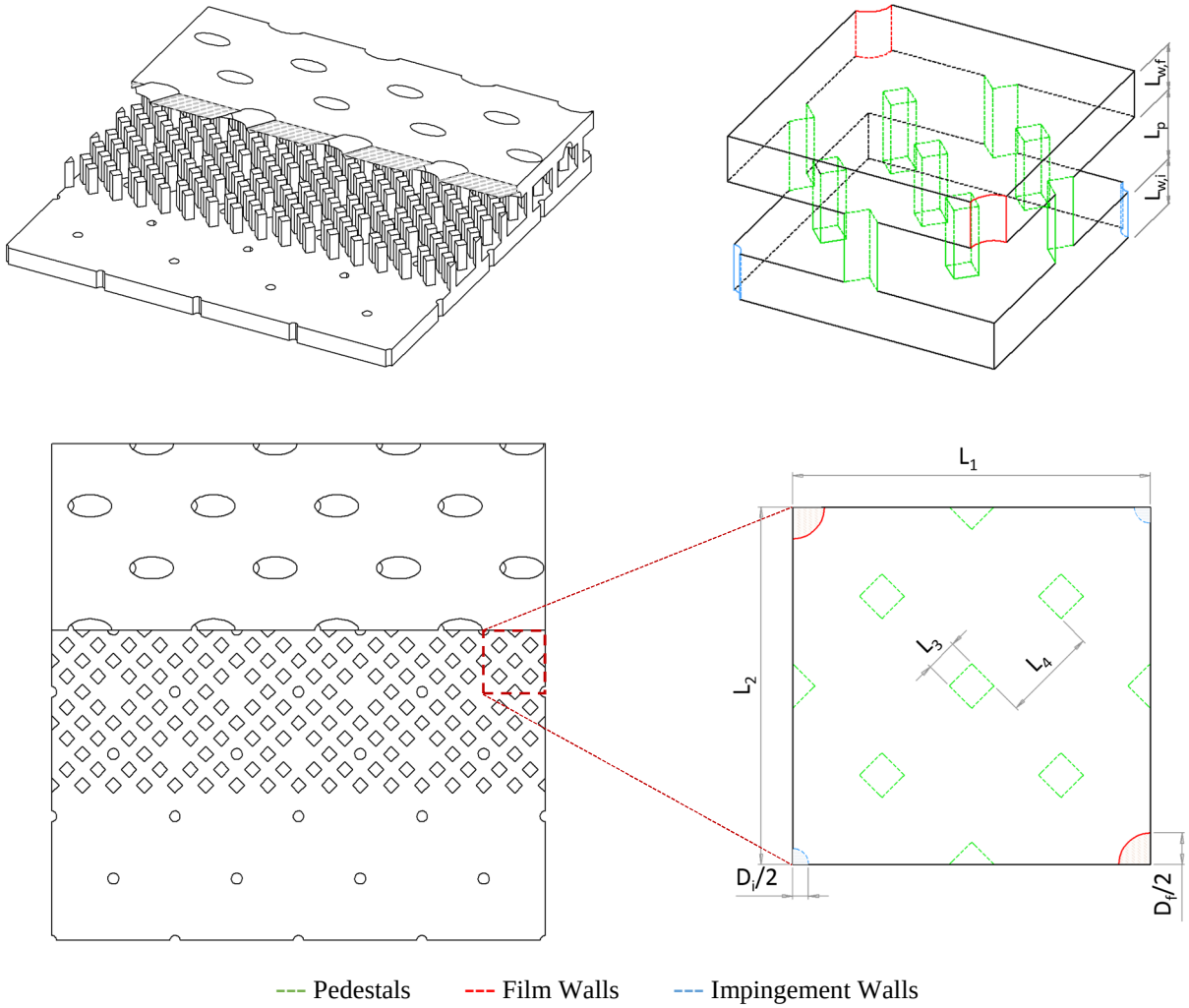


Figure 4.1 – Diagram demonstrating the diamond pedestal geometry considered in this work where the basic repeating unit cell has been enlarged on the right-hand side

Circular Pedestal Geometries

Table 4.2 - Parametric values for the seven circular pedestal geometries selected based on a fractional factorial Design of Experiments methodology

	L_w (*mm*)	L_p (*mm*)	L_3 (*mm*)	D_p (*mm*)	D_i (*mm*)	D_f (*mm*)	$P_{primary}$	Outer Wall Porosity, ϕ_f
C1	1.0	1	1.5	1.0	1.0	1.0	10.0	3.14%
C2	1.0	1	0.5	2.0	1.0	1.0	10.0	3.14%
C3	1.0	1.5	1.5	1.0	1.0	1.0	10.0	3.14%
C4	1.0	1.5	0.5	2.0	1.0	1.0	10.0	3.14%
C5	1.0	1.25	1.0	1.5	1.0	1.0	10.0	3.14%
C6	1.0	1.25	1.0	1.5	0.75	0.75	13.33	1.77%
C7	1.0	1.25	1.0	1.5	1.25	1.25	8.0	4.91%

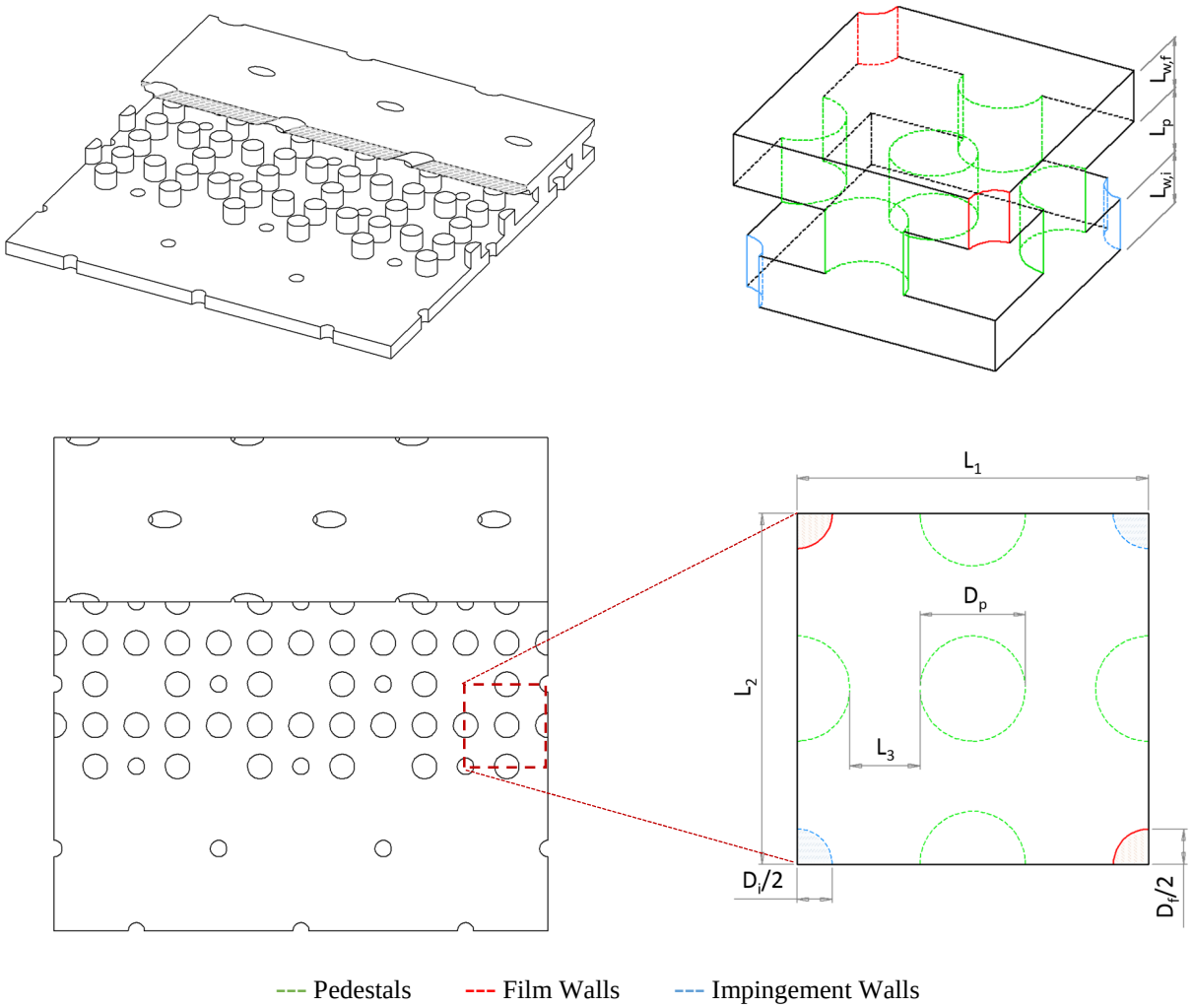


Figure 4.2 - Diagram demonstrating the circular pedestal geometry considered in this work where the basic repeating unit cell has been enlarged on the right-hand side

Crenulation Concept Geometry

Table 4.3 - Parametric values for the concept, crenulation geometry

	L_3 (*mm*)	L_4 (*mm*)	L_5 (*mm*)	L_6 (*mm*)	L_7 (*mm*)	L_w (*mm*)	$P_{primary}$
G1	0.5	0.3	0.47	0.5	1.5	1.0	5.5
	$L_{c,1}$ (*mm*)	$D_{c,1}$ (*mm*)	$D_{c,2}$ (*mm*)	D_i (*mm*)	D_f (*mm*)	**Outer Wall Porosity, ϕ_f**	
	1.5	1.1	1.4	0.5	1.0	10.39%	

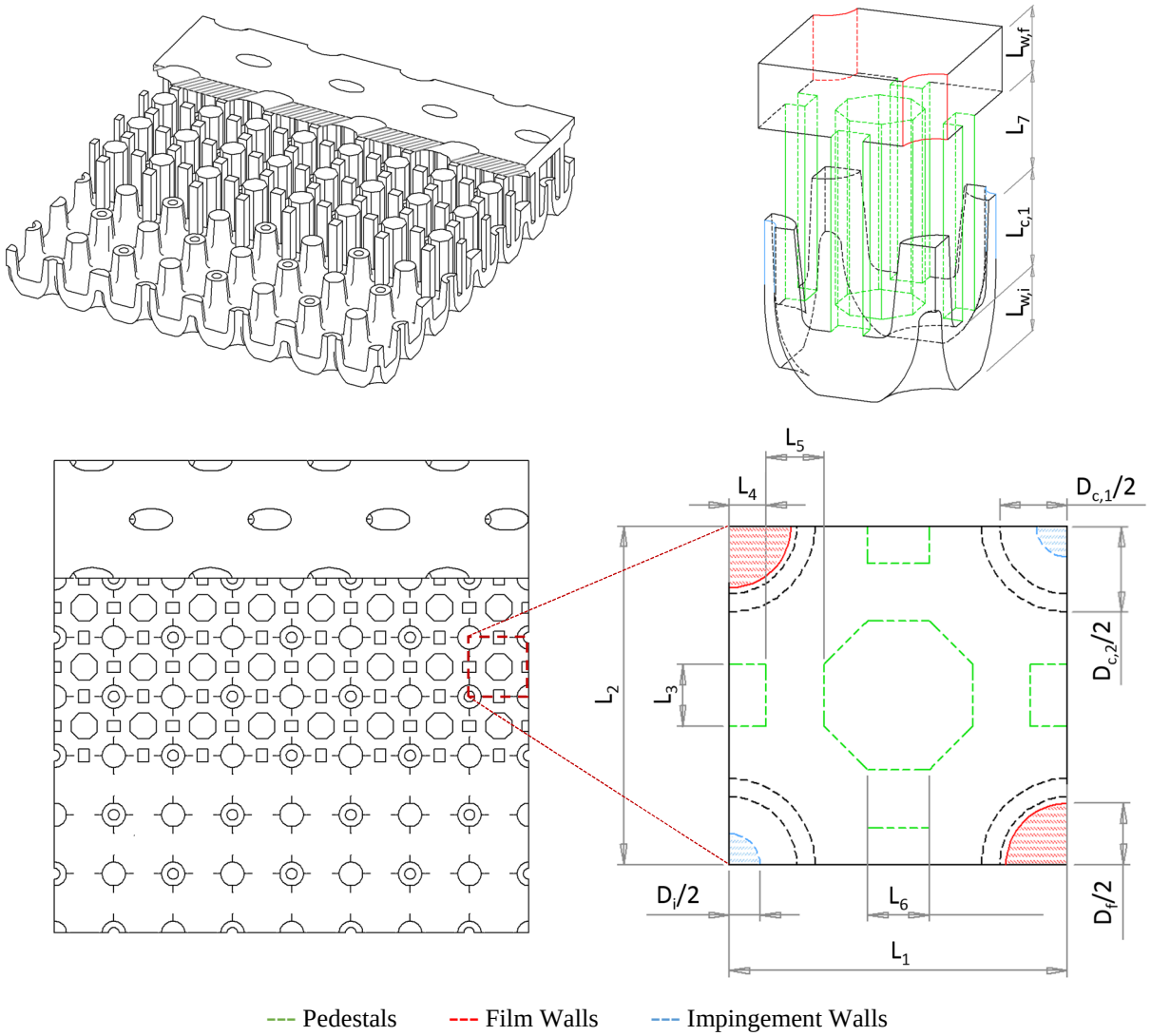


Figure 4.3 - Diagram demonstrating the concept, crenulation geometry considered in this work where the basic repeating unit cell has been enlarged on the right-hand side

5 Decoupled Conjugate Method for Predicting Double-Wall, Effusion Cooling Performance

5.1 Chapter Overview

This chapter discusses the development of a computationally efficient, "decoupled" method for assessing the steady-state aerothermal performance of double-wall cooling geometries. The development of such a process is a necessary tool in the early stages of designing double-wall systems where a relatively quick method of predicting cooling performance for a new design could significantly reduce both the cost and time associated with more complex simulations or experiments. Through use of such a method then, the likely success of a particular double-wall iteration could be rapidly ascertained.

5.2 Internal Convective Cooling Model

In the decoupled method developed, internal heat transfer characteristics were modelled separately to those external to the outer wall. This internal cooling performance was assessed via a conjugate CFD model of the unit cell domain in which plenum fed coolant entered through the impingement holes and was simulated up to the exit of the film holes. No external flow field was modelled in the simulations. It is noted that perpendicular film holes were simulated in the internal CFD simulations. Periodic boundary conditions were considered which would allow for 30^{o} inclined holes, however, the commercial CFD software used (*ANSYS Fluent v16.2*) advised solid domains must not cross the periodic boundary [81]. Additionally, this would result in an enlarged domain increasing simulation times. It is appreciated that 30^{o} inclined holes are a more realistic proposition and this is further considered later.

5.2.1 Boundary Conditions

Boundary conditions used in the simulations were based upon a typical modern civil aviation turbine, the details of which are further elaborated upon in [82]. However, a basic summary of the conditions are demonstrated in Table 5.1, with a graphical description of the boundary condition types shown in Figure 5.1. Due to the symmetrical nature of the unit cell simulated, symmetry boundary conditions were specified around the edges of the solid and fluid domains. Inlet boundary conditions were based upon a total pressure and total temperature specified at the inlet of the plenum. It is noted that the plenum was sufficiently large so that the static pressure and temperature at the inlet were almost identical to the total pressure and temperature. For each geometry, four simulations were performed in which coolant mass flow was varied. This was achieved by varying the outlet static pressure in the different simulations. For all geometries, a pressure drop condition of 0.41 MPa was run (i.e. $p_{s,out}$ = 3.4 MPa). As no mainstream flow was modelled in the simulations, a convective boundary condition was specified on the external surface of the outer wall with the mainstream temperature set as the temperature driving heat transfer into the solid.

Fluid properties (density, thermal conductivity and viscosity) were set to be a function of temperature. Solid properties were also a function of temperature and based upon data for CMSX-4, a nickel superalloy used for manufacturing turbine components.

Table 5.1 – Boundary conditions (gauge) specified for the internal convective cooling unit cell CFD simulations based upon [82]. Outlet pressure varied in different simulations and geometries to vary coolant mass flow

$p_{0,in}$	$p_{s,out}$	$T_{0,in}$	T_∞	h_{ext}
3.81 MPa	1.80 – 3.75 MPa	1000 K	1870 K	7.5 kW/(m^2.k)

5.2.2 Mesh Independence Study and Turbulence Model Selection

In selecting the turbulence model to be utilised in the simulations, four RANS models were investigated: Spalart-Allmaras, standard k-ε, realisable k-ε and k-ω SST. Impingement zone

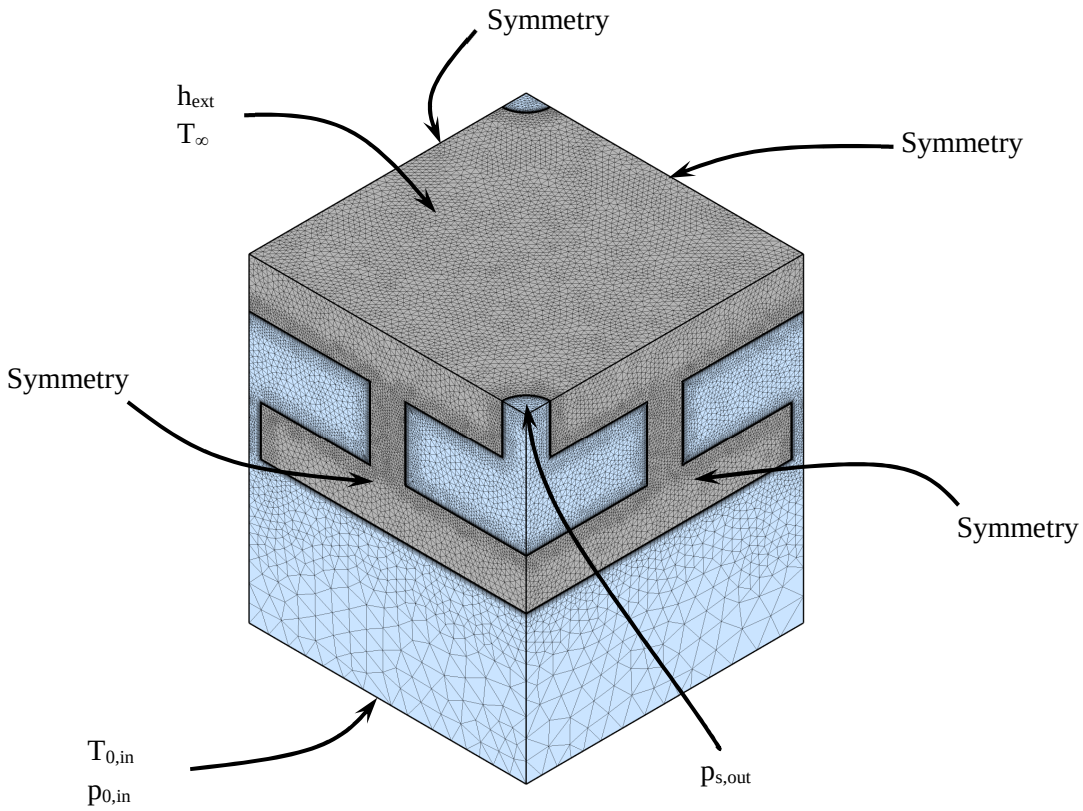


Figure 5.1 – Example of CFD domain and mesh along with specified boundary condition types. The blue surfaces denote the fluid whilst the grey surfaces denote the solid

Nusselt numbers for each model were compared to one another, and to experimental data. As observed in the literature [19], due to the complex flow features associated with jet impingement, the CFD over-predicted impingement zone *Nu* in all cases. Whilst the k-ω SST model was expected to provide the most accurate impingement zone *Nu* predictions [19], it exhibited the least stability and contour plots showed asymmetry in the solutions. Both k-ε and Spalart-Allmaras models demonstrated much greater convergence stability. The results of this comparison, along with industry experience, indicated that the realisable k-ε model would be a suitable turbulence model for the simulations that would provide good convergence stability and solution accuracy. The simulations also utilised enhanced wall treatment.

A mesh independence study was performed to ensure sufficient mesh fidelity without excessive computational requirements. The general construction of the mesh entailed tetrahedral elements in the bulk of the domain, with prism layers around the solid/fluid interfaces to more accurately resolve the boundary layer. Mesh refinements were made along

the film/impingement holes, pedestal surfaces and either side of the two walls. The prism cells created totalled fifteen layers with an overall height of 0.1 mm and a growth rate of 1.2. This ensured that average y^+ values in all simulations did not exceed unity consequently minimising the need for analytical wall functions during the simulations. An example of the meshed domain is displayed above in Figure 5.1. Three metrics were used in determining adequate mesh sizing. These were, area-averaged internal heat transfer coefficient, volume-averaged solid temperature and coolant mass flow rate. The results of the mesh independence study are displayed in Figure 5.2 which shows only a very small variation in these metrics in the finer meshes including that chosen.

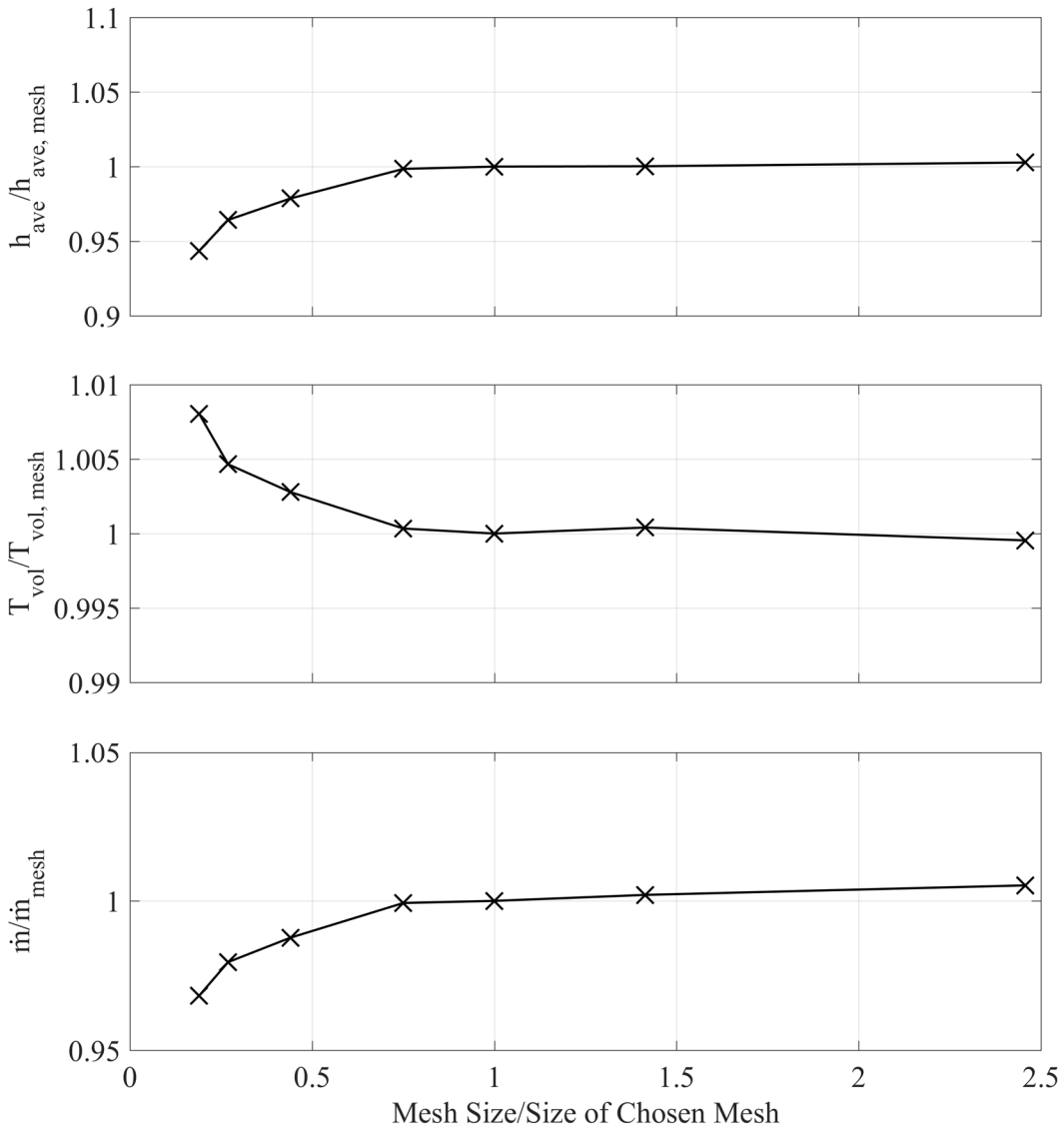


Figure 5.2 – Mesh independence study for the unit cell internal flow conjugate CFD simulations

5.3 External Film Model

CFD was not used in modelling the external flow field and film cooling performance. This was, in part, due to the well document difficulties in CFD accurately capturing the complex features associated with film cooling (see for example [22]), but also due to the vast increase in computational resources and simulation times this would entail, not least due to the much larger domain size that would need to be simulated to capture the development of films over multiple rows of film holes.

To model the external adiabatic film effectiveness, it was decided that a film cooling correlation approach would be used which would again vastly reduce simulation times. Bradley [83] discusses a number of available correlations, however, very few model two-dimensional (spanwise and streamwise) film performance. One correlation that does attempt to model film decay in both directions was developed by Goldstein [84]. The original form of the equation is demonstrated in equation 5.1 where α_t describes the turbulent thermal diffusivity and $z_{1/2}$ describes the spanwise distance at which the film effectiveness is half the value along the centreline. Values for both these parameters were set based on experimental and more up-to-date correlation data – some of which can be found in [26], [85] – where these values varied at different blowing ratios and film hole pitches. Indeed, to more closely match this data, the Goldstein correlation was modified where a new variable – termed x_{decay} – was introduced in the place of the constant *0.5*. This updated form of the correlation is provided in equation 5.2.

$$\eta_f = \frac{Mv_\infty D}{8\alpha_t({}^{x}/_{D} + 0.5)} \exp\left(-0.693\left(\frac{z}{z_{1/2}}\right)^2\right) \qquad (5.1)$$

$$\eta_f = \frac{Mv_\infty D}{8\alpha_t({}^{x}/_{D} + x_{decay})} \exp\left(-0.693\left(\frac{z}{z_{1/2}}\right)^2\right) \qquad (5.2)$$

Whilst the correlation does not directly model jet lift-off, the setting of these parameters based upon available data means that reductions in film effectiveness are accounted for in the

correlation. Consequently, a reduction in film performance at higher blowing ratios indicates the effect of jet lift-off. Values for blowing ratio were based upon the coolant density and velocity at the exit of the film holes obtained from the internal CFD simulations (section 5.2).

The correlation estimates the film effectiveness achieved via a single film hole ejection. To model the development of the films over multiple rows of holes, the additive superposition model proposed by Sellers – the performance of which was discussed in Chapter 3 – was employed. A demonstration of the superposition method when applied to the modified Goldstein correlation is provided in Figure 5.3 for a staggered array of holes with non-dimensional hole pitching (in both x and z) of 10 between the primary holes. Due to the limitations of the correlation, the discrete nature of the individual films is apparent in the figure; however, it is noted that this effect is smoothed out in the coupling procedure discussed below.

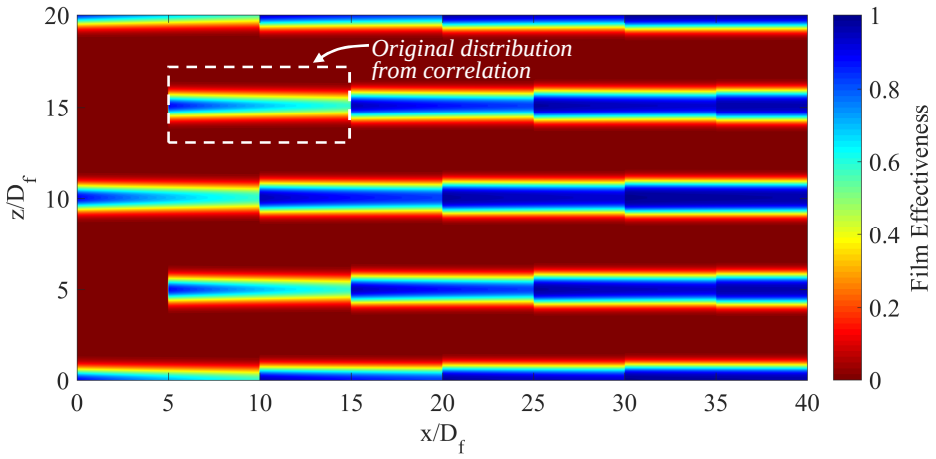


Figure 5.3 Graphical demonstration of the superposition method when applied to the modified Goldstein correlation for $P_x = P_z = 10$

5.4 Coupling of the Internal and External Cooling Models

To permit an overall assessment of the cooling performance achieved by the double-wall effusion geometries, it was necessary that both the internal and external cooling analyses be combined, or "coupled" allowing a final temperature profile to be developed across the geometries.

Thermomechanical simulations (the subject of discussion in Chapter 6) based on the temperature profiles developed via the decoupled conjugate method required constrained edges (to prevent rigid body motion) which result in large stress concentrations near these areas (and around the free-edges of the geometry). This required the domain over which the final temperature profile was to be developed to be sufficiently large to avoid the skewing of the mechanical results due to these stress concentrations. Additionally, a domain size was desired over which the effect of film development from multiple film ejections could be observed. Based on previously performed work by the author, the domain size selected over which the final temperature profile was to be developed was approximately 40 mm in both the streamwise and spanwise directions. As previously discussed, the internal cooling simulations modelled a small repeating unit of the geometry with edge dimensions between ~2.8 – 17 mm depending on the specific geometry. However, owing to the symmetrical nature of the unit cell, results of the CFD simulations could be exported to *MATLAB* (along with the corresponding mesh node locations) and the domain size enlarged via a replication of the CFD results with an offset based on the original domain size. During this process the wall heat flux and surface temperature data from the simulations was used to calculate the internal heat transfer coefficients with the coolant inlet temperature as the fluid reference temperature. Additionally, a further modification was made to the CFD mesh data. As described above, due to restrictions in employing periodic boundary conditions, 90^o film holes were modelled in the internal flow simulations permitting the use of symmetry conditions. However, inclined holes are more representative of the shaped film holes that are typically used in practice. Consequently, the heat transfer coefficients calculated in the *MATLAB* script were interpolated from the original 90^o film holes onto 30^o inclined holes. As eluded to by Hu and Ji [45], one effect of varying film hole inclination angle is the resulting change it makes to the inner hole area for convective cooling. Byerley [86] experimentally demonstrated the change in discharge coefficient between 30^o and 90^o holes as being 0 – 30% depending on the pressure drop. The interpolation method used in this study is

deemed acceptable given that it captures the increased inner hole convective effect and that the discharge coefficient here is a function of the losses across the entire double-wall geometry and not just across the film hole.

In developing the coupled temperature profile, the calculated internal heat transfer coefficients were interpolated onto the enlarged domain which included the 30º inclined film holes and utilised a driving temperature based on that of the coolant inlet used in their calculation. The external surface boundary condition specified was the adiabatic wall temperature calculated via the film effectiveness correlation-superposition method with a constant heat transfer coefficient of 7.5 kW/m^2.K. The final, coupled temperature profile was developed across the model using a three-dimensional Fourier law conduction analysis in *ANSYS Mechanical (v16.2)*. A graphical representation of this enlargement and coupling procedure is demonstrated in Figure 5.4 where the temperature contour at each stage of the process is demonstrated for an example case.

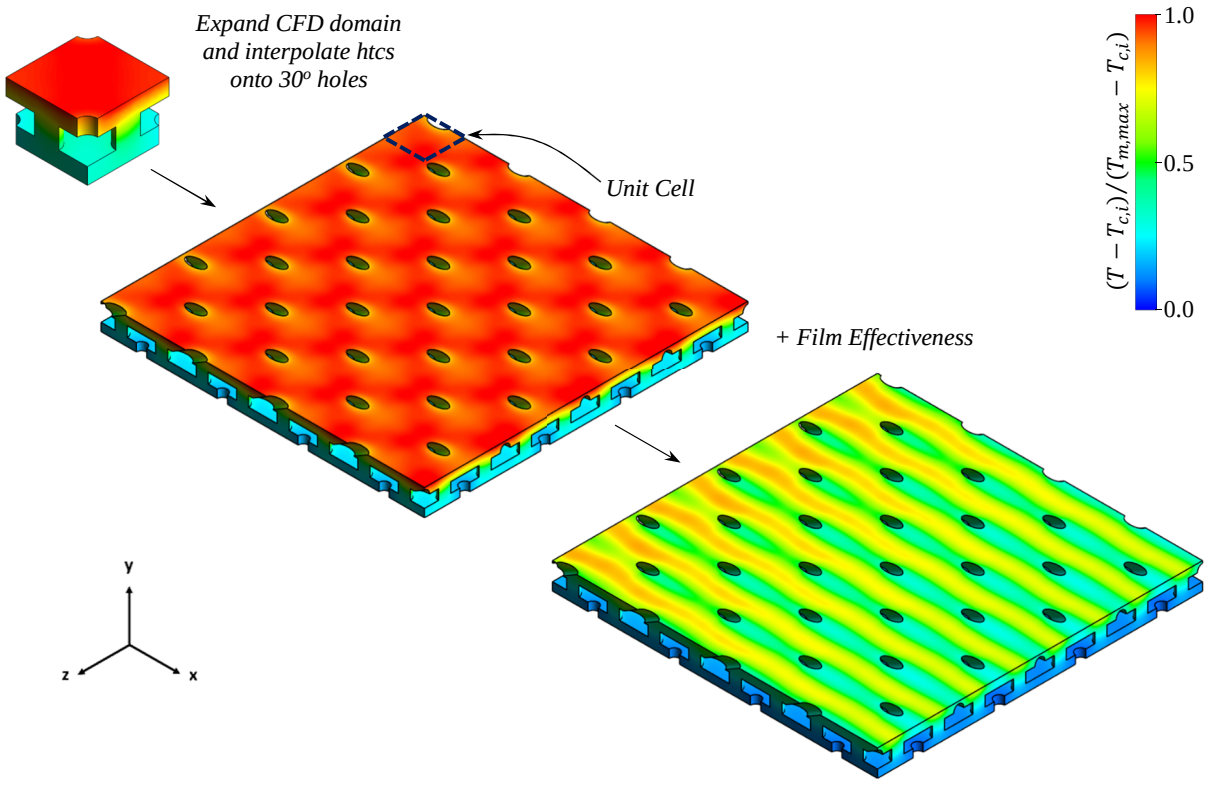


Figure 5.4 - Graphic showing the domain enlargement and coupling of the external and internal cooling methods to form the final thermal profile

5.5 Aerothermal Results

The decoupled conjugate methodology developed has allowed for detailed aerothermal performance predictions to be ascertained at a relatively low computational cost. These calculations permit a comparison to be made between the performance of the various geometries investigated. Figures 5.5 – 5.7 demonstrate the overall effectiveness based on both the area-averaged external film wall surface temperature and volume-averaged solid temperature, along with film effectiveness achieved at different values of m^* and blowing ratio for the diamond, circular and crenulation geometries presented in Chapter 4 respectively.

5.5.1 Film Effectiveness

Plots demonstrating the area-averaged film effectiveness achieved at a range of blowing ratios using the two-dimensionally varying, modified Goldstein [84] correlation with Sellers' [78] additive superposition method applied are demonstrated in the bottom right of Figures 5.5 – 5.7. The plots very clearly demonstrate the effect of jet lift-off at high blowing ratios where high jet momentum reduces the likelihood of jet adhesion to the external wall surface thereby reducing the protective effect of the film. In all cases, peak film effectiveness occurs at blowing ratios of approximately 0.6 – 0.7. This is similar to the findings of Chapter 3 and concurs with the findings of Ling et al. [79]. Indeed, this demonstrates that the modifications made to the Goldstein equation, along with the setting of the variables α_t, $z_{1/2}$ and x_{decay} have successfully captured the expected trends in film effectiveness. The plots also very clearly demonstrate the potential benefits of highly porous film walls, a characteristic of effusion systems which demonstrates closely pitched holes. In Figure 5.5, D3 and D6 demonstrate the lowest non-dimensional hole pitch ($P=5.66$ between primary film holes) from the diamond pedestal geometries and consequently, the most regular ejection of coolant films. The result of this is a much smaller variation in spanwise film effectiveness, along with shorter streamwise distance for films to decay before another film jet is ejected from the double-wall geometry; this leads

to a very high area-averaged film effectiveness. On the other end of the scale, geometries D4 and D11 demonstrate the sparsest array of film holes (with a primary hole pitching of $P=33.92$). Consequently, area-averaged film effectiveness is low with very pronounced stripes of films visible and minimal spanwise film interactions. The trend is much the same for the circular geometries in Figure 5.6. It is noted that, given that geometries C1 – C5 had the same non-dimensional hole pitch ($P=10.0$), their film performance is very similar and, in the plot, nearly indistinguishable. Finally, the crenulation concept G1 demonstrated in Figure 5.7 shows similar area-averaged film effectiveness to geometries D3 and D6, a result of the similar hole pitching of $P=5.5$.

The bottom left plots in Figures 5.5 – 5.7 demonstrate the same area-averaged film effectiveness, but this time plotted against non-dimensional coolant mass flow. The figures indicate that, the more porous geometries with regular, closely positioned films are more insensitive to variations in coolant mass flow rate demonstrating good film performance over a wide range of coolant mass flows. The less porous geometries (for example D4 and D11 in Figure 5.5) demonstrate a very small range over which optimal film performance (for the specific geometry) is observed. This result is to be anticipated – geometries which exhibit high porosity require significantly increased coolant mass flow before blowing ratios become sufficiently high for jet lift-off to occur. Whereas for less porous geometries, relatively low coolant flow rates result in high momentum film jets and, as a result, peak film effectiveness occurs at very low coolant flow rates.

The results of the above very strongly support the reasoning behind the use of effusion cooling type systems which are characterised by highly porous walls incorporating low film hole pitching. Film jets consequently operate at low blowing ratios across a wide range of coolant mass flows resulting in a film performance which is relatively insensitive to coolant flow rate. It is noted, however, that on the suction side of a turbine where a preferable pressure gradient exists, a highly porous external wall may not be necessary; consequently, a less porous

film wall may occasionally be a desirable feature (dependent on the internal cooling performance).

5.5.2 Overall Effectiveness

The two top plots in Figures 5.5 – 5.7 demonstrate overall cooling effectiveness against non-dimensional mass flow for the various geometries where the figure on the left provides overall effectiveness based on area-averaged external film wall temperature, and that on the right based on the volume-averaged solid temperature. As mentioned previously, it is noted that, for each geometry, the CFD simulations were run at four pressure drop conditions (denoted by the crosses in the plot) based on the boundary conditions in Table 5.1. For less porous geometries, coolant mass flow was reduced for the same pressure drop. Characteristic curves were fitted to these points. Note that these only consider the internal convective cooling performance simulated in the internal CFD simulations. The plots also provide an assessment of the increase in overall cooling effectiveness when the additional effect of external cooling films is considered based upon the results of the modified Goldstein-Sellers' superposition approach using the temperature obtained via the decoupled conjugate methodology presented. These results are denoted by the circular points and conform to the outlet pressure condition ($p_{s,out}$) of 3.4 MPa (i.e. a total inlet to static outlet pressure drop of 0.41 MPa) for all geometries.

For the diamond pedestal geometries shown in Figure 5.5, geometry D6 displays preferable internal cooling performance over a wide range of m^*. This geometry includes the largest passage height, as well as high density of pedestals, a result of which is the relatively large internal surface area over which convective heat transfer can occur. Additionally, this dense pedestal configuration results in a relatively large heat flux being conducted away from the hotter film wall and transferred to the coolant via convection. This significant internal convective cooling performance is coupled with the aforementioned high film effectiveness exhibited in the geometry due to the dense film hole array. This high film hole density has the

additional result of increasing film hole wetted area. Indeed, for the Δp condition of 0.41 MPa for which the coupling of the internal and external cooling methods was run, and which for geometry D6 conforms to an m^* of 4, the additional cooling contribution of the films resulted in an increase in external overall effectiveness of around 0.25. The significant boost in cooling performance arising from the films in the more porous geometries is thus evident.

Geometry D3 also displays interesting cooling characteristics. As with D6, geometry D3 displays the highest pedestals density and film hole density and differs only in having a smaller pedestal layer height and a larger impingement hole diameter. The consequence of the latter is an increase in impingement wall porosity and therefore increased coolant flow rates at similar pressure drop conditions; although at similar values of coolant flow rate, impingement jet Reynolds numbers will be reduced with a likely reduction in impingement zone heat transfer coefficients. The overall cooling effectiveness based on the outer wall temperature is relatively similar to D6 (ignoring the fitted curve at low values of m^* where data points are sparse). However, the overall effectiveness based on volume-averaged temperature is around 0.05 – 0.1 lower than geometry D6. This is almost certainly a consequence of the reduced passage height where internal wetted area is much reduced. It is noted, however (and elaborated upon in Chapter 6 and Appendix C) that this results in a more uniform temperature across the geometry which may have benefits from a thermomechanical perspective.

Among the diamond pedestal geometries with intermediate porosity, geometry D8 appears to display interesting cooling performance. It is noted that in turbine applications where a strong pressure gradient exists over the surface of the blade, reduced porosity geometries which exhibit relatively high internal convective cooling performance may be desirable in some locations on the blade. Indeed, based on the volume-averaged overall cooling effectiveness plot, geometry D8 exhibits high internal convective cooling performance at low coolant flow rates and is consequently of interest. The geometry features a relatively sparse array of small pedestals and so conduction between the walls is low which results in a relatively large thermal gradient

across the layers. This causes a more ordinary overall cooling effectiveness based on only the area-averaged film wall temperature.

The trends observed for the circular pedestal geometries in Figure 5.6 are similar to those made above and for brevity are not elaborated upon here – although the reader can find an elaboration on this in a paper by the author explicitly discussing the circular pedestal geometries (see [87]).

To further investigate the effect of varying the geometric parameters on cooling performance, *main effects* plots were developed and, for the diamond pedestal geometries are shown in Figure 5.8. Main effects plots explore the effect of an individual variable (here the geometric parameter) on the quantity of interest (in this case overall effectiveness, or in Chapter 6 the volume-averaged Von Mises stress). The plots are for the pressure drop condition of 0.41 MPa with volume-averaged overall effectiveness shown and accounting for both internal convective cooling and film cooling effects. Given the relatively small and non-exhaustive range of geometries investigated, the effects of some of the parameters will be confounded; in other words, there will be some interactions present between the different geometric variable which will be indistinguishable in the plots. However, the graphs provide an interesting insight into some of the observed behaviour. It should also be noted that the plots only indicate potential geometric design rules from a thermal perspective and consequently disregard possible associated aerodynamics penalties. The results of the plots are discussed below:

- As expected, increasing the impingement hole diameter results in an increase in cooling performance. In the case of the presented simulations, larger impingement hole diameter typically resulted in a greater coolant flow rate at a constant pressure drop condition due to the increased wall porosity. The greater hole diameter also resulted in an elevated impingement wall wetted area for internal convection to occur.
- As has been previously mentioned, increasing film hole diameter appears to have a benefit on cooling performance. In the current simulations, increasing the film hole

diameter typically resulted in a reduction in film hole non-dimensional pitch resulting in more complete cooling films being formed on the outer surface of the film wall. Additionally, once again the greater wall porosity increases coolant wetted area whilst also reducing jet blowing ratio minimising the likelihood of jet lift-off.

- The graphs indicate that preferable cooling performance is achieved when pedestal edge length is reduced, but the density of pedestals is increased. It is hypothesised that this is the result of two effects. The first is the increased wetted internal surface area over which convective cooling can occur. The second is the increased pedestal/wall contact area that occurs in the geometries with small but densely configured pedestals. This results in an increased conduction of heat away from the hotter wall which is then transferred via convection to the coolant.
- The trend in passage height appears to be less conclusive with the results appearing to indicate that cooling performance is relatively invariant of passage height. The presence of confounding is suggested to be occurring in this plot. It was anticipated that as passage height was increased, more surface area would be available over which convection could occur. Whilst increased passage height may result in a slight reduction in impingement zone Nusselt numbers, this effect is relatively small over the range of impingement hole/target plate spacings tested. Indeed, the main effects plots for the circular pedestal geometries (see [87]) supports the notion of increasing the passage height to improve cooling performance, although the effect of doing so appears secondary to the other geometric variables.

The findings of the above investigations on the diamond and circular pedestal geometries were used in the development of the crenulation concept geometry G1.

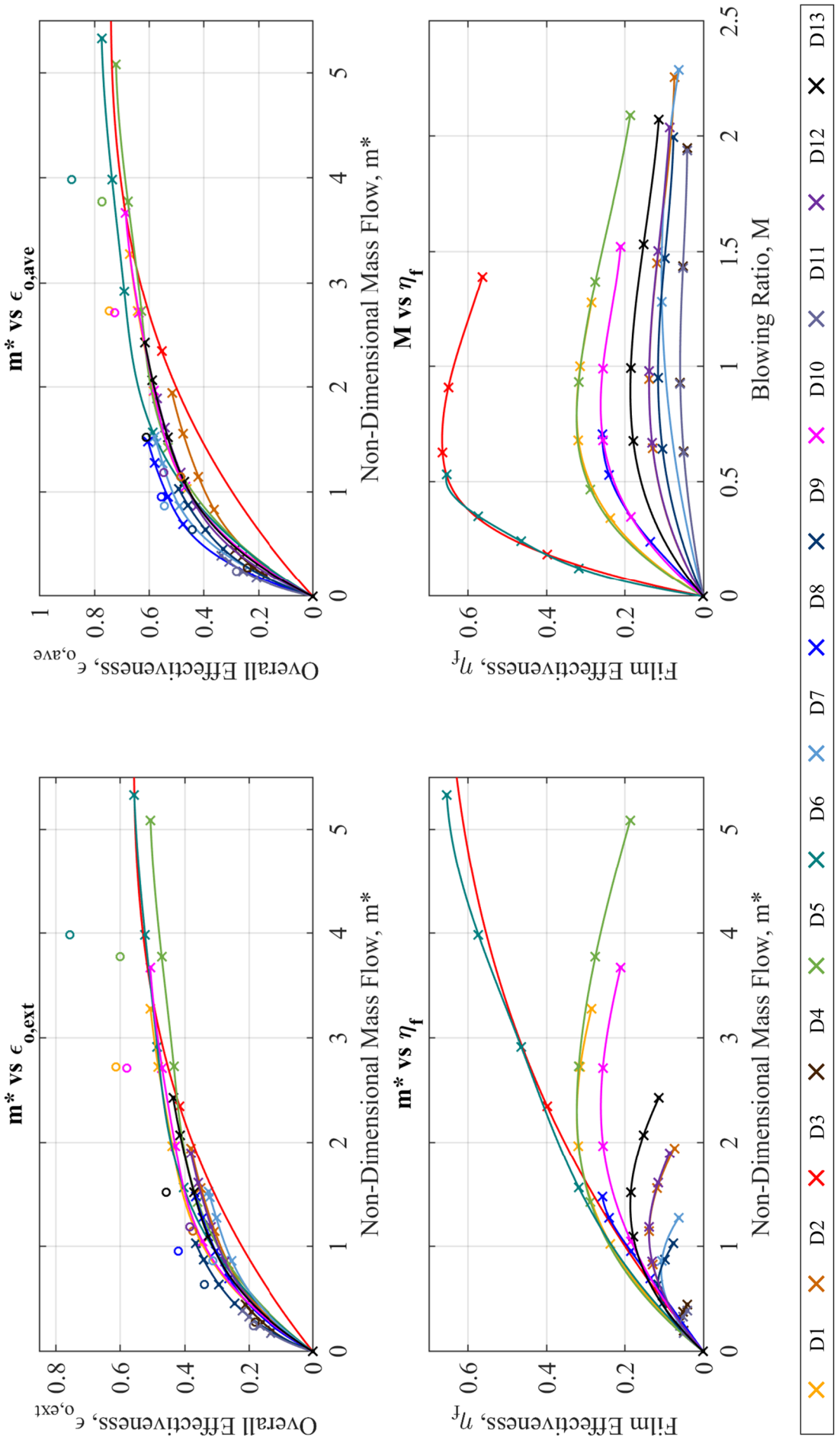


Figure 5.5 – Plots demonstrating the aerothermal performance of the diamond pedestal geometries. Top left and right figures demonstrate overall effectiveness based on the area-averaged external surface and volume-averaged solid temperatures respectively. Crosses and solid lines denote internal convective cooling performance only, whilst circular points denote the cooling achieved including the effect of films at a pressure drop of 0.41 MPa. Bottom left and right figures demonstrate film effectiveness vs m and blowing ratio respectively*

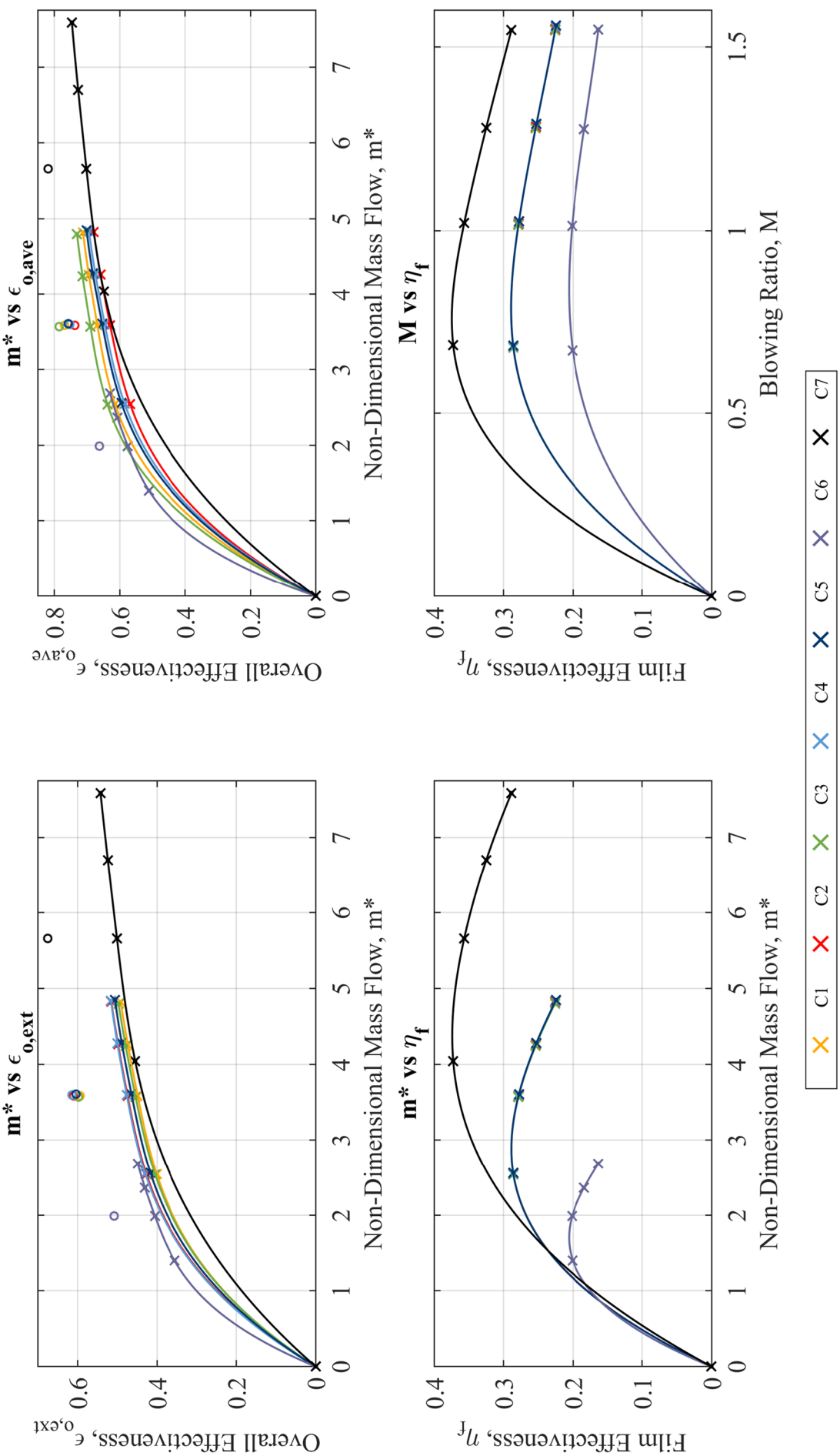


Figure 5.6 - Plots demonstrating the aerothermal performance of the circular pedestal geometries. Top left and right figures demonstrate overall effectiveness based on the area-averaged external surface and volume-averaged solid temperatures respectively. Crosses and solid lines denote internal convective cooling performance only, whilst circular points denote the cooling achieved including the effect of films at a pressure drop of 0.41 MPa. Bottom left and right figures demonstrate film effectiveness vs m and blowing ratio respectively*

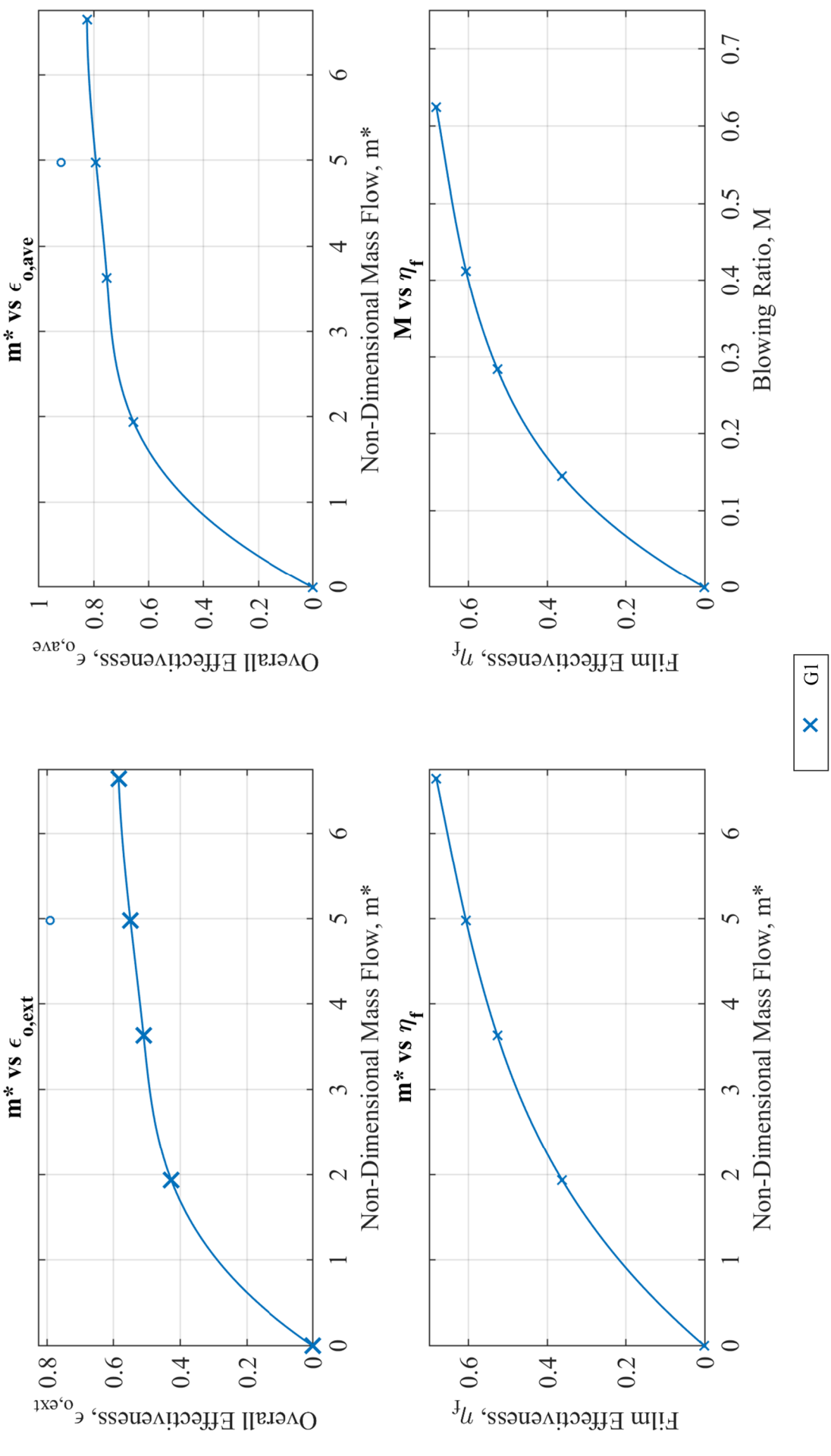


Figure 5.7 - Plots demonstrating the aerothermal performance of the concept crenulation pedestal geometry. Top left and right figures demonstrate Overall effectiveness based on the area-averaged external surface and volume-averaged solid temperatures respectively. Crosses and solid lines denote internal convective cooling performance only, whilst circular points denote the cooling achieved including the effect of films at a pressure drop of 0.41 MPa. Bottom left and right figures demonstrate film effectiveness vs m and blowing ratio respectively*

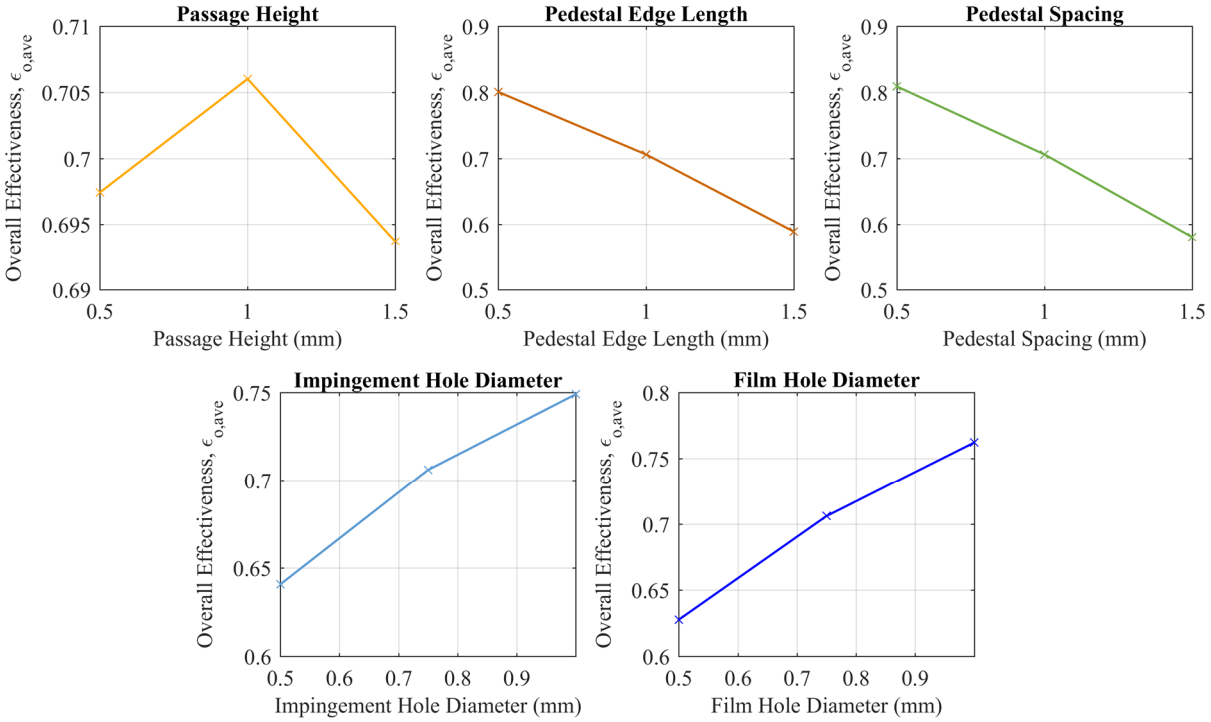


Figure 5.8 – Aerothermal main effects plots for the diamond pedestal geometries showing the effect of varying the geometric parameters on volume-averaged overall cooling effectiveness (including film cooling performance) for the pressure drop condition of 0.41 MPa

5.5.3 Effective Porosity

The above analysis has proved effective in allowing the comparison of various double-wall geometries to one another in an effort to identify features preferable from an aerothermal perspective. However, whilst the use of the non-dimensional mass flow variable, *m**, permits such a comparison between geometries and with more conventional cooling systems, the need for a metric that allows for some prediction of potential geometry cooling performance without the need for multiple simulations was identified.

In developing such a metric, the outer wall geometric porosity (ϕ_f) shown in Table 4.1 was initially considered. However, such a geometric porosity alone does not capture both the level of internal blockage as well as the variation in perceived blockage at varying pressure ratios (and consequently mass flows). Consequently, to account for this an effective porosity (ϕ_{eff}) was defined as the product of both the discharge coefficient (as calculated from the decoupled conjugate method) and outer skin porosity and this is demonstrated in equation 5.3 where the Mach number was calculated using isentropic flow relations as per equation 5.4.

$$\phi_{eff} = \phi_f C_d = \phi_f \frac{\dot{m}_{actual}}{\dot{m}_{ideal}} = \phi_f \frac{\dot{m}_{actual}}{\left({}^{p_{out}}\!/_{RT}\right) Ma (\gamma RT)^{1/2} \pi \left({}^{D_f}\!/_{2}\right)^2} \qquad (5.3)$$

where:

$$Ma = \left(\frac{2\left(\left({}^{p_{out}}\!/_{p_o}\right)^{-(\gamma-1)/\gamma} - 1 \right)}{\gamma - 1} \right)^{1/2} \qquad (5.4)$$

Figure 5.9 displays the variation in overall effectiveness (based on volume-averaged temperature and excluding the added cooling effect of the films) with effective porosity for the diamond pedestal geometries. It is noted that the trends for the circular pedestal geometries were very similar. The plot demonstrates the variation in both effective porosity and overall effectiveness at three pressure drops: Δp = 0.21, 0.41 and 0.81 MPa. Characteristic curves are fitted to the data for each pressure drop condition.

As expected, discharge coefficient increases slightly with Reynolds number due to a reduction in both viscous losses and friction factor, and this effect is more prominent in the more porous geometries. The figure provides some prediction as to the potential cooling effectiveness that can be achieved from a geometry based on the effective porosity alone and regardless of the specific internal geometric configuration. As anticipated, as effective porosity is increased, there is a corresponding elevation in overall effectiveness at a particular pressure drop condition. This indicates a greater coolant volume is being utilised in cooling the geometry. The graph also demonstrates that, at similar levels of ϕ_{eff}, as pressure ratio (and hence coolant volume) is increased, overall cooling effectiveness rises. However, this benefit is reduced as pressure ratio is further increased which is indicative of a reduction in convective efficiency confirming the trends observed in Figures 5.5 – 5.7.

Whilst the characteristic curves allow for a prediction of overall cooling effectiveness for a known effective porosity, the plots do demonstrate some potential deviation from the curves among the various geometries. It is hypothesised that such variations arise due to a range of

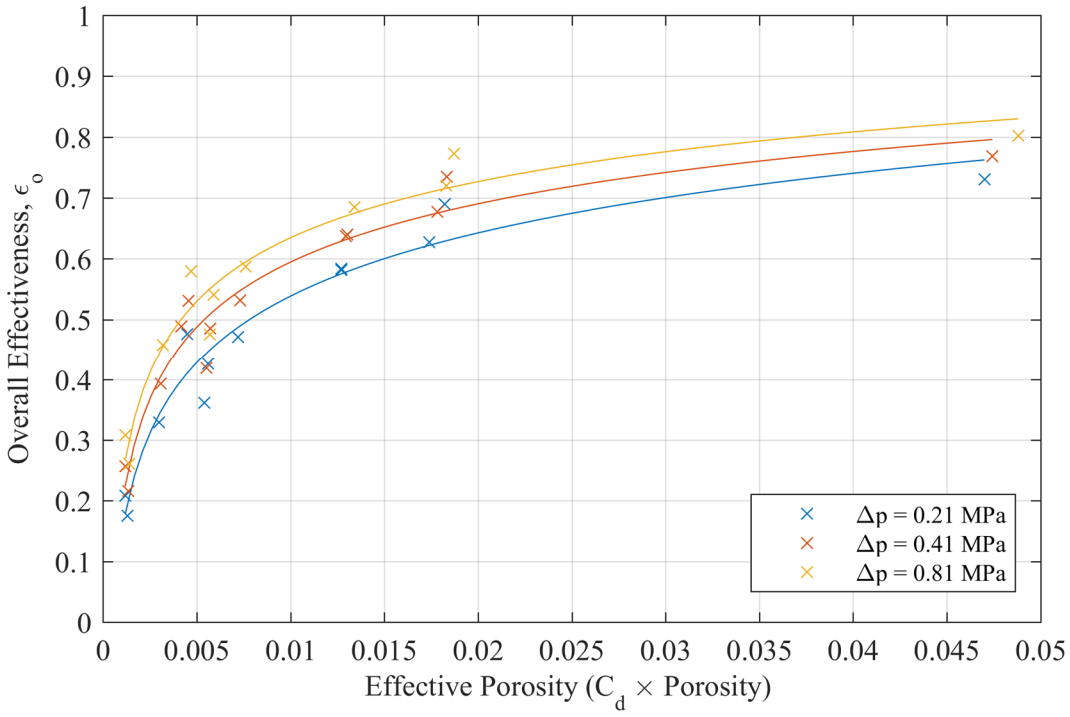


Figure 5.9 – Effective porosity against overall effectiveness based on volume averaged solid temperature (excluding effect of films) for the diamond pedestal geometries

factors not considered in the definition of effective porosity, for example the variations in solid properties with temperature. It is also speculated whether simply using the film hole diameter in the definition of the ideal mass flow rate is the correct diameter or if some ratio accounting for the impingement hole diameter, for example, would be more suitable. However, the plots are very useful in providing some initial prediction of the achievable cooling effectiveness from a double-wall geometry for which the effective porosity is known, or indeed, the effective porosity required to achieve a certain cooling benefit. As such the metric provides a useful tool in the initial cooling design stage, where the data can be used to identify double-wall geometries suitable for further computational or experimental analyses.

The above definition of effective porosity can be considered somewhat analogous to that of the Darcy-Forchheimer equation which describes the pressure drop across a porous medium (i.e. that of a transpiration system). It is repeated in equation 5.5 where K_D and K_F represent the Darcy coefficient and Forchheimer coefficient respectively which are material specific.

$$-\frac{dp}{dx} = \frac{\mu}{K_D} v + \frac{\rho}{K_F} v^2 \qquad (5.5)$$

It is noted that the two terms on the right hand side of the equation represent a viscous term (Darcy's Law) which is dominant for low velocity flows, and an inertial term arising due to flow resistance (the Forchheimer term) which dominates at higher flow speeds [88], [89]. Consequently, some comparisons can be drawn to the effective porosity that has been defined for double-wall systems which accounts for internal losses at varying flow speeds.

5.6 Summary

A computational method has been developed for assessing the aerothermal performance of double-wall type cooling geometries (although the method could potentially find use in other types of cooling systems). The method is described as being "decoupled" in that the internal and external cooling performance of the system are modelled in separated simulations and coupled in a thermal FEA analysis. Internal convective cooling performance is calculated for a small repeating unit using conventional conjugate CFD methods. External film performance is based upon a modified two-dimensionally varying correlation with an additive superposition method to model streamwise film development. The benefit of the method is the vast reduction in computational resources and simulation time required to obtain a prediction of the cooling performance achievable from a particular double-wall geometry.

The method was used to analyse the double-wall geometries developed and presented in Chapter 4. The results of the simulations were used to identify geometrical features preferable from an aerothermal perspective with main effects plots developed to support the conclusions. This data was used in the development of a novel, crenulation concept geometry (G1) for which data is also presented (and for which a patent application has been filed).

Finally, a metric, termed the *effective porosity*, has been developed that permits some initial prediction of the cooling performance achievable from a geometry based on knowledge of only the outer wall geometric porosity and discharge coefficient. Such a plot provides a designer with some effective porosity target necessary to achieve a particular cooling target.

6 Steady-State Thermomechanical Analyses

6.1 Chapter Overview

Research into double-wall cooling systems has been ongoing in some capacity since the 1970s [32]. Whilst manufacturing capabilities have (particularly in the past) presented one barrier to entry, what has perhaps been a more significant barrier are the stresses developed in such systems arising from the large thermal gradients developed under thermal load [35]. It is surprising then that almost no literature is openly available on the mechanical considerations of these cooling geometries (and indeed, is somewhat sparse on turbine cooling systems in general) given the direct consequence of these on technology adoption. Developments in material technologies and manufacturing methods are certainly helping to mitigate this issue, however, it is still necessary to consider the thermomechanical performance of these systems at the early design stages and not simply optimise for aerothermal performance.

This chapter outlines some of the thermomechanical work performed across the research. Specifically, the work presented here uses the temperature profiles obtained from the previously presented decoupled conjugate method (see Chapter 5) in thermomechanical FEA analyses. The Design of Experiments method utilised in creating the design matrix permits some early stage conclusions to be drawn as to features preferable from a thermomechanical perspective which demonstrate interesting parallels to those features desirable from an aerothermal perspective.

A second complementary study, which took a more grassroots approach to double-wall system analysis (and conducted in collaboration with the University of Oxford's Solid Mechanics group), is presented in Appendix C.

6.2 Thermomechanical Simulations of the Developed Double-Wall Geometries

To provide some initial insight into the stress field developed in double-wall systems as a result of the solid temperature gradients, the steady-state temperature profiles produced using the decoupled conjugate methodology present in Chapter 5 were used in a thermomechanical FEA solver (*ANSYS Mechanical v16.2*). The simulations were performed on the diamond pedestal geometries presented in Chapter 4 for which the thermal data was presented in Chapter 5. Note, simulations were also performed on the circular pedestal geometries and data for these can be seen in [87]. In the same manner in which the thermal simulations had permitted some insight into geometrical features advantageous from an aerothermal perspective, the mechanical simulations presented here were used to obtain some understanding of how the various geometrical parameters impacted the stress field. Clearly, both the aerothermal and thermomechanical effects are strongly coupled and so the discussion following the mechanical analyses makes reference to the thermal simulations.

6.2.1 FEA Domain and Setup

In selecting a suitable, representative domain size for the thermomechanical simulations, several considerations were identified. The first was the requirement of geometric constraints within the simulations to prevent rigid body motion. These constraints result in significant local stresses. An adequately sized domain was necessary for which it could be assumed that the stress concentrations arising from these constraints were negligible. Similarly, towards the free-edges of the flat plate, stress concentrations are also present (although on a much smaller scale to those from the constraints). As these free-edges are not representative of a turbine geometry, a domain size was again necessary where these concentrations could be assumed to be negligible. As mentioned in the previous chapter, an additional consideration was a domain of adequate size to model film development. Based on earlier work performed by this author ([90],

[91]) a domain size of 40 × 40 mm was identified as being sufficiently large to meet these requirements.

Whilst the nature of the constraints required in the simulation to prevent rigid body motion did not form a primary focus in the study, care was taken in their selection. The constraints were chosen to model the cantilever type nature of a turbine rotor and permitted lateral expansion in one direction that results from the thermal expansion of the material at elevated temperatures. The constraints are depicted in Figure 6.1 in which the constraint highlighted orange allows for zero displacement along all three axes, whilst that highlighted red permits movement in one direction.

Thermal boundary conditions for the simulations were steady-state and directly based upon the results of the decoupled conjugate method and thus accounted for both internal convective cooling and external film cooling. As with the aerothermal simulations, material properties were based upon the nickel superalloy CMSX-4

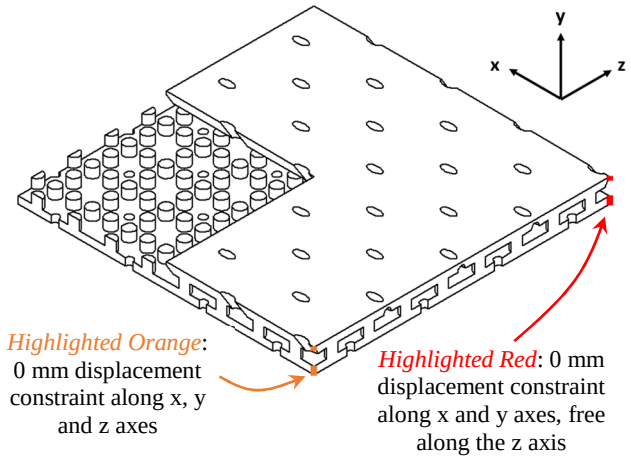


Figure 6.1 – Diagram showing the mechanical constraints specified in the thermomechanical simulations

6.2.2 Results

Prior to a more in-depth comparison of the stresses experienced across the geometries investigated, some comments are made regarding the general form of the stress field which demonstrate similar trends across all geometries. The coefficient of thermal expansion describes how the dimensions of a material change under thermal load, where a larger temperature increase results in a greater volume change. It is evident, therefore, that based on the temperature profile shown in Figure 5.4, the hotter outer wall will expand more than the

cooler inner wall. Furthermore, in the hotter wall, the outer surface will attempt to expand more than the cooler inner surface of the same wall. Consequently, as the inner surface will resist this expansion, the outer surface will be in compression whilst the inner surface will experience primarily tensile stresses. Indeed, this was the predominant trend observed. On the external surface of the outer wall, tensile stresses were sometimes witnessed for geometries with high film cooling performance where metal temperatures were locally lower due to the film cooling.

An example of the maximum principal stresses experienced on the internal surface of the impingement wall is demonstrated on the left-hand side of Figure 6.2 for geometry D6 from which several interesting features can be observed.

As mentioned, the effect of the free-edges are apparent on the stress field. In the case of the maximum principal stress distribution on the impingement wall, these free-edges cause a local stress reduction as highlighted by the area enclosed by the red boxes. Additionally, towards the two constraints, there is a very local but considerable increase in the stress levels (highlighted by the two dashed orange boxes). Given these areas are not representative of an engine component, they are not considered in analysis of the stress field; to this end the image on the right-hand side of Figure 6.2 highlights the region considered in the discussion on the developed stress field. Also noticeable is the general reduction in the magnitude of the stresses in the streamwise direction (i.e. left to right of the contour). This can be explained with reference to Figure 5.4 in which the development of the protective film can clearly be seen in the temperature profile used in the mechanical analysis. The development of this film acts to reduce the temperature gradient and, consequently, thermal stresses between the two walls. Stress concentrations are also observed around the impingement holes. This is in line with theoretical predictions of the stress concentration factor (K_σ) which estimate an increase of around two times the nominal stress around circular holes subjected to a biaxial tensile load [92]. This was found to be the case for the inner surface of the impingement wall shown here.

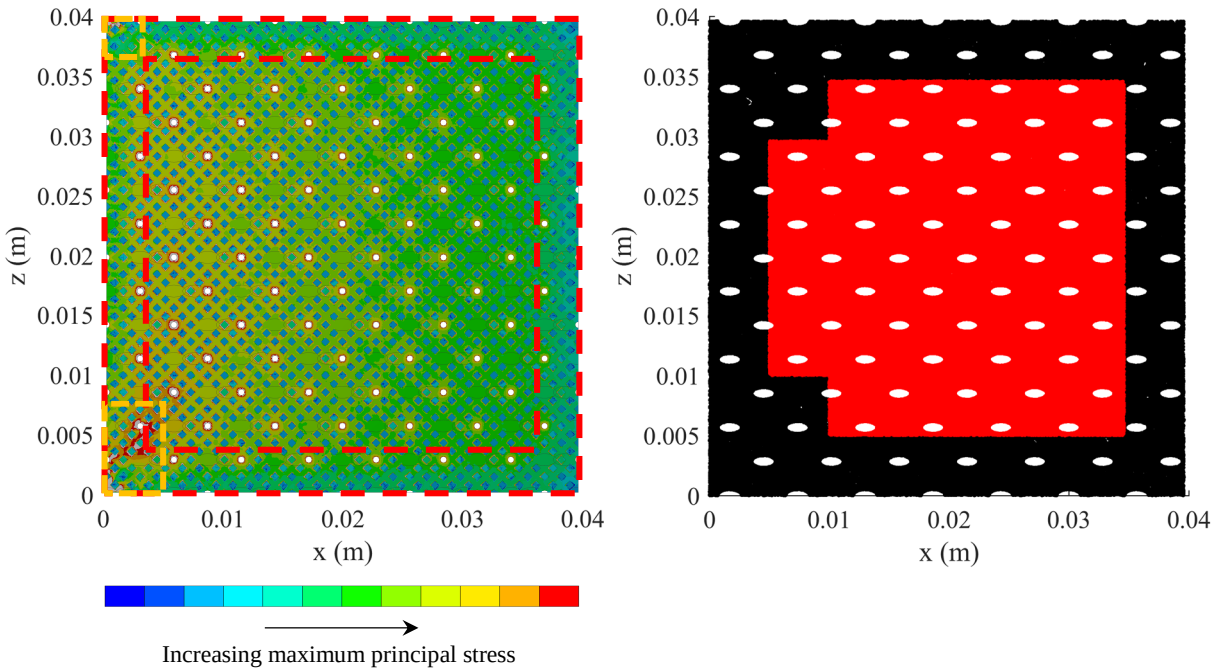


Figure 6.2 - Left) Example maximum principal stress contour for the internal surface of the impingement wall (from geometry D6) with areas of stress concentrations arising from the constrained and free-edges highlighted. Right) Region used in the analysis of mechanical performance highlighted in red which is assumed to be unaffected by the aforementioned stress concentrations

General comparisons between the geometries were then made based upon volume-weighted averaged Von Mises stresses (σ_{VM}). Von Mises stresses provide an assessment of the plastic deformation of a material which is particularly relevant for failure by creep. Figure 6.3 demonstrates the volume-averaged Von Mises stresses (for the $p_{s,out}$ = 3.4 MPa condition) for each diamond pedestal geometry, along with the maximum and minimum principal stresses which show somewhat similar trends (to be expected given the definition of the Von Mises stress). The results of the analyses are discussed below with particular respect to the varying geometric features. Main effects plots were also developed (see Figure 6.4), this time showing the variation in the volume-weighted averaged Von Mises stresses as each of the geometric parameters were varied. As for the case of the aerothermal main effects plots, it is noted that some confounding will be present, however, clear trends are evident, and these are elaborated upon below.

- *Passage Height:* Geometries D2 and D12, and D4 and D11 differed from each other only in the passage height with all other parameters being the same. The results of Figure 6.3 appears to indicate that D11 and D12, which exhibited the larger of the two passage heights, demonstrate a net reduction in volume-averaged stresses. Whilst the magnitude of the temperature difference across the two walls is slightly greater in the larger passage height models (due to the increased wetted area for heat transfer), the temperature gradient between the walls is reduced. This lower temperature gradient results in a reduction in the thermal stresses exhibited. Indeed, the main effects plots (Figure 6.4) appear to support this hypothesis. It is also noted in passing that, at this larger passage height, cooling performance was generally increased and thus the magnitude of the temperatures was, on average, lower. CMSX-4 exhibits improved mechanical performance at these lower temperatures and so material capabilities also increase at this larger passage height. However, it should be noted that, geometry D3 exhibited the lowest thermal stresses and this geometry had the lowest passage height. It is anticipated that this results from the relatively high cooling performance observed in this geometry attributed to its high porosity (commented on below) along with the resulting low temperature difference between the two walls.

- *Film Hole Diameter:* As demonstrated in the main effects plots, the results of the mechanical simulations indicate that increasing the diameter of the film holes is preferable from a mechanical perspective; note that geometries with larger film holes generally had reduced hole pitching. This observation is expected to be the result of the increased film cooling performance. The closer non-dimensional film hole pitch results in more complete films being developed on the outer wall. This consequently reduces the variations in temperature, particularly on this external wall surface, reducing the thermal stresses developed. The more complete films also result in a more uniform

temperature between the two walls reducing the difference in the magnitude of the thermal expansions experienced and transmitted across the pedestals. The kink in the main effects plot is expected to be the result of confounding due to only a single geometry being assessed which featured the intermediate value of film hole diameter. Indeed, for the circular geometries (the results of which can be seen in [87]), the simulations strongly indicated the benefit of increasing film hole diameter. It is worth noting that the film hole location needs to also account for pedestal proximity to minimise excessive stress generation. As mentioned, stress concentrations around the holes are approximately twice that of the far-field and stress concentrations (albeit on a more localised scale) are observed around the pedestal-wall interface. Consequently, to avoid exacerbating the effect of these stress concentrations, the holes and pedestals should be positioned far enough apart (an effect visible in a study by Li et al. [60], although not explicitly identified by the authors).

- *Impingement Hole Diameter:* The main effects plot appears to indicate that increasing impingement hole diameter results in an increase in volume-averaged Von Mises stresses. It was anticipated that, by increasing impingement hole diameter, the porosity of the wall would be increased with a potential increase in coolant utilisation (dependent on the porosity of the pedestal layer and film wall). By increasing the coolant flow rate, the temperature difference across the geometry would consequently be reduced resulting in a reduction in thermal stresses. However, the plot appears to indicate a general increase in the stress field with increasing impingement hole diameter. One possible explanation for this follows the aforementioned effect of stress exacerbation around holes which may be in close proximity to stress concentrations arising around the pedestal-wall interface. However, it is anticipated that a similar observation would have been made for the film holes. It could also be hypothesised that geometries which

featured larger impingement holes may have been more porous which would result in more coolant utilisation and an increase in film blowing ratio which may result in a poorer cooling effect. However, the aerothermal main effects plot indicated that an increased impingement hole diameter had preferable cooling effects. One other explanation then is the potential confounding of the results. Indeed, the plot is almost the inverse of that obtained for varying the film hole diameter. Only four of the thirteen diamond pedestal geometries had different impingement and film hole diameters and from a stress perspective, those with larger film holes and smaller impingement holes did display preferable cooling performance as demonstrated in Figure 5.5, with corresponding reductions in the magnitude of the stresses as shown in Figure 6.3.

- *Pedestal Edge Length and Spacing:* The results of the simulations, as demonstrated by the main effects plots, indicate that the magnitude of the stress field was reduced when there was a high density of small pedestals. In the diamond geometries, this resulted in a greater pedestal-to-wall conduction area. This larger contact area increases the level of thermal conduction that can occur between the two walls thereby reducing the magnitude of the temperature difference (and gradients) between them. Indeed, the main effects plot indicates that varying this pedestal-to-wall contact area provided the most significant means by which the magnitude of the stress field could be varied. This observation was also supported by the results of the circular pedestal geometries.

Whilst the above discussion and figures presented are for the volume-averaged stress components, the trend in peak stress was much the same with geometry performance order unchanged. It is appreciated that whilst volume-averaged Von Mises stress provides only one metric of potential component life-span, in combination with the similar trends observed in the peak stresses, the above discussion is useful in early indications as to those geometrical features that demonstrate preferable performance from a thermomechanical perspective.

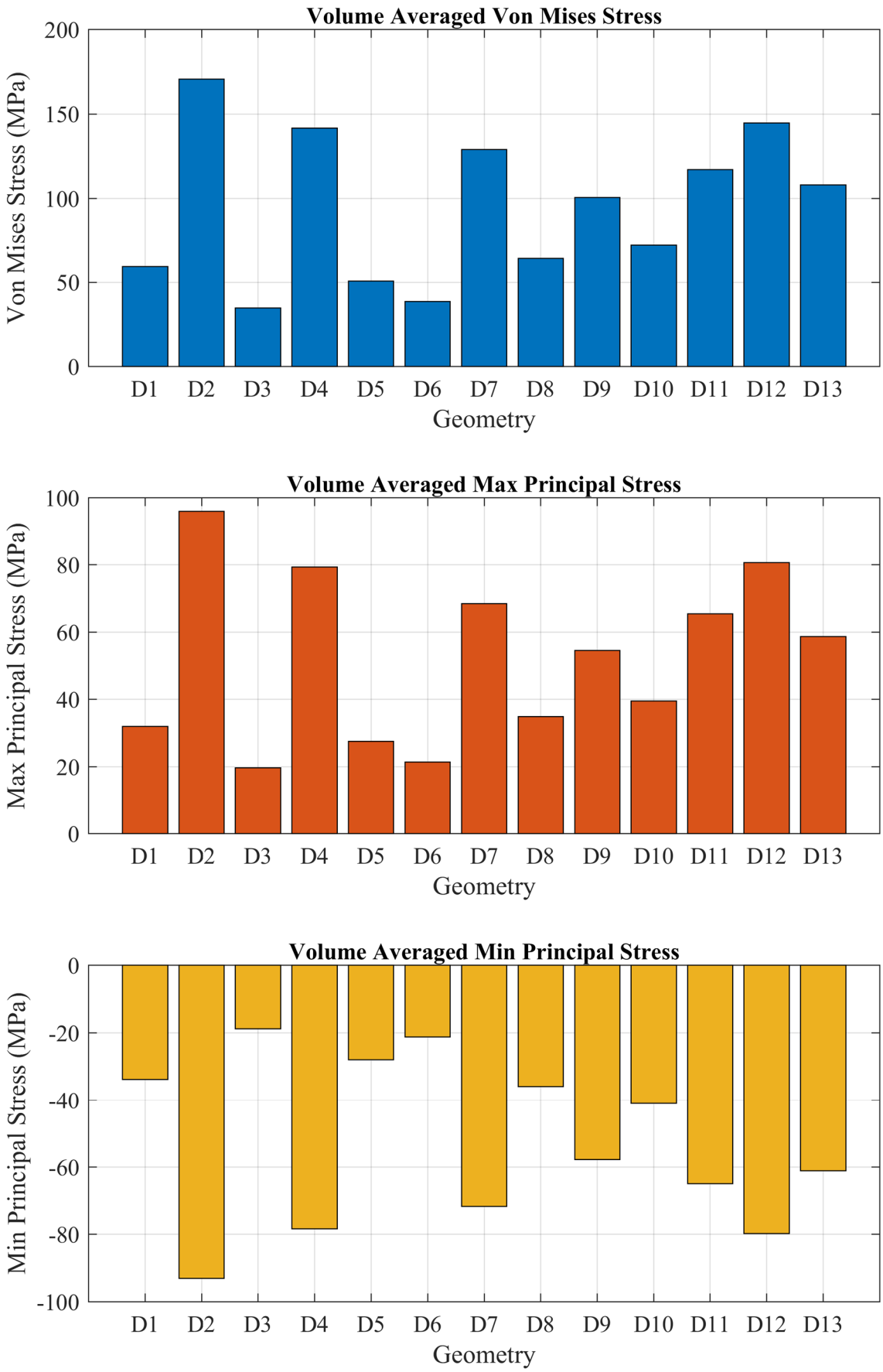


Figure 6.3 - Volume-averaged Von Mises stress and maximum and minimum principal stress for the thirteen diamond pedestal geometries

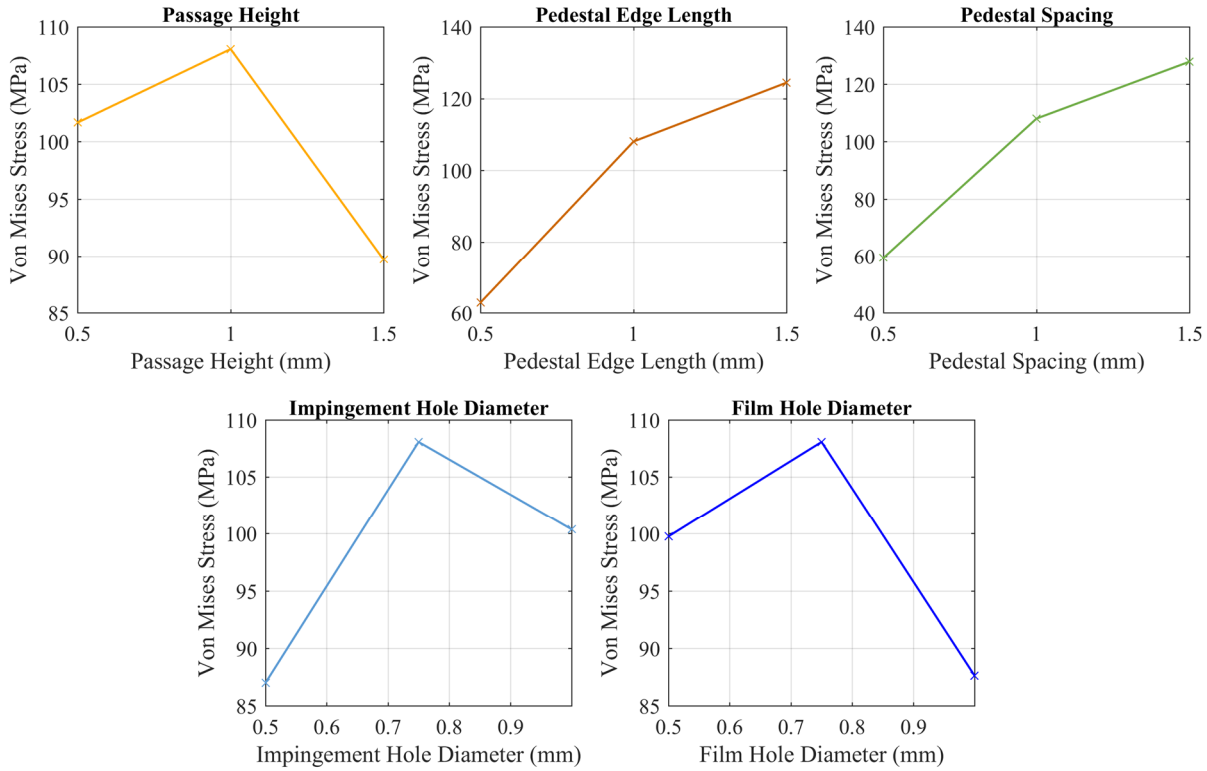


Figure 6.4 - Thermomechanical main effects plots for the diamond pedestal geometries showing the effect of varying the geometric parameters on volume averaged Von Mises stresses (including film cooling performance) for the pressure drop condition of 0.41 MPa

6.3 Summary

This chapter has discussed some of the thermomechanical analyses performed on double-wall cooling systems. Clearly, whilst the double-wall system may present some advantageous cooling features, the thermomechanical stresses that arising due to thermal loading need to be considered in the early design stages. A summary of the study is provided below:

- The study utilised the temperature profiles developed using the decoupled conjugate method presented in Chapter 5, to perform thermomechanical simulations on the diamond pedestal geometries (analyses for the circular pedestal geometries can be seen in [87]).
- The simulations were three-dimensional and considered a section of a double-wall system which experienced minimal influence arising from stress concentrations around constrained- and free-edges.

- The results of the simulations were used to identify features of the general stress field (such as which surfaces experienced predominantly compressive or tensile stresses), and how the magnitude of the stresses were influenced by the development of cooling films.
- The results were used to identify geometrical features which produce lower stresses and which contribute to prolonged component life.
- In general, features which improved conduction between the walls were preferable due to the associated reduction in the temperature gradient across the system.
- Increasing film hole density also appeared preferable for similar reasons.
- Some confounding of the results was expected, however, and this was used to explain the trend observed for varying impingement hole diameter.

7 Double-Wall Experimental Facility: Design and Commissioning

7.1 Chapter Overview

Very little experimental data is available in the open literature that quantifies the performance of double-wall effusion type cooling geometries. At an early stage of the research, the author identified the need for a facility capable of assessing the aerothermal performance of double-wall systems. The aim of the facility was to validate the performance of the decoupled conjugate computational method. The facility requirements, design and commissioning are documented in this chapter.

7.1.1 Facility Characteristics

The facility was designed to assess the thermal performance of flat plate, double-wall geometries at test conditions which matched relevant dimensionless numbers: namely the mainstream and impingement Reynolds numbers and the Biot number. Consideration was also given to enabling the facility to achieve engine representative mainstream-to-coolant temperature ratios in the range of 1.8 – 2.0.

Table 7.1 shows the mainstream engine conditions used to determine the relevant parameters for the experimental facility. The film cooling hole diameter was taken as the relevant length scale for calculating the mainstream Reynolds number.

Table 7.1 – Approximate engine mainstream conditions considered in developing the experimental facility

Pressure	Temperature	Speed of Sound	Mach Number	Velocity	$Re_\infty = \rho v_\infty D_f / \mu$
3.4 MPa	2000 K	900 m/s	0.3	270 m/s	24×10^3

In calculating the required facility mainstream conditions to match $Re_{\infty,engine}$, three temperature conditions were considered, specifically 350, 400 and 450 K. Table 7.2 demonstrates the mainstream Mach number required to provide mainstream *Re* similarity in the facility, along with the corresponding mainstream mass flow, when the double-wall test geometry has been scaled up by a factor of 10.

Table 7.2 – Rig conditions required to match mainstream Re at ×10 engine scale for three different mainstream flow temperatures

Pressure	Temperature	Speed of Sound	Ma_∞	Velocity	Area	Mass Flow	$Re_\infty = \rho v_\infty D_f/\mu$
101250 Pa	350 K	375 m/s	0.161	60.4 m/s	0.0225 m^2	1.3 kg/s	24×10^3
	400 K	400 m/s	0.172	69.0 m/s		1.3 kg/s	
	450 K	425 m/s	0.182	77.4 m/s		1.3 kg/s	

The facility was also required to provide a sufficiently wide range of coolant mass flows. This would permit the performance of the double-wall geometries to be assessed at various coolant flow rates where the relative effects of impingement and film cooling would differ. The designing of the coolant supply system is discussed in sections 7.2.3.

The facility was also designed with the aim of providing Biot number (defined in equation 7.1) similarity for overall metal effectiveness measurements. The Biot numbers for both the experimental facility and rig are defined in equation 7.2.

$$Bi = \frac{hL}{k_{sd}} = \frac{hL}{k_{fl}}\frac{k_{fl}}{k_{sd}} = Nu\frac{k_{fl}}{k_{sd}} \tag{7.1}$$

$$Bi_{engine} = \frac{h_{engine}L_{engine}}{k_{sd,engine}} \quad = \quad Bi_{rig} = \frac{h_{rig}L_{rig}}{k_{sd,rig}} \tag{7.2}$$

Equation 7.1 shows that the Biot number can be expressed as the product of the Nusselt number and fluid-solid conductivity ratio. However, for cases of forced convection, the Nusselt number is found to be a function of both Reynolds and Prandtl numbers with correlations often

expressed as a power law as shown in equation 7.3 where *a*, *b* and *c* are constants that are dependent upon, amongst other things, the geometry and flow regime.

$$Nu = aRe^{b}Pr^{c} \tag{7.3}$$

At both engine conditions and the experimental rig conditions, there is little variation in the Prandtl number ($Pr_{engine} \sim 0.72$ and $Pr_{rig} \sim 0.69$), and, furthermore *c* is usually 0.33. Given that the facility provides Re_{∞} similarity it is therefore the case that $Nu_{engine} \approx Nu_{rig}$. Consequently, equation 7.2 can be simplified to equation 7.4. This equation demonstrates that, to provide a match for Biot number, the solid thermal conductivity required in the facility can be calculated from knowledge of the fluid conductivities in both the facility and engine, along with the wall material conductivity in the engine.

$$Bi = Nu_{engine}\frac{k_{fl,engine}}{k_{sd,engine}} = Nu_{rig}\frac{k_{fl,rig}}{k_{sd,rig}} \Rightarrow k_{sd,rig} = k_{fl,rig}\frac{k_{sd,engine}}{k_{fl,engine}} \tag{7.4}$$

The properties of the Nickel superalloy CMSX-4 were evaluated at a temperature corresponding to engine conditions and at an overall cooling effectiveness of 0.5 yielding a thermal conductivity of 31 W/m.K [93]. Equation 7.4 was then used together with the gas temperature ratios to calculate the thermal conductivity of the solid required in the facility to match engine Biot number – this would be 11.25 W/m.K. Of the more common, inexpensive and relatively machinable metals, none could be found that would accurately match this thermal conductivity. However, for the range of solid temperatures anticipated in the experiments, stainless steel 316 (*SS-316*) provides a relatively close match on Biot number, with a thermal conductivity of around 14.5 W/m.K. Consequently, dependent on the mainstream temperature, the facility was designed to provide a Biot number match of within approximately 25%. The effect of this is further discussed in Chapter 10.

7.2 Experimental Facility Design

Figure 7.1 and Figure 7.2 illustrate the design for the facility from two angles with several features enlarged in the latter figure. Figure 7.2 shows a flat plate, ×10 scale double-wall test geometry located on the upper surface of the wind tunnel. The impingement holes are supplied from a plenum with the coolant, whilst the wall with the film holes is positioned flush with the internal surface of the wind tunnel. Several features are elaborated upon in the following subsections.

7.2.1 Tunnel Fan Selection

In selecting the fan to provide the mainstream airflow several requirements were specified; namely:

- the fan should be capable of running for long durations at the maximum thermal conditions for the facility being designed (around 475 K).
- at the required volumetric flow rate, the pressure rise provided by the fan was sufficient to match the pressure losses through the tunnel at the designed flow rate.

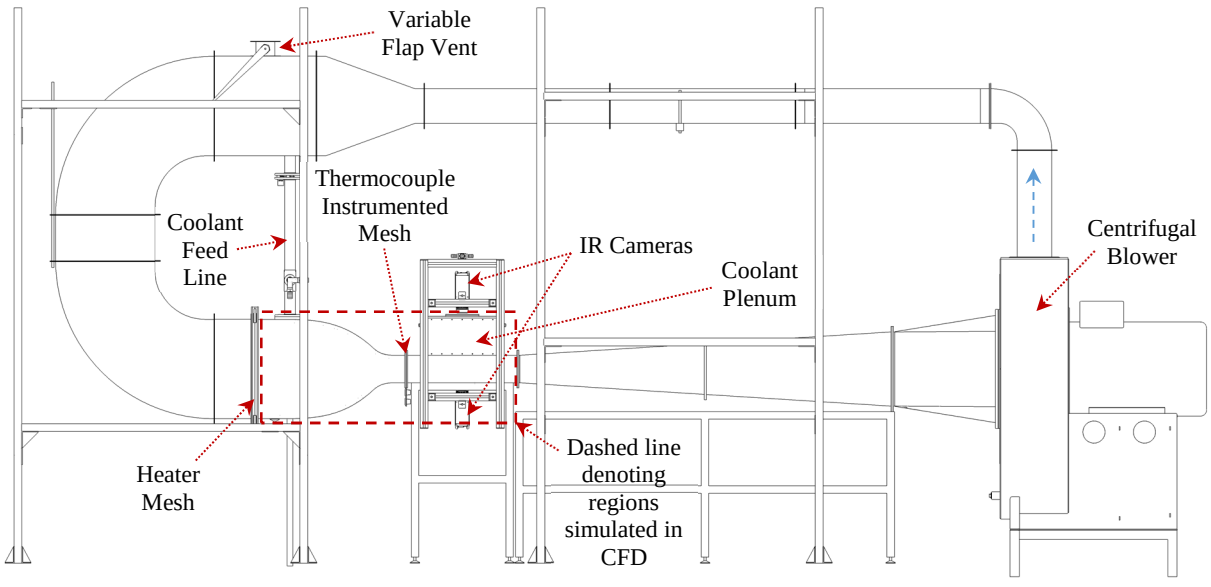


Figure 7.1 - Schematic showing the side of the experimental facility design incorporating mainstream flow recirculation with several key features annotated

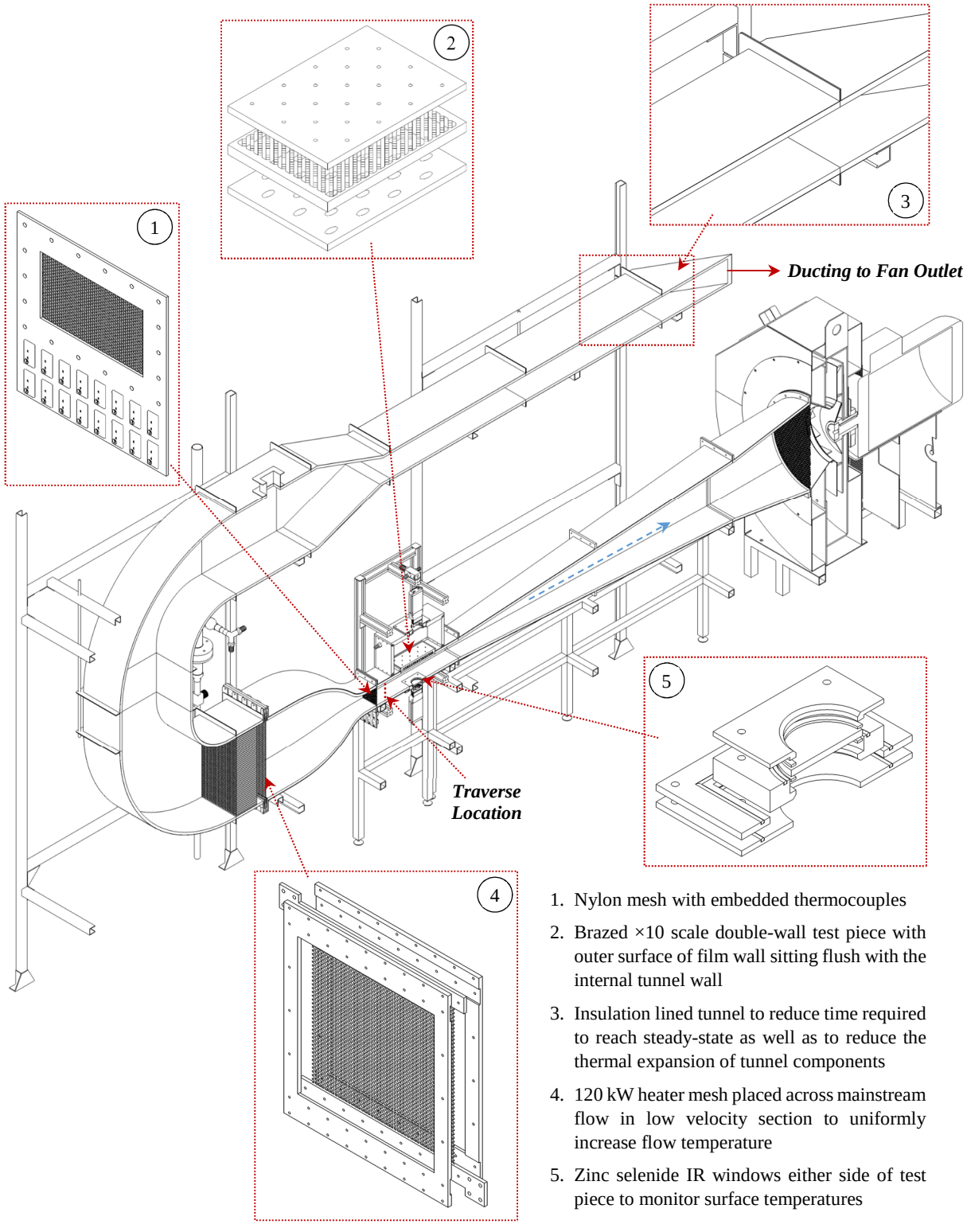


Figure 7.2 - Isometric section view of the experimental facility design incorporating mainstream flow recirculation with several features enlarged

An approximate analysis was performed to estimate the pressure losses through the facility. A lumped element analysis of the recirculating tunnel (shown in Figure 7.3) was used to calculate the pressure losses anticipated. The tunnel section dimensions were specified which

allowed the flow speed and Reynolds number (based on hydraulic diameter) to be calculated across the different component sections. The loss coefficients for each section of the tunnel were based upon a combination of tabulated data [94] for sections such as the bends and contractions, the Blasius formula for turbulent flow through smooth pipes for straight sections, and lab experience for the mesh heater [95]. Table 7.3 demonstrates the calculated section losses with a total pressure loss expected across the loop of approximately 2.5 kPa. The selected fan provided around a 6.5 kPa pressure rise at the required conditions with a continuous temperature capability of 500 K.

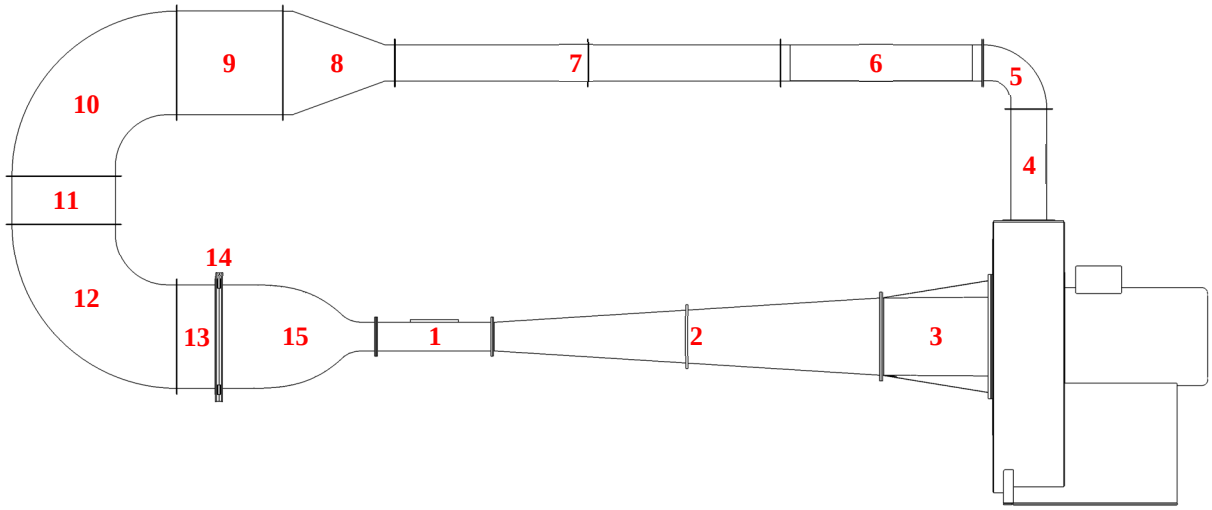


Figure 7.3 – Mock-up of a recirculating facility used in assessing the pressure rise required for the centrifugal blower. Section numbers correspond to Table 7.3

7.2.2 Mainstream Heating Method and Flow Recirculation

A heater mesh (as described in [96]) was used to provide a temperature difference between the mainstream flow and the coolant feed and has the potential to provide approximately 120 kW of power. The heater mesh is comprised of a fine stainless steel wire (of diameter 40 μm) arranged to form small square apertures. The mesh is soldered onto brass busbars across which a voltage is applied causing a current to be passed across the mesh resulting in a rise in the temperature of the metal strands. The mainstream airflow passes through the apertures in the mesh causing a uniform increase in the wind tunnel flow temperature. The mesh time constant

	Section	x (m)	y (m)	z (m)	Area (m^2)	D_h (m)	Velocity (m/s)	Reynolds Number	Friction Coefficient	Loss Coefficient, K_{loss}	Dynamic Head (m)	Dynamic Pressure (Pa)	Loss (Pa)
1	*Test Section*	0.20	0.11	0.60	0.023	0.14	74.62	3.64E+05	0.00322	0.054	283.80	2155.69	115.55
2	*Diffuser - Fan*	0.28	0.24	2.00	0.067	0.26	24.98	2.19E+05	0.00365	0.113	31.82	241.66	27.32
3	*Transition*	-	-	0.57	0.229	0.54	7.33	1.34E+05	0.00413	0.017	2.74	20.81	0.36
4	*Fan Outlet*	0.51	0.16	0.58	0.078	0.24	21.45	1.72E+05	0.00388	0.038	23.45	178.12	6.71
5	*Fan Outlet Bend*	0.51	0.16	-	0.078	0.24	21.45	1.72E+05	-	0.750	23.45	178.12	133.59
6	*Offset*	0.51	0.16	-	0.078	0.24	21.45	1.72E+05	0.00388	2.000	23.45	178.12	356.23
7	*Straight Section Top*	0.51	0.16	2.00	0.078	0.24	21.45	1.72E+05	0.00388	0.131	23.45	178.12	23.29
8	*Diffuser - Top*	0.51	0.16	2.00	0.078	0.24	21.45	1.72E+05	0.00388	5.000	23.45	178.12	890.58
9	*Straight Section Top (Large)*	0.51	0.51	0.51	0.255	0.51	6.58	1.13E+05	0.00431	0.018	2.21	16.78	0.29
10	*First Large Bend*	0.51	0.51		0.255	0.51	6.58	1.13E+05	-	0.750	2.21	16.78	12.58
11	*Mid Bend Straight*	0.51	0.51	0.25	0.255	0.51	6.58	1.13E+05	0.00431	0.009	2.21	16.78	0.14
12	*Second Large Bend*	0.51	0.51		0.255	0.51	6.58	1.13E+05	-	0.750	2.21	16.78	12.58
13	*Bend-Heater Section*	0.51	0.51	0.20	0.255	0.51	6.58	1.13E+05	0.00431	0.007	2.21	16.78	0.11
14	*Heater Mesh*	0.50	0.50	-	0.250	0.50	6.72	1.14E+05		6.000	2.30	17.46	104.77
15	*Contraction*	0.20	0.11		0.023	0.14	74.62	3.64E+05	0.00322	0.370	283.80	2155.69	797.60
													2481.73

Constants							
P_{in} (Pa)	100000	R_{gas} ($J/kg.K$)	287	T_∞ (K)	450	$\dot{m}_\infty$ (kg/s)	1.3
Gravity (m^2/s)	9.81	**Contraction** A_2/A_1	0.09	μ_∞ ($Pa.s$)	2.29×10^{-5}	ρ_∞ (kg/m^3)	0.93

Table 7.3 – Rig pressure loss calculations for the recirculating facility where the constants used in the calculation of the total pressure losses are shown in the bottom table

is very short which means that this initial temperature rise (when the heater is first switched on) approximates a step change which minimises waiting times for the fluid to reach a steady-state temperature. The busbars and edges of the mesh were restrained within a Tufnol® frame. Tufnol® was selected on account of its features of good electrical and thermal insulation, ease of machining, and relatively high temperature capability. The heater mesh was positioned upstream of the contraction section to capitalise on both the higher convective efficiency of the mesh at lower flow velocities, as well as reduced pressure losses through the heater.

Heater meshes have typically been used in transient and short duration heat transfer tests (see for example [20], [95]–[100]) with open loop flows. In such applications, to a close approximation, all the power sent to the heater is assumed to be transferred to the airflow. Through knowledge of the electrical power and the mass flow of air through the heater mesh, an accurate prediction of the temperature increase across the mesh can be determined from equation 7.5. Indeed, as demonstrated by Ireland et al. [96], this method demonstrates a prediction for temperature rise to within 2.5% of measured values. For the current facility with an approximate mass flow of 1.3 kg/s, the maximum temperature rise across the mesh was calculated to be near 100 K for an open loop flow.

$$\Delta T = \frac{IV}{\dot{m} c_p} \tag{7.5}$$

However, the present work is the first application of such a heater – to the author's knowledge – in steady-state heat transfer experiments with a recirculating flow. As demonstrated by Gillespie [95], the convective efficiency for such a mesh at a flow speed of 6.72 m/s (approximately that at the location of the mesh in the current experimental facility), is around 0.55. Consequently, the temperature of the mesh itself at full power was anticipated to be near 455 K, and indeed, hotter at the edges of the mesh where it was clamped between the Tufnol® frame and not being cooled by the airflow. As a result, the longevity of the heater mesh

and frame under such conditions was uncertain. Potential modifications were considered, including active cooling of the frame and insulation of the Tufnol® frame with a high temperature insulating material. Indeed, early testing indicated that, at higher heater powers, some slight charring of the frame occurred over longer duration experimental runs. Consequently, a design change was incorporated which involved the machining of a 2 mm ridge in the Tufnol® frame in locations where it contacted either the mesh or busbars. A 2 mm thick gasket (composed of aramid fibres bonded with nitrile rubber) was then positioned in the ridge which had a high temperature capability of 675 K and provided both good thermal and electrical insulation.

One of the most notable features of the designed facility (as apparent in Figure 7.1 and Figure 7.2) is the incorporation of recirculation of the mainstream flow, the primary motive of which was to enable an increase in mainstream flow temperatures relative to an open flow configuration in which the fan outlet would simply vent to atmosphere. The elevation of the mainstream temperature would consequently permit a closer match of mainstream-to-coolant temperature ratio to engine conditions.

A second benefit of the mainstream flow recirculation was the ability to significantly decrease the heater power necessary to provide a certain mainstream temperature relative to and equivalent open loop facility. Indeed, it was found that recirculation of the flow provided a reasonable mainstream temperature increase even without the power being supplied to the heater. An additional result of the reduced heater power requirement was a more uniform mainstream temperature profile in the test section that was less susceptible to the small non-uniformities in heating from the heater mesh that scaled with the power drawn (and quantified in section 7.3).

The 180^{o} turn in the tunnel ducting upstream of the test section was designed to include a large cross-sectional area with large radius of curvature to reduce potential skewing of the flow. To further mitigate this potential skewing of the flow, a settling section with honeycomb flow

straightener was positioned after the turn, upstream of the contraction section, with the mesh heater providing some additional flow straightening properties. The contraction section was also designed using an in-house tool based on the method proposed by Fang [101] who suggested a design methodology to provide uniform outlet velocity and turbulence profiles. Figure 7.1 highlights the use of a variable dual-flap vent positioned at the top of the facility which could be adjusted to avoid rig pressurisation whilst also avoiding too large a loss of heated mainstream flow.

All of the tunnel ducting was lined with 15 mm thick high performance, microporous insulative panels with a thermal conductivity of between 0.02 – 0.03 W/m.K over a temperature range of 300 – 850 K [102]. The insulation was included to reduce heat losses through the duct wall, to decrease the time taken to reach steady-state, and to minimise the likelihood of leakages occurring as a result of the expansion of tunnel sections at elevated mainstream temperatures. The surface of the insulation was clad in a thin, impermeable mica layer.

7.2.3 Coolant Supply System

In designing the coolant supply system consideration was given to a design which would permit fine control of the coolant flow rate as well as an accurate measurement of the coolant mass flow. Additionally, a system was needed that would ensure a uniform supply of coolant to each impingement hole. The designed system supplied coolant to the double-wall test piece via the laboratory 100 psi compressed air supply at approximately atmospheric temperature. The coolant mass flow was measured by means of a critical flow Venturi nozzle (*CFVN*), where knowledge of only the upstream stagnation pressure and temperature along with nozzle throat area were required in determining the mass flow (assuming an adequate pressure ratio was maintained across the nozzle). Cylindrical throat nozzles conforming to the ISO 9300:2005 standard [103] were manufactured (with 5.5 mm and 10 mm throat diameters) and installed in the compressed air line with instrumentation positioned to conform to the standard. Upstream

pressure was varied by means of a flow regulator. The mass flow through the nozzle could be calculated using equation 7.6.

$$\dot{m} = \rho_0 a_0 A_{nt} c_d \frac{a}{a_0}\bigg|_{Ma=1} \frac{\rho}{\rho_0}\bigg|_{Ma=1} \tag{7.6}$$

The value of the nozzle discharge coefficient is a relatively weak function of the flow Reynolds number (based on the nozzle diameter) with the exact value specified using tabulated data within the ISO standard. Flow downstream of the nozzle was fed to an aluminium rectangular plenum via a hosing/manifold system with flow entering the plenum in a symmetrical fashion via four hoses of equal length (with an internal diameter of ½"). The plenum then directly fed the double-wall test geometry where the impingement wall was fed from the plenum.

In designing the aluminium plenum, the maximum plenum pressure was evaluated based upon the range of coolant mass flows required and porosity of the double-wall test geometries. This calculated pressure (of 40 kPa) was used to evaluate the maximum stresses and deflections in the plenum side walls to determine the integrity of the plenum at the design pressures.

7.2.4 Facility Instrumentation

A range of instrumentation was installed in the facility to obtain thermal measurements for the double-wall test pieces, and to characterise the mainstream flow.

Whilst selecting the instrumentation method by which thermal measurements could be obtained from the double-wall test geometries, several desirable features were identified. Specifically, that the method could provide a high spatial resolution of data, have low uncertainty, be suitable for the anticipated facility temperatures, be non-intrusive, be cost effective and have a suitably fast response time. Using these assessment criteria, infrared (*IR*) thermography was selected as a suitable method for making thermal measurements. Although

the initial cost of the cameras is relatively high, the camera reusability makes this approach more cost effective than some alternative methods such as a multitude of surface thermocouples. Two IR cameras were placed to observe the two external surfaces of the double-wall test piece (i.e. the external surfaces of both the impingement and film walls). To provide optical access to the outward facing surfaces of the test piece, IR windows were installed at the locations shown in Figure 7.1 and Figure 7.2. The selection of the windows was important to ensure good IR transmissivity at the wavelengths of interest (based on Wein's displacement law, $\lambda_{max} = (2.898 \times 10^{-3})/T_w$), and to ensure adequate material strength and thermal capabilities at the design pressures and temperatures. Zinc Selenide (*ZnSe*) demonstrated suitable properties and has been used previously in similar facilities [47], [54], [104]. Window diameters of 75 mm were selected to permit the observation of a sufficiently large area. The rupture modulus of ZnSe was used to calculate the minimum window thickness necessary to withstand the fluid pressures with an absolute minimum (with no safety factor) of around 0.175 mm calculated assuming the window was simply supported around the edges and with a maximum window differential pressure of 0.5 bar. The windows purchased [1] were 6 mm thick providing a large safety factor and future-proofing these windows for applications that require larger pressure differences. Window mounts were designed and manufactured that permitted some material expansion during rig operation whilst maintaining an adequate seal due to the use of both high temperature gasket material and O-ring seals (as demonstrated in enlargement 5 in Figure 7.2).

In order to more accurately calculate the cooling performance of the double-wall test geometry, it was necessary to measure the temperature uniformity of the mainstream flow upstream of the test piece. To this end an instrumentation method developed by Tsang et al. [100] was applied to the facility. The method utilises a porous mesh, as shown in Figure 7.4,

[1] TECHSPEC® Zinc Selenide windows, Edmund Optics®, York, UK

which was shown by Wang et al. [105] to be essentially non-intrusive. The mesh spans the flow path as shown in enlargement 1 in Figure 7.2. Embedded in the mesh are nine thermocouples of 0.076 mm diameter. Previous work has shown the use of such a mesh incurs a pressure loss of around 8% of the dynamic head. This instrumented mesh was positioned immediately after the contraction section to obtain the flow temperature just upstream of the test piece leading edge (the exact location is shown by enlargement 1 in Figure 7.2).

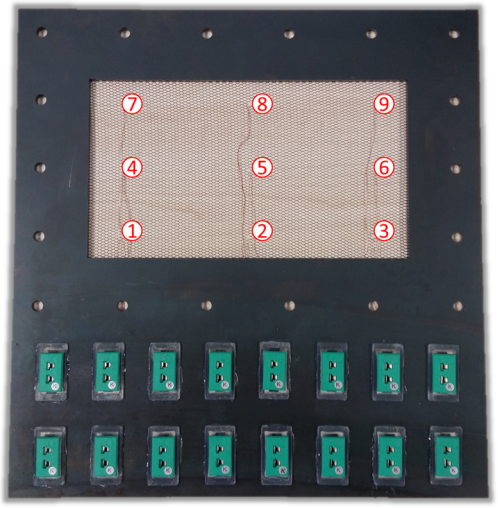


Figure 7.4 – Thermocouple instrumented nylon mesh

In addition to the thermocouple instrumented adiabatic nylon mesh used to assess mainstream flow temperature uniformity at moderate temperatures, a second instrumented flange was manufactured that could be used to assess mainstream thermal uniformity at higher temperatures in the place of the thermocouple instrumented mesh (specifically during the experimental runs where mainstream temperatures would be in excess of 375 K). Five, high temperature, ceramic sheathed thermocouples were positioned 9.5 mm from the top surface of the tunnel at regular spanwise intervals as demonstrated in Figure 7.5a). The thermocouples were used to record the variation in mainstream temperature towards this top surface of the test section against which the double-wall test piece rests and were used to monitor mainstream gas temperature throughout experimental runs. Through measuring the spanwise variation in mainstream temperature towards the test piece during experiments, the local mainstream temperature could be used in place of a single thermocouple measurement in calculating the overall effectiveness, consequently minimising the effect of any thermal non-uniformities.

To further characterise the mainstream flow approaching the test piece, a total pressure probe rake was installed in the tunnel approximately 60 mm upstream of the test plate leading edge; the location is shown by the dashed red line in Figure 7.1 and Figure 7.2. The traverse system comprised of 5 total pressure probes with the central probe aligned with the spanwise centreline of the test section and the remaining four probes spaced at 35 mm intervals either side of the central probe as such permitting some assessment of the spanwise flow uniformity. A static pressure tapping on the inside of the tunnel was aligned with the front of the total pressure probes allowing the axial velocity to be measured. The total pressure probe rake was mounted on a dummy flat plate that was positioned where the double-wall test piece would normally be placed in the facility. A drawing of the design is demonstrated in Figure 7.5b).

Additionally, a single-wire hot-wire probe (a *Dantec 55P03*) was mounted on the same dummy flat plate near the LE (with the pressure probes removed). The hot-wire was intended only to provide an estimation of the turbulence intensity of the mainstream flow field. Consequently, the hot-wire was positioned in the centre of the flow and designed to take a point measurement at this location (using a data acquisition rate of 10 kHz).

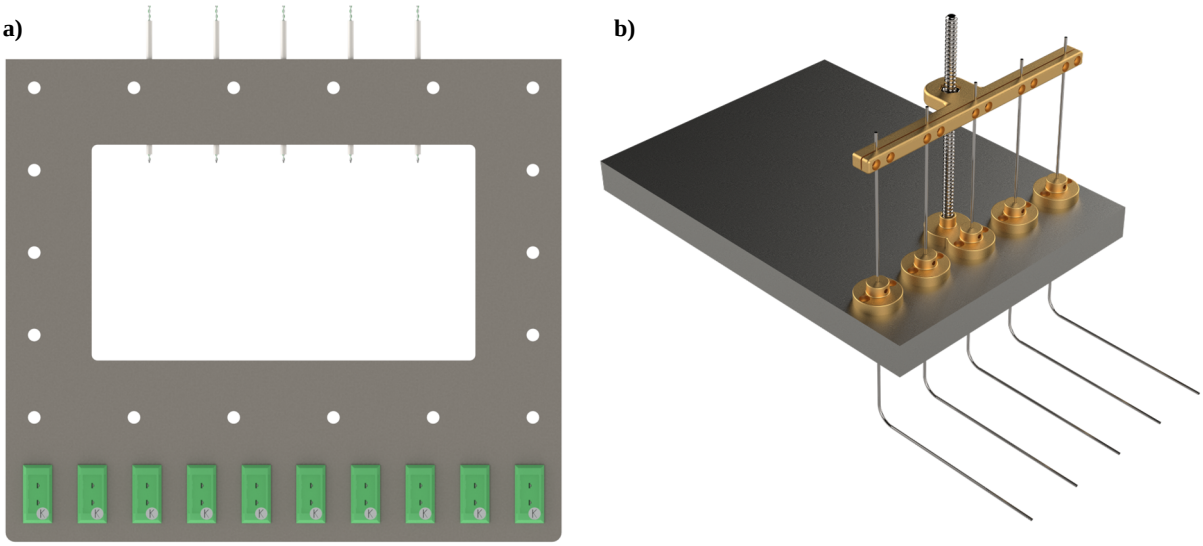


Figure 7.5 – a) High temperature ceramic sheathed thermocouple instrumented flange, and b) total pressure probe traverse system

7.2.4.1 Infrared Camera Calibration

The motivations for the selection of IR thermography in the double-wall experimental facility are presented above. However, the accuracy of the method is subject to several effects which must be accounted for in a calibration procedure that considers the specific setup from which the IR measurements are being obtained. Namely, the calibration must calculate the blackbody temperature based on the detected incident heat radiation; account for transmissivity variations due to the optical pathway between the IR detector and surface of interest; account for the effect of thermal reflections from the surroundings; account for the emissivity of the surface being observed. This section discusses the calibration method employed in the facility and based upon the methods discussed by Kirollos [106] and Holgate [107].

Two *FLIR A655sc* [2] infrared cameras were used to observe the two outward facing surfaces of the test piece simultaneously during experimental runs with data recorded using the *FLIR ResearchIR* software package. The cameras were both equipped with wide angle, 13 mm, 45^{o} field of view (*FoV*) lenses. The maximum camera resolution was 640×480 pixels at a frame rate of 50 Hz, with a maximum frame rate of 200 Hz for smaller window sizes of 640×120.

In making the steady-state overall effectiveness measurements a frame rate of 6.25 Hz was specified to minimise data file sizes. This is as the solid thermal conductivity is significant for the overall effectiveness measurements and consequently small fluctuations in the mainstream or coolant flow would have little effect on the measured surface temperature. However, for the steady-state film effectiveness measurements, the thermal conductivity of the solid is assumed to be negligible. As a result, small variations in the flow field would be reflected on the surface of the test piece. The frame rate of the camera monitoring the film wall was therefore increased to 25 Hz to permit some assessment of the flow unsteadiness (with some measurements taken

[2] FLIR A655SC, FLIR Systems, Inc, USA; *Supplier:* The Macintosh Consultancy, UK

at a higher frame rate of 50 Hz for this purpose). In processing the overall effectiveness measurements, 10 seconds (63 frames) of data was averaged, whilst for film effectiveness measurements 15 seconds (375 frames) of data was averaged.

The IR camera uses an array of microbolometers which each have an electrical resistance that is dependent upon temperature. The temperature of each microbolometer is dependent upon the incident electromagnetic radiation. For the *FLIR A655sc* cameras used in the present study, the microbolometers respond to IR electromagnetic radiation in the spectral range of 7.5 – 14 μm [108]. The voltage measured across each microbolometer is a function of the microbolometer's electrical resistance. The measured voltage is converted from an analogue to a 16-bit digital signal – i.e. the raw count processed by the software can have a raw count value between 0 – 65,535 dependent on the pixel voltage. A calibration is necessary to deduce the surface temperature from the raw count output by the camera. The calibration procedure can be split into two parts:

1) That required to calculate the ideal blackbody parameters
2) That required to calculate the greybody parameters that arise due to non-ideal surface emission

Through a combination of these parameters, the total radiation power (or *radiance*) received by the camera is given by equation 7.7 [109] where σ_b is the Stefan-Boltzmann constant, ξ is the emissivity of the observed surface, τ is the transmissivity of the optical pathway, T_w is the temperature of the surface of interest and temperatures T_{bb}, T_{amb} and T_{opt} are the blackbody, surrounding ambient and optical pathway temperatures respectively.

$$\sigma_b T_{bb}^4 = \sigma_b \xi \tau T_w^4 + \sigma_b (1-\xi)\tau T_{amb}^4 + \sigma_b (1-\tau) T_{opt}^4 \tag{7.7}$$

Blackbody Calibration

The raw count (C_R) output by the camera varies approximately linearly with the incident radiation (termed q_{cam}) [106], [109]. Consequently, the camera radiance based, on the ideal blackbody temperature, follows from equation 7.8.

$$q_{cam} = \sigma_b T_{bb}^4 = aC_R + b \tag{7.8}$$

To calculate the constants *a* and *b*, an isothermal cavity calibration method was employed where a matt black, cylindrical object was submerged in hot water. A thermocouple was positioned on the inside of the cavity to monitor the temperature of the isothermal body whilst the same internal surface was being monitored by the infrared camera which was recording the corresponding raw counts. The calibration procedure involved recording both the thermocouple temperature and camera raw count over a range of water (and therefore cavity) temperatures with an ordinary least squares regression then performed on the measured data to calculate constants *a* and *b*. The resulting blackbody calibration data and least squares linear regression fits are shown in Figure 7.6. The figure confirms the linear nature of the relationship between camera count and incident radiation. The calibration constants for both cameras are included in equations 7.9 and 7.10. The slight difference demonstrated between the cameras is anticipated to arise due to small manufacturing differences in each of the camera sensors.

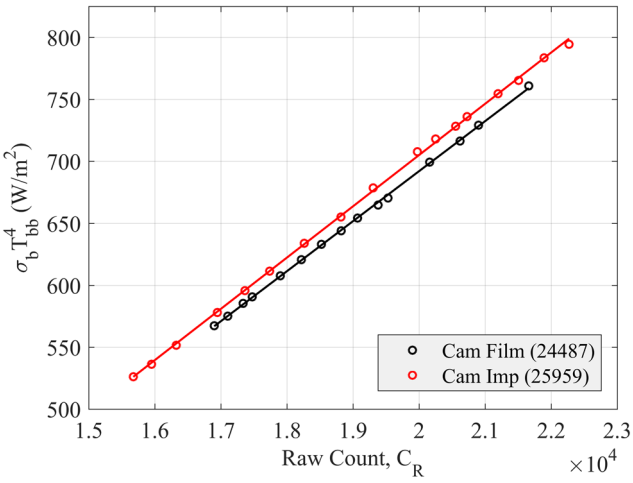


Figure 7.6 – Camera raw count against camera incident radiance from the blackbody calibration

Cam Film (24487) $$\sigma_b T_{bb}^4 = 0.0394C_R - 102.72 \tag{7.9}$$

Cam Film (25959) $$\sigma_b T_{bb}^4 = 0.0414C_R - 122.60 \tag{7.10}$$

Greybody Calibration

The test piece surface is not truly a blackbody due to a less than unity surface emissivity, reductions in IR transmittance through the optical pathway and radiance contributions that arise from reflections from the surroundings which are at a different temperature to the double-wall surface temperature. These additional greybody considerations lead to the additional terms shown in equation 7.6 where the camera incident total radiance is comprised of the individual greybody considerations. The right-hand side of equation 7.7 can be split into two terms: contributions that arise directly from the temperature of the surface of interest (the first term), and those that result from the surroundings and optical pathway (the last two terms). These latter two terms can be combined into a surrounding radiance term, q^* defined in equation 7.11 where the two terms have been normalised by $1 - \tau\xi$ making the term independent of the greybody parameters under isothermal conditions (i.e. when $T_{amb} = T_{opt}$) [106]. It is noted that, in the current study, the emissivity is assumed to be independent of surface location which, given that a uniform coating of matt black paint was applied to the surface, was judged acceptable. Additionally, the surface of interest is normal to the camera and the effect of viewing angle on emissivity is negligible [106]. Likewise, the variation in the surrounding radiance over the surface of interest is assumed negligible. Holgate et al. [110] quantified the variation of q^* for more complex, curved geometries and demonstrated a small variation in q^*. However, for the flat surface being viewed here, a constant, run-to-run obtained radiance term is sufficient.

$$q^* = \frac{\sigma_b(\tau(1-\xi)T_{amb}^4 + (1-\xi)T_{opt}^4)}{(1-\tau\xi)} \tag{7.11}$$

Consequently, equation 7.7 can be rearranged to make the surface temperature of interest the subject as shown in equation 7.12.

$$T_w = \sqrt[4]{\frac{\sigma_b T_{bb}^4 - (1-\tau\xi)q^*}{\sigma_b \tau\xi}} \tag{7.12}$$

T_{bb} is calculated from the raw counts signal and the blackbody calibration. However, the greybody terms ξ, τ and q^* are unknown. The emissivity and transmissivity are determined via an in-situ calibration procedure using a high conductivity, thin aluminium flat plate. The aluminium plate is instrumented with two thermocouples, attached using a thermally conductive paste, to the wall surface being observed by the IR camera. The aluminium plate surface is coated with the same matt black paint used to coat the double-wall test pieces. The aluminium test piece is heated away from the facility before being placed in the facility where the double-wall test piece is positioned in the test section. In this way, the surrounding surfaces can be assumed to be isothermal and at ambient temperature. The temperature of the aluminium plate is recorded over a period of thirty minutes as it cools whilst the IR camera simultaneously records the corresponding raw counts for the image from the same surface. Since the surroundings can be assumed isothermal (i.e. $T_{amb} = T_{opt}$) for this calibration, equation 7.7 can be rearranged as shown in equation 7.13, from which the product $\tau\xi$ can be determined. Note that $T_{w,thermo}$ corresponds to the thermocouple measured temperature, whilst $T_{bb,thermo}$ corresponds to the IR camera blackbody measured temperature of the pixels surrounding the thermocouple.

$$\tau\xi = \frac{T_{bb,thermo}^4 - T_{amb}^4}{T_{w,thermo}^4 - T_{amb}^4} \tag{7.13}$$

The product $\tau\xi$ was calculated as being 0.961 for the film wall surface and 0.953 for the impingement wall surface and this was relatively invariant with temperature (less than a 0.5% deviation across the temperature range of interest).

The surrounding radiance term, q^*, is strongly dependent on the temperature history of the internal surface of the facility around the test piece during a particular test and consequently it

is necessary to measure q^* from experiment. To this end, the double-wall test pieces are instrumented with a thermocouple on each surface of interest which are again attached using a high conductivity thermal paste after which the test piece is sprayed with matt black paint. Equation 7.12 can be rearranged to yield equation 7.14, where $T_{w,thermo}$ denotes the thermocouple measured temperature during each experiment, whilst $T_{bb,thermo}$ denotes the corresponding IR camera blackbody measured temperature of the pixels surrounding the thermocouple. Consequently, through monitoring of these temperatures during an experiment, a run-to-run surrounding radiance can be obtained. In general, accounting for the surrounding radiance resulted in a reduction in surface temperature as obtained using the calibration procedure of approximately 2 – 4 K on the impingement wall and 4 – 7 K on the film wall.

$$q^* = \frac{\sigma_b(T_{bb,thermo}^4 + \tau\xi T_{w,thermo}^4)}{(1-\tau\xi)} \tag{7.14}$$

The above text has outlined the calibration method used to determine both the blackbody and greybody parameters required to convert the raw camera counts to an accurate surface temperature measurement and is used for all IR temperature measurements in this study henceforth.

7.3 Commissioning Data for the Facility

A selection of commissioning data for the second phase of the rig incorporating mainstream flow recirculation is presented in this section.

The test section was traversed several times – just upstream of the test piece leading edge (where a static pressure tapping was also positioned) – at different mainstream Reynolds numbers to ascertain the uniformity of the mainstream flow field. The results of one of these traverses, which demonstrated Reynolds number similarity to engine conditions, is provided in Figure 7.7 where the calculated axial velocity profile is presented. It should be noted that a

vertical distance y/y_{max} of unity describes the surface of the tunnel against which the film cooled wall of the test piece rests. The traverse results indicate a boundary layer thickness of approximately 10% of the test section height corresponding to an absolute thickness of 11 mm. However, particularly striking is the strongly uniform flow outside of the boundary layer where all five probes indicate very similar axial flow velocities with a less than 1% variation from the average measured velocity. This, along with the symmetry of the plot, indicates that the contraction section – designed to provide velocity and turbulence uniformity – along with the honeycomb flow straightener and heater mesh positioned after the 180° bend in the tunnel, have resulted in a uniform flow field. The velocity profile was similar for the different Reynolds numbers for which traverses were performed. Traverse predictions from a CFD analysis of the rig (discussed in Chapter 10) also demonstrated good agreement with the experimental traverse data. Probe 1 and 2 do indicate a very slight flow separation towards the top of the tunnel which is thought to arise from modest deviations to the surface of the insulating panels in the contraction section, however, the slight non-uniformity was not expected to significantly influence the effectiveness measurements. It is also noted that towards the walls (i.e. near a y/y_{max} of zero or unity), the profile in Figure 7.7 appears to indicate an increase in axial velocity. This is attributed to blockage effects from the probes which, when near the wall, cause a

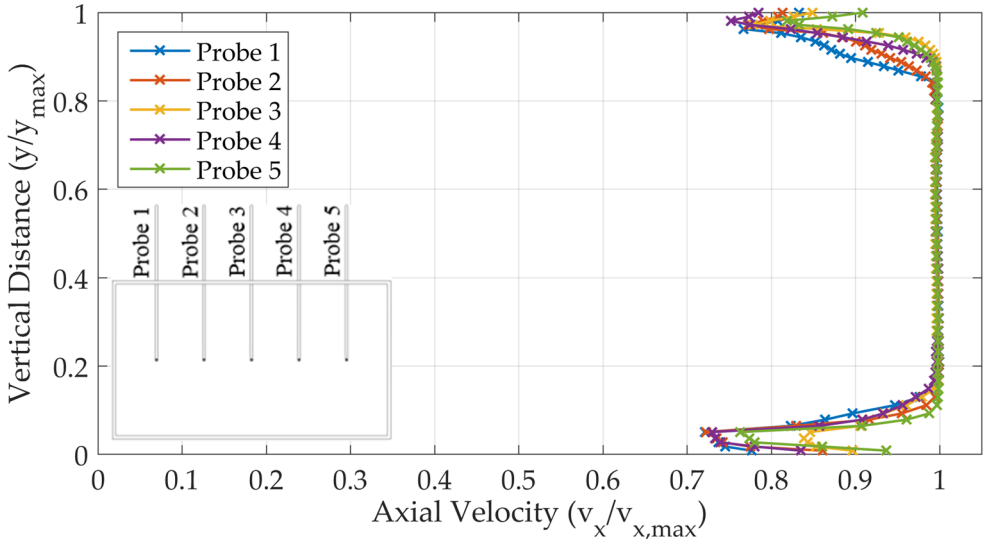


Figure 7.7 – Axial velocity traverse data from five probe pressure rake 60 mm upstream of the test piece LE

localised variation in the static pressure not captured by the static pressure tapping used in calculating the axial velocity. The turbulence intensity in the centre of the flow field at the test piece LE, as measured using the hot-wire, was calculated to be 1.07%, where Re_∞ matched that at engine conditions. This low turbulence intensity is the result of the flow straighter, heater mesh and contraction upstream of the test section.

The temperature uniformity of the mainstream flow, as obtained using the instrumented nylon mesh, is demonstrated in Figure 7.8 where mainstream flow temperatures were elevated from 295 K to 325 K. The crosses denote the placement of the thermocouple at the location of the test section duct. The values indicate (as a percentage) the local increase in temperature from the upstream temperature, over the average temperature increase from the upstream temperature measured by all nine thermocouples (described mathematically by equation 7.15).

$$\Psi = \frac{T_{mesh,local} - T_0}{T_{mesh,ave} - T_0} \times 100 \tag{7.15}$$

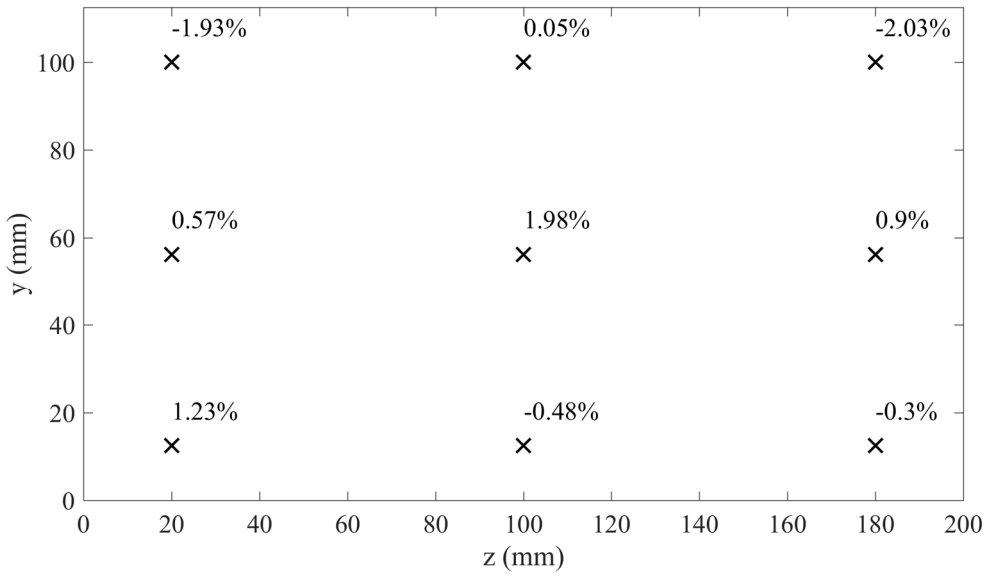


Figure 7.8 – Measurement data from the instrumented nylon mesh for the second generation facility where the difference in individual thermocouple readings from the average measured by all nine thermocouples is shown along with the locations of the thermocouples relative to the duct area

The figure demonstrates the high temperature uniformity in the mainstream flow profile where a maximum temperature variation of 0.6 K was observed from the average temperature

rise which corresponds to a variation of 2% of this average temperature increase and is well within the thermocouple measurement uncertainty. It is suggested that this uniformity is predominantly the result of the recirculating mainstream flow which – when compared to an open loop facility – requires lower heater power to produce a certain temperature rise. The author had previously observed [111] that irregularities on the heater mesh surface arising from, for example, dirt or solder splats, caused localised hot spots. The absolute temperature of these hot spots (and their effect on local mainstream flow temperature) scaled with power to the mesh. Consequently, a lower heater power resulted in a more uniform gas temperature field. Additionally, the fan driving the mainstream flow also contributes to the increase in the flow temperature further reducing the power requirements for the mesh heater.

Several lower power warming-up temperature transients of the facility are provided in Figure 7.9. The figure shows the mainstream temperature rise over the course of an hour at two medium fan speeds (for which Re_∞ approximately matches engine conditions) and various low power settings on the heater. It should be noted that the heater mesh power could be significantly increased if required – the maximum used in Figure 7.9 is 7.1 kW whereas the maximum possible power is around 120 kW. Indeed, varying heater power during warm-up

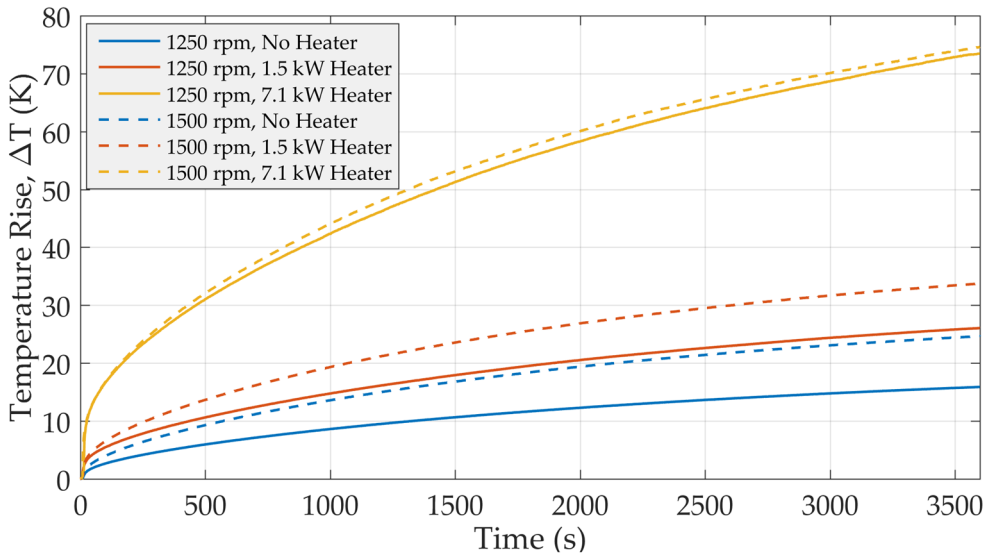


Figure 7.9 – Mainstream temperature rise at various fan and heater powers over an hour (note the maximum possible fan speed is 2900 RPM and maximum heater power is approximately 120 kW)

was one method whereby steady-state operating conditions were attained more quickly than for a constant step warm-up.

7.4 Experimental Uncertainties

The experimental uncertainty was assessed using the root-sum-squares method described by Moffat [17] for the overall effectiveness, film effectiveness and non-dimensional mass flow (equations 2.1, 2.9 and 2.3). Uncertainty contributions arising from both precision (due to the size of the data set) and bias (due to instrumentation uncertainty) were considered, and it was found that the bias uncertainties were dominant.

Equation 7.16 demonstrates the general form of the uncertainty equation used in assessing the uncertainties in overall and film effectiveness along with non-dimensional mass flow where I_n represents the relevant measured variable and ω represents the derived quantity for which the uncertainty is being calculated. Table 7.4 shows the instrumentation uncertainties used in these calculations.

$$U_\omega = \sqrt{\left(\left(\sum_{n=1}^{N}\sqrt{\left(\frac{\partial\omega}{\partial I_n}\right)^2 {B_{I_n}}^2}\right)^2 + \left(\sum_{n=1}^{N}\sqrt{\left(\frac{\partial\omega}{\partial I_n}\right)^2 {C_{I_n}}^2}\right)^2\right)} \tag{7.16}$$

Table 7.4 – Uncertainty in instrumentation measured values

Instrumentation	Associated Uncertainty
Thermocouples	±1.5 K [112]
IR Camera	±2.0 K [108]
Pressure Transducers	±0.25 % of the transducer range [113]

7.5 Summary

A new experimental facility for assessing the aerothermal performance of flat plate, double-wall, effusion cooled systems has been designed and commissioned. The facility was used to obtain the experimental results presented in the following chapters. Listed below are some of the key features of this facility:

- Closed loop recirculating facility permitting higher mainstream temperatures to be achieved at reduced heater power relative to an open loop facility.
- Facility lined with high performance insulative panels reducing rig settling times and minimising the likelihood of flow leakages due to the thermal expansion of tunnel sections.
- Highly uniform mainstream velocity and temperature profiles obtained at the tunnel test section.
- Fully controllable coolant supply system installed incorporating critical flow Venturi nozzles conforming to an ISO standard permitting coolant mass flow to be accurately measured.
- The facility mainstream and impinging jet Reynolds numbers match engine conditions. The test piece Biot numbers are within 25% of engine values.

8 Results – Overall Effectiveness Measurements

8.1 Chapter Overview

This chapter presents some of the aerothermal data obtained from the experimental facility during steady-state experiments. The thermal data presented includes the overall cooling effectiveness for the five manufactured double-wall geometries (D3, D6, D8, C5 and G1). Several aerodynamic measurements made during the experimental runs are also presented. The data are used to compare the performance of the various geometries.

8.2 Processing

For the experimental results presented here, the mainstream flow speed was set to provide Reynolds number similarity with engine conditions (Re_∞ ~ 25000 based on film hole diameter). Similarity was also achieved for the Reynolds number based on the impingement flow (2400 < Re_i < 88200). The mainstream-to-coolant temperature ratio achieved in the experiments was approximately 1.25 (with the mainstream flow around 75 K hotter than that of the coolant). A combination of a flow regulator and CFVNs were used to vary and measure coolant mass flow which is presented in the results using the definition of non-dimensional coolant mass flow (m^*) provided in equation 2.3. The value of heat transfer coefficient used in defining m^* is that obtained from equation 8.1 which shows a Nusselt number correlation for turbulent flow over a flat plate [94].

$$Nu = 0.0296 Re^{4/5} Pr^{1/3} \qquad (8.1)$$

In calculating overall effectiveness, local mainstream gas temperature measurements were used rather than the average mainstream gas temperature. These local measurements were

obtained using the five ceramic sheathed thermocouples (discussed in section 7.2.4) which were positioned 9.5 mm from the top surface of the tunnel and spaced at regular spanwise intervals. In this way any small spanwise non-uniformities in the mainstream gas temperature are accounted for when calculating the overall effectiveness.

Figure 8.1 shows a section view of one of the experimental test pieces (geometry D3), along with the areas of both the impingement and film walls captured by the IR cameras during experimental runs for which the overall effectiveness was calculated.

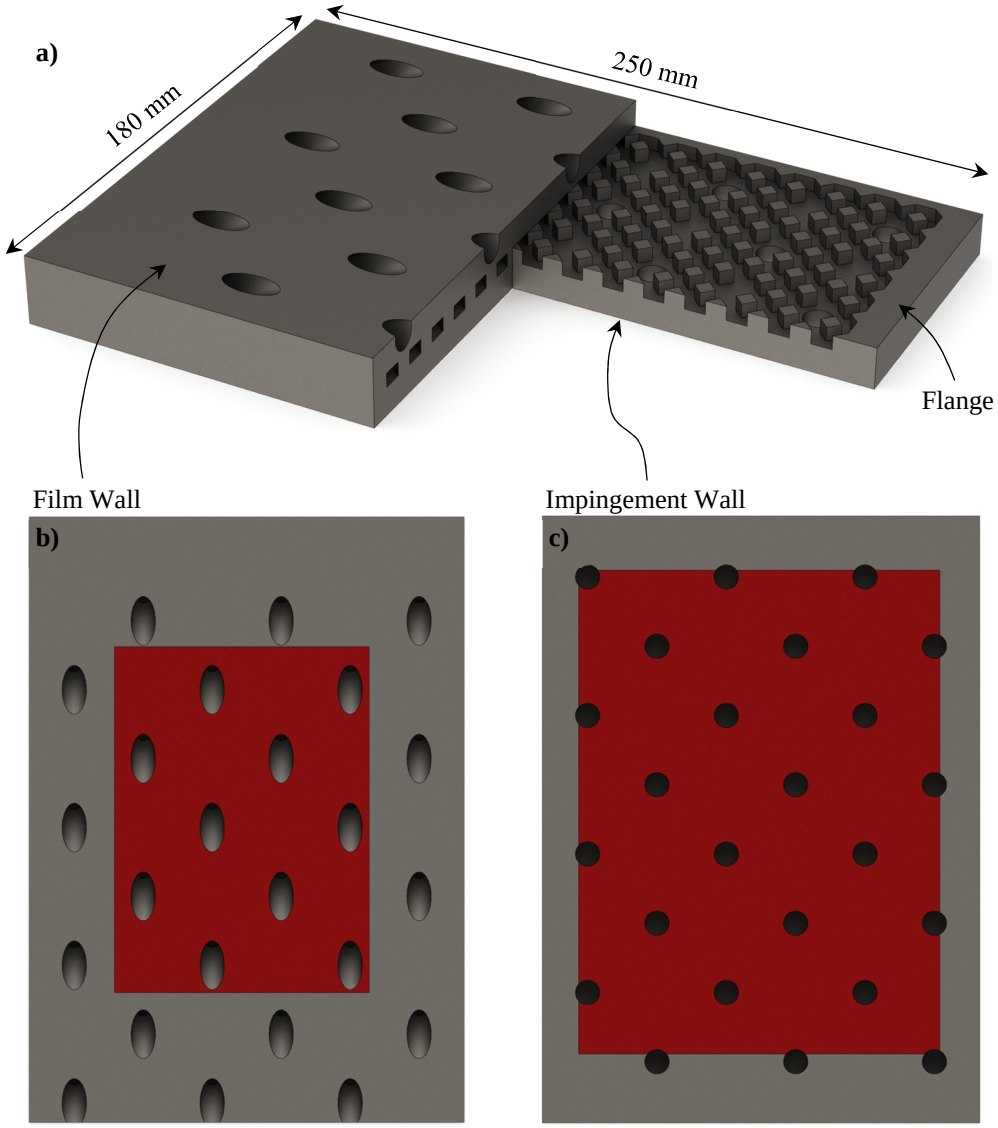


Figure 8.1 - a) *Section view of one of the test geometries (geometry D3). Area of the* b) *film wall and* c) *impingement wall captured by the IR cameras during experimental runs*

8.3 Results

The following section provides a set of experimental data obtained during the overall effectiveness test runs for a range of conditions. Some of the data obtained are summarised below:

- Figures 8.2 – 8.11 show measured overall effectiveness contours for both the external surfaces of the film and impingement walls over a range of m^* for geometries D3, D6, D8, C5 and G1. These geometries had demonstrated interesting cooling characteristics in the decoupled conjugate simulations presented in Chapter 5. Note that approximate feature locations have been overlaid on top of the contours (although, due to camera distortion, the alignment is imperfect).

- Figure 8.12 shows an area-weighted average of overall effectiveness for all five geometries at both external surfaces of the impingement and film cooled walls for varying m^* with curves fitted to the data points.

- Figure 8.13 shows impingement jet Reynolds number plotted against non-dimensional mass flow for each geometry.

- Figure 8.14 shows the difference in area-averaged overall effectiveness between the impingement wall and film wall for each geometry.

- Figure 8.15 shows the required pressure ratio to achieve a certain value of non-dimensional mass flow for each geometry.

- Figure 8.16 shows the variation in discharge coefficient for each test geometry at varying impingement jet Reynolds numbers. Note discharge coefficient ideal flow rate is based upon the film hole diameter.

- Figure 8.17 shows area-averaged overall effectiveness versus non-dimensional mass flow for the five test geometries along with uncertainty bars showing the calculated uncertainties in non-dimensional coolant mass flow and overall effectiveness. Contours showing the variation in overall effectiveness uncertainty across the five test geometries at the minimum and maximum coolant flow rate cases are shown in Figure 8.18.

8.3.1 Overall Effectiveness Data

Geometries D3 and D6 only differ in the height of the pedestal layer and impingement hole diameter. At lower values of m^*, the overall effectiveness achieved on the film cooled wall for each geometry is similar, both in a quantitative sense (as attested to by Figure 8.12) and qualitatively (see Figures 8.2 and 8.4). However, as m^* is increased, the overall cooling effectiveness achieved on the film wall of geometry D6 begins to exceed that of geometry D3. Two reasons are hypothesised for this. The first – and that which is expected to be most significant – is the result of the increased surface area available for convective cooling within the pedestal layer of D6 where the pedestals are thrice as tall as those of D3. The other reason for the differing performance at higher m^* is the increased impingement jet Reynolds numbers exhibited in D6 at equivalent mass flows (a result of the quarter-area impingement holes); note that the impingement jet Reynolds numbers with m^* are compared in Figure 8.13. This results in an increased impingement jet stagnation point Nusselt number (as demonstrated by the correlations in Figure C.2). Additionally, the target plate spacing to impingement jet diameter (y/D_i) in geometry D6 is 3 compared to 0.5 for D3. As shown by both the correlations in Figure C.2, as well as experimental data [16], the stagnation point Nusselt number generally increases up until a y/D_i of around 6 and consequently D6 is expected to exhibit higher stagnation point Nusselt numbers, although as shown by Jambunathan et al [16], the area of the impingement zone may be increased at smaller values of y/D_i. Qualitatively, there is little visible evidence of local impingement conducted through to the external surface of the film cooled wall for either

geometry. This is, in-part, expected to arise due to the relatively low values of Re_i in both D3 and D6, a consequence of the large number of impingement holes and relatively high impingement wall porosities (particularly for D3). The lack of observable impingement cooling is also expected to result from the dominant effect of film cooling observed in both geometries – a product of the closely pitched holes and relatively low blowing ratios across all mass flows resulting in films that are well adhered to (don't lift-off from) the external surface. In addition, the location of the impingement holes, as demonstrated in the contours, is directly downstream of the ejection point of the films and, consequently, the visual effect of impingement may manifest itself as an apparent increase in film performance. A significant increase in streamwise effectiveness is also observed and results from the build-up of the films. It is also possible that the difference in outer wall overall effectiveness in the two geometries at higher m^* could also be caused by varying film cooling performance that may result from the difference in pedestal height. However, as further discussed later on, in Chapter 9, there was minimal observed difference in film effectiveness between these geometries at similar coolant mass flows; although the higher convective effectiveness in D6 will result in slightly warmer cooling films which may have a small effect on film cooling performance.

Figure 8.12 also shows that geometry D6 exhibits significantly improved overall effectiveness on the impingement wall compared to geometry D3. This is almost certainly a result of the increased pedestal height which causes a higher convective efficiency for the D6 case at equivalent mass flows (an effect observed in the decoupled analyses performed in Chapter 5). Consequently, more heat is removed by the fluid in the internal passage of D6 resulting in less heat being conducted through to the impingement wall and a corresponding increase in overall effectiveness when compared to D3.

D8 differs from D6 only in the spacing of the pedestals which exhibit reduced density in the former case. Consequently, for D8, the pitch of both the impingement and film holes is twice as large as was the case for D6. The result of this is very apparent in Figure 8.6 where

there is no observable spanwise interaction between films. Additionally, the low porosity of the film cooled wall causes jet lift-off to occur at much lower values of m^* than would occur for geometries D3 and D6, and these ineffective films are very apparent in Figure 8.6. However, the low porosity of the impingement wall does result in high impingement jet Reynolds numbers as shown by Figure 8.13 (Re_i between 19400 – 88200) and correspondingly high impingement zone Nusselt numbers. Indeed, the effect of these high Nusselt numbers is visible on the outer surface of the film wall, where, immediately downstream of the location of the film exit, there appears to be a lateral widening of the films (as shown by the increase in overall effectiveness).

Despite the relatively low effectiveness achieved on the film wall, Figure 8.7 shows that D8 demonstrates reasonably high cooling effectiveness on the impingement wall with an approximate reduction in area-averaged overall effectiveness of only around 0.04 when compared to the best performing geometries tested (D6 and G1). The D8 geometry, once again, exhibits the largest pedestal height. In this case the ratio of pedestal wetted area to unit cell external wetted area is 65.5% which is lower than the 87.4% exhibited by geometry D3. Consequently, this higher impingement wall effectiveness is not the result of the pedestal layer wetted area in the case of D8. Instead, it arises from the reduced wall-to-pedestal conduction area compared to geometries D3 and D6. The longer pedestal for D8 means that less heat is conducted from the hotter film wall to the colder impingement wall resulting in the relatively high impingement wall cooling effectiveness. However, it is noted that this results in a large thermal gradient across these two walls, which, as discussed in Chapter 6 and Appendix C, has undesirable thermomechanical effects due to their mismatched thermal expansions.

Geometry C5 also displays a relatively low film cooling performance, once more due to the low film wall porosity resulting in high blowing ratios and jet lift-off at moderate values of m^*. Whilst for geometry C5, the effect of jet impingement is again visible on the film wall contour (via an apparent lateral widening of the film jets), it is not as prominent as it was in geometry D8. This is a result of the larger impingement hole diameters in geometry C5 causing a

reduction in impingement jet Reynolds numbers (Re_i between 9500 – 44500). However, despite the low film cooling performance and inferior impingement effect when compared to D8, C5 displays superior overall cooling effectiveness on the film wall as attested to by both Figure 8.8 and Figure 8.12. This is thought to result from the much-increased wall-to-pedestal contact area which permits greater conduction between the two walls. Consequently, it is anticipated that more heat is being conducted away from the film wall for the C5 geometry resulting in superior cooling of the wall compared to D8. However, a secondary result of this is the reduced overall effectiveness of the impingement surface of C5 as demonstrated in Figure 8.12.

The crenulation concept geometry, G1, exhibited very high overall cooling effectiveness on both walls as demonstrated in Figures 8.10 – 8.12. Indeed, as indicated by Figure 8.12, a reduction in m^* of around 30% is possible to achieve a similar value of overall effectiveness on the film wall to D6, or otherwise an absolute increase in cooling effectiveness of around 0.06 is possible at the same value of m^*. The impingement wall overall effectiveness, however, is similar for the two geometries, particularly at lower coolant flow rates. At higher values of m^*, an increase in impingement wall absolute cooling effectiveness of around 0.025 is possible at similar values of m^* compared to D6. Three reasons are suggested for this improved performance, all of which were factors in the development of the design. The first is the increased passage height between the walls with a high coolant wetted area arising from the crenulations on the impingement wall. It is likely that this increased wetted area results in a superior convective efficiency compared with the other geometries (further discussed in Chapter 9). Secondly, the crenulations allow for a close impingement hole to target plate (y/D_i) spacing to be maintained whilst increasing the pedestal height. The third factor is the slightly reduced film hole pitch in the geometry with a primary hole pitching of $P = 5.5$ compared to $P = 5.66$ in geometries D3 and D6. This results in a slightly improved film cooling performance. A secondary effect of this reduced pitch is a more uniform spanwise temperature profile on both the impingement and film walls which is preferable from both aerothermal and mechanical

perspectives. It is also suggested that the moderate increase in impingement wall overall cooling effectiveness, compared with the more significant increase in film wall overall effectiveness, is preferable from a thermomechanical perspective as it signifies good temperature uniformity across the geometry, potentially reducing thermomechanical stresses.

In general, it is preferable that both the film and impingement walls demonstrate high overall effectiveness. However, the magnitude of the thermal difference between the two walls is also an important consideration as this represents a significant factor in the magnitude of the thermal stresses developed in the geometry which have an effect on the lifespan of the system. This is shown in Figure 8.14 where the difference in area-averaged overall effectiveness between the impingement and film walls are plotted at the different coolant mass flows. Note that, in the plot, the area of the impingement wall considered was cropped to align to the region of the film wall captured by the IR camera. In general geometry D3 demonstrates a relatively low and invariable difference in overall effectiveness between the two walls. This is expected to result from the aforementioned high wall-to-pedestal conduction area, low passage height and good film coverage. System D8, on the other hand, shows a large disparity between the overall effectiveness achieved on the two walls and this arises from the poor film coverage, low conduction area and larger passage height. C5, although also demonstrating poor film coverage, shows a lower difference in overall effectiveness between the walls and this arises from the increased pedestal conduction area when compared to D8 and reduced passage height. Such a geometry may permit an increase in potential service time due to the reduced thermal gradient between the walls. This would of course need to be weighed-up against the reduction in material properties that would occur at hotter conditions (corresponding to lower values of overall effectiveness). In general, a high temperature difference contributes to failure by low cycle fatigue, whilst higher maximum temperatures increase the likelihood of material creep [114]. Consequently, the suitability of a specific double-wall geometry is dependent on the region of application.

Consideration should also be given to the flange around the edge of each test geometry and that is apparent in Figures 7.10 and 8.1, and also in Appendix D. The flange was needed for the manufacturing process and varied slightly in size between the different geometries depending on the exact form of the internal geometry and unit cell size and was designed to minimise flow disruption in the pedestal layer (the variation is shown for each geometry in Appendix D). However, the presence of the uncooled flange resulted in some conduction occurring between the film and impingement walls towards the edges of the flat plate. Whilst the effect of the flange conduction is expected to be minimal on the temperature of the film cooled wall analysed during the experiments, its effect is greater on the impingement wall where the area captured by the camera was greater (see Figure 8.1). Indeed, the effect of the flange is evident on the impingement wall, particularly for geometries D8 and C5 which exhibited poor film performance (see Figure 8.7 and Figure 8.9), where a reduction in overall effectiveness is observed around the edges of the captured area towards the flange. Whilst some of this effect may be the result of modest coolant biasing towards the central impingement holes, it is largely expected to result from conduction from the hotter film wall. Consequently, it is suggested that impingement wall effectiveness may be slightly higher than that obtained from the experiments although the effect is thought to be relatively small – particularly in geometries D3 and D6 where only a very small effect of the flange is observed at the lower coolant flow rates. Further, it is noted that geometry G1, which was manufactured later than the other geometries, was slightly modified to further reduce the effect of conduction between the film and impingement walls due to the flange. As can be seen in Figure D.7 (Appendix D), a pocket was machined out of the flange prior to brazing the test piece significantly reducing the conduction area of the flange. Consequently, there is no observable effect of the flange on geometry G1 in Figure 8.11. The effect of the flange on the flow field is discussed further in Chapter 10 based on the CFD simulations performed.

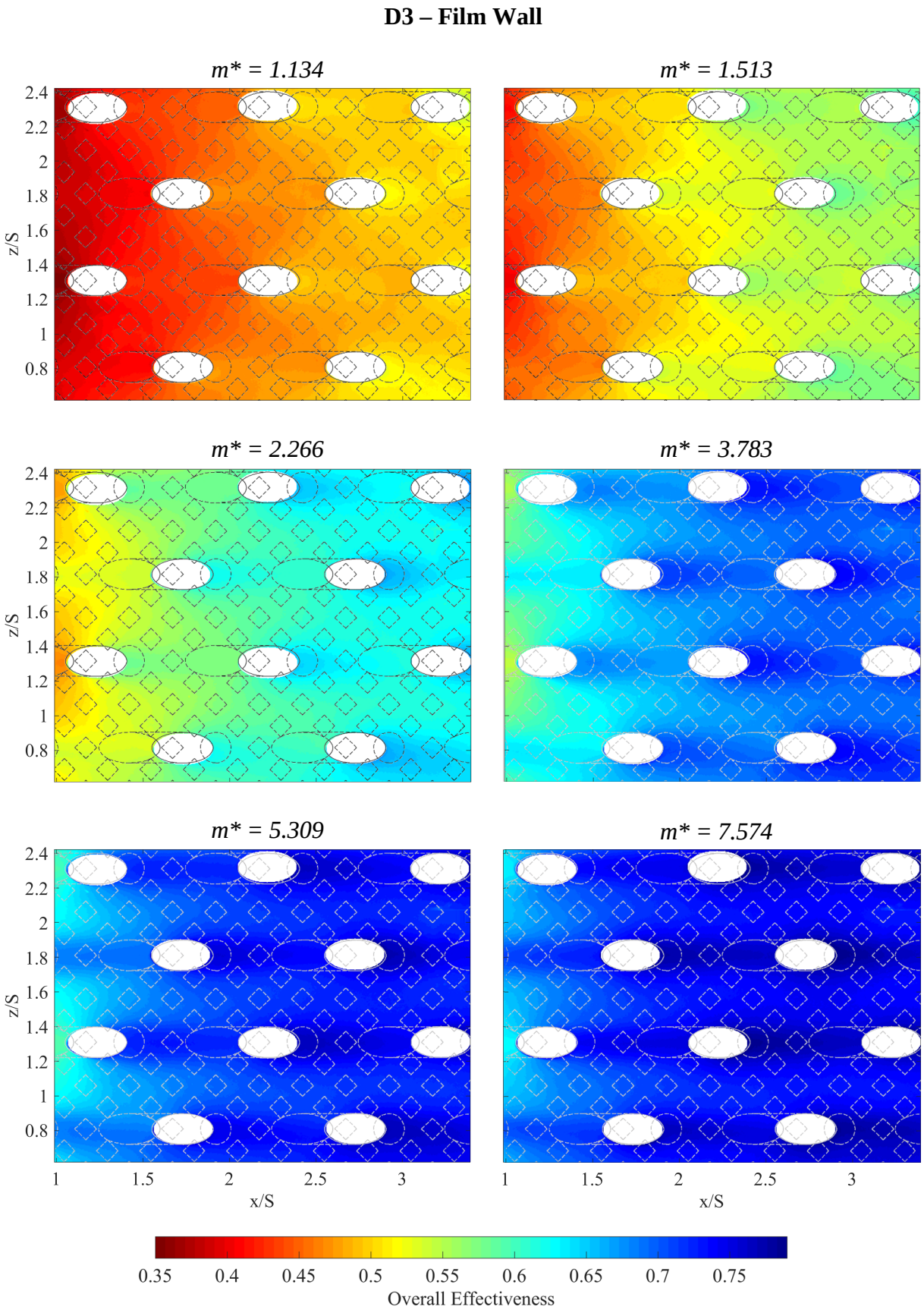


Figure 8.2 – Experimental overall effectiveness contours for geometry D3 showing the external surface of the film wall at various coolant non-dimensional mass flows

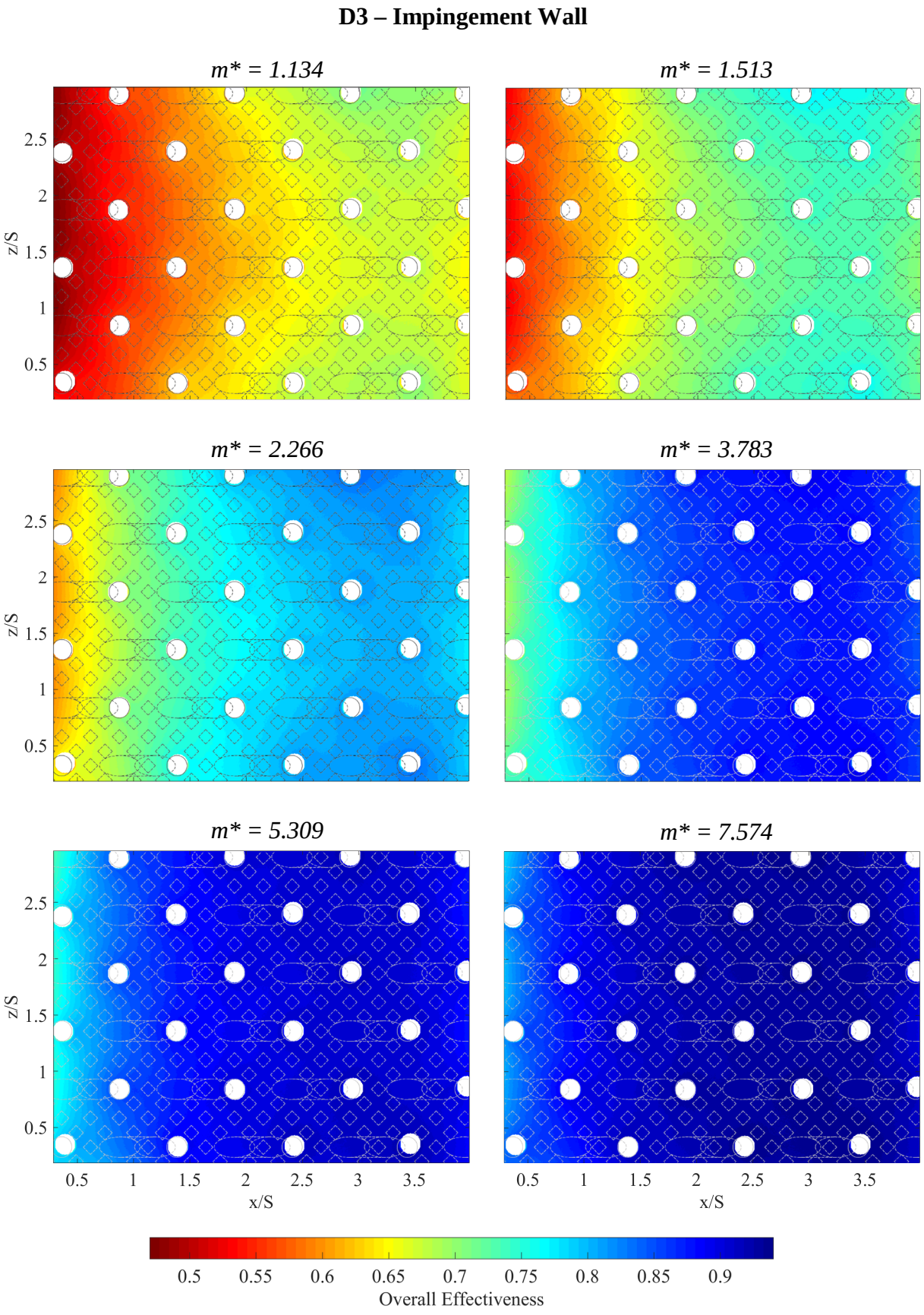


Figure 8.3 - Experimental overall effectiveness contours for geometry D3 showing the external surface of the impingement wall at various coolant non-dimensional mass flows

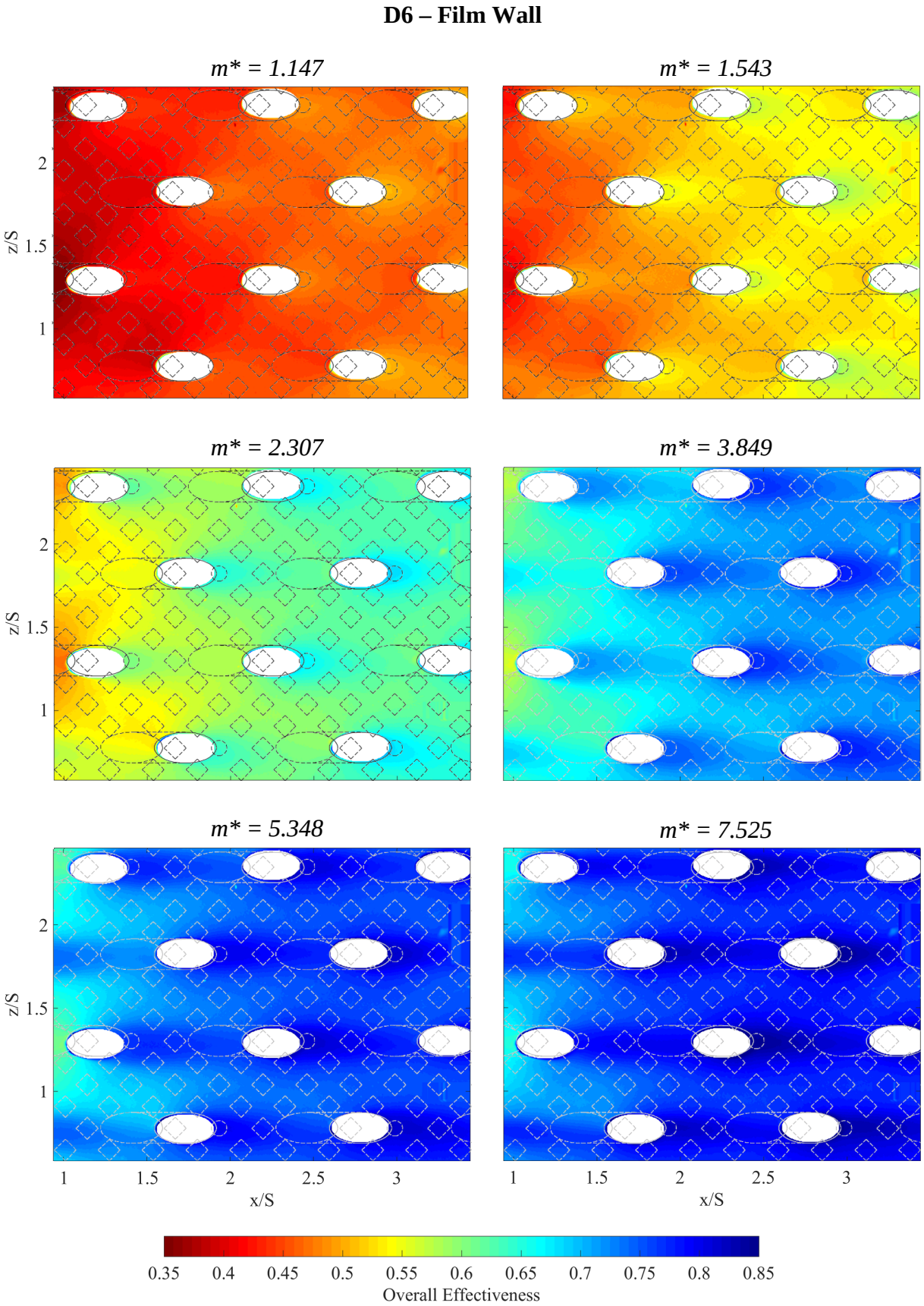


Figure 8.4 - Experimental overall effectiveness contours for geometry D6 showing the external surface of the film wall at various coolant non-dimensional mass flows

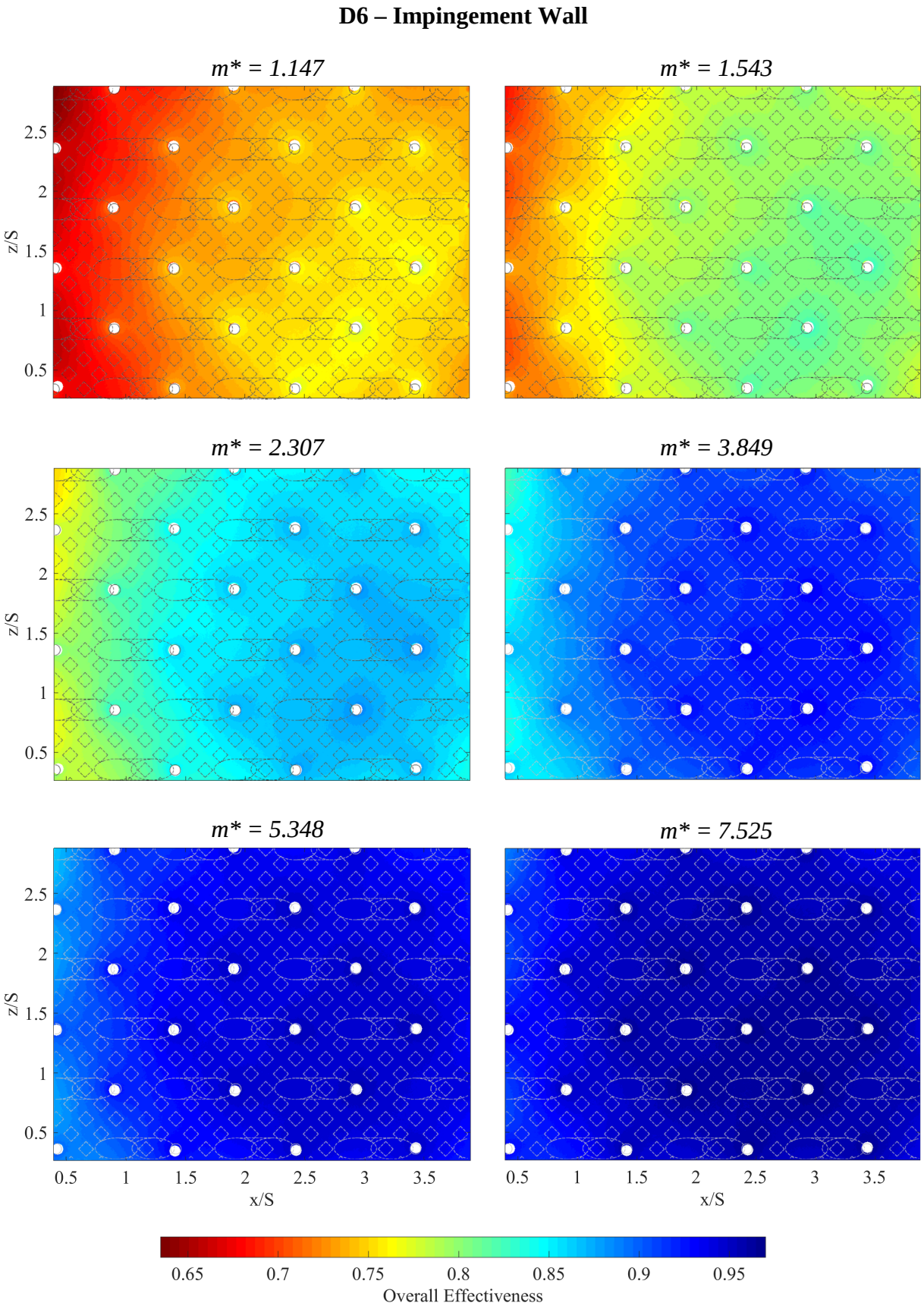


Figure 8.5 - Experimental overall effectiveness contours for geometry D6 showing the external surface of the impingement wall at various coolant non-dimensional mass flows

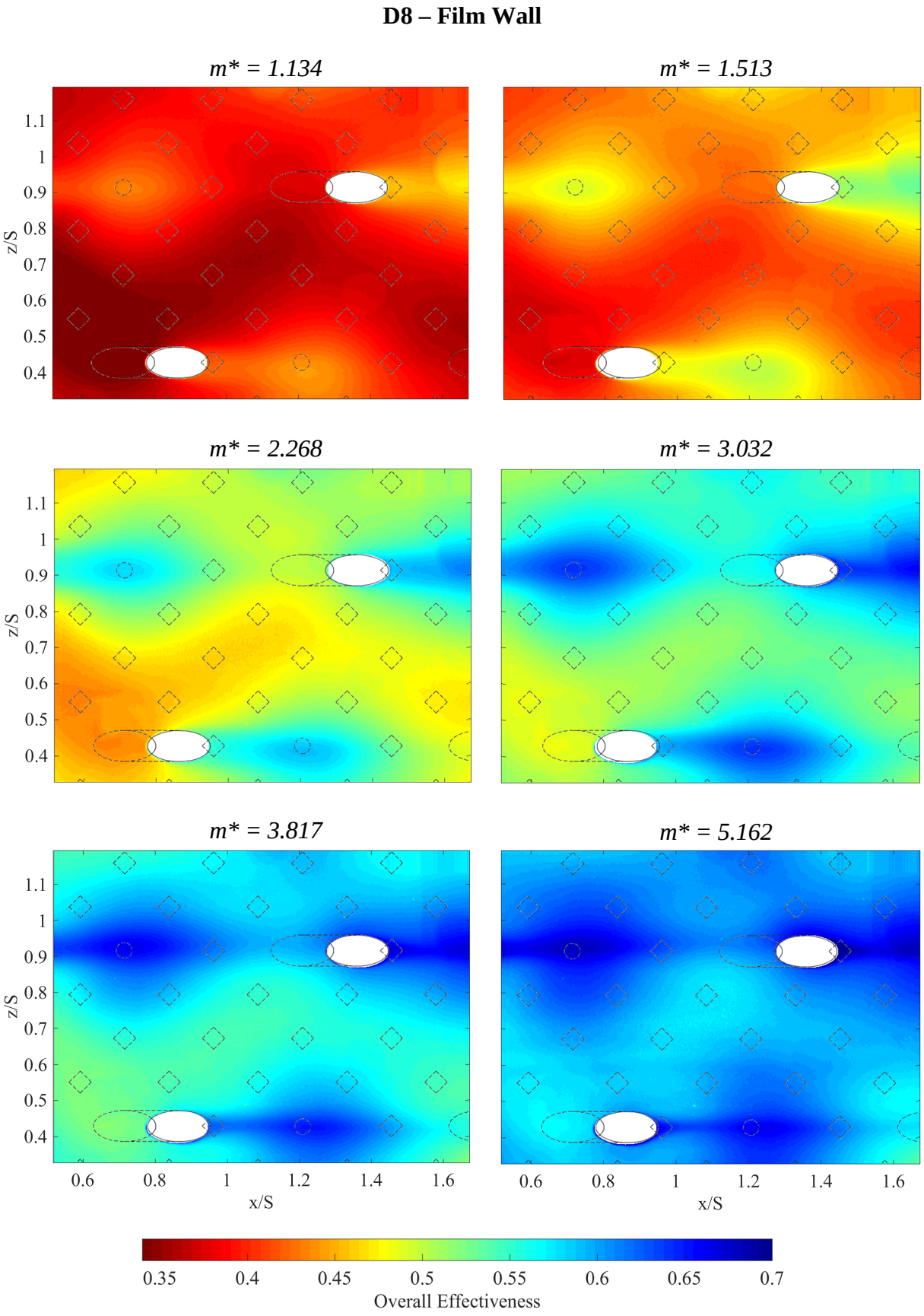


Figure 8.6 - Experimental overall effectiveness contours for geometry D8 showing the external surface of the film wall at various coolant non-dimensional mass flows

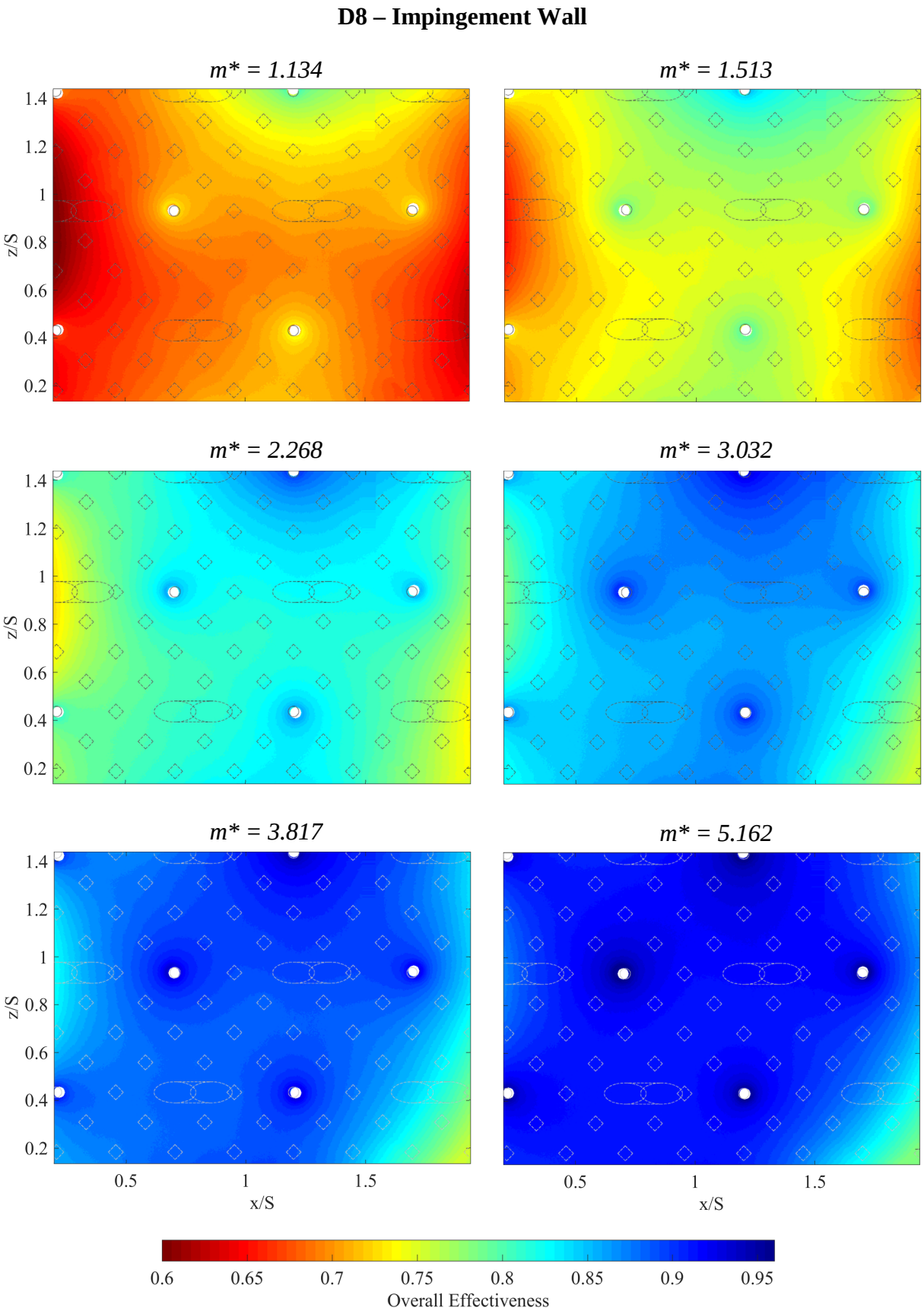


Figure 8.7 - Experimental overall effectiveness contours for geometry D8 showing the external surface of the impingement wall at various coolant non-dimensional mass flows

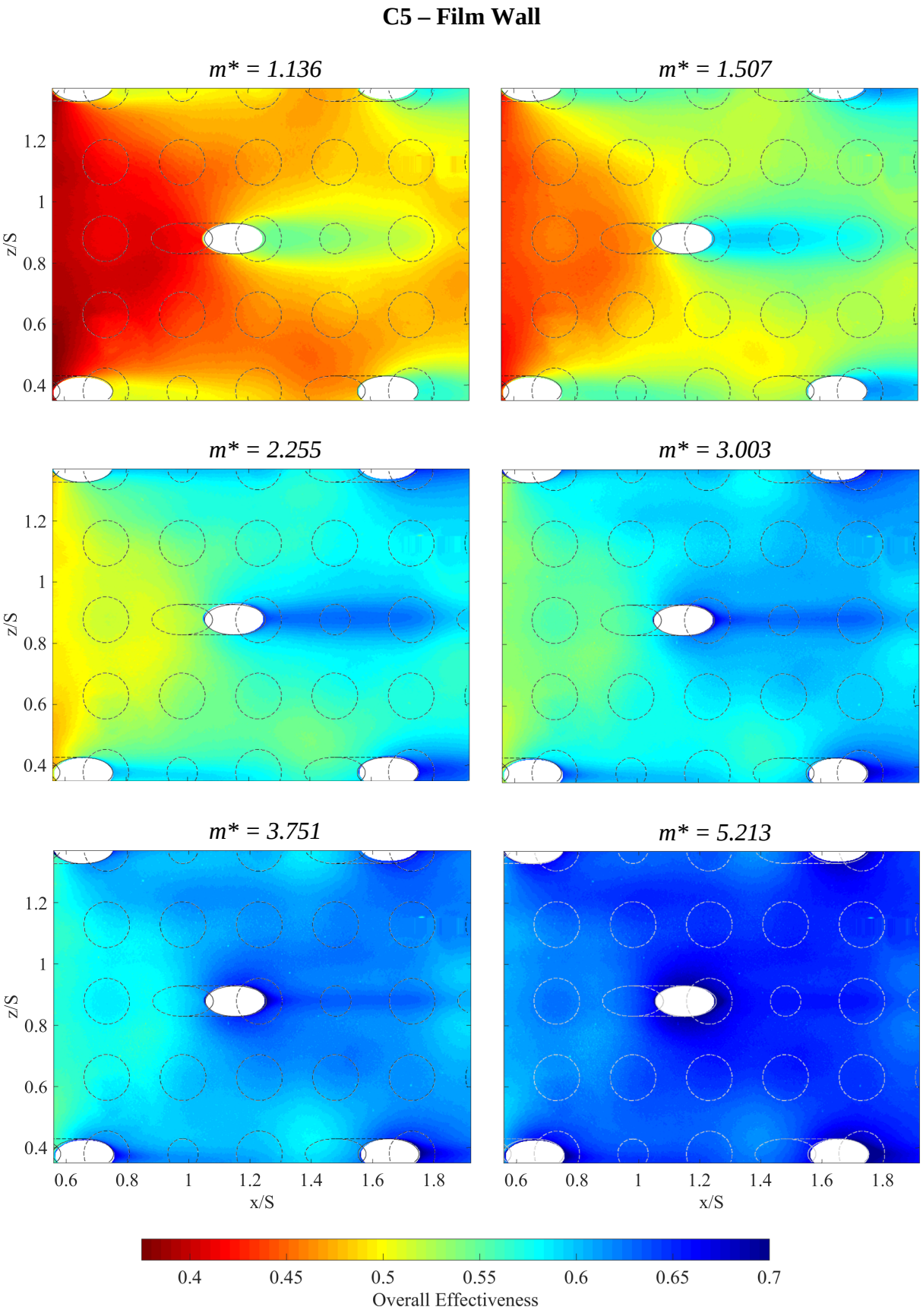


Figure 8.8 - Experimental overall effectiveness contours for geometry C5 showing the external surface of the film wall at various coolant non-dimensional mass flows

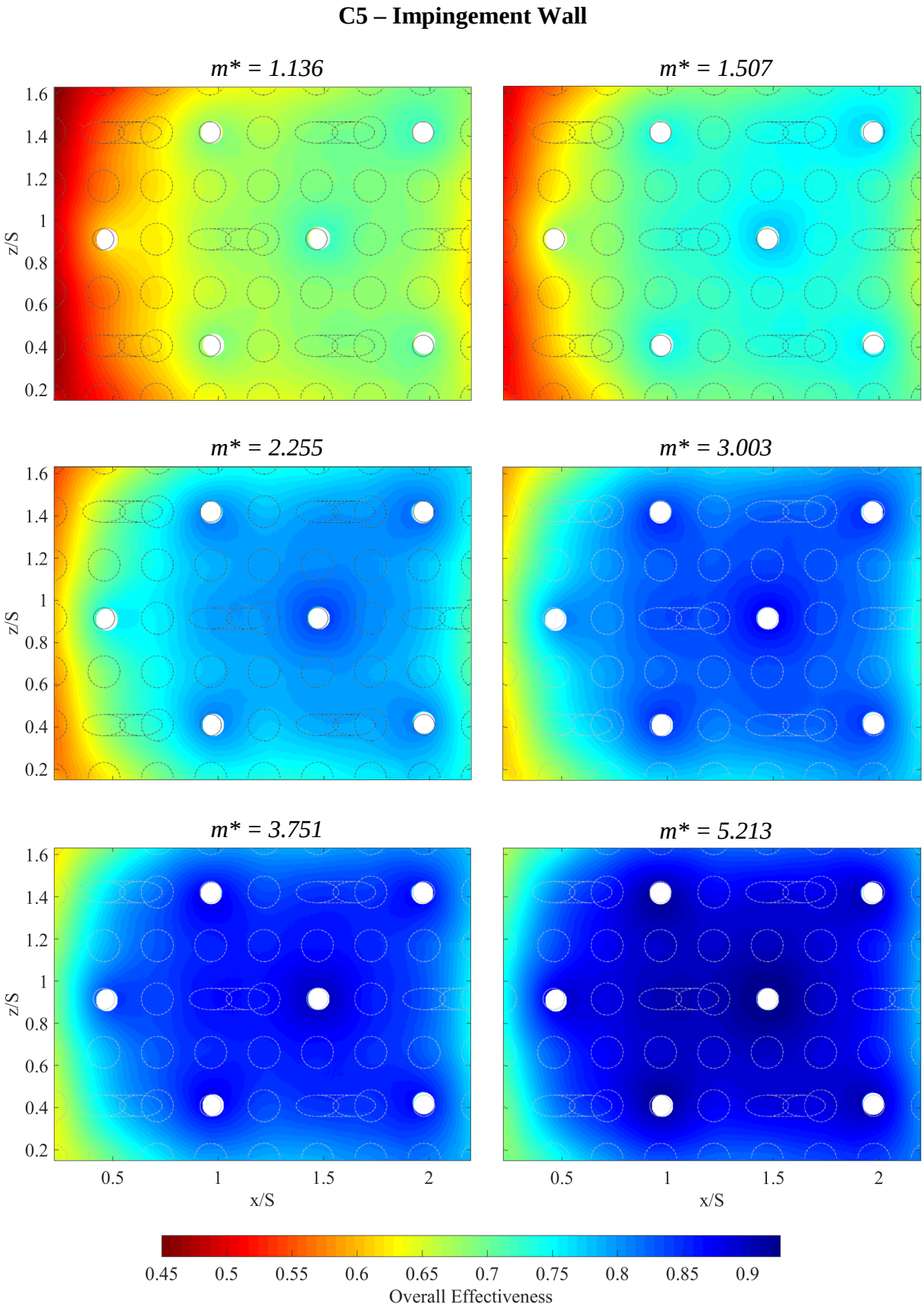


Figure 8.9 - Experimental overall effectiveness contours for geometry C5 showing the external surface of the impingement wall at various coolant non-dimensional mass flows

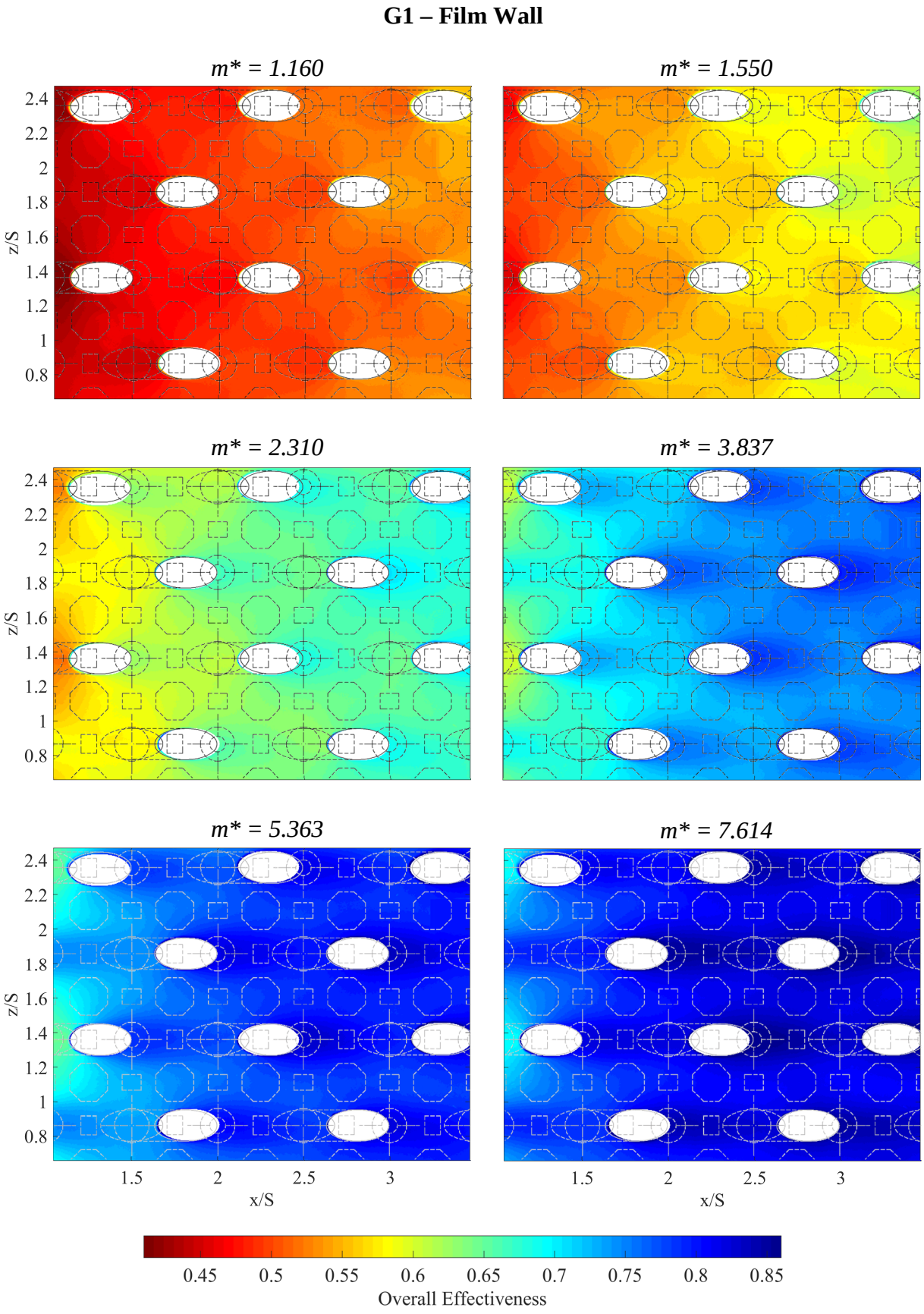


Figure 8.10 - Experimental overall effectiveness contours for geometry G1 showing the external surface of the film wall at various coolant non-dimensional mass flows

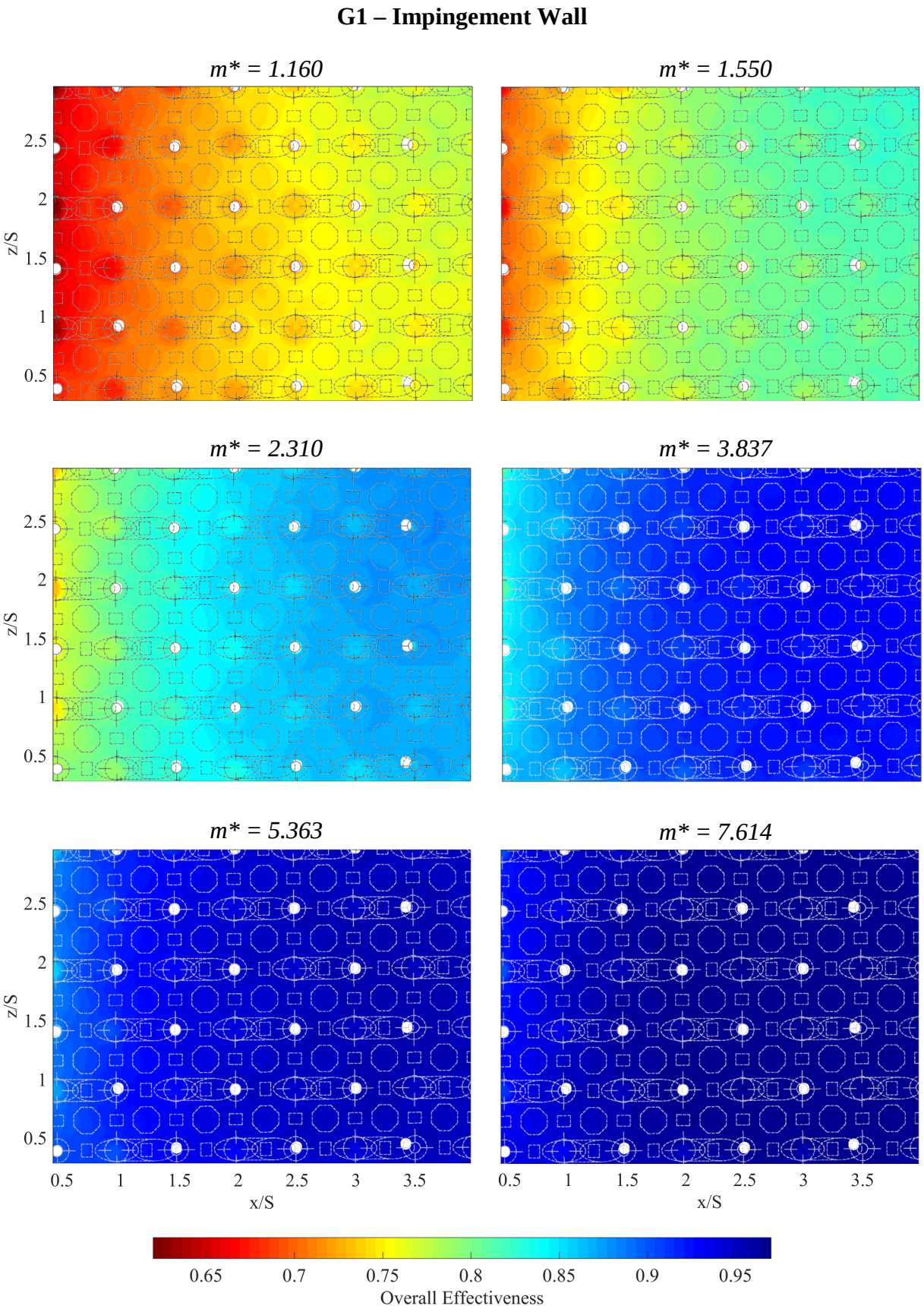
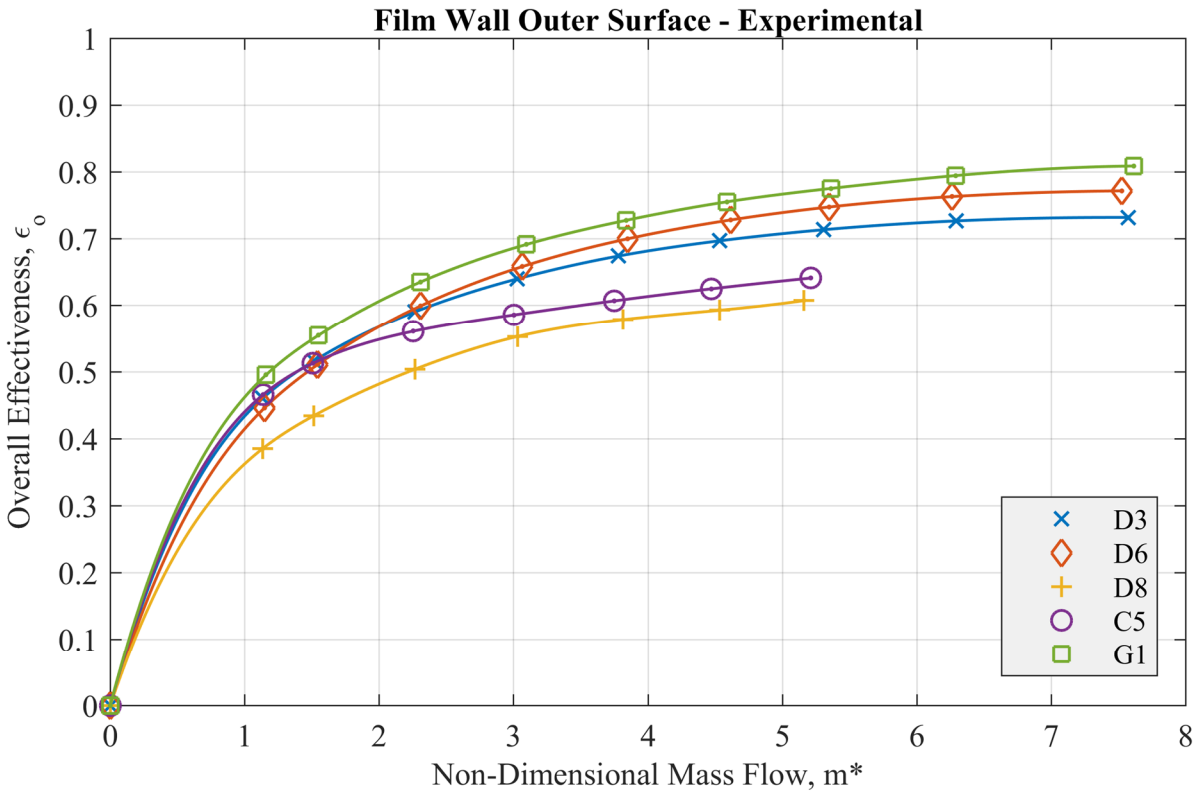
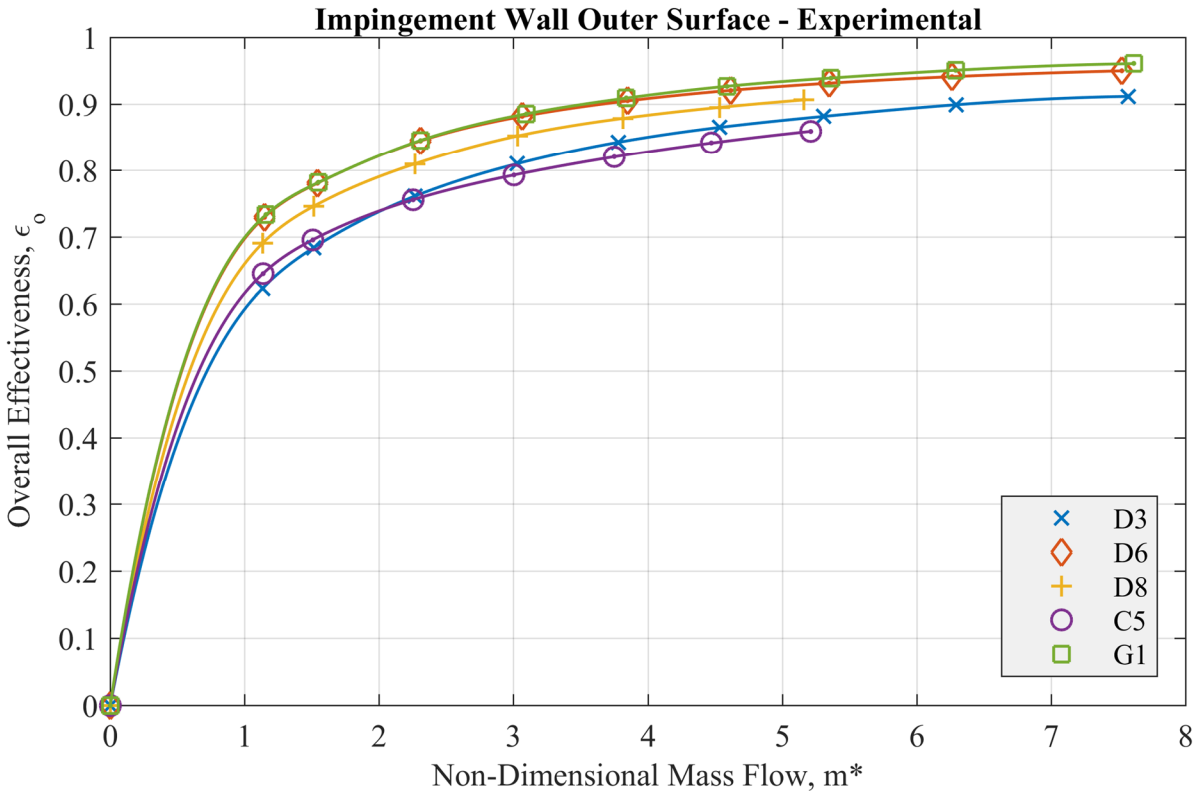


Figure 8.11 - Experimental overall effectiveness contours for geometry G1 showing the external surface of the impingement wall at various coolant non-dimensional mass flows

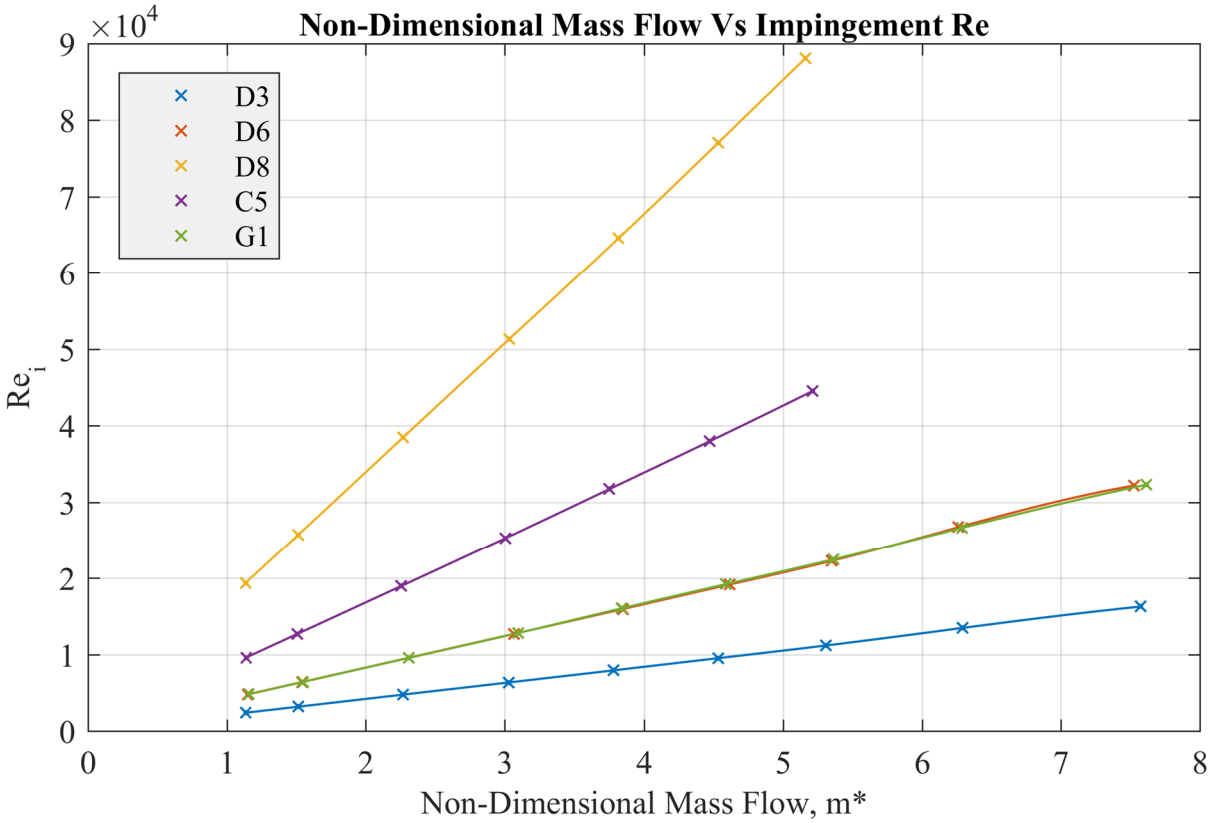




Unit Cell Wall Porosities: D3: ϕ_i = 4.91% & ϕ_f = 9.82% D6: ϕ_i = 1.23% & ϕ_f = 9.82%

D8: ϕ_i = 0.31% & ϕ_f = 2.45% C5: ϕ_i = 1.57% & ϕ_f = 3.14% G1: ϕ_i = 1.30% & ϕ_f = 10.39%

Figure 8.12 - Area-weighted averaged experimental overall effectiveness for all five test geometries on both the external surfaces of the film and impingement walls. Unit cell wall geometric porosities are shown at the bottom of the figure



Unit Cell Wall Porosities: D3: ϕ_i = *4.91%* & ϕ_f = *9.82%* D6: ϕ_i = *1.23%* & ϕ_f = *9.82%*

D8: ϕ_i = *0.31%* & ϕ_f = *2.45%* C5: ϕ_i = *1.57%* & ϕ_f = *3.14%* G1: ϕ_i = *1.30%* & ϕ_f = *10.39%*

Figure 8.13 - Non-dimensional mass flow against resulting impingement jet Reynolds number (note h_∞ was approximately 170 as calculated using equation 8.1). Unit cell wall geometric porosities are shown at the bottom of the figure

8.3.2 Pressure Ratio and Discharge Coefficient

When considering the suitability of a cooling system to a particular application – in this case turbine cooling – the pressure ratio required to achieve the necessary cooling effect is a key design feature. The use of excess coolant reduces the cycle efficiency. Additionally, the pressure margin (coolant total inlet pressure to static outlet pressure) needs to be sufficient to minimise the likelihood of hot gas ingestion. Whilst the current work principally pertains to investigating the characteristics of double-wall systems that result in preferable cooling performance, some consideration was also given to the pressure ratios required by the various geometries to achieve a particular cooling benefit and this is further discussed below.

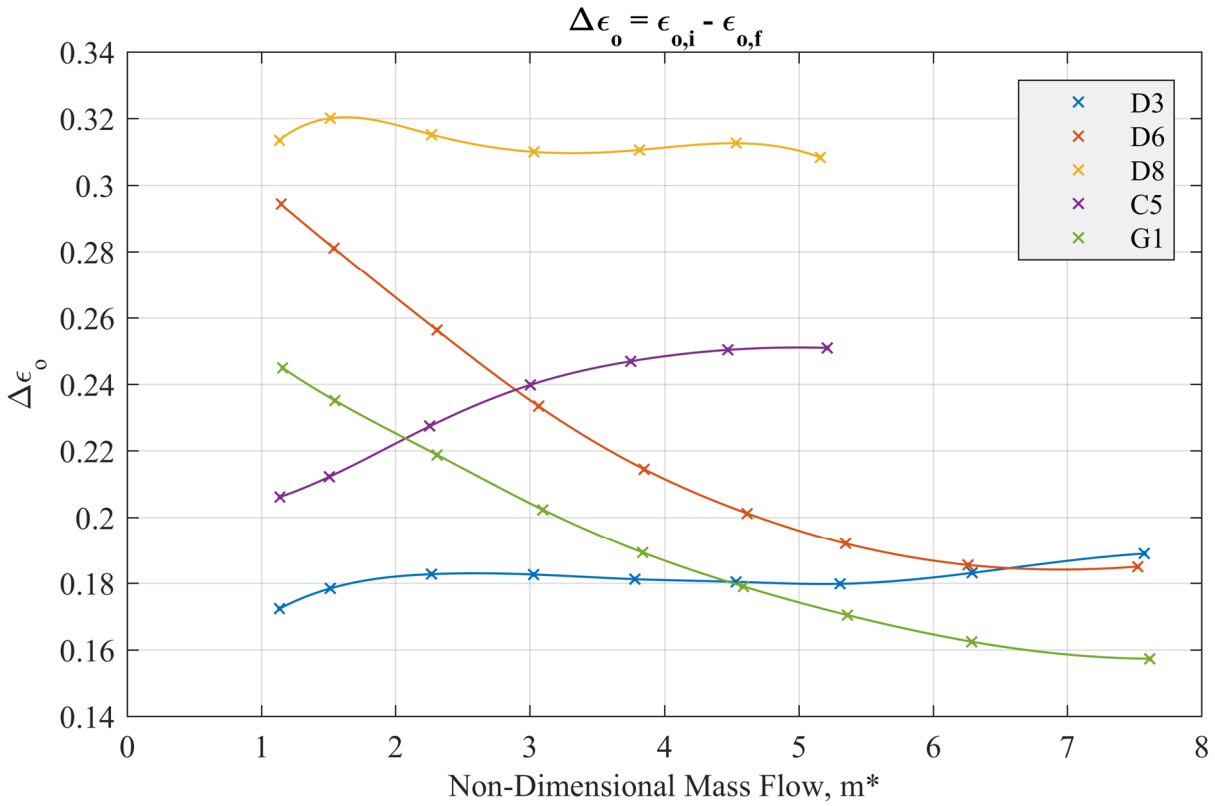
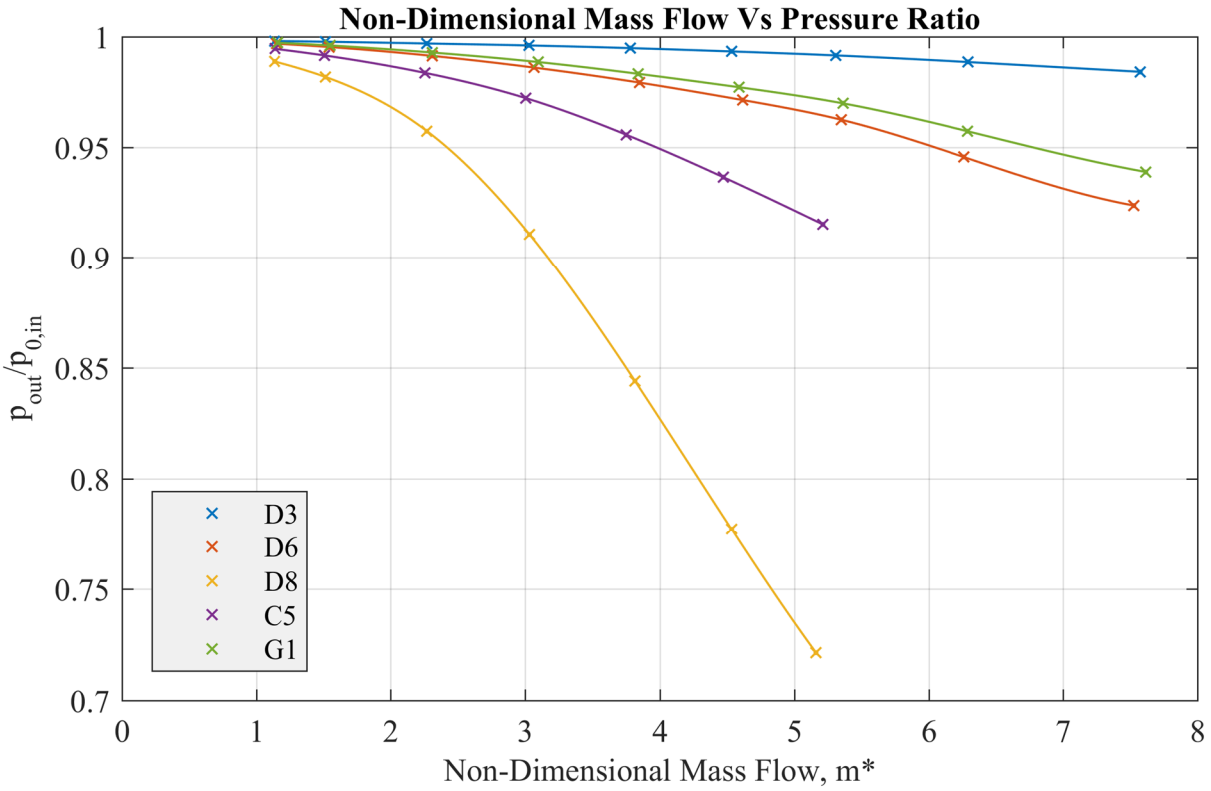


Figure 8.14 – Difference in area-averaged overall effectiveness between the impingement and film wall of each geometry as a function of m. In calculating this difference, the area of the impingement wall considered was equivalent in size and location to that of the film wall*

Figure 8.15 demonstrates the pressure ratio required to achieve a particular coolant non-dimensional mass flow rate for the five test geometries. As expected, those geometries which exhibit high porosity for both the impingement and film walls, as characterised by close non-dimensional cooling hole pitch, demonstrate significantly reduced pressure ratios required to achieve a certain coolant mass flow rate. Geometry D3, which using the decoupled conjugate method at engine conditions displayed an effective porosity (defined in equation 5.3) of near 4.5%, demonstrates a low pressure ratio requirement to achieve relatively large coolant mass flows. The least porous geometry, D8 (with an effective porosity at engine conditions of just under 0.5%) requires a significantly larger pressure ratio to achieve similar coolant mass flow rates. To permit an assessment of the feasibility of implementing these systems on a turbine blade, the pressure distribution data around a turbine blade, as demonstrated by Azad et al. [115], was used. The data presented indicated that the ratio of static pressure to inlet-total



Unit Cell Wall Porosities: D3: ϕ_i = *4.91%* & ϕ_f = *9.82%* D6: ϕ_i = *1.23%* & ϕ_f = *9.82%*

D8: ϕ_i = *0.31%* & ϕ_f = *2.45%* C5: ϕ_i = *1.57%* & ϕ_f = *3.14%* G1: ϕ_i = *1.30%* & ϕ_f = *10.39%*

Figure 8.15 - Non-dimensional mass flow against pressure ratio. Unit cell wall geometric porosities are shown at the bottom of the figure

pressure around a turbine blade at the midspan varied from near unity at the stagnation point to approximately 0.76 on the suction surface. Whilst it is appreciated that the coolant total pressure will exceed that at the leading edge of a turbine (for example due to losses in the combustor, upstream NGVs etc.), the data roughly corresponds with industrial experience.

The pressure distribution data was used for the below discussion which considers how the double-wall system may be implemented on a turbine geometry:

- The first implication of the pressure distribution data is that, in its most optimal configuration, the geometry of the double-wall system would vary across a turbine blade depending on the external pressure distribution and specific cooling requirements. The early suction surface, for example, features a favourable pressure gradient for film cooling. Consequently, to reduce aerodynamic losses, a less porous geometry, but

featuring high internal convective cooling, may be preferable in this location. A geometry like D8 may be more suited to such a location due to the sparser array of films and reasonable internal convective cooling performance. At the leading edge and pressure side, more porous geometries with a high effusion cooling effect may be more suitable.

- Methods to control internal coolant pressure may also be an alternative way to control coolant mass flow rate, particularly in the more porous geometries which still exhibit relatively high cooling effectiveness at low m^*.

The varying gradient of the pressure ratio curves are explained with reference to the discharge coefficients which are presented in Figure 8.16 where they are plotted against impingement jet Reynolds number for the five test geometries. Note, ideal mass flow rate has been calculated using the film hole cross-sectional flow area.

The general form of the discharge coefficient curves demonstrate an increasing discharge coefficient up until an impingement jet Reynolds number of approximately 25,000. Two reasons are hypothesised for this initial increase. The first is the size of the effective flow area through the impingement hole which, at lower Re_i (and pressure ratio) is anticipated to be increasing. This effect decreases as Re_i is further increased. It is also suggested that a similar effect to that characterised by the Moody diagram for pipe flow may be occurring, in which a decrease in friction coefficient is observed with increasing Reynolds number becoming asymptotic depending on the relative surface roughness. For the most porous of the tested geometries, D3, the impingement jet Reynolds numbers do not exceed approximately 17,000 and start off in the transitional flow regime. Consequently, a relatively wide range of discharge coefficients are displayed for this geometry for the mass flows tested. Across the other geometries, impingement jet Reynolds numbers exceed 25,000 at some of the coolant flow rates tested. The discharge coefficient reduces slightly and reaches a value which becomes relatively insensitive as Re_i is further increased. The least porous geometry which displays the highest

impingement jet Reynolds numbers shows a similar trend but exhibits a slightly larger decrease in discharge coefficient over a wider range of Re_i. Two reasons are suggested for the magnitude of the reduction in discharge coefficient observed in this geometry. The first pertains to the specific pedestal configuration in the geometry, where, Chyu et al. [11] demonstrated how

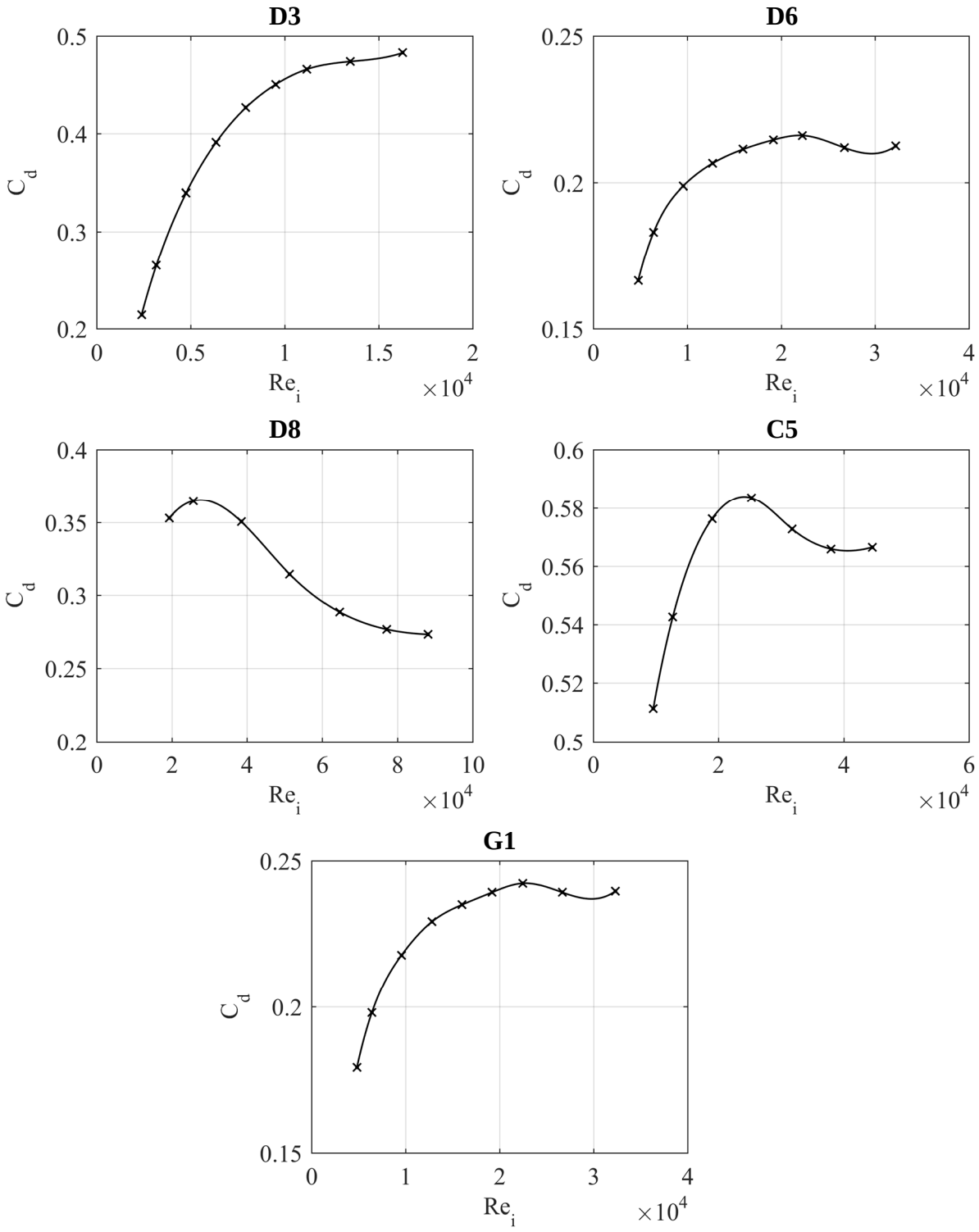


Figure 8.16 - Discharge coefficient (based on film hole diameter) against impingement Reynolds number for the five test geometries

pressure losses for various pedestal geometries in channel flow were relatively insensitive to crossflow Reynolds number but varied significantly for different pedestal configurations. Indeed, the authors demonstrated that, particularly for diamond and square pedestals, pressure losses were observed to slightly increase with Reynolds number for both staggered and inline configurations. The second reason, and that expected to be most significant here, is that the calculation of the discharge coefficient assumed incompressible flow. For all the other geometries the impingement flow velocities could be assumed incompressible and thus this assumption was valid. However, for geometry D8 which exhibited the smallest impingement wall porosity, impingement flow Mach numbers exceeded 0.3 with this first occurring at the data point for which the discharge coefficient is observed to begin dropping. Consequently, compressibility effects are expected to be the reason for the difference in the reduction in discharge coefficient observed in this current study for geometry D8.

8.3.3 Summary of Overall Effectiveness Performance

Table 8.1 provides a summary of some of the above overall effectiveness data for the five test geometries. Specifically, area-averaged overall effectiveness data for both the impingement and film walls are provided for several of the tested coolant flow rates. The table also provides geometric porosities of both the impingement and film walls of the geometries. Furthermore, two relevant area ratios are given. These are:

- The ratio of the internal coolant wetted area to external area of the unit cell (A_{int}/A_{ext}).
- The ratio of the pedestal conduction area to the external area of the unit cell (A_{cond}/A_{ext}).

The table succinctly summarises several features identified in the above discussion. In conclusion, the crenulation concept geometry, G1, shows the highest impingement and film wall overall effectiveness performance across the range of coolant mass flow rates tested. As clearly demonstrated in the table, the geometry exhibited the highest film wall porosity (ϕ_f).

Consequently, film blowing ratios were among the lowest exhibited by the tested geometries with the result that films demonstrated minimal effects of film jet lift-off. The geometry also exhibited the highest ratios of pedestal conduction area to external surface area, and internal coolant wetted area to external surface area. The result of the former is the relatively high levels of heat conducted away from the hotter outer wall, with the result of the latter that much of this conducted heat was transferred to the coolant via convective cooling. Impingement wall porosity (ϕ_i) was comparable to a couple of the other tested geometries, although, when compared to C5, the hole diameter (D_i) was smaller and therefore levels of Re_i were increased.

Table 8.1 – Summary of experimental area-averaged overall effectiveness data for the five test geometries at several coolant mass flow rates. The data includes the unit cell geometric porosities for the impingement and film walls, along with the ratios of internal-to-external wetted area and pedestal conduction-to-external wetted area

Geometry		$m^* \approx 1.15$		$m^* \approx 2.30$		$m^* \approx 3.80$		$m^* \approx 5.25$		$m^* \approx 7.60$	
		$\varepsilon_{o,i}$	$\varepsilon_{o,f}$	$\varepsilon_{o,i}$	$\varepsilon_{o,f}$	$\varepsilon_{o,i}$	$\varepsilon_{o,f}$	$\varepsilon_{o,i}$	$\varepsilon_{o,f}$	$\varepsilon_{o,i}$	$\varepsilon_{o,f}$
D3	$\phi_i = 4.91\%$ $\phi_f = 9.82\%$ $A_{int}/A_{ext} = 4.25$ $A_{cond}/A_{ext} = 0.24$	0.62	0.46	0.76	0.59	0.84	0.67	0.88	0.71	0.91	0.73
D6	$\phi_i = 1.23\%$ $\phi_f = 9.82\%$ $A_{int}/A_{ext} = 6.16$ $A_{cond}/A_{ext} = 0.24$	0.73	0.44	0.85	0.60	0.91	0.70	0.93	0.75	0.95	0.77
D8	$\phi_i = 0.31\%$ $\phi_f = 2.45\%$ $A_{int}/A_{ext} = 3.73$ $A_{cond}/A_{ext} = 0.06$	0.69	0.38	0.81	0.50	0.88	0.58	0.91	0.61	-	-
C5	$\phi_i = 1.57\%$ $\phi_f = 3.14\%$ $A_{int}/A_{ext} = 3.52$ $A_{cond}/A_{ext} = 0.22$	0.65	0.47	0.76	0.56	0.83	0.61	0.86	0.64	-	-
G1	$\phi_i = 1.30\%$ $\phi_f = 10.39\%$ $A_{int}/A_{ext} = 8.06$ $A_{cond}/A_{ext} = 0.27$	0.73	0.50	0.85	0.64	0.91	0.73	0.94	0.78	0.96	0.81

8.3.4 Experimental Uncertainties

The experimental uncertainty in the measured overall effectiveness and non-dimensional mass flow quantities were calculated for each experimental run using the root-sum-squares method described in Chapter 7.

The uncertainty in overall effectiveness was calculated on a pixel-by-pixel basis for both the impingement and film wall data and consequently, contours were produced showing the variation in absolute overall effectiveness uncertainty across the monitored test piece surfaces. Figure 8.18 demonstrates these contours over the film wall for the minimum and maximum coolant flow rate cases for each geometry. In general, absolute overall effectiveness uncertainty varied between 0.045 – 0.053 with the main contribution to uncertainty arising from the relatively large uncertainty quoted for the cameras of ±2.0 K. Due to the updated, in-house calibration it is anticipated that the experimental uncertainty may be lower. For the current work, this wasn't quantified and as such the default manufacturer value was used in the presented uncertainty calculations which is expected to provide a worst-case prediction of measurement uncertainty. However, quantifying whether the updated in-house calibration does result in a reduced IR temperature measurement uncertainty is a potential topic for future work. As an indication to the reader, an uncertainty in camera temperature of ±1.0 K reduced overall effectiveness uncertainties by around 35% relative to those obtained using the manufacturer quoted value.

The contours in Figure 8.18 demonstrate that, as expected, colder regions of the test geometry were associated with a larger measurement uncertainty. For geometries D3, D6 and G1 which exhibited the largest reduction in temperatures across the mass flows tested, higher overall cooling effectiveness uncertainties were displayed at increased coolant flow rates as metal temperatures correspondingly decreased. For geometries D8 and C5, higher coolant mass flows demonstrated a fractionally reduced overall effectiveness uncertainty. This was the result of a small increase in mainstream temperatures during the experimental runs.

Figure 8.17 demonstrates the uncertainties in both non-dimensional coolant mass flow and area-averaged overall effectiveness for both the impingement and film walls of each geometry at each coolant flow rate. It is apparent that the overall effectiveness uncertainty is dominant with only a very small uncertainty arising from the coolant mass flow measurement (due to the small uncertainty in the calibrated pressure sensor reading). Indeed, absolute uncertainties in m^* varied between 0.013 – 0.047, with the higher values exhibited for the larger diameter CFVN.

8.4 Summary

This chapter has presented data obtained from the commissioned recirculating facility during overall effectiveness experimental runs. Five double-wall geometries were selected for manufacture and testing with the choice based on the findings of the decoupled conjugate method presented in Chapter 5. These were three diamond pedestal geometries (D3, D6 and D8), one circular pedestal geometry (C5), and the crenulation concept (G1).

High resolution overall effectiveness contours are presented for the five test geometries at a range of coolant mass flows (presented using non-dimensional mass flow, m^*). Both the external surfaces of the film and impingement walls were monitored, with overall effectiveness data presented for each surface. Area-weighted averaged overall effectiveness against non-dimensional coolant mass flow plots are presented for the geometries permitting an assessment of the geometrical features that resulted in preferable cooling performance. In general, the trends agreed well with the preliminary aerothermal assessment made using the decoupled conjugate method (with more detailed comparisons between the computational methods and experimental results presented in Chapter 10). Tests were repeated on separate days with processed, area-averaged overall effectiveness showing less than a 0.01 variation from the results presented, thus demonstrating the high repeatability of the tests and providing confidence in the data obtained from the facility.

Aerodynamic data was also presented for the geometries. In particular, the variation in pressure ratio required to achieve a particular coolant flow rate was measured. The information is essential for integration of these systems into different locations on a turbine blade. The data showed, for example, that lower film wall porosity would most likely be needed on the suction side. The variation in discharge coefficient for each geometry is also presented at varying impingement jet Reynolds numbers where, generally, peak discharge coefficients occurred at impingement jet Reynolds numbers of around 25,000. At higher Reynolds numbers, a small reduction in discharge coefficient was observed and at still higher Re_i the discharge coefficient became relatively insensitive to Reynolds number.

Experimental uncertainties were also calculated for the derived coolant mass flows and overall effectiveness values. The uncertainty in coolant mass flow is relatively small with the uncertainty in overall effectiveness being more significant – largely arising from the uncertainty in the infrared camera measurement. The local variation in absolute overall effectiveness uncertainty is presented for all five geometries at the minimum and maximum coolant flow rates demonstrating the slightly increased uncertainty in the cooler regions of the double-wall geometry (for example in the location of the films).

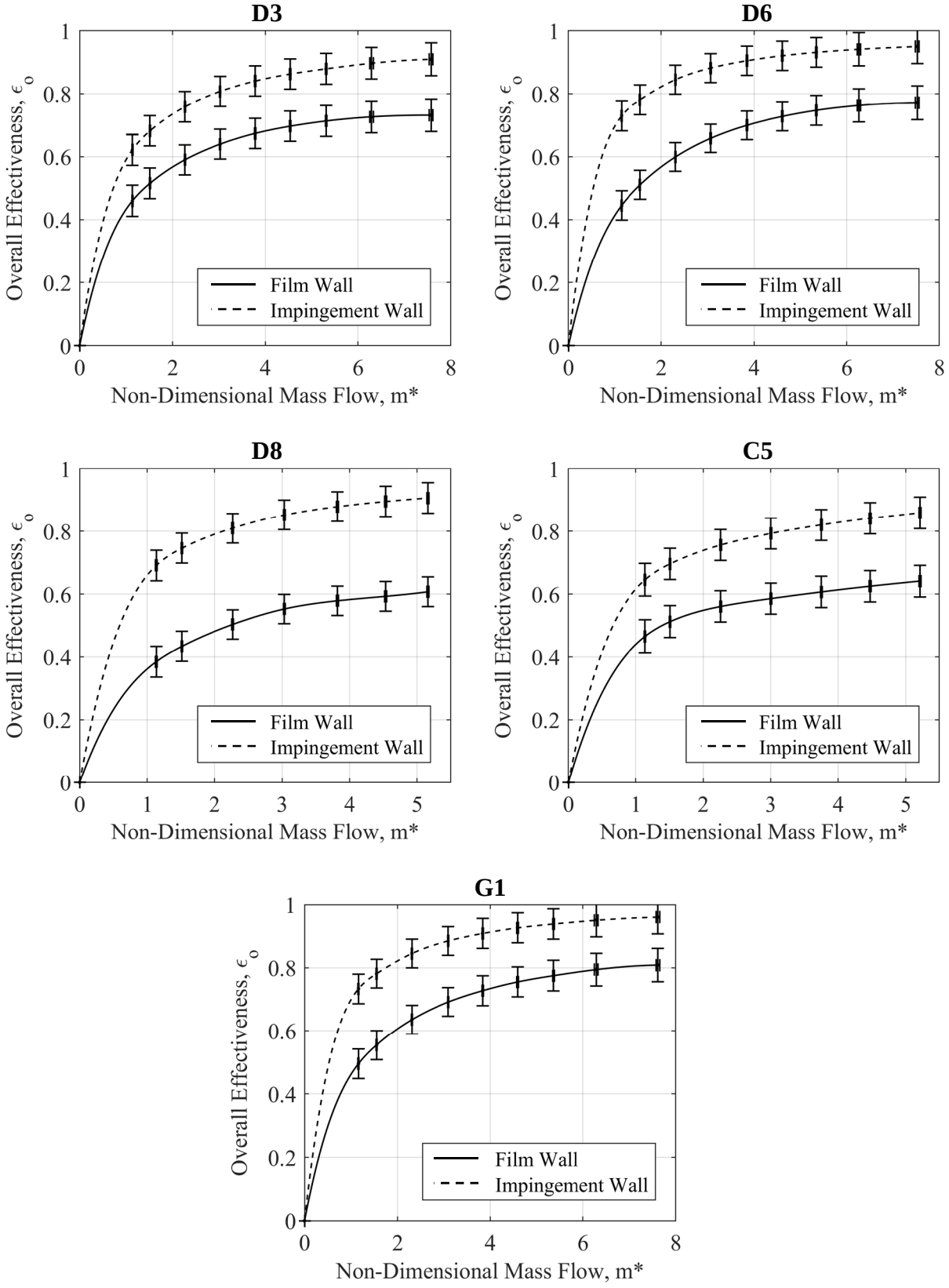


Figure 8.17 - Area-weighted averaged experimental overall effectiveness vs non-dimensional mass flow for both the film and impingement walls of all five test geometries along with the associated measurement uncertainties at each data point

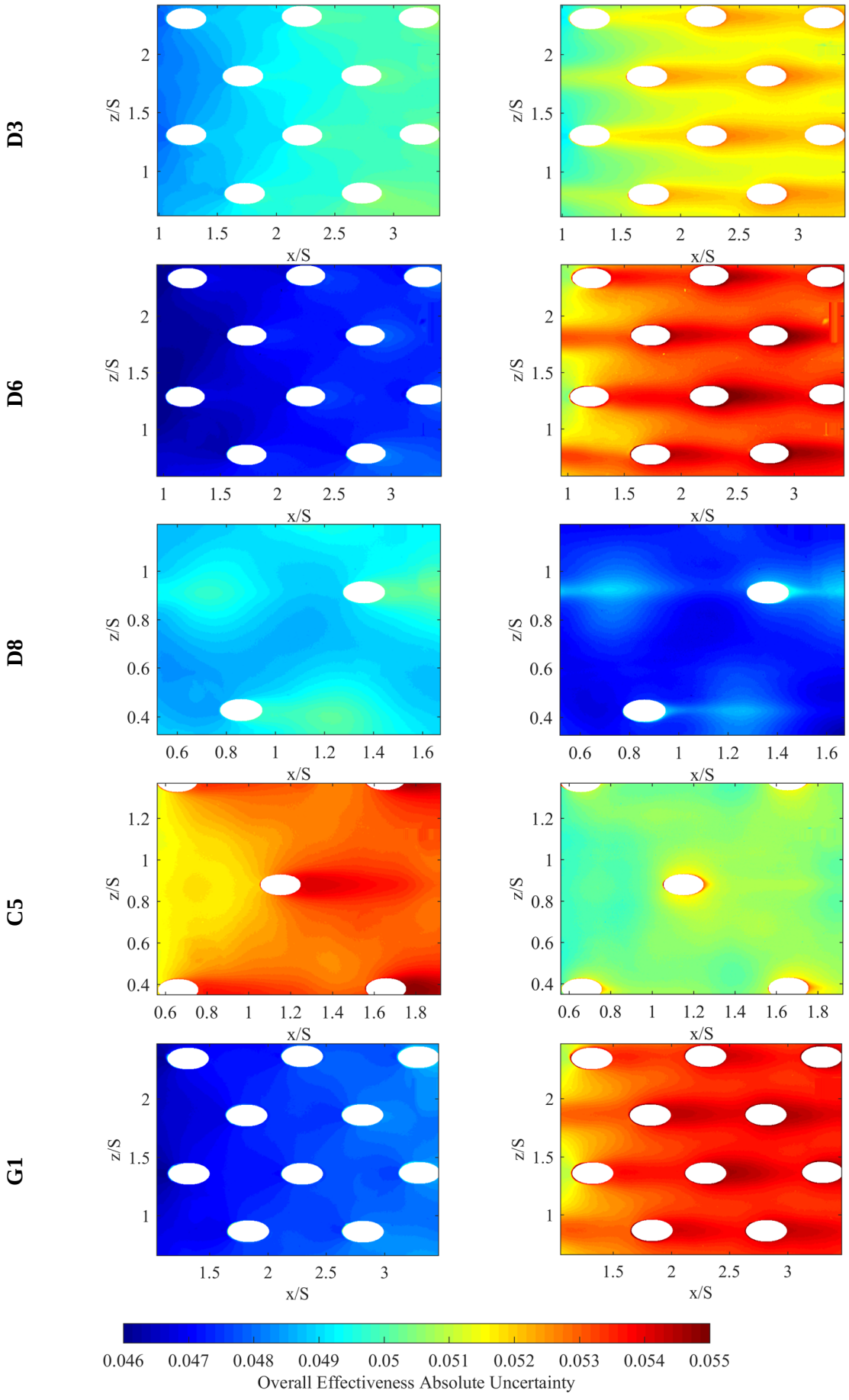


Figure 8.18 - Absolute uncertainty in the film wall experimental overall effectiveness contours for the lowest and highest coolant mass flow rate cases for each of the five test geometries

9 Results – Film Effectiveness and Internal Convective Cooling Measurements

9.1 Chapter Overview

This chapter presents steady-state, adiabatic film effectiveness measurements obtained from the experimental facility for the five double-wall test geometries (D3, D6, D8, C5 and G1). As for the data in Chapter 8, the thermal measurements were obtained using IR thermography. The data was used in quantifying the effusion cooling performance for the different geometries. Additionally, through an analytical model, the previously presented overall effectiveness measurements are combined with the adiabatic film effectiveness measurements presented here to ascertain the internal convective cooling efficiency of each double-wall geometry at varying non-dimensional mass flows. Consequently, the overall cooling effectiveness is separated into contributions arising from both the internal convective, and external film cooling, performance.

9.2 Processing

As was the case for the overall effectiveness experiments, the tunnel and coolant flow rates were set to provide Reynolds number similarity to engine conditions for both the mainstream flow ($Re_\infty \sim 25000$) and impingement jets ($2400 < Re_i < 52000$). For all the geometries, maximum coolant mass flow was capped due to the reduced structural integrity of the low conductivity hybrid PLA/Rohacell® test pieces (see Appendix D) used for the film effectiveness measurements. Rohacell® has been used previously for film cooling studies (see for example [47], [116], [117]) on account of the low value of thermal conductivity and thus the approximation that it is adiabatic. The mainstream-to-coolant temperature ratio was, again, set

to approximately 1.25. The following thermal results are presented against either non-dimensional mass flow (where the value of heat transfer coefficient is that obtained using equation 8.1), or film blowing ratio. Local mainstream gas temperature measurements based on the five ceramically sheathed thermocouples were used in the calculation of the film effectiveness.

9.3 Results

The following section provides a comprehensive collection of experimental data obtained during the film effectiveness tests or calculated using data from both the film effectiveness and overall effectiveness experimental runs. Some of the data obtained are summarised below:

- Figures 9.2 – 9.6 show processed adiabatic film effectiveness contours on the film wall for all five test geometries at varying film blowing ratios.

- Figure 9.7 shows spanwise-averaged film effectiveness (averaged across one primary film hole pitch for geometries D3, D6, C5 and G1, and half pitch for D8 as a whole pitch was not visible in the camera field of view). The spanwise-averaged data was provided for various blowing ratios.

- Figure 9.8 demonstrates the internal convective efficiency for each geometry at varying non-dimensional mass flows. The convective efficiency was calculated based on an analytical model using the area-averaged overall effectiveness and film effectiveness achieved at a particular non-dimensional mass flow.

- Figure 9.10 presents a contour showing an example of the absolute uncertainty in measured film effectiveness.

- Figure 9.11 shows the area-averaged overall effectiveness and film effectiveness achieved on the film wall at varying non-dimensional mass flows. The overall

effectiveness contribution arising from internal convection alone (i.e. excluding the effect of films) is also plotted based upon the aforementioned analytical model.

9.3.1 Film Effectiveness

Film effectiveness contours at a range of blowing ratios are shown for geometries D3 and D6 in Figures 9.2 and 9.3. Both geometries exhibited the highest film wall porosity from among the diamond pedestal geometries (9.82%), and consequently demonstrated low film blowing ratios across the range of m^* investigated agreeing well with the findings presented for the decoupled conjugate method in Chapter 5. This results in films that exhibit minimal film jet lift-off and are well adhered to the film cooled surface at high values of m^*. It is noted that a consequence of this is that optimal film blowing ratios are only achieved at higher coolant flow rates.

For geometries D3 and D6, film hole non-dimensional pitch was 5.66 between the primary film holes. Whilst, as previously demonstrated in Chapter 3, this pitch still has a relatively low lateral film interaction for circular, streamwise inclined holes, the streamwise film development is reasonably high. Indeed, this is confirmed by the spanwise-averaged film effectiveness plots in Figure 9.7 across the range of blowing ratios investigated for the two geometries. Both the contours and spanwise-averaged film effectiveness plots also indicate that both geometries exhibit very similar film cooling performance at comparable values of blowing ratio. This indicates that, for these flat plate geometries where the variation in external surface static pressure is small and internal crossflow effects are minimal, the film cooling performance is insensitive to the specific internal pedestal configuration (assuming pedestals are positioned sufficiently far from the film hole inlet). The spanwise-averaged plots also indicated that the benefit of increasing blowing ratio was reducing up to the maximum blowing ratio tested of 0.38. This is in keeping with the findings presented in Chapter 3 where optimal films for

effusion geometries with this pitch were observed to occur at blowing ratios of near 0.5 with only small changes in film effectiveness observed around this optimal blowing ratio value.

The performance of the crenulation concept geometry, G1, is also relatively similar to those of D3 and D6. This geometry had a slightly closer pitching of film holes (P = 5.5), and this is reflected by the small benefit in spanwise-averaged film effectiveness at similar blowing ratios (as shown in Figure 9.7). Slightly greater lateral film interactions are also observable in the contours demonstrated in Figure 9.6. Once again, this supports the hypothesis that the film performance is relatively insensitive to internal geometry given the vastly different pedestal layer configuration in geometry G1.

Geometry C5 exhibited a larger primary film hole non-dimensional pitch of 10. The result is the increased blowing ratios achieved at similar m^*. Consequently, as demonstrated in Figure 9.5, the effect of jet lift-off was observed at higher coolant mass flows. Indeed, a very visible decrease in film jet lateral spreading is observed for blowing ratios above approximately 0.8. This is also captured in the spanwise-averaged plots which indicate that between blowing ratios of 0.5 – 0.8, peak film effectiveness values after each film hole were similar, but the streamwise decay in effectiveness is accelerated at the higher blowing ratios. Above blowing ratios of 0.8, both the peak in film effectiveness reduces, and film decay rate further increased.

A similar trend was anticipated for geometry D8 which had a further elevated film hole non-dimensional pitch of 11.32. However, as demonstrated by the spanwise-averaged film effectiveness plots for the geometry, film effectiveness appears to increase as blowing ratio is raised (with a maximum of 0.86 tested). Also unexpected is the reduction in spanwise-averaged effectiveness in the streamwise direction. Although the film hole pitching has been increased, a small streamwise film development was anticipated. Both these trends are explained with reference to the film effectiveness contours in Figure 9.4. The contours demonstrate that, as blowing ratio (and m^*) is elevated, there is an apparent increase in film effectiveness away from the films (i.e. the dark red of the contour demonstrating no film effectiveness at lower blowing

ratios is now light red/orange). This is not thought to result from the effect of film cooling attributed to a film cooling jet. Rather, it is suggested to result from the significantly larger plenum pressures required to achieve these higher coolant flow rates (see Figure 8.14 in Chapter 8). It is expected that the large pressure drop across the test piece resulted in a leakage of flow from the plenum around the edge of the test piece rather than through the impingement holes. Whilst every effort was made to seal the geometry, it is anticipated that, in this case, the sealing may have failed.

In general, the assumption that the hybrid PLA/Rohacell® test pieces are adiabatic appears to be valid. There is only a very small conduction region around the film holes, and indeed, during testing, the response of the surface to variations in coolant mass flow were immediate. Additionally, the impingement wall temperatures scarcely deviated from that of the coolant plenum indicating minimal conduction from the external surface of the film wall to the impingement wall. An effectiveness contour for the impingement surface of C5 is demonstrated in Figure 9.1. This is assumed to be the worst-case given the high conduction area between the film and impingement walls, along with this contour being for the lowest coolant flow rate case. What is observed is an effectiveness of near unity across the whole surface which indicates the surface temperature is the same as the coolant thereby confirming the assumption that the test piece is indeed near adiabatic.

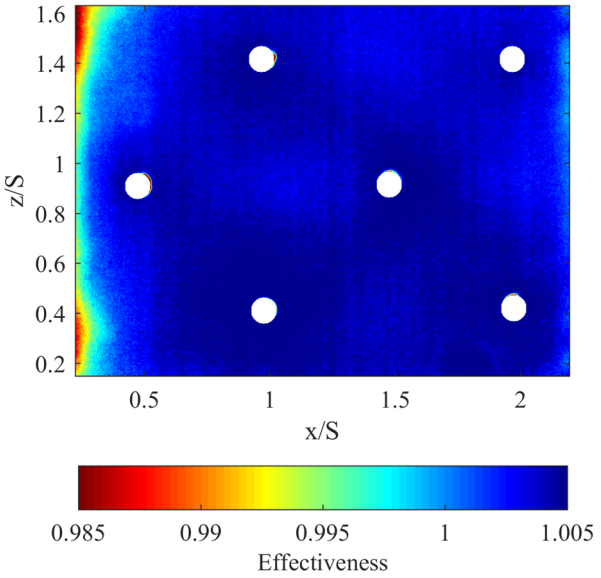


Figure 9.1 - Impingement wall cooling effectiveness for the assumed adiabatic test piece for geometry C5 at the lowest coolant flow rate

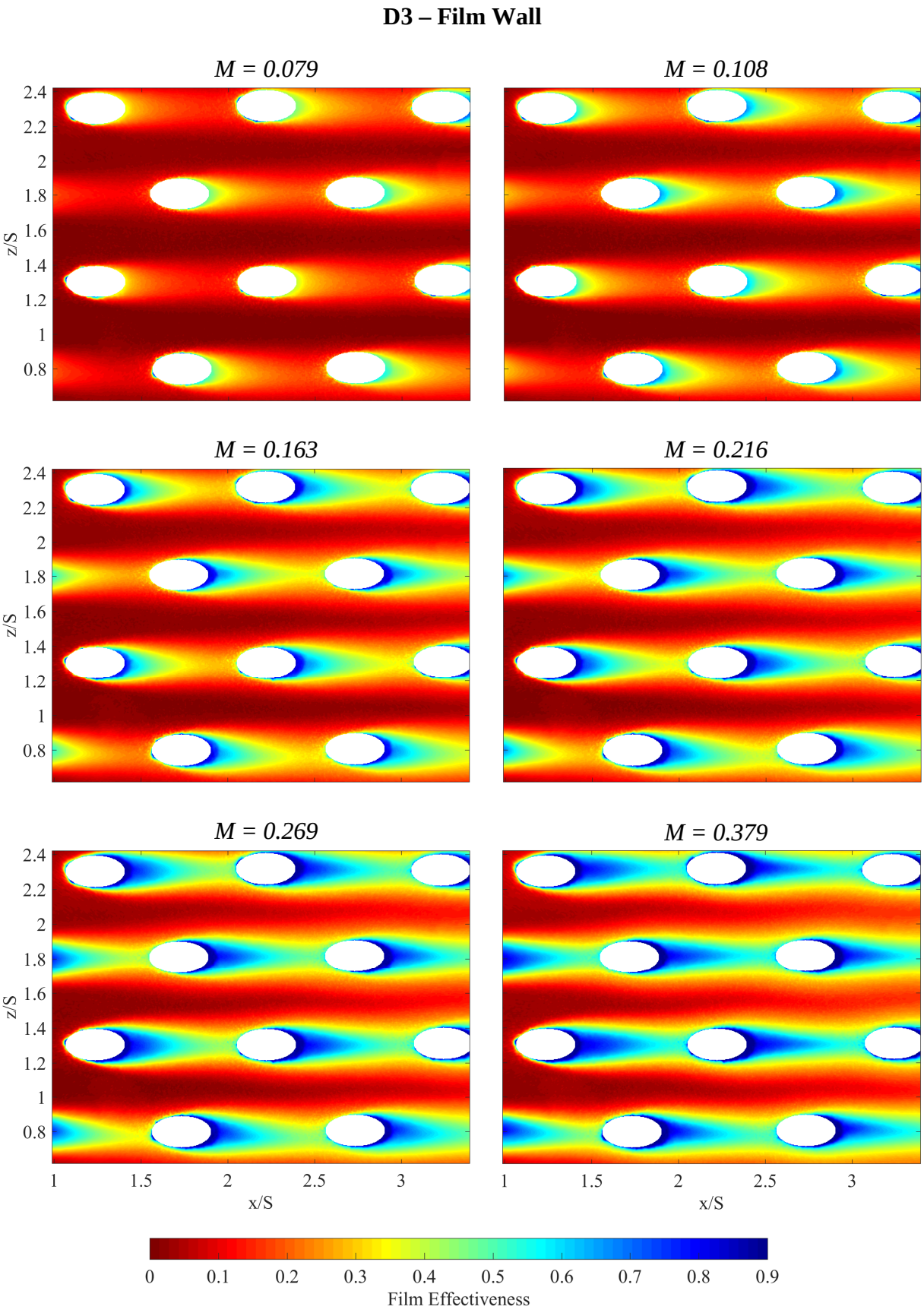


Figure 9.2 - Experimental film effectiveness contours for geometry D3 showing the external surface of the film wall at various film blowing ratios

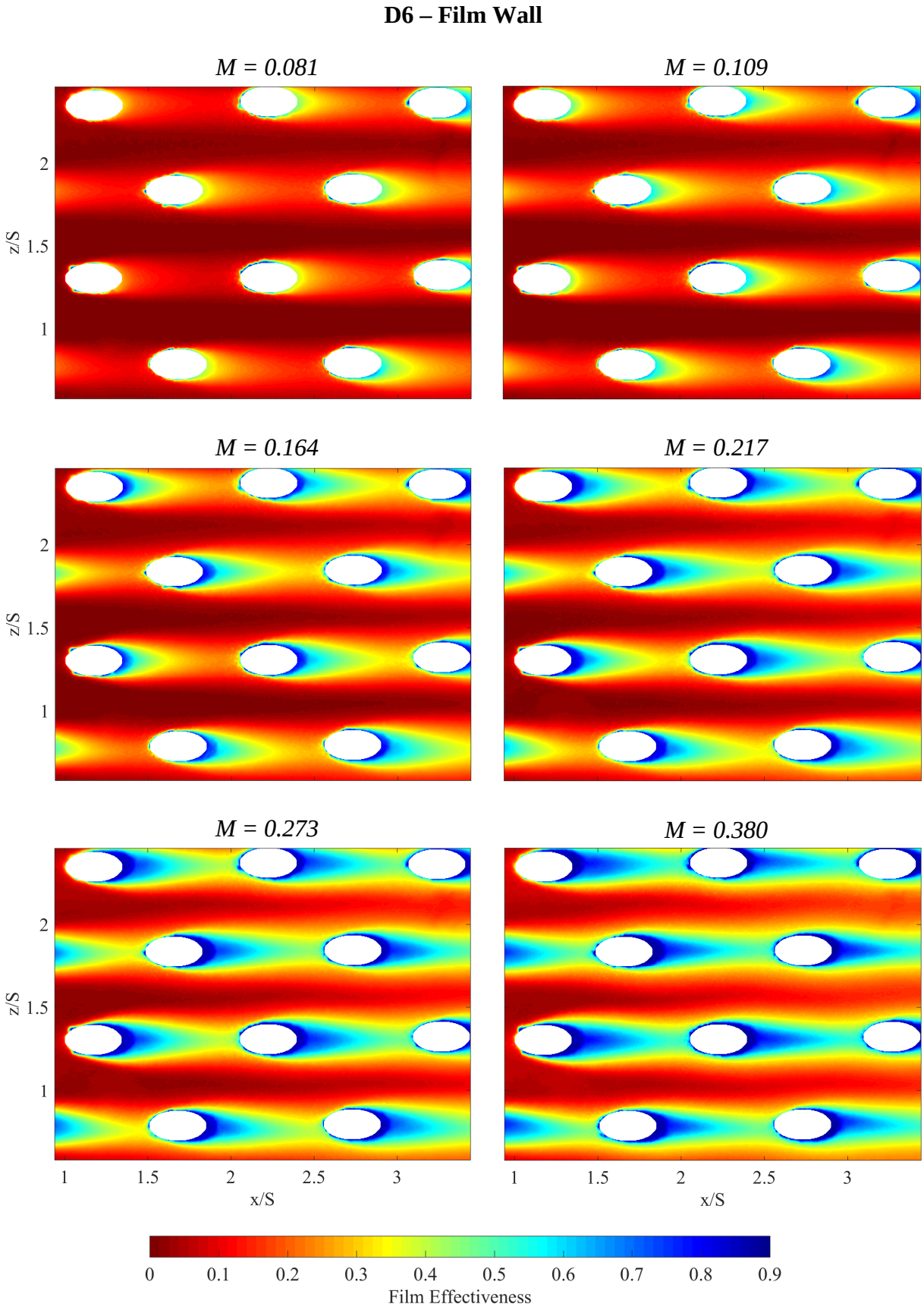


Figure 9.3 - Experimental film effectiveness contours for geometry D6 showing the external surface of the film wall at various film blowing ratios

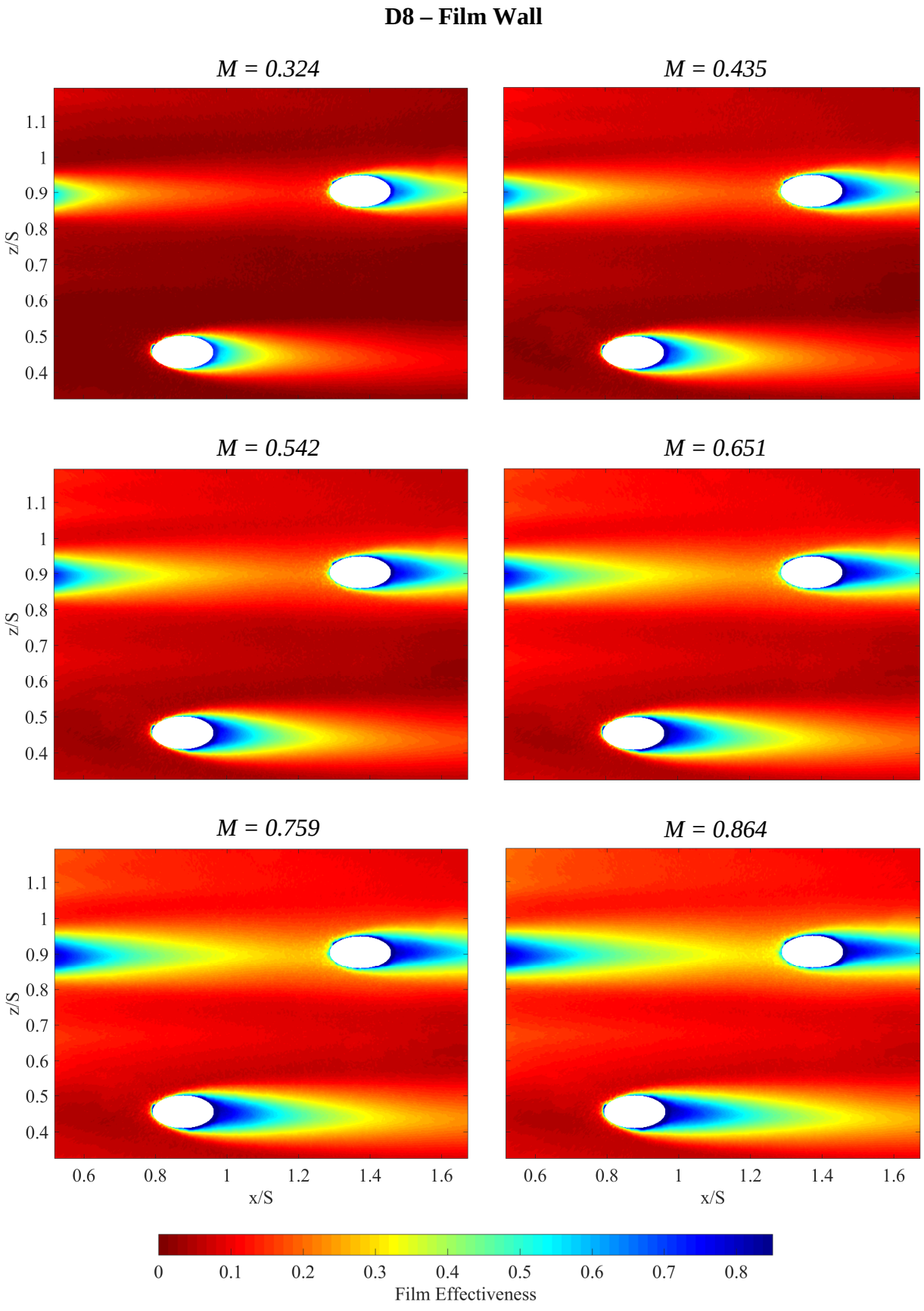


Figure 9.4 - Experimental film effectiveness contours for geometry D8 showing the external surface of the film wall at various film blowing ratios

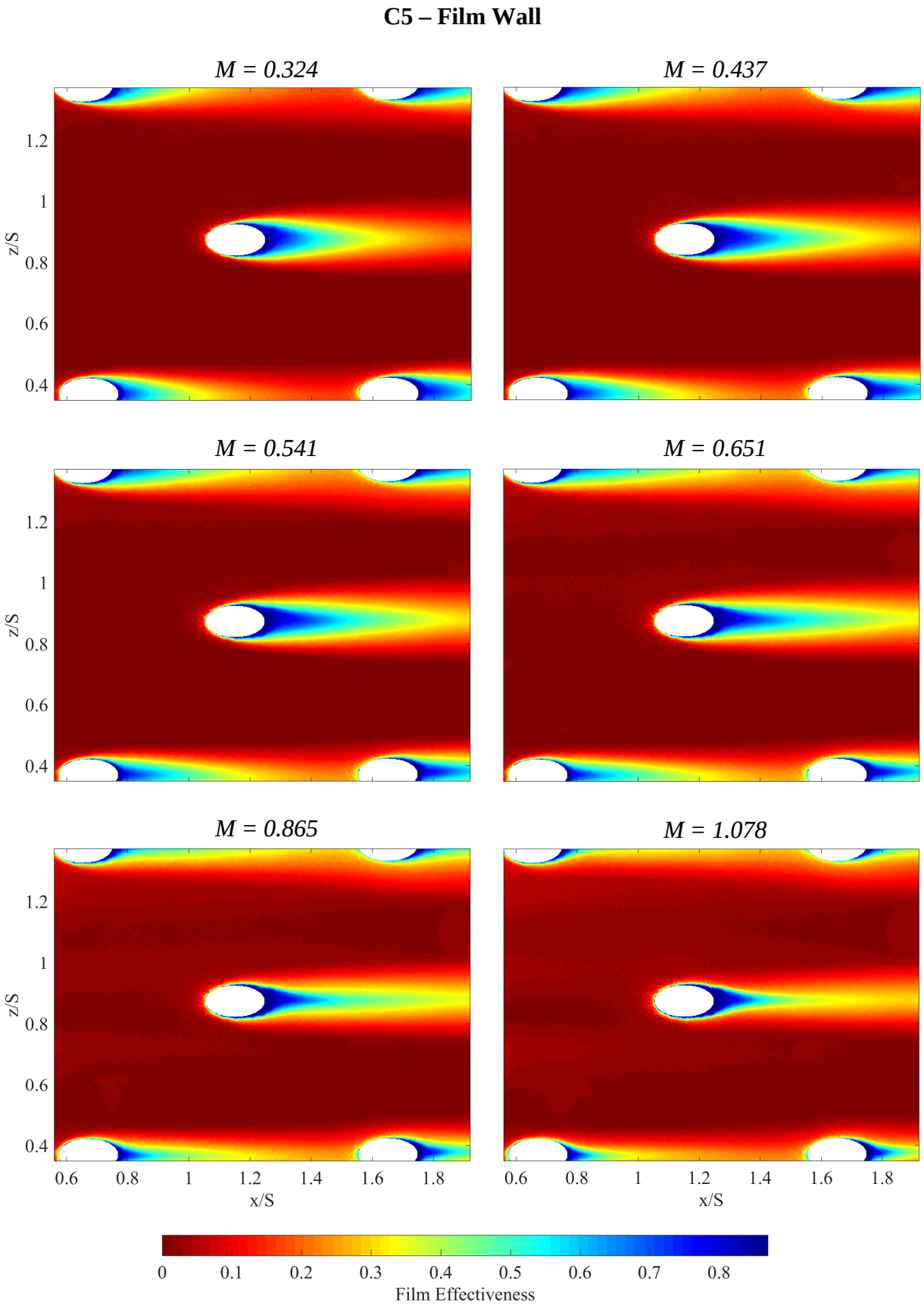


Figure 9.5 - Experimental film effectiveness contours for geometry C5 showing the external surface of the film wall at various film blowing ratios

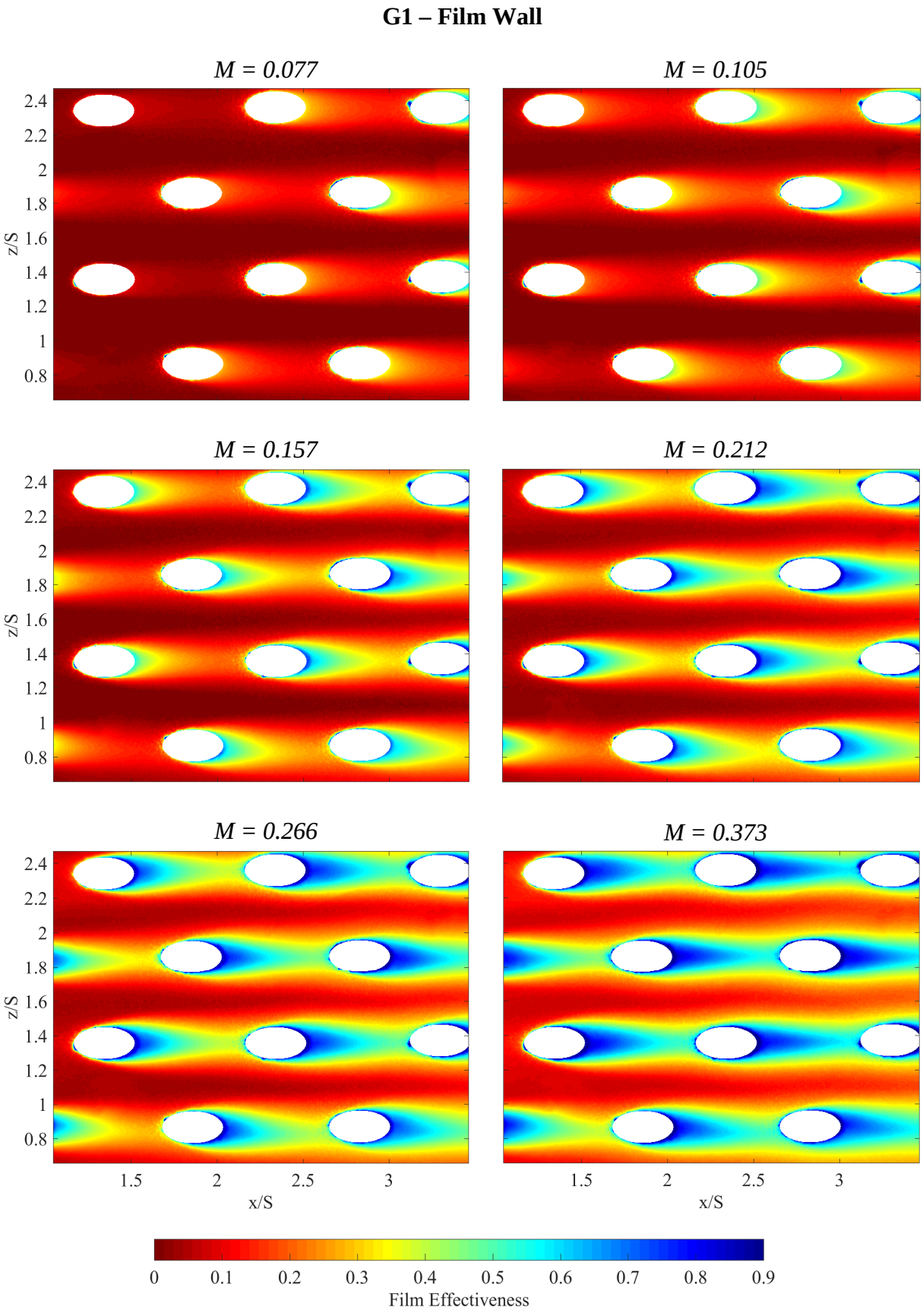


Figure 9.6 - Experimental film effectiveness contours for geometry G1 showing the external surface of the film wall at various film blowing ratios

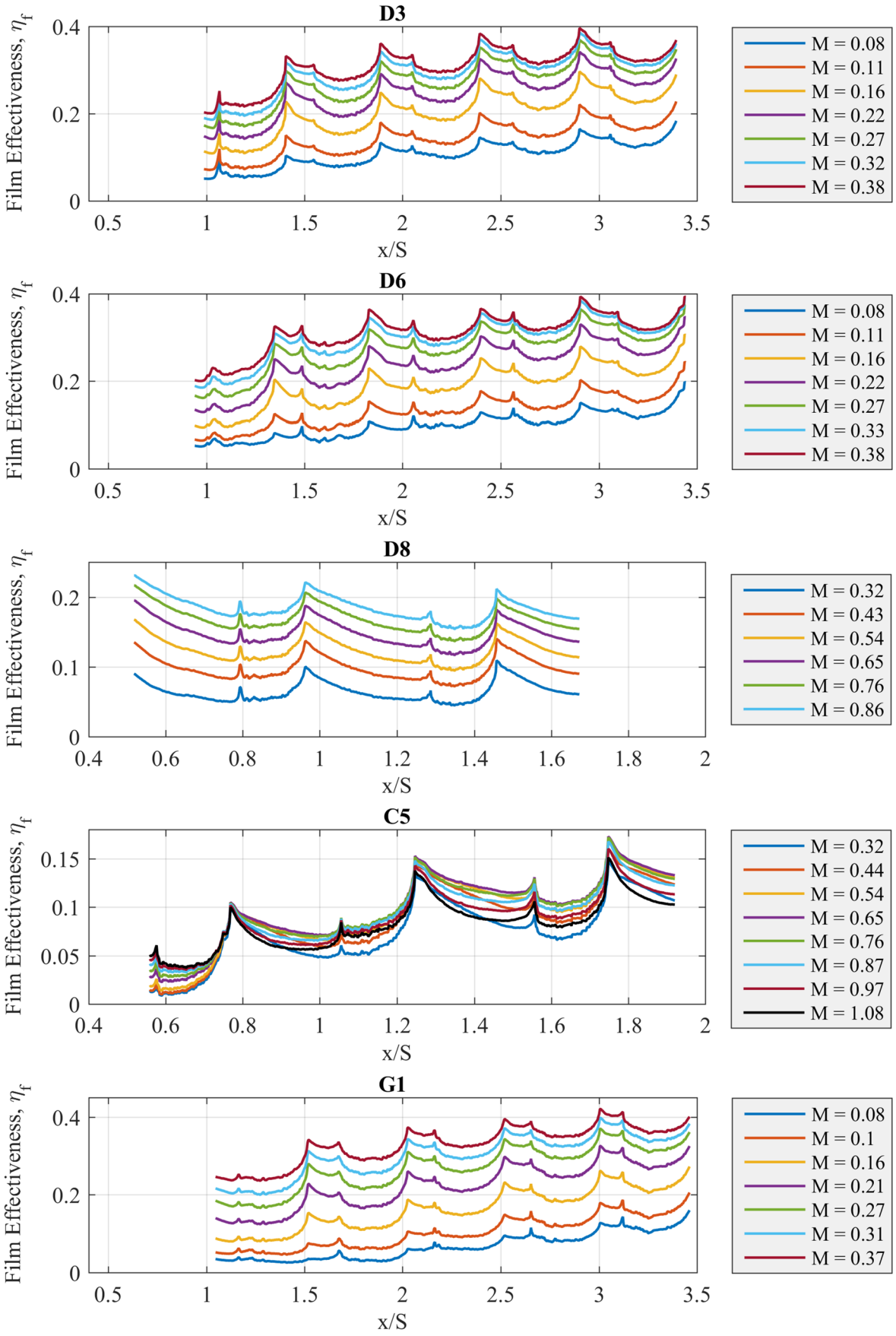


Figure 9.7 – Spanwise-averaged film effectiveness (averaged across two primary holes) against streamwise distance at various blowing ratios for the five test geometries

9.3.2 Convective Efficiency

It is useful to be able to separate the overall cooling effectiveness contributions arising from internal convection and external film cooling performance for the double-wall systems – something achieved directly in the decoupled conjugate method developed (see Chapter 5). Knowledge of such information, along with pressure ratios required to achieve a certain coolant mass flow, help dictate what double-wall geometry may be best suited to different regions of a turbine blade. Additionally, such information may be useful in predicting blade lifing in the eventuality that film hole blockage occurs.

Whilst there is no simple way to directly measure the internal convective efficiency of the double-wall geometries, simplified models can be developed to predict the overall cooling effectiveness achieved based on a certain internal convective efficiency at a particular coolant mass flow rate, or indeed, obtain the convective efficiency based on a measured overall effectiveness. The derivation of such a simplified model for a convectively cooled isothermal blade subjected to uniform external conditions is demonstrated in Appendix A with the result repeated in equation 9.1.

$$\varepsilon_o = \frac{m^* \eta_c}{1 + m^* \eta_c} \tag{9.1}$$

Holland and Thake [118] demonstrated how such a model could be adapted to also account for a blade cooled via both internal convection and external film cooling with the result repeated in equation 9.2.

$$\varepsilon_o = \frac{m^* \eta_c + \eta_f (1 - \eta_c)}{1 + (m^* - \eta_f)\eta_c} \tag{9.2}$$

Equation 9.2 can be rearranged to make convective efficiency the subject of the equation yielding equation 9.3. Consequently, with knowledge of the overall effectiveness, film

effectiveness and non-dimensional mass flow, the convective efficiency of a particular double-wall geometry can be predicted. With the convective efficiency calculated, this can be used – along with the non-dimensional mass flow – to calculate an approximate overall cooling effectiveness arising from internal convective cooling alone using equation 9.1.

$$\eta_c = \frac{\varepsilon_o - \eta_f}{m^* - \eta_f - \varepsilon_o(m^* - \eta_f)} \tag{9.3}$$

Figure 9.8 demonstrates the convective efficiencies of the five test geometries as calculated using equation 9.3. It is noted that area-weighted averaged experimental overall and film effectiveness values over the film wall were used in calculation of this convective efficiency.

As expected, the general form of the plots indicate a decrease in convective efficiency as mass flow – and consequently coolant velocity – is increased. As hypothesised in the previous chapter, geometry G1 displays a high cooling effectiveness – a likely consequence of the impingement-to-target plate spacing being maintained whilst internal surface area is

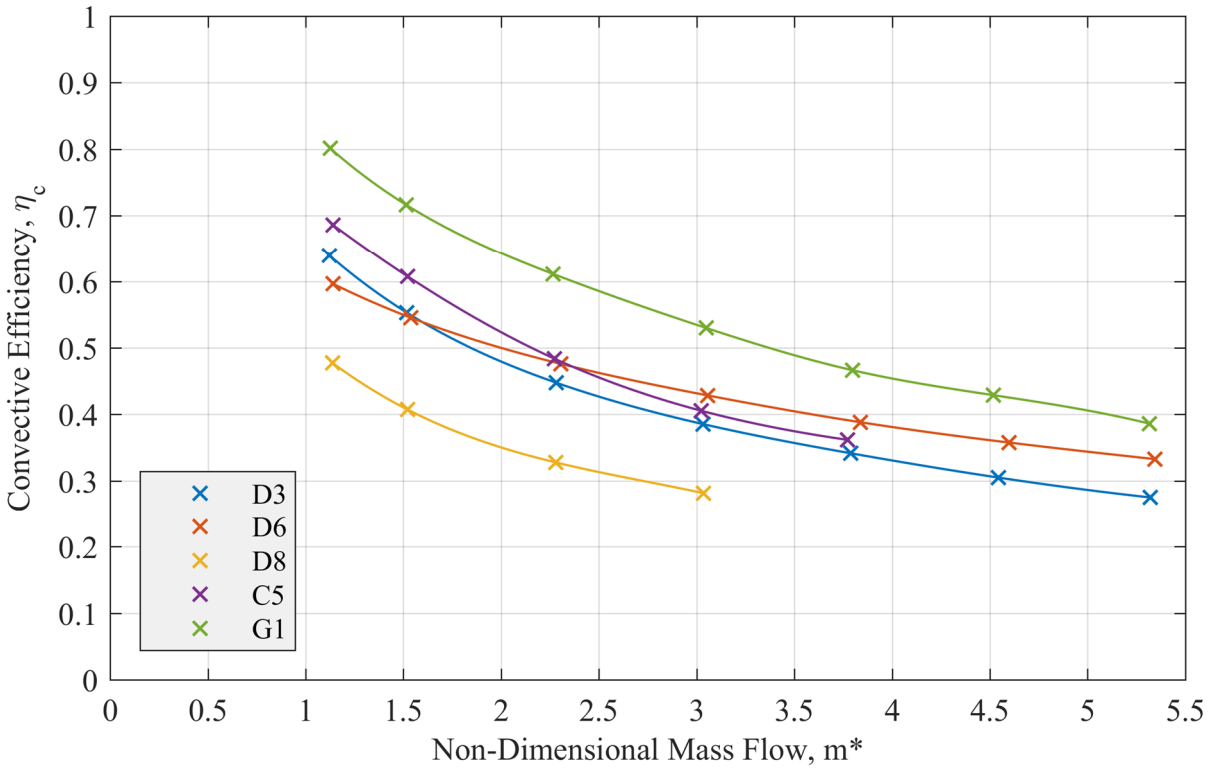


Figure 9.8 - Estimated convective efficiency of the five test geometries based on the film wall, area-weighted averaged overall effectiveness and film effectiveness

significantly increased compared to the other geometries. Geometry D8, on the other hand, displays much lower convective efficiency due to the very sparse array of pedestals and resulting low coolant wetted area. Additionally, whilst each individual impingement cooling jet causes a very large local increase in heat transfer coefficients, they have a very high pitch (P_i = 22.64 between primary impingement holes) and consequently they are sparse. Whilst the specific internal geometries of D3 and C5 are very different, the convective efficiencies achieved in each are similar. Thus, disregarding the effect of cooling films, the internal convective performance of these geometries would be similar. Geometry D6 is similar in make-up to D3, although it has a much larger passage height and achieves higher impingement jet Reynolds numbers at the same coolant flow rate. At low coolant mass flows, geometry D3 achieves a higher convective efficiency. At these mass flows the impingement cooling effect in both geometries would be low. As coolant m^* exceeds 1.5, however, the convective efficiency of geometry D6 quickly exceeds that of D3. This is a likely result of both the increased coolant wetted area, and superior impingement cooling effect achieved in D6.

It is noted that the decrease in convective efficiencies with mass flow demonstrated in Figure 9.8 are slightly faster than might be anticipated. This is thought to arise due to Biot number effects (i.e. a non-uniform solid temperature profile) as equations 9.1 – 9.3 are based on the assumption of an isothermal blade.

To further explore the cooling contributions arising from both the internal convective cooling and external film cooling in each of the double-wall geometries, the experimental overall effectiveness and film effectiveness achieved on the film wall, is plotted against m^* in Figure 9.11. Additionally, included in the figure is the predicted overall effectiveness achieved in each geometry based on internal convective cooling alone, as calculated using equations 9.1 and 9.3.

As previously mentioned, the film cooling performance achieved in geometries D3 and D6 is very similar. Figure 9.11 shows that at lower coolant mass flows, the films result in only a

very small additional increase in overall effectiveness over that attributed to internal convective cooling alone. This is because the films are operating at a very low blowing ratio and consequently display reasonably poor film effectiveness. However, as m^* is increased, the films begin to near their optimal operating point. Consequently, at these higher mass flows the films are responsible for an additional absolute increase in overall effectiveness of approximately 0.12. However, the cooling performance due to internal convection alone is still encouraging.

Geometry D8 appears to display relatively poor cooling performance due to internal convection alone, which is in agreement with the data presented in Figure 9.8. However, it is noted that, as previously discussed, the film effectiveness measurements for the geometry at high m^* (and blowing ratio) are thought to be erroneous and overpredicting film performance. Indeed, in Figure 9.11, area-averaged film effectiveness is seen to be increasing for all mass flows shown. It was, however, expected that the film effectiveness would have begun to decrease by an m^* of approximately 2.0 – 2.5. Consequently, the overall effectiveness contribution arising from internal convection alone is expected to be greater than that demonstrated in the figure.

Geometry C5 demonstrates a relatively high overall effectiveness achieved by internal convection alone and is comparable with those exhibited by geometries D3 and D6. Consequently, it is suggested that such a geometry may be particularly suited to the mid-chord region of the suction side of a turbine blade where sparse films may be beneficial from an aerodynamic loss perspective, whilst high internal convective cooling is still desirable. The geometry demonstrates the reduction in film effectiveness at higher non-dimensional mass flows arising from film jet lift-off and this is a similar trend to that which was expected for geometry D8.

Finally, Figure 9.11 demonstrates the high cooling performance of the crenulation concept geometry, G1. The geometry displays the highest internal convective cooling performance across the range of m^* investigated, and, displays amongst the highest film cooling

effectiveness values (particularly at high *m**). Even at the lowest coolant flow rates, where film blowing ratios are less than 0.1, the area-averaged film effectiveness achieved is comparable with geometries D8 and C5 which are operating near optimal film blowing ratios (of around 0.4). The result of this is the very high overall cooling performance observed in Chapter 8 and in Figure 9.11. Consequently, the cooling features implemented on this geometry with the specific intent of achieving high combined internal and external cooling, appear to have been successful.

9.3.3 Idealised Overall Effectiveness Trajectory

Based on the data presented in both this chapter and the preceding chapter, a diagram demonstrating idealised film effectiveness and overall effectiveness for different impingement and film wall porosities was produced and is shown in Figure 9.9. It is noted that the additional effect of varying pedestal configuration on effectiveness isn't considered here; however, the trends permit a basic insight into the effect of wall porosities as informed by the experiments conducted. The basic features of Figure 9.9 are explained below:

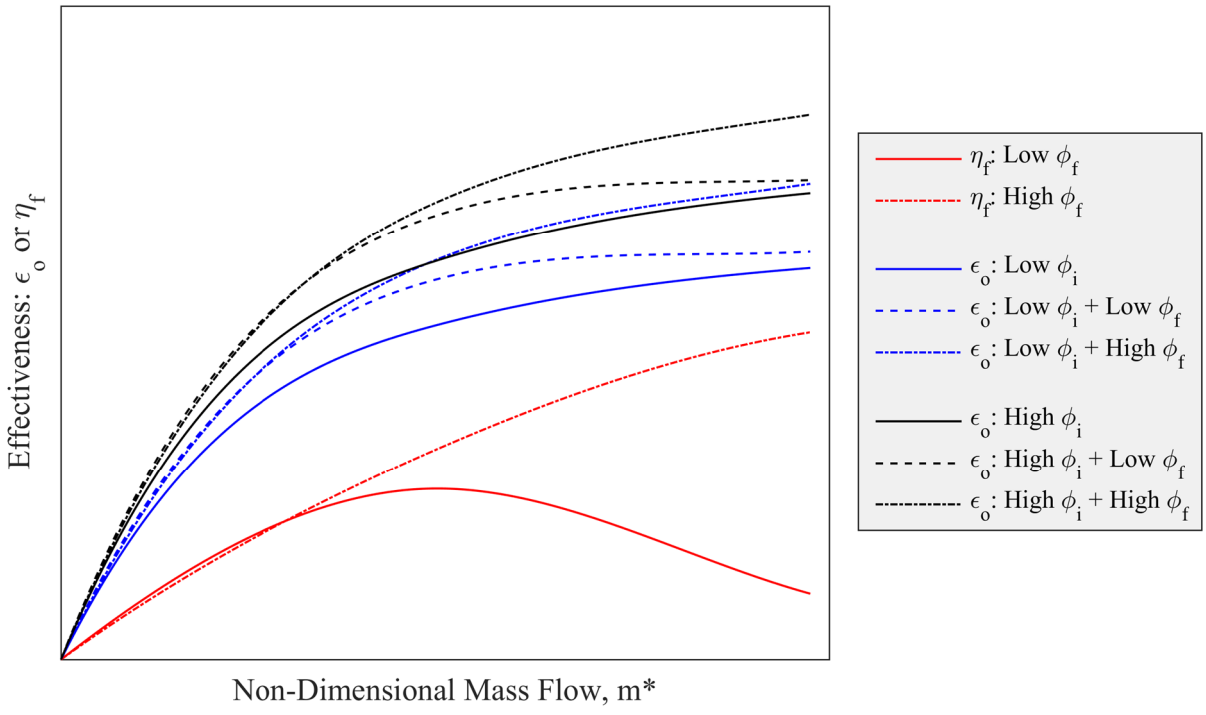


Figure 9.9 – Idealised m – ε_o trajectories. The figure demonstrates how the porosity of the impingement and film walls effect both the film effectiveness and overall effectiveness achieved as coolant flow rate is varied*

- Film effectiveness is shown by the two red lines. The film effectiveness achieved from a low porosity film wall is shown by the solid line where a peak value is observed (where film blowing ratios would be approximately in the range of 0.4 – 0.6) before a decay in the film effectiveness is observed as the film jet mass flux causes jet lift-off to occur. For the higher porosity film wall, at an equivalent coolant flow rate, blowing ratios will be lower when compared to the lower porosity film wall. Consequently, higher coolant flow rates are achieved prior to jet lift-off occurring. Additionally, the higher porosity wall exhibits higher peak film effectiveness due to the more regular ejection of cooling films.
- The blue lines show overall effectiveness for an impingement wall with a relatively low porosity. Specifically, the solid line shows overall effectiveness based on internal convection only. When the additional cooling effect from the low porosity film wall is added, an increase in overall effectiveness is observed, with the additional cooling effect being most significant when the films are operating at their optimal blowing ratios. At higher coolant flow rates, where the films are lifting-off, the increase overall effectiveness is seen to reduce. For the more porous film wall, however, the increase in overall effectiveness attributed to the films is more significant across a wider range of coolant mass flow rates.
- The black lines show overall effectiveness for an impingement wall with a relatively high porosity. It is noted that, as demonstrated in Appendix C, the benefit to impingement zone Nusselt number of increasing impingement jet Reynolds number (Re_i) reduces at higher Re_i. Consequently, the slope of the overall effectiveness curves for the higher impingement wall porosity flattens later than for the lower porosity wall as Re_i is reduced relative to the lower porosity impingement wall for the same coolant flow rate. The discussion around the additional effect of the cooling films, however, is similar to that of the lower porosity impingement wall.

9.4 Experimental Uncertainties

Experimental uncertainties were calculated for both coolant mass flow and film cooling effectiveness using the same approach used for the overall effectiveness data. As the film temperatures are generally lower than the metal temperatures observed in the overall effectiveness measurements, film effectiveness uncertainties were slightly higher. Figure 9.10 demonstrates the absolute uncertainty in film effectiveness for the worst-case test – geometry G1 at maximum coolant flow rate. Area-averaged absolute uncertainty in film effectiveness varied between 0.047 – 0.053 across the geometries.

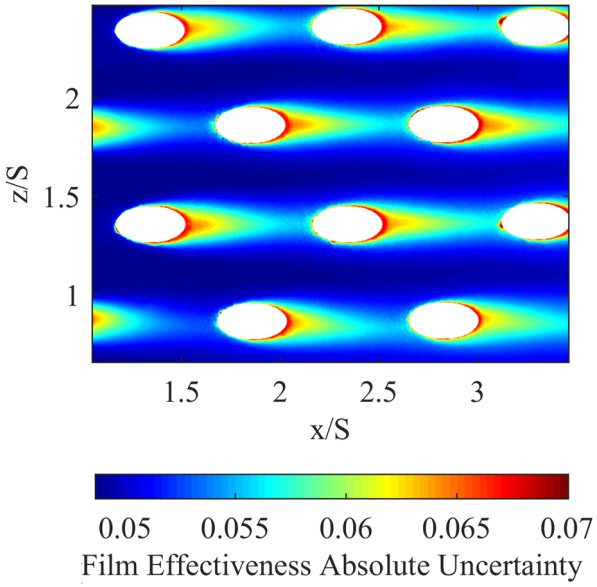


Figure 9.10 - Absolute uncertainty in film effectiveness measurement for maximum coolant flow rate case in geometry G1

9.5 Summary

This chapter has presented adiabatic film effectiveness data obtained from the experimental facility for the five double-wall test geometries. Film effectiveness data was obtained for a range of non-dimensional mass flows (and corresponding blowing ratios). During the experimental runs both the film and impingement walls were observed. The impingement wall temperatures were near identical to that of the coolant verifying the near adiabatic nature of the film effectiveness test pieces – a feature necessary to obtain adiabatic film effectiveness measurements.

Film effectiveness contours are demonstrated for the five geometries. Peak film effectiveness values were achieved at blowing ratios between 0.4 – 0.6 and this is in agreement with the data obtained for the single wall effusion study (presented in Chapter 3). Additionally,

the effect of jet lift-off was observed to occur in geometries for which higher blowing ratios were tested. Uncertainties were also calculated for the measured film effectiveness values.

A simplified thermal model was used to predict the internal convective efficiencies of the geometries at varying non-dimensional mass flows based upon experimentally measured values of overall effectiveness, film effectiveness and coolant flow rate. This information is useful in ascertaining the potential benefits of each system at different locations on a turbine blade, dependent on, for example, required overall effectiveness, likelihood of film hole blockage, and aerodynamic losses attributed to film cooling. The data demonstrated that the crenulation concept, G1, in general, achieved both the highest internal convective cooling and external film cooling performance.

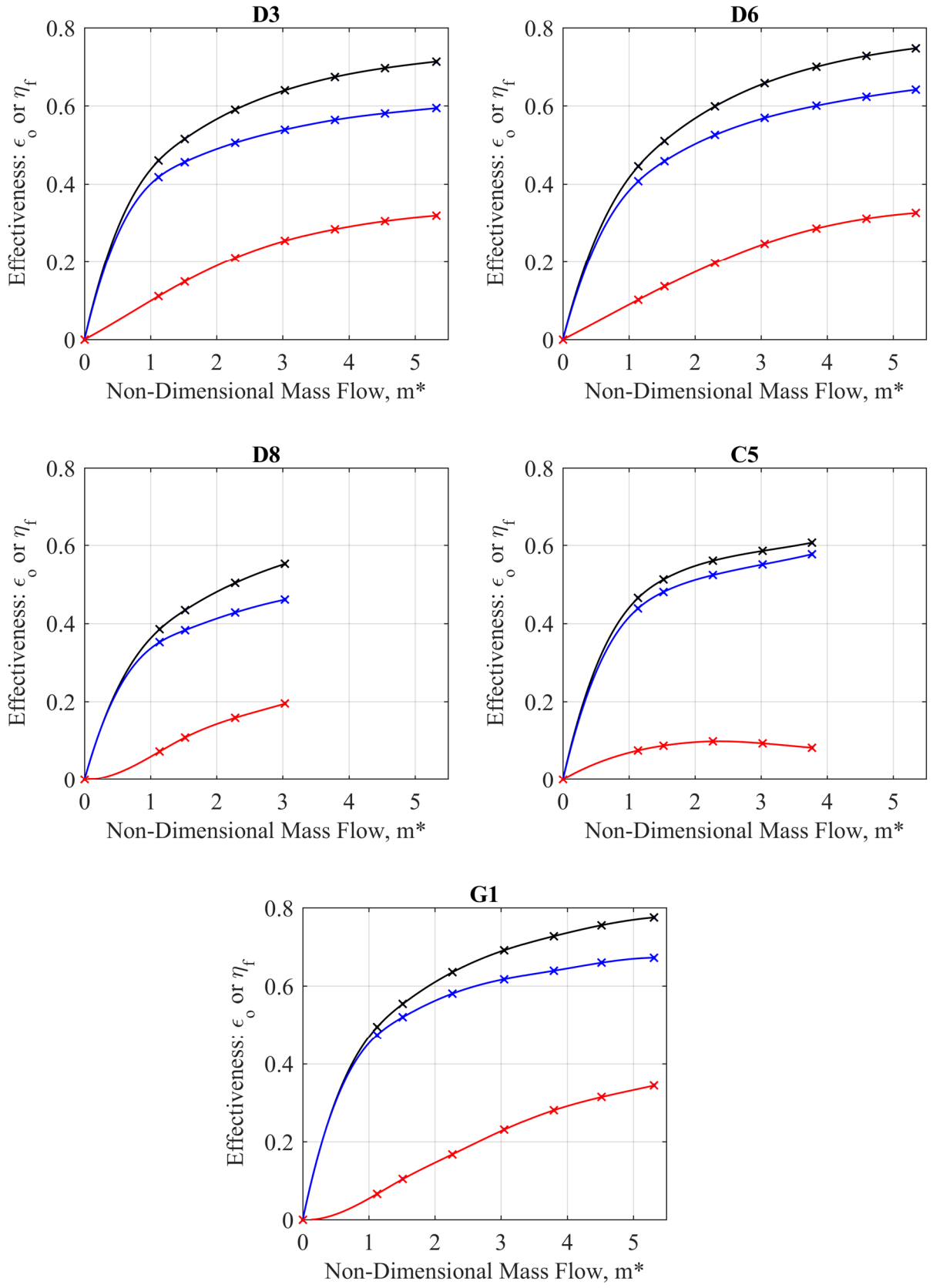


Figure 9.11 - Area-weighted averaged experimental overall effectiveness and film effectiveness for all five test geometries against non-dimensional mass flow. Contributions to overall effectiveness arising due to internal convection only (i.e. excluding films) is also plotted as calculated using equations 9.1 and 9.3

10 Computational Methods to Simulate the Experimental Setup

10.1 Chapter Overview

The following chapter discusses the computational simulations performed on the experimental test geometries using boundary conditions obtained during experiments. In this way the accuracy of the simulations could be verified. The simulations were of two kinds: a fully conjugate solver modelling the experimental setup verbatim, and an adapted version of the decoupled conjugate method presented in Chapter 5. Assessing the ability of both simulation methods to capture the cooling performance of the double-wall geometries was the primary purpose of this investigation. However, the data were also used to discuss some of the flow features occurring within the cooling geometries. Simulations were performed for geometries D3, D6, D8 and C5 for which experimental data was presented in Chapters 8 and 9.

10.2 Conjugate CFD of the Experimental Domain

The first of the two computational methods employed for assessing the cooling performance of double-wall systems was a fully conjugate CFD solver. The domain investigated (and highlighted in Figure 7.1 and in Figure 10.1) modelled the experimental setup from directly downstream of the heater mesh up to the diffuser section in two separate simulations.

The first of the simulations modelled the contraction section to obtain the velocity and turbulence profiles specified as the inlet mainstream boundary condition in the second simulation which modelled the test section. In specifying the inlet boundary conditions for this first simulation, the bulk average velocity and mainstream temperature obtained from the experimental facility during each run were used. Turbulence intensity was based upon Reynolds

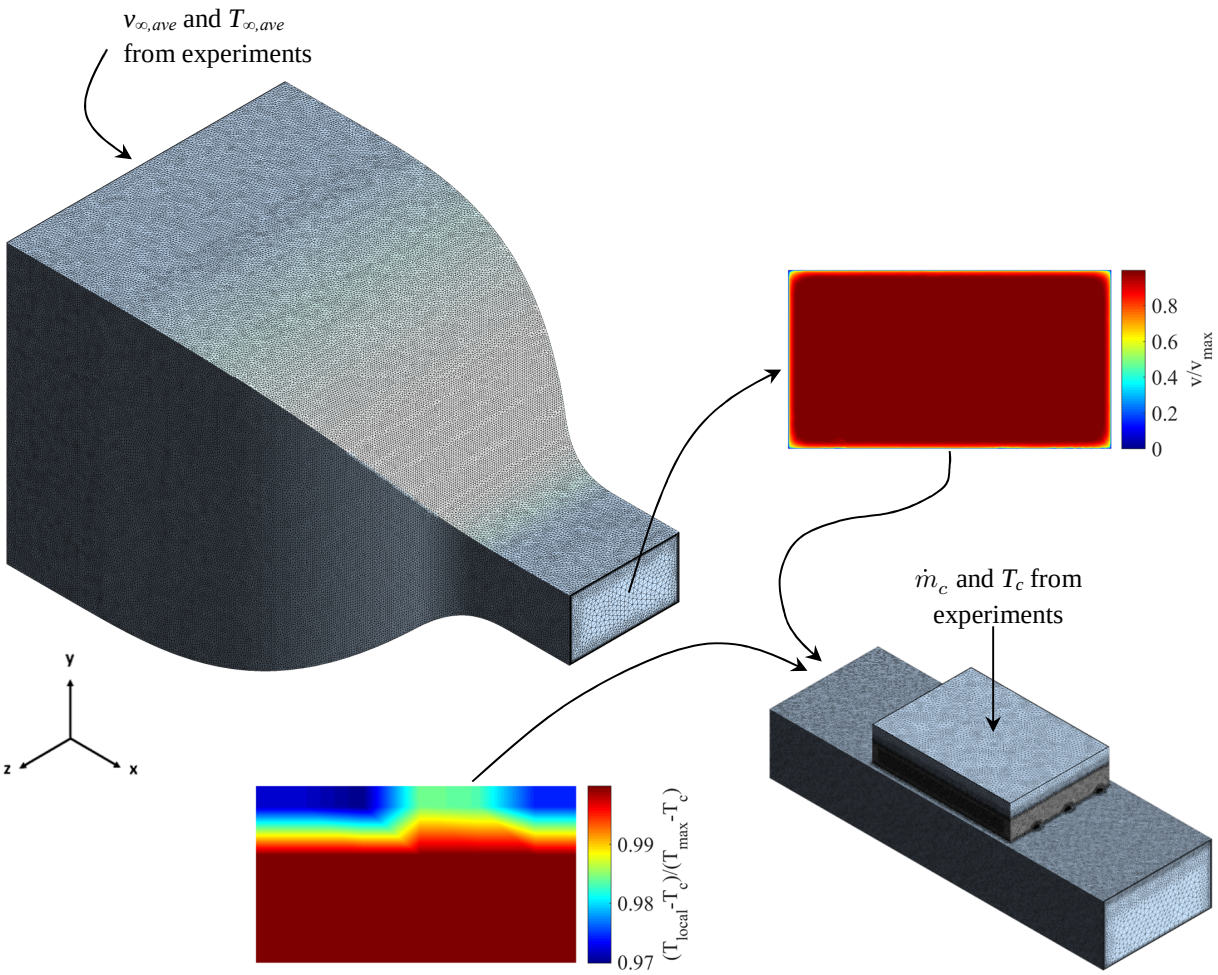


Figure 10.1 - Domains modelled in the fully conjugate CFD simulation of the experimental setup along with the main boundary conditions specified in each

number (with the relevant length scale being the hydraulic diameter) [81]. It is noted that the outlet velocity profile obtained from this first simulation was in close agreement with that obtained by the traverse (shown in Chapter 7). Additionally, the turbulence intensity obtained from the fully conjugate CFD at the location of the hot-wire measurement was found to be 1% which closely agrees with the experimentally measured value of 1.07%. Area-averaged turbulence intensity in the simulations was found to be between 2 – 4% as a result of the increased intensity towards the boundary layer. This variation in turbulence intensity is expected to have a negligible effect on the film performance and is supported in both [119] and [27] where a wider range of intensities were investigated and compared (0.5%, 1.5%, 4% and 18%) with the authors demonstrating a very weak influence on the resulting film performance. Typical combustor exit turbulence intensities vary widely (between 7 – 20%) [120].

The second domain simulated comprised the tunnel test section, double-wall test piece and plenum and utilised tetrahedral elements in the bulk of the domain, with 10 prism layers used at the solid/fluid interfaces to more accurately resolve the boundary layer. Meshes varied between approximately 40 – 65 million elements in the different geometries. A mesh independence study was performed using D3 (due to the high density of pedestals and both impingement and film holes) to determine the required mesh sizing, where metrics such as solid body temperature were used in assessing adequate mesh fidelity. A cross-sectional enlargement of an example mesh (D8) is demonstrated in Figure 10.2. Inlet mainstream velocity along with turbulence intensity and dissipation rates were based upon the results from the simulation of the upstream contraction section. Coolant inlet conditions were based upon the mass flow measured by the CFVN with coolant temperature evaluated by a thermocouple placed in the plenum. The mainstream temperature profile at the inlet of the test section was based upon extrapolated measurements from the five ceramic sheathed thermocouples in the experimental facility thereby capturing the small non-uniformities observed in the temperature profile. The area below the five sheathed thermocouples had a specified value based on a single thermocouple place centrally in the test section. An example temperature profile is shown in Figure 10.1.

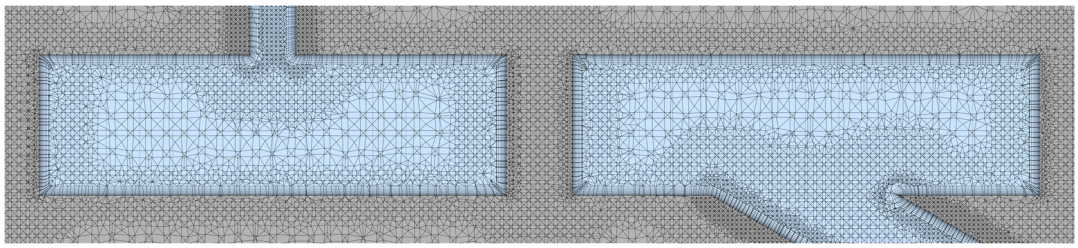


Figure 10.2 - Example mesh of the internal double-wall passage demonstrating the regions of mesh refinement

Simulations utilised a steady-state, pressure based solver with the realisable k-ε turbulence model and enhanced wall treatment. Solid properties were based upon SS-316 (from which the overall effectiveness test pieces were manufactured) with fluid density, viscosity and thermal conductivity set to be a function of temperature.

The results of the simulations were used both to assess the ability of the conjugate model to capture the temperature profile in the double-wall geometry, and to provide an assessment of the flow features occurring that could not be so easily ascertained from the facility.

10.3 Adapted Decoupled Conjugate Method

The decoupled conjugate method (*DCM*) developed and presented in Chapter 5 was modified to suit the form of experimental test geometries investigated in the experimental facility. This adapted process is outlined below.

The internal convective unit cell simulations remained largely unchanged from the process discussed in Chapter 5 with only the boundary conditions adapted to suit the data obtained from the experimental facility as follows:

- *Coolant Inlet*: Coolant mass flow and inlet total temperature specified based on the values recorded during experimental runs.
- *Film Wall External Surface*: Convective boundary condition with the mainstream driving temperature based on the average of the five ceramic sheathed thermocouples and a average heat transfer coefficient based on a correlation for turbulent flow over a flat plate (equation 10.1).

$$Nu = 0.0296 Re^{4/5} Pr^{1/3} \qquad (10.1)$$

In these simulations fluid and solid properties were again a function of temperature and, for the solid, based upon SS-316 as used in the experimental test pieces.

For the external film cooling correlation/superposition method, mainstream velocity, density and temperature utilised values measured during the experimental runs. The mass flux of the film cooling jets was based upon the jet fluid density and velocity obtained from the above internal convective unit cell simulations. The film temperature at the point of injection into the

mainstream was also obtained from these simulations. Finally, the external heat transfer coefficient was obtained using equation 10.1.

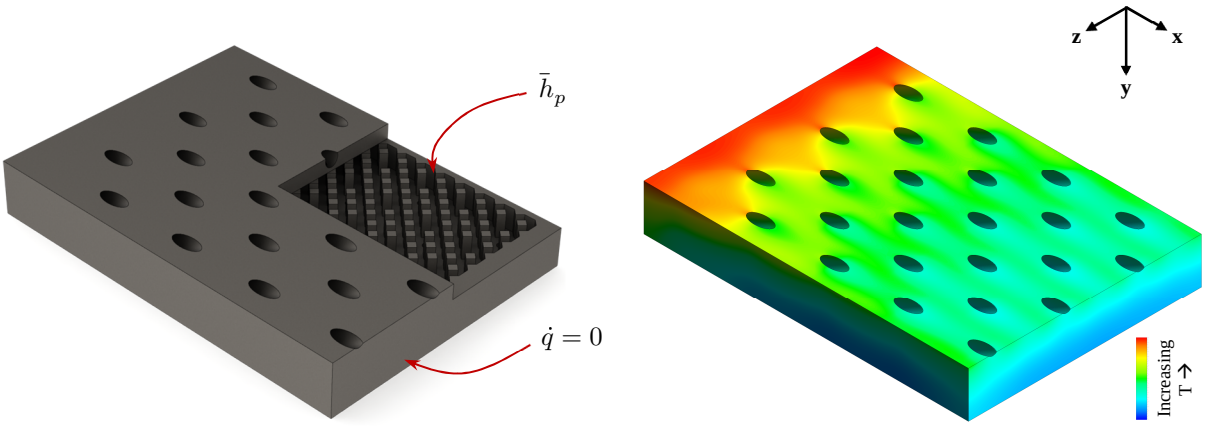


Figure 10.3 – Left) Cutaway view of the domain simulated in the modified decoupled conjugate method where the boundary conditions around the flange are highlighted. Right) An example of the resulting temperature profile obtained from the modified decoupled conjugate method

The most significant difference between the method presented in Chapter 5, and the test geometries being assessed in the facility and analysed here is the presence of a metal flange around the edge of the test piece (as demonstrated in Appendix D). Consequently, the adapted method accounted for this flange where a heat transfer coefficient was specified on the internal surface of the flange based upon the average heat transfer coefficient obtained on the pedestal surfaces during the internal convective simulations. The outside surface of the flange was assumed to be perfectly insulated, an approximation assumed valid as this surface of the test piece is surrounded by the high-performance insulation in the experimental facility. Figure 10.3 demonstrates an example of the domain assessed here via the decoupled conjugate method with the additional boundary conditions required to mimic the experimental setup identified. The figure also demonstrates an example of the temperature profile obtained via the adapted method.

10.4 Results – Flow Aerodynamics and Heat Transfer

Both the fully conjugate and decoupled conjugate computational methods were used in assessing the overall cooling effectiveness of the double-wall, effusion geometries using

boundary conditions that were obtained during the overall effectiveness experimental runs (see Chapter 8).

Figure 10.4 displays the external film wall overall effectiveness contours obtained for both computational methods as well as from the experimental facility for geometry D3 at two of the tested values of *m**; 1.13 and 3.02. In both cases, the fully conjugate CFD very accurately captures, in both a quantitative and qualitative sense, the trend in overall effectiveness exhibited during experimental testing. The result obtained from the decoupled method are also very encouraging, particularly at the larger of the two mass flows. It is noted that, for the decoupled method, at both mass flows, upstream metal temperature is lower than that captured by the fully conjugate simulations and experiments. It is suggested that the correlation used in calculating

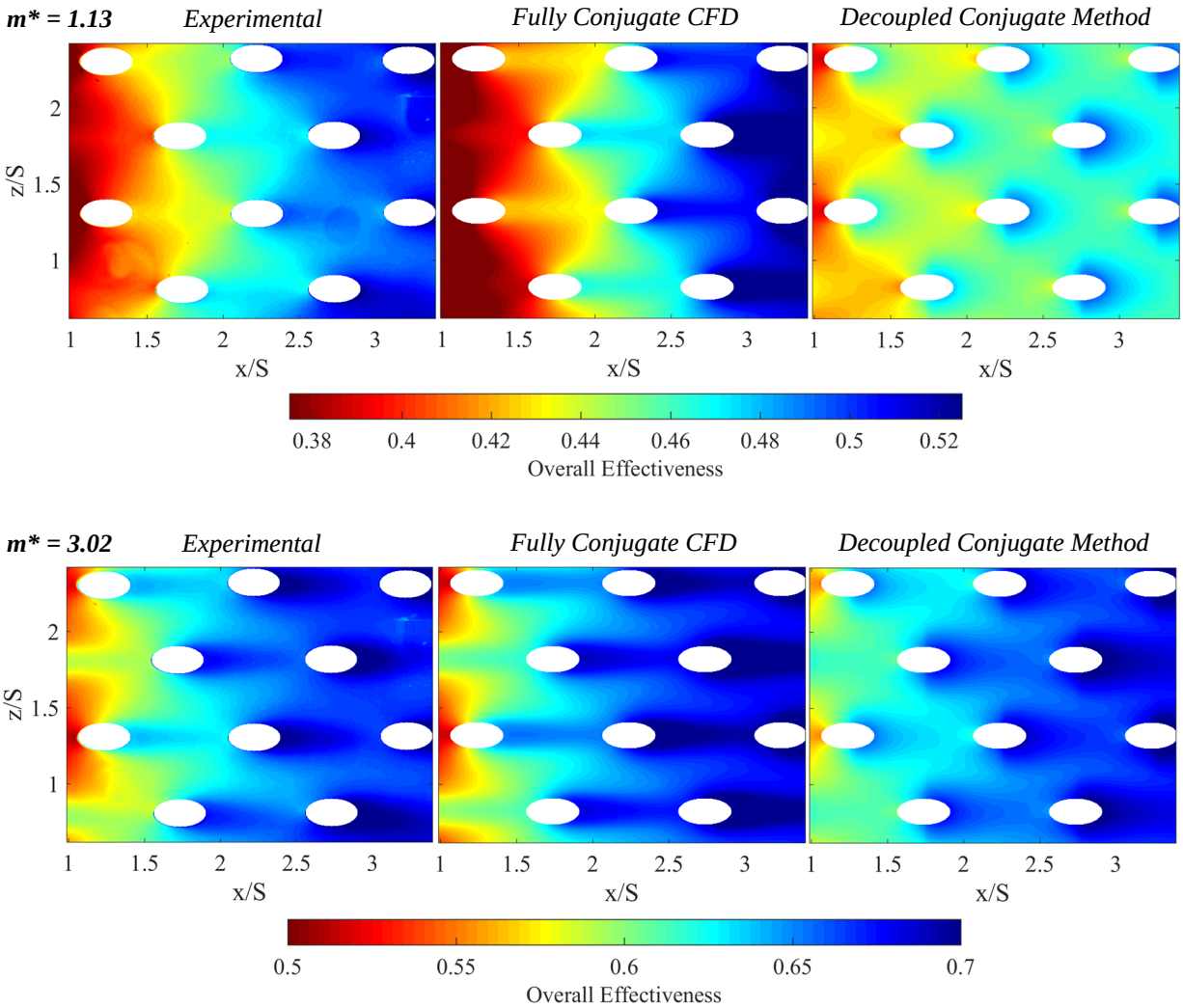


Figure 10.4 - Comparison of the experimental and computational overall effectiveness contours for the film wall of D3. Top) *m* of 1.13*, Bottom) *m* of 3.02*

the specified external surface heat transfer coefficient (equation 10.1) – which was also used in calculating m^* – is potentially underpredicting h resulting in a slightly reduced upstream metal temperature in the DCM simulations. At the lower mass flow, blowing ratios are very low and the modified version of the Goldstein correlation (discussed in Chapter 5) underpredicts the length of the films. However, as blowing ratio is increased, the performance of the correlation improves and the trend in film performance more accurately captured. At the highest blowing ratios, for the most porous film wall geometries, a slight overprediction in streamwise film development was observed. This is in keeping with the findings of Chapter 3 where the superposition method was observed to overpredict streamwise film development. However, the test geometries have a limited number of rows of holes and so this overprediction is not expected to be too significant in the simulations. Furthermore, geometries D8 and C5 have increased hole pitching and this will further reduce the significance of the film effectiveness overprediction as demonstrated in Chapter 3. Indeed, given the significantly reduced computational resources required when compared to the fully conjugate simulations, the results from the method are very encouraging.

Area-weighted averaged overall effectiveness plots for all four geometries which compare the experimental and computational results, are shown in Figure 10.5. The figure includes data for both the film and impingement walls. One of the features evident in the plots that is visible across three of the simulated geometries (D3, D6 and C5), was the underprediction of overall cooling effectiveness achieved on the visible surface of the impingement wall in both computational methods. The extent of this underprediction appears to vary depending on the wall-to-pedestal contact area. Geometry C5, which has the greatest pedestal contact area relative to surface wetted area, demonstrates the greatest underprediction. D8, on the other hand, demonstrates little underprediction and has the lowest wall-to-pedestal contact area. It is therefore anticipated that this underprediction in overall cooling effectiveness is

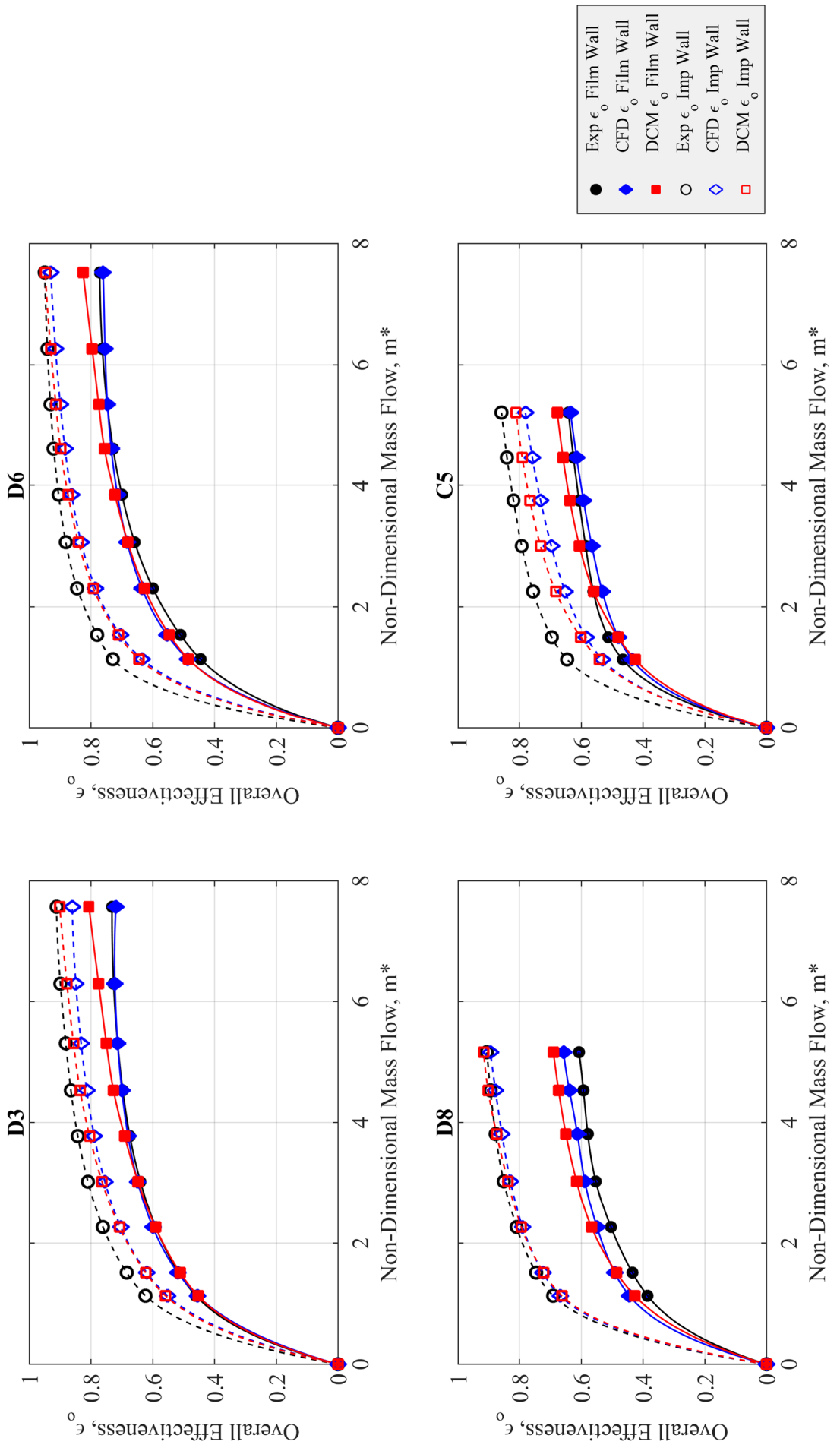


Figure 10.5 – Area-weighted averaged overall effectiveness for four of the test geometries (D3, D6, D8 and C5) comparing the data from both the experimental and computational methods

resulting from both computational methods overpredicting the level of conduction occurring from the hotter film wall. This may, in-part, result from the specified value of SS-316 thermal conductivity whose book value differs depending on the manufacturer, as well as some variation in the material properties that arise due to the vacuum brazing process used in manufacturing the experimental test pieces which utilises a thin nickel based preform (see Appendix D). Additionally, there is a possibility of contact resistance between the two bonded walls where some small gap may remain between the expected bonded surfaces. However, this is not anticipated to be significant as rapid heating of the bonded geometry whilst the sample was observed with an IR camera indicated that a good thermal bond had been achieved.

In general, the results of Figure 10.5 demonstrate that both computational methods generally perform well and capture the overall effectiveness achieved by the geometries. Both the results from the fully conjugate and decoupled conjugate method perform comparably, with each performing better in different geometries and at different values of m^*. For geometries D3 and D6, which exhibit the closest film hole pitching, the decoupled conjugate method demonstrates an overprediction of overall cooling effectiveness at the larger m^* values tested and again, this is expected to result from the slight overprediction of film development using the Sellers superposition method [78] at these pitches. Indeed, it is expected that, with further refinement to the film model, the results from the decoupled method will outperform the fully conjugate CFD.

Results from the fully conjugate simulations were used in calculating a value of heat transfer coefficient on the external surface of the film cooled wall (i.e. h_∞) for comparison with the value calculated using the flat plate correlation shown in equation 10.1. The results from the CFD were near identical to that obtained from the correlation. However, the discussion around Figure 10.4 indicated that this value of h_∞ may be an under-prediction and indeed the challenges in accurately capturing heat transfer coefficient in CFD simulations are well-known. Furthermore, the ejection of films results in a potential heat transfer augmentation (further discussed later)

and this effect is naturally disregarded in the decoupled method. Consequently, it is suggested that future work may entail experimental measurements to verify h_{∞}.

The results of both the fully conjugate CFD and decoupled conjugate methods are very encouraging, particularly given the many complex flow features occurring in the geometries. Both computational methods rank the performance of the geometries in the same order as that measured by the experiments – providing confidence in the use of both numerical methods for initial benchmarking of various double-wall cooling systems incorporating different geometric features. However, the value of the decoupled method in providing a fast and computationally light assessment of cooling performance in double-wall systems is apparent. Trials showed that, based on the CPU time used, the decoupled method converges approximately one-hundred times faster than the fully conjugate simulations. This total CPU time was calculated as the number of processing cores multiplied by the simulation time. With further work it is anticipated that the extent of the slight overprediction in film build-up could be reduced, further increasing the accuracy of the method.

Some of the flow features present within the double-wall geometries, and responsible for the various cooling benefits, are further discussed below.

As commented upon in Chapter 5, the decoupled conjugate method disregards potential internal crossflow effects which may result in some variation in, for example, impingement zone heat transfer coefficient due to the jet being affected by crossflow. In order to ascertain the effect of crossflow, the local impingement zone Nusselt numbers were calculated and compared for both computational methods for the maximum coolant flow rate case (m^* of 7.52) for geometry D6. The data for a centrally positioned impingement hole (with the specific hole indicated in Figure D.4 in Appendix D) was used for the fully conjugate simulations. The fully conjugate simulations modelled the whole test piece, and so selecting a centrally positioned impingement hole reduced the effect of potential impingement jet deflections that may result from the flange around the edge of the test piece – a phenomenon further commented upon

later. The resulting impingement zone local Nusselt numbers are presented in Figure 10.6 as a function of dimensionless radial distance from the stagnation point. The agreement between the Nu_i plots for both simulations is encouraging with the maximum discrepancy being approximately 25%. It is interesting to note that, for y/D_i of 3 (geometry D6), the maximum Nusselt number occurs at approximately z/D_i equal to 0.5 – 0.7 [16] for both computational methods. The decoupled conjugate method displays a slightly reduced value of Nu_i (~10 – 25% lower) for a radial distance within one impingement hole diameter of the stagnation region and beyond that both simulations produce near identical values. Several reasons for the discrepancy near the stagnation point are hypothesised. Simulations were steady-state, however, the impingement region is characterised by high unsteadiness. Small variations in Nusselt number were consequently observed around each impingement zone. There may also be some small beneficial effect resulting from simulation of the whole test piece internal flow field captured in the fully conjugate simulations which also result in a slightly higher impingement zone Nu_i. However, the results are encouraging given the different setup between the two methods and the small difference in peak Nu_i is expected to have a minimal effect on the overall solid

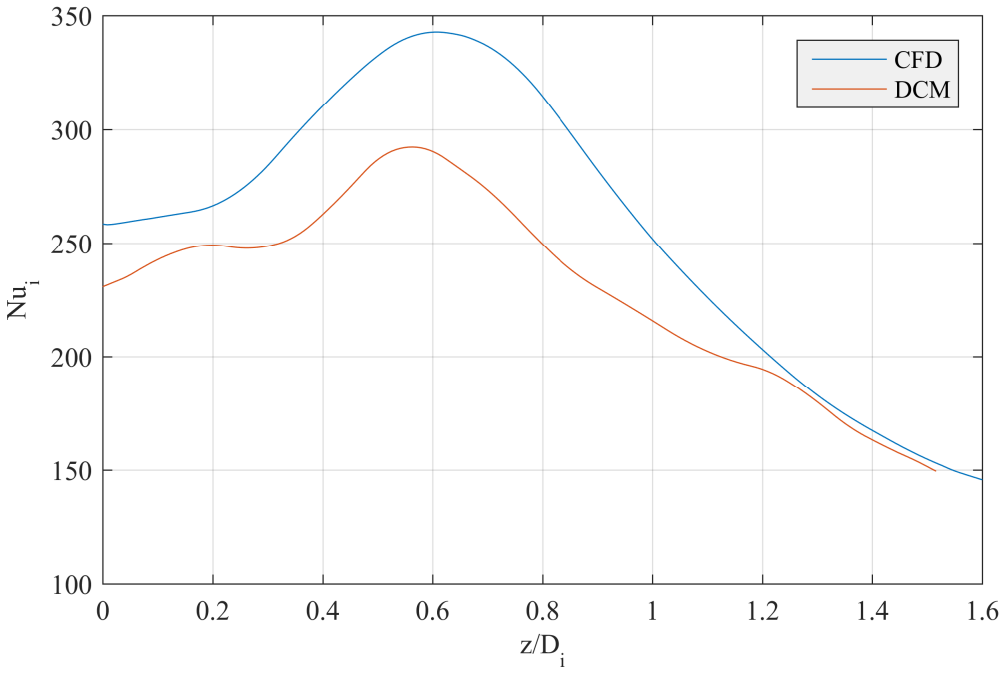


Figure 10.6 - Impingement zone Nusselt number for geometry D6 for the maximum coolant flow rate case (m = 7.52) where Re_i = 32200*

temperature profile. It is also noted that similar observations were made at other coolant flow rates as well as between the different geometries, thus providing confidence in the implementation of the two computational methods.

Both the discussion above and that in Chapters 8 and 9 considered the presence of the flange surrounding the edge of the test piece (a necessity of the manufacturing process). The effect of conduction across the flange has already been discussed. Furthermore, the flange was also designed to minimise the impact on the internal flow field. To ascertain the success of this, approach, velocity contours and velocity vector arrows for a plane mid-height along the pedestals for two geometries are shown in Figure 10.7. These two geometries were C5 and D6. Geometry C5 was expected to display the greatest flow disruption from the flange due to both the relatively large size of the flange, and the small number of repeating unit cells in the geometry. D6 on the other hand was expected to be the geometry least susceptible to flow disruption from the flange due to the large number of pedestals which would act to minimise crossflow effects from the flange. D6 also has a large number of impingement and film holes which were also expected to keep flange effects localised. It is noted that velocity has been scaled by the average mainstream inlet velocity which was approximately 59 m/s across the geometries during these experiments (providing Re_∞ similarity to engine conditions).

The velocity contours for geometry C5 in Figure 10.7 clearly demonstrate some effect on the internal flow arising from the flange. The two corner impingement jets (those on the right of the image) exhibit some untypical jet deflection. This results from a localised crossflow effect due to proximity to the flange. Indeed, the vectors demonstrate the redirection of flow near this surrounding rim. The temperature contours also show the higher temperature in the uncooled flange when compared with the pedestals. Given the relative size of this uncooled flange, this additional heat conduction was expected to give rise to a lower overall effectiveness around the edges of the impingement wall than would otherwise be expected (an effect observed in the experiments, see Chapter 8). Consequently, the flange in geometry C5 has the most

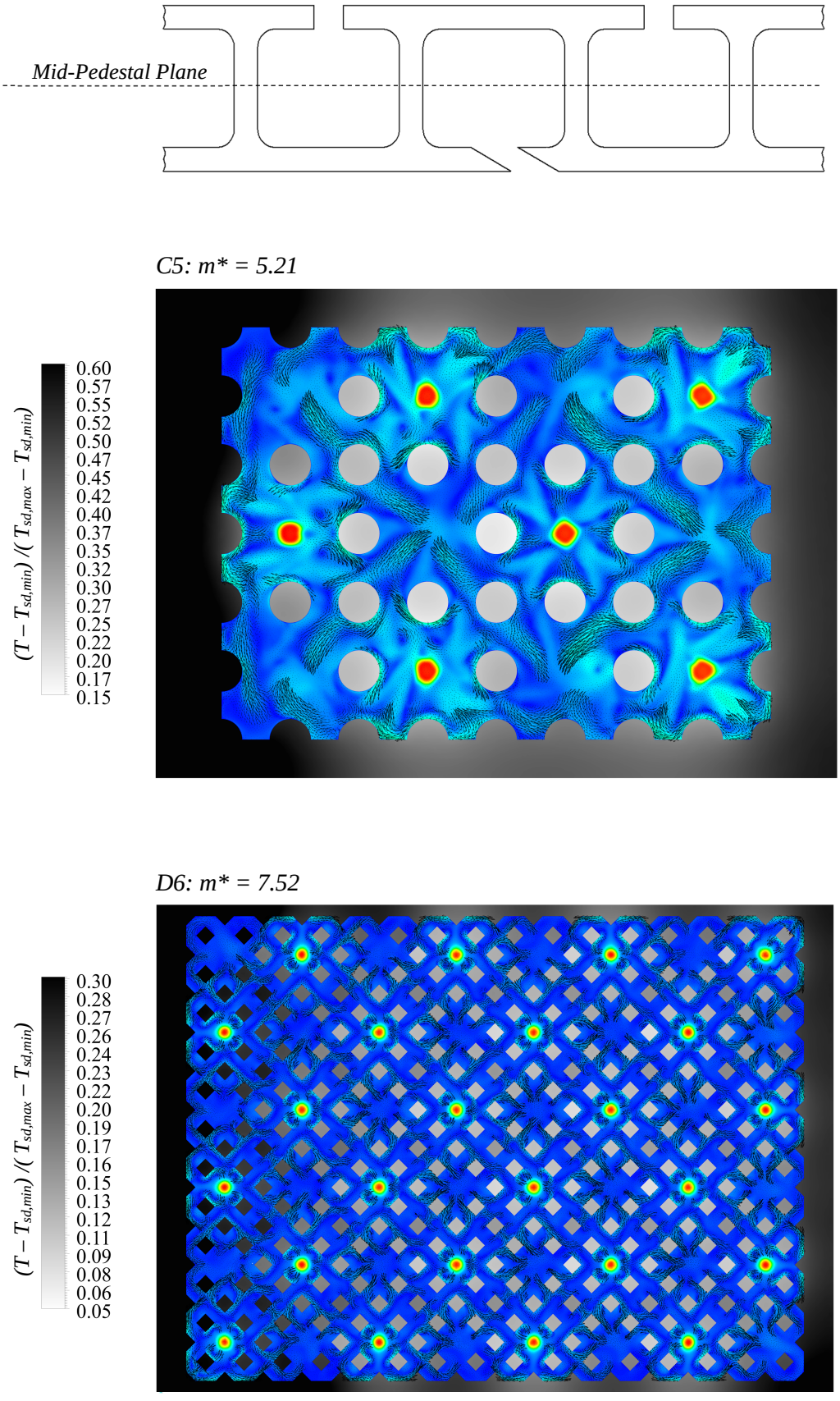


Figure 10.7 - Normalised velocity and temperature contours from the fully conjugate CFD simulations, taken mid-height along the pedestal and including velocity vector arrows. The location of the plane is shown in the schematic at the top. The contours for geometries C5 (middle) and D6 (bottom) are shown for the maximum experimental flow rate case for each geometry

significant effect from amongst the tested geometries. The velocity vectors also indicate a very slight asymmetry in the solution. This arises due to the inherent unsteadiness associated with vortex shedding around the pedestals.

In contrast to the above, the velocity contours for geometry D6 demonstrate very little effect on the flow field due to the flange with the small effect appearing very localised. Impingement jet deflection is not observed and there is minimal propagation of flow redirection arising from the flange. It is suggested that the relatively high density and configuration of pedestals results in significant resistance to crossflow effects and this concurs with the findings of Hong et al. [57] who, for similar systems, demonstrated a significant reduction in crossflow effects in the presence of pedestals. Both figures also demonstrate a general reduction in solid temperature in the streamwise direction, an effect which is particularly apparent in D6 due to the higher film cooling performance. The figures also show that the pedestal elements in immediate proximity to the impingement zone demonstrate lower metal temperatures than the surrounding pedestals. This results from a secondary impact arising from the impingement jet, which, after initially impacting the target plate moves radially outwards from the stagnation point and is directed towards the adjacent pedestals. This is clear from the velocity vectors which show that this flow impacts the surrounding pedestals resulting in high heat transfer coefficients on the pedestal surface and a consequent reduction in pedestal temperature agreeing with the findings in previous studies [99].

This effect of this wall jet on the surrounding pedestals is further demonstrated in Figures 10.8 and 10.9. The figures again show the normalised velocity and temperature contours obtained from the internal simulations in the decoupled conjugate method for geometry D6. The figures clearly show the impact of the flow from the impingement zone on the surrounding pedestals – an effect demonstrated in Appendix C in the two-dimensional thermal model developed. As demonstrated in Figure 10.8, the temperature profile in these immediate pedestals show a greater temperature reduction on the faces surrounding the impingement zone

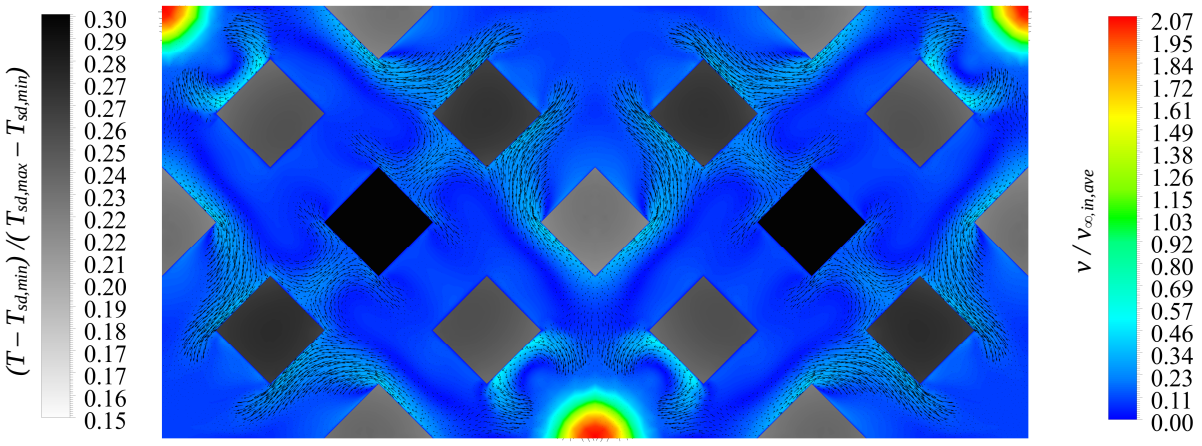


Figure 10.8 - Normalised velocity and temperature contours from the decoupled conjugate method internal flow simulation for geometry D6 in the maximum coolant flow rate case. The location is mid-height along the pedestals and includes velocity vector arrows.

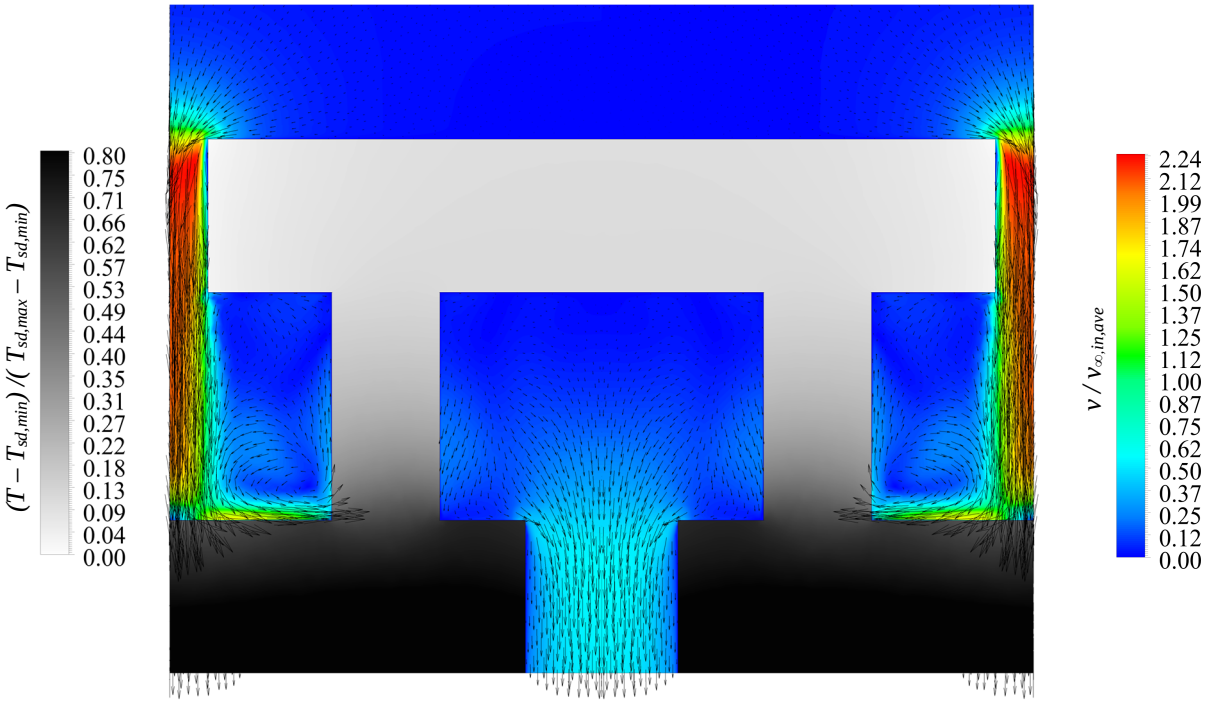


Figure 10.9 - Normalised velocity and temperature contours from the decoupled conjugate method internal flow simulation for geometry D6 for the maximum coolant flow rate case, including velocity vectors. The location is a vertical plane midway through the impingement and film holes

due to the higher heat transfer coefficients. It is the turbulent flow features that result from the impingement zone and pedestals, along with the high coolant wetted area, which contribute to the high internal convective cooling performance observed in double-wall geometries. Figure 10.10 shows normalised velocity and solid temperature contours in a vertical plane (the *x-y* plane in Figure 10.1) midway through the impingement and film holes for geometries C5 and

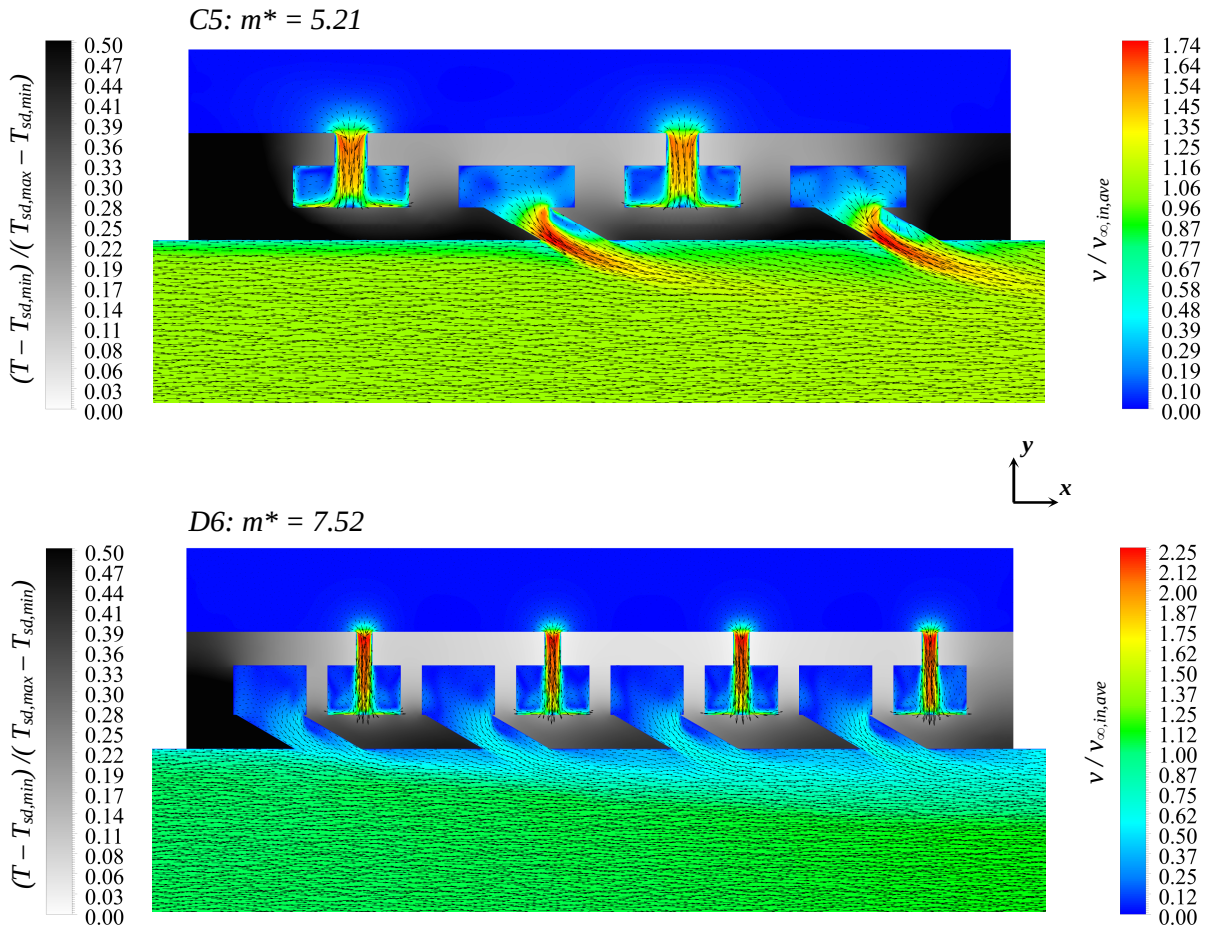


Figure 10.10 - Normalised velocity and temperature contours from the fully conjugate CFD simulations for geometries C5 (top) and D6 (bottom) for the maximum coolant flow rate cases, including velocity vectors. The location is a vertical plane (the x-y plane in Figure 10.1) midway through the impingement and film holes

D6. The contours are again for the maximum coolant flow rate cases in each geometry and the results are from the fully conjugate CFD simulations. Geometry C5 has relatively low film wall porosity. Consequently, as discussed in Chapters 8 and 9, high film blowing ratios were observed across most of the coolant flow rates tested with a resulting poor film cooling performance. This is demonstrated in Figure 10.10 where the high film jet momentum results in the jets mixing with the mainstream flow and exhibiting very poor adhesion to the external surface of the film wall. For geometry D6, however, the film wall porosity was four times higher than that of C5, and is more typical of effusion cooling systems. Consequently, even at higher coolant flow rates, the films were well adhered to the film wall surface resulting in good film cooling performance. Indeed, this is apparent even for the highest m^* tested in Figure 10.10

where the ejected films are seen to adhere to the external film wall surface and demonstrate a reduction in near wall flow velocity. This reduced near wall velocity is also seen to develop in the streamwise direction as the films from multiple jets build-up – an effect not observed for geometry C5. The velocity contours for both geometries also demonstrate the effect of jetting within the film holes resulting from the 30^{o} hole inclination angle and the corresponding sharp edge. The result is a reduction in heat transfer coefficient in some regions inside the film holes.

As discussed in Chapter 2, the total cooling benefit arising from film cooling must account for any heat transfer augmentation effects due to the ejection and mixing of the film jets with the mainstream flow. In general, in keeping with the findings of Dittmar et al. [121], higher heat transfer coefficients were anticipated at high film blowing ratios due to increased flow mixing and the higher flow speed resulting from the increased film speed. To verify this hypothesis, the heat transfer coefficient occurring on the external film wall surface for geometry C5 was compared for both the lowest and highest coolant flow rate cases which had corresponding blowing ratios of 0.45 and 1.62 respectively. The resulting heat transfer coefficient distributions are presented in Figure 10.11 where they have been normalised by the average heat transfer coefficient along a line just downstream of (and parallel to) the test piece leading edge in each simulation. The figure very clearly demonstrates the heat transfer augmentation occurring at the higher blowing ratio due to the turbulent flow features associated

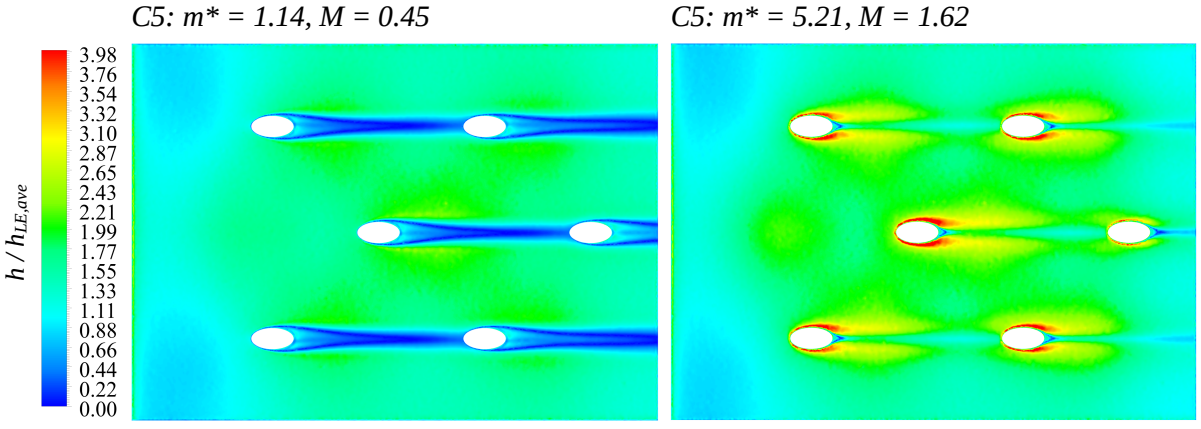


Figure 10.11 – Heat transfer augmentation arising from the film jets in geometry C5 at the minimum (left) and maximum (right) coolant flow rates tested

with the jet mixing, whereas only moderately increased heat transfer coefficients are observed for the lower blowing ratio case where the film jets are observed to be well adhered to the film wall surface after ejection.

The heat transfer augmentation observed for the higher blowing ratio in Figure 10.11 is explained with reference to Figure 10.12. The figure demonstrates the counter rotating vortex pair resulting from the ejected film jets. The locations of the vortex pairs correspond to the regions in which particularly high heat transfer coefficients are observed in Figure 10.11.

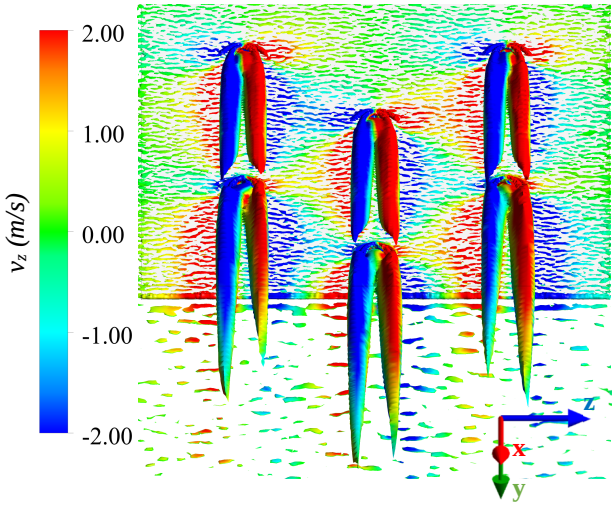


Figure 10.12 - Counter rotating vortex pair arising from the film jets for geometry C5 at an m of 5.21 (M = 1.62)*

10.4.1 Effect of Varying Temperature Ratio and Biot Number

As discussed in Chapter 7, the experimental facility was designed to achieve mainstream temperatures of up to 475 K with coolant drawn at ambient temperature consequently providing a temperature ratio capability of approximately 1.6. For the experimental results presented, the facility was run at a lower temperature ratio of 1.25. Additionally, for the overall effectiveness measurements obtained, the stainless steel 316 test pieces permitted Biot number similarity to within 25%, with the thermal conductivity of the test pieces being slightly greater than that required for a perfect match on Biot number. It is appreciated that, as a consequence of this, the cooling performance of each geometry will differ slightly from that which would be achieved if both parameters were perfectly matched. The primary effect is anticipated to be a variation in the relative cooling effects of internal convection and external film cooling performance. However, the observations made across the previous chapters for the five cooling geometries

investigated are anticipated to be equally valid. Indeed, in the case of cooling films, where blowing ratio has been held constant, density ratio, which is directly affect by the temperature ratio, is observed to have a relatively small effect [29].

To demonstrate the potential effects of the reduced temperature ratio and Biot number on the cooling performance of the geometries, a fully conjugate simulation was re-run for geometry D6 at an intermediate m^* case ($m^* = 3.85$) with a temperature ratio of 1.6 and a perfect match on Biot number. The temperature ratio was selected as it approaches engine representative temperature ratios and is the maximum possible ratio achievable in the facility. The geometry was selected due to the high film wall porosity which is more typical of effusion systems, high pedestal conduction area, and high internal convective cooling performance. Mainstream Reynolds number was unchanged as this matched engine conditions and maintained the film wall surface heat transfer coefficient.

The results of the simulation are shown in Figure 10.13 along with those obtained using the rig conditions at the same value of m^*. The area-averaged overall effectiveness for both conditions are provided in Table 10.1. Several features are identified and discussed below.

Table 10.1 demonstrates that the average overall effectiveness achieved on the film wall of the double-wall geometry is reduced by around 3% for the matched Biot number and higher T ratio condition when compared to those used in the experimental runs. This is reaffirmed by the contours in Figure 10.13 where there is a relatively constant offset in effectiveness between the figures for the two conditions of between 2 – 4%. Indeed, the film cooling performance appears very similar between the two test conditions with similar levels of lateral film spreading and streamwise decay; an expected outcome given the blowing ratio varies little between the two sets of conditions (0.397 for the experimental test case and 0.382 for the matched case). For the higher temperature ratio case, coolant-to-mainstream density ratio was increased, however, as confirmed by the open literature, the effect of density ratio is significantly less than that of blowing ratio [29] and this is confirmed by the simulation results. The reduction in the film wall

overall effectiveness is therefore expected to be the result of the reduced solid thermal conductivity of the matched Biot number test case resulting in a reduction in the heat flux conducted away from the film wall to the impingement wall. This is confirmed by the results for the impingement wall in which both qualitatively, and quantitively, there is little variation in the cooling effectiveness achieved at both conditions. This signifies that the experimental results correctly capture the cooling trends with only a small variation in raw cooling effectiveness resulting from the slight mismatch in Biot number and temperature ratio.

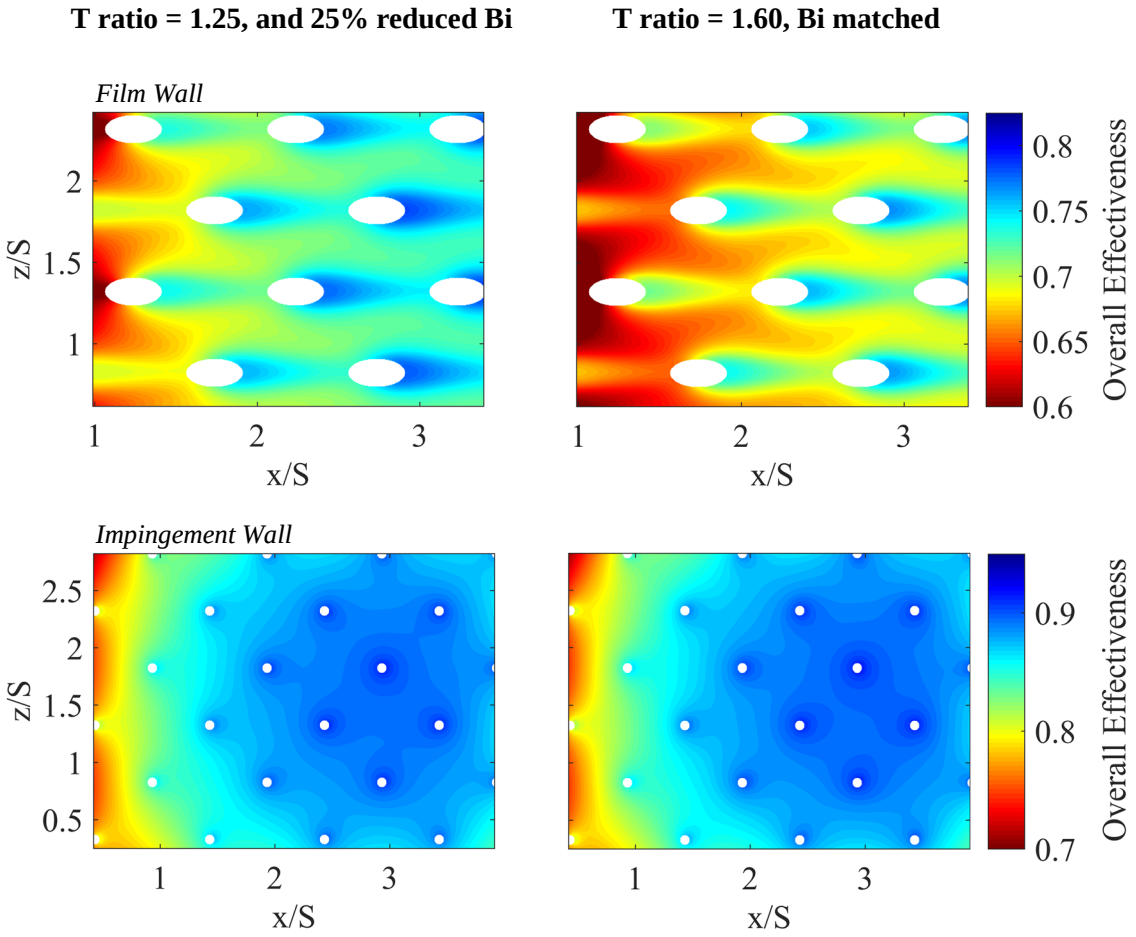


Figure 10.13 - Overall effectiveness contours for geometry D6 from the fully conjugate simulations demonstrating the variation in effectiveness which results from the disparity between the temperature ratio and Biot number achieved during the experimental runs presented in Chapter 8, and those of near engine conditions

Table 10.1 – Area-averaged overall effectiveness for the impingement and film walls of geometry D6 demonstrating the variation in effectiveness which results from the disparity between the temperature ratio and Biot number achieved during the experimental runs presented in Chapter 8, and those of near engine conditions

m* = 3.85	**T ratio = 1.25, and 25% reduced Bi**	**T ratio = 1.60, Bi matched**
Film Wall	0.7144	0.6813
Impingement Wall	0.8628	0.8648

10.5 Summary

This chapter has presented the computational simulations performed to replicate the experimental setup, making use of experimentally obtained data for the boundary conditions. Two computational methods were presented. The first utilised a fully conjugate commercial CFD solver with a setup mimicking the experimental domain. The simulations modelled the rig contraction section, test section, coolant plenum and double-wall test piece. The second method utilised an adapted version of the decoupled conjugate method presented in Chapter 5 which now modelled the exact form of the experimental test pieces. Simulations were performed for geometries D3, D6, D8 and C5.

The heat transfer results from both simulation methods show agreement that is very encouraging. Overall effectiveness data on the film wall for all geometries demonstrated both qualitative and quantitative similarity to the experimental results. Impingement wall overall effectiveness data showed a slight underprediction in both computational methods and this is partially expected to result from the material conductivity specified in the simulations. The results from the decoupled conjugate method developed are particularly encouraging given simulations ran in a fraction of the time required by the fully conjugate simulations. Aerodynamic data from the simulations are also presented and used to explain some of the heat transfer phenomena observed. Finally, the fully conjugate setup is used to demonstrate the anticipated discrepancy in cooling performance due to the slight mismatch in Biot number and temperature ratio in the experimental facility.

11 Summary and Concluding Remarks

This thesis has discussed a range of experimental and computational research performed to advance understanding of both the aerothermal and thermomechanical performance of double-wall, effusion cooling systems.

More in-depth summaries have been provided at the close of each individual chapter. Here, however, are provided some of the specific highlights of the research. Following this are several suggestions for future research into this cooling technology.

11.1 Summary of the Experimental Work

- An existing low-speed facility was adapted to investigate single wall effusion cooling performance. The facility utilised pressure sensitive paint to obtain adiabatic film effectiveness measurements from two effusion geometries with non-dimensional primary hole pitches of *3.0* and *5.66* at varying blowing ratios. The results demonstrated the high film cooling performance achievable in effusion systems. The lower pitched geometry demonstrated strong spanwise jet interactions and developed complete spanwise films at blowing ratios as low as 0.3. For the larger pitch geometry, complete films were not formed at any blowing ratio, although area-averaged effectiveness was still observed to be high.

- An experimental facility has been designed, commissioned and used to ascertain the cooling performance of double-wall, effusion cooling geometries via IR thermography. The facility incorporates several novel features to improve the quality of results including the use of flow recirculation, internal insulative panels and bespoke instrumentation which demonstrated high mainstream temperature uniformity. The facility matches mainstream

and impingement Reynolds numbers to engine conditions and, with stainless steel 316 test pieces, provides Biot number similarity to within 25%.

- The aforementioned commissioned facility was used to obtain both overall effectiveness and adiabatic film effectiveness measurements for five double-wall test geometries which had demonstrated interesting cooling characteristics in computational simulations. Indeed, the trends from the experimental results demonstrated good agreement with those of the simulations. The results permitted an assessment as to the geometric features which contributed to preferable aerothermal performance. The facility was also used to obtain certain aerodynamic measurements including the variation in pressure ratio for each geometry required to achieve a certain coolant flow rate and the discharge coefficient of each geometry. Such information is potentially useful in indicating the geometries best suited to particular regions of a turbine blade. A simplified isothermal model was used to predict the convective efficiency of each geometry based on the experimental overall effectiveness and film effectiveness data. In general, those geometries exhibiting a relatively high impingement and film wall porosity, demonstrated good cooling performance and this was particularly true for geometries with high internal pedestal wetted area.

11.2 Summary of the Aerothermal Computational Work

- A computational method has been developed for assessing the cooling performance of double-wall, effusion geometries. The method is computationally inexpensive and takes advantage of the repeating nature of the double-wall geometries investigated. The method is termed a “decoupled” conjugate method in that it models the internal convective cooling performance and external film cooling performance of the geometries in two separate simulations. The first is a conjugate CFD simulation of a small repeating geometric unit,

whilst the second is a superposition/correlation method. These simulations are then coupled in a thermal FEA analysis forming the final solid temperature profile which accounts for both internal and external cooling. In this way the streamwise development of films is captured in a computationally efficient manner.

- The above method was used in the assessment of 21 double wall geometries: 13 designed via a DoE method featuring diamond pedestals, 7 designed via a DoE method featuring circular pedestals, and 1 novel geometry featuring an array of octagonal and rectangular pedestals along with a crenulated impingement wall. The simulations were used to identify aerothermally preferable geometrical features with main effects plots developed to support the conclusions. Data from the simulations was also employed in defining an effective porosity which could be used to predict the expected cooling performance from a geometry regardless of the specific internal features. The results of the simulations were used in identifying the five geometries to be manufactured and assessed experimentally.

- Computational methods were developed which replicated the experimental setup. In this way, the accuracy of the computational solutions could be ascertained through comparison with the experimental results. Two computational methods were implemented. The first was a fully conjugate CFD solver which mimicked the experimental setup verbatim and implemented boundary conditions obtained during experimental runs. The second method utilised an adapted version of the developed decoupled conjugate method which modelled the exact form of the experimental test pieces. These simulations also utilised boundary conditions from experimental runs where possible. Both computational methods captured the temperature profile occurring in the double-wall geometry well when compared to the experimental data in both a qualitative and quantitative sense, particularly with regards to the film wall. Indeed, the results from both computational simulations were very similar to one another. However, the decoupled conjugate method provided data in a fraction of the

time taken for the fully conjugate simulations and consequently provides a means whereby the cooling performance for a double-wall geometry can be very quickly benchmarked at an early design stage. The results from the computational simulations were also used to discuss some of the flow features occurring within the double-wall geometries which give rise to their high cooling performance, as well as to ascertain the potential implications of the reduced temperature ratio and Biot number used in the experimental tests.

11.3 Summary of the Thermomechanical Computational Work

- The temperature profiles developed via the decoupled conjugate method were used in assessing the thermomechanical performance of the diamond pedestal geometries. The simulations were three-dimensional and were used to identify features in the general stress field and how the development of films influenced the magnitude of the stress field. The simulations were then used to identify geometrical features that result in a reduction in the general magnitude of the stresses with the trends verified via main effects plots. In general, highly conductive geometries and those featuring more complete external films demonstrated preferable stress characteristics due to an increased temperature uniformity between the two walls.

- A second, and more fundamental study (shown in Appendix C) that was conducted in collaboration with the University of Oxford Solid Mechanics group, investigated a simple unit cell, axisymmetric double-wall geometry with periodicity boundary conditions. A simple thermal model was developed using a combination of correlation and CFD data allowing for a temperature profile to be developed based on only the impingement jet Reynolds number. The external temperature field was then decomposed into first and higher order approximations. The first order approximations were used to assess the effect of varying several geometric ratios on the developed stress field for systems featuring high

internal convective cooling in which the thermal gradient was predominantly concentrated in the film wall. The effect of varying coolant mass flow was then investigated with the potentially negative effect of over-cooling internally identified. Finally, a second order temperature profile was investigated for the external, film cooled surface with an optimal film hole pitch identified from a thermomechanical perspective.

11.4 Suggestions for Future Work

Below follow several suggestions pertaining to potential further developments to the work presented here.

11.4.1 Developments to the Experimental Facility

- Continuing work may involve the implementation of an automated traverse system in the experimental facility. The traverse could include both multi-hole probe and hotwire measurements to capture more detail about the upstream flow profile which could be imposed in further computational simulations. The traverse system could also be designed to permit flow measurements to be taken directly downstream of the test piece allowing the impact of various double-wall geometries on the mainstream flow field to be captured.

- The current iteration of the facility has been designed to permit mainstream gas temperatures nearing 475 K to be achieved with coolant fed at around 300 K. Consequently, the potential temperature ratio achievable in the facility is approximately 1.5. To provide a closer match to engine conditions, it is worth considering cooling of the coolant supply. This will also permit mainstream temperatures to be reduced to match currently achievable temperature ratios which it is expected will aid the longevity of some of the facility components. Furthermore, the addition of foreign gases to the mainstream may warrant consideration as this could provide a closer match on density ratio and Biot number.

- Other adaptions to the facility may include alternative instrumentation which may allow for other heat transfer characteristics to be ascertained. For example, Perspex test pieces with internal coatings of thermochromic liquid crystals could be used to investigate internal thermal characteristics.

11.4.2 Developments to the Aerothermal Computational Work

- The decoupled method developed currently negates potential internal crossflow effects. This internal crossflow may cause impingement jet deflection and vary maximum pedestal heat transfer coefficients. It is therefore suggested that an investigation could be performed to ascertain potential crossflow effects. A transfer function could then be developed to be applied in the domain enlarging procedure in the decoupled method to model any observed crossflow effects on the heat transfer coefficients.

- The single wall effusion work identified some limitations of the additive superposition method when applied to closely pitched film holes. It is suggested further work may wish to investigate alternate models, or indeed modifications to the two-dimensional film correlation, to more closely match experimental data for multiple rows of film holes. Whilst not an issue in the current study, a model for spanwise superposition may be useful if spanwise film hole pitching is further reduced.

- It is suggested that a study could be performed to investigate the sensitivity of the cooling performance to material solid thermal conductivity to try and gain a further understanding into the apparent over-conduction occurring in the computational methods. This study could also use laser sintering to manufacture a SS-316 test piece which could be experimentally investigated and the results compared to the current CNC/brazed test pieces to ascertain if local variations in thermal conductivity caused by the brazing preform are having a significant effect on thermal conduction.

11.4.3 Developments to the Thermomechanical Computational Work

- Future work into the thermomechanical performance of these double-wall systems may wish to extend the fundamental axisymmetric analyses. It is suggested a basic three-dimensional unit cell could be created with periodicity boundary conditions and a similar approach taken in which a simplified thermal model is developed. The study could then investigate the effect of varying a range of geometric parameters on the stress field developed.

- No work has yet been performed into the effect of curvature on double-wall systems. Consequently, it is suggested further work may involve a simple thermomechanical analysis of a two-dimensional extruded double-wall turbine geometry to gauge the effect of curvature, particularly towards the leading edge. A further development would then implement pressure boundary conditions to ascertain the additional stresses caused by the pressure difference across the blade.

12 Bibliography

[1] ACARE, 'Strategic Research & Innovation Agenda, 2017 Update, Volume 1', Advisory Council for Aviation Research and Innovation in Europe, 2017.

[2] N. Cumpsty, *Jet Propulsion*, 2nd ed. Cambridge, UK: Cambridge University Press, 2013.

[3] N. P. Padture, M. Gell, and E. H. Jordan, 'Thermal barrier coatings for gas-turbine engine applications', *Science*, vol. 296, no. 5566, pp. 280–284, 2002.

[4] F. J. Cunha, M. T. Dahmer, and M. K. Chyu, 'Heat Transfer Analysis', in *The Gas Turbine Handbook*, US Department of Energy, 2006, pp. 389–411.

[5] R. S. Bunker, 'Cooling design analysis', in *The Gas Turbine Handbook, US Department of Energy NETL*, 2006.

[6] J.-C. Han, S. Dutta, and S. Ekkad, *Gas Turbine Heat Transfer and Cooling Technology*, 2nd ed. CRC Press, Taylor & Francis Group, 2012.

[7] C. Soares, *Gas Turbines: A Handbook of Air, Land and Sea Applications*. Oxford: Butterworth-Heinemann/Elsevier, 2015.

[8] S. C. Lau, Y. S. Kim, and J. C. Han, 'Effects of fin configuration and entrance length on local endwall heat/mass transfer in a pin fin channel', in *ASME 1985 International Gas Turbine Conference and Exhibit*, Houston, Texas, 1985.

[9] M. K. Chyu, Y. C. Hsing, T. I.-P. Shih, and V. Natarajan, 'Heat Transfer Contributions of Pins and Endwall in Pin-Fin Arrays: Effects of Thermal Boundary Condition Modeling', *J. Turbomach.*, vol. 121, no. 2, pp. 257–263, Apr. 1999.

[10] M. K. Chyu, 'Heat Transfer and Pressure Drop for Short Pin-Fin Arrays With Pin-Endwall Fillet', no. 79160, p. V004T08A011, 1989.

[11] M. K. Chyu, Y. C. Hsing, and V. Natarajan, 'Convective Heat Transfer of Cubic Fin Arrays in a Narrow Channel', *J. Turbomach.*, vol. 120, no. 2, pp. 362–367, Apr. 1998.

[12] D. E. Metzger, R. A. Berry, and J. P. Bronson, 'Developing Heat Transfer in Rectangular Ducts With Staggered Arrays of Short Pin Fins', *J. Heat Transf.*, vol. 104, no. 4, pp. 700–706, Nov. 1982.

[13] Z. Wang, P. Ireland, T. V. Jones, and S. T. Kohler, 'Measurements of local heat transfer coefficient over the full surface of a bank of pedestals with fillet radii', *ASME Pap.*, no. 94-GT, p. 307, 1994.

[14] K. Funazaki, Y. Tarukawa, T. Kudo, S. Matsuno, R. Imai, and S. Yamawaki, 'Heat Transfer Characteristics of an Integrated Cooling Configuration for Ultra-High Temperature Turbine Blades: Experimental and Numerical Investigations', in *ASME Turbo Expo 2001: Power for Land, Sea, and Air*, 2001, p. V003T01A031–V003T01A031.

[15] R. J. Goldstein and A. I. Behbahani, 'Impingement of a circular jet with and without cross flow', *Int. J. Heat Mass Transf.*, vol. 25, no. 9, pp. 1377–1382, Sep. 1982.

[16] K. Jambunathan, E. Lai, M. A. Moss, and B. L. Button, 'A Review of Heat Transfer Data For Single Circular Jet Impingement', *Int. J. Heat Mass Transf.*, vol. 13, no. 2, pp. 106–115, Jun. 1992.

[17] D. H. Rhee, J. H. Choi, and H. H. Cho, 'Flow and Heat (Mass) Transfer Characteristics in an Impingement/Effusion Cooling System With Crossflow', *J. Turbomach.*, vol. 125, no. 1, p. 74, 2003.

[18] L. W. Florschuetz, D. E. Metzger, and C. C. Su, 'Heat Transfer Characteristics for Jet Array Impingement with Initial Crossflow', p. 10.

[19] N. Zuckerman and N. Lior, 'Impingement Heat Transfer: Correlations and Numerical Modeling', *J. Heat Transf.*, vol. 127, no. 5, p. 544, 2005.

[20] P. Forsyth, M. McGilvray, and D. R. H. Gillespie, 'Secondary flow and heat transfer coefficient distributions in the developing flow region of ribbed turbine blade cooling passages', *Exp. Fluids*, vol. 58, no. 1, Jan. 2017.

[21] S. C. Lau, R. D. McMillin, and J. C. Han, 'Heat Transfer Characteristics of Turbulent Flow in a Square Channel With Angled Discrete Ribs', *J. Turbomach.*, vol. 113, no. 3, pp. 367–374, Jul. 1991.

[22] J.-C. Han, 'Fundamental gas turbine heat transfer', *J. Therm. Sci. Eng. Appl.*, vol. 5, no. 2, p. 021007, 2013.

[23] D. G. Bogard and K. A. Thole, 'Gas Turbine Film Cooling', *J. Propuls. Power*, vol. 22, no. 2, pp. 249–270, Mar. 2006.

[24] D. G. Bogard, 'Airfoil film cooling', *Gas Turbine Handb. Natl. Energy Technol. Lab. Dep. Energy Morgant. WV Sect*, vol. 4, no. 2.1, 2006.

[25] B. Lakshminarayana, *Fluid Dynamics and Heat Transfer of Turbomachinery*. John Wiley & Sons Inc., 1996.

[26] S. Baldauf, A. Schulz, and S. Wittig, 'High-Resolution Measurements of Local Effectiveness From Discrete Hole Film Cooling', *J. Turbomach.*, vol. 123, no. 4, p. 758, 2001.

[27] S. Baldauf, M. Scheurlen, A. Schulz, and S. Wittig, 'Correlation of Film Cooling Effectiveness From Thermographic Measurements at Engine Like Conditions', p. 14, 2002.

[28] W. J. Mick and R. E. Mayle, 'Stagnation Film Cooling and Heat Transfer, Including Its Effect Within the Hole Pattern', *J. Turbomach.*, vol. 110, no. 1, pp. 66–72, Jan. 1988.

[29] L. M. Wright, S. T. McClain, and M. D. Clemenson, 'Effect of Density Ratio on Flat Plate Film Cooling With Shaped Holes Using PSP', *J. Turbomach.*, vol. 133, no. 4, p. 041011, 2011.

[30] C. Saumweber, A. Schulz, and S. Wittig, 'Free-Stream Turbulence Effects on Film Cooling With Shaped Holes', p. 9, 2002.

[31] H. Moustapha, M. F. Zelesky, N. C. Baines, and D. Japikse, *Axial and Radial Turbines*. USA: Concepts NREC, 2003.

[32] G. Cerri, A. Giovannelli, L. Battisti, and R. Fedrizzi, 'Advances in effusive cooling techniques of gas turbines', *Appl. Therm. Eng.*, vol. 27, no. 4, pp. 692–698, Mar. 2007.

[33] A. Ceccherini, B. Facchini, L. Tarchi, and L. Toni, 'Adiabatic and overall effectiveness measurements of an effusion cooling array for turbine endwall application', in *ASME Turbo Expo 2008: Power for Land, Sea, and Air*, 2008, pp. 775–788.

[34] K. M. B. Gustafsson and T. G. Johansson, 'An Experimental Study of Surface Temperature Distribution on Effusion-Cooled Plates', *J. Eng. Gas Turbines Power*, vol. 123, no. 2, p. 308, 2001.

[35] R. Krewinkel, 'A review of gas turbine effusion cooling studies', *Int. J. Heat Mass Transf.*, vol. 66, pp. 706–722, Nov. 2013.

[36] P. Renze, W. Schröder, and M. Meinke, 'Large-Eddy Simulation of Interacting Film Cooling Jets', in *Volume 3: Heat Transfer, Parts A and B*, Orlando, Florida, USA, 2009, pp. 81–90.

[37] G. E. Andrews, A. A. Asere, M. L. Gupta, and M. C. Mkpadi, 'Full coverage discrete hole film cooling: the influence of hole size', in *ASME 1985 International Gas Turbine Conference and Exhibit*, 1985, p. V003T09A003–V003T09A003.

[38] B. Gustafsson, 'Experimental Studies of Effusion Cooling', Doctor of Philosophy Thesis, Chalmers University of Technology, Goteborg, Sweden, 2001.

[39] A. M. Al Dabagh, G. E. Andrews, R. A. A. Abdul Husain, C. I. Husain, A. Nazari, and J. Wu, 'Impingement/Effusion Cooling: The Influence of the Number of Impingement Holes and Pressure Loss on the Heat Transfer Coefficient', *J. Turbomach.*, vol. 112, no. 3, pp. 467–476, Jul. 1990.

[40] L. Arcangeli, B. Facchini, M. Surace, and L. Tarchi, 'Correlative Analysis of Effusion Cooling Systems', *J. Turbomach.*, vol. 130, no. 1, p. 011016, 2008.

[41] D. Bohn and R. Krewinkel, 'Conjugate calculation of effusion cooling with realistic cooling hole geometries', in *ASME Turbo Expo 2009: Power for Land, Sea, and Air*, 2009, pp. 31–40.

[42] S. H. Kim, K. H. Ahn, J. S. Park, E. Y. Jung, K.-Y. Hwang, and H. H. Cho, 'Local heat and mass transfer measurements for multi-layered impingement/effusion cooling: Effects of pin spacing on the impingement and effusion plate', *Int. J. Heat Mass Transf.*, vol. 105, pp. 712–722, Feb. 2017.

[43] G. E. Andrews, A. A. Asere, M. C. Mkpadi, and A. Tirmahi, 'Transpiration Cooling: Contribution of Film Cooling to Overall Effectiveness', *Int. J. Turbo Jet Engines*, vol. 3, no. 2–3, pp. 245–256, 1986.

[44] R. S. Bunker, 'A Review of Shaped Hole Turbine Film-Cooling Technology', *J. Heat Transf.*, vol. 127, no. 4, p. 441, 2005.

[45] Y. Hu and H. Ji, 'Numerical study of the effect of blowing angle on cooling effectiveness of an effusion cooling', in *ASME Turbo Expo 2004: Power for Land, Sea, and Air*, 2004, pp. 877–884.

[46] S. J. Andrews, H. Ogden, and J. Marshall, 'Some Experiments on an Effusion Cooled Turbine Nozzle Blade', Ministry of Supply: Aeronautical Research Council, London, UK, Technical Report 267, 1956.

[47] A. Martin and S. J. Thorpe, 'Experiments on combustor effusion cooling under conditions of very high free-stream turbulence', in *ASME Paper No. GT2012-68863*, 2012.

[48] J. J. Scrittore, K. A. Thole, and S. W. Burd, 'Investigation of Velocity Profiles for Effusion Cooling of a Combustor Liner', *J. Turbomach.*, vol. 129, no. 3, p. 518, 2007.

[49] A. B. Wassell and J. K. Bhangu, 'The development and application of improved combustor wall cooling techniques', in *ASME 1980 International Gas Turbine Conference and Products Show*, 1980, p. V01AT01A066–V01AT01A066.

[50] K. H. Chua, J. Carrotte, P. Denman, and A. Spencer, 'Experimental Characterization of the Coolant Film Issuing From a Cooling Tile', in *Volume 1: Turbo Expo 2004*, Vienna, Austria, 2004, pp. 271–281.

[51] P. A. Denman, A. G. Barker, C. W. Jayatunga, and J. J. McGuirk, 'Modelling and Measurements of Combustor Cooling Tile Flows', in *Volume 2: Turbo Expo 2003*, Atlanta, Georgia, USA, 2003, pp. 585–592.

[52] G. L. Peacock and S. J. Thorpe, 'Experimental Study of Impingement Jet Cooling Above Pedestal Roughened Channels', in *Volume 5A: Heat Transfer*, Montreal, Quebec, Canada, 2015, p. V05AT11A027.

[53] V. Savarianandam, S. J. Thorpe, J. F. Carrotte, and M. Zedda, 'An Investigation of an Impingement / Pin-Fin Cooling System for Gas Turbine Combustor Applications', in *Volume 4: Heat Transfer, Parts A and B*, Copenhagen, Denmark, 2012, p. 871.

[54] P. C. Sweeney and J. F. Rhodes, 'An Infrared Technique for Evaluating Turbine Airfoil Cooling Designs', *J. Turbomach.*, vol. 122, no. 1, pp. 170–177, 1999.

[55] K. Manzhao, Z. Huiren, L. Songling, and Y. Hepeng, 'Internal heat transfer characteristics of Lamilloy configurations', *Chin. J. Aeronaut.*, vol. 21, no. 1, pp. 28–34, 2008.

[56] C. Nakamata *et al.*, 'Spatial Arrangement Dependance of Cooling Performance of an Integrated Impingement and Pin Fin Cooling Configuration', in *Volume 3: Turbo Expo 2005, Parts A and B*, Reno, Nevada, USA, 2005, pp. 385–395.

[57] S. K. Hong, D.-H. Rhee, and H. H. Cho, 'Effects of Fin Shapes and Arrangements on Heat Transfer for Impingement/Effusion Cooling with Crossflow', *J. Heat Transf.*, vol. 129, no. 12, p. 1697, 2007.

[58] R. S. Bunker, 'Gas Turbine Cooling: Moving From Macro to Micro Cooling', in *Volume 3C: Heat Transfer*, San Antonio, Texas, USA, 2013, p. V03CT14A002.

[59] M. K. Chyu and S. C. Siw, 'Recent Advances of Internal Cooling Techniques for Gas Turbine Airfoils', *J. Therm. Sci. Eng. Appl.*, vol. 5, no. 2, p. 021008, 2013.

[60] L. Li, H. Wan, W. Gao, F. Tong, and S. Sun, 'Investigation on Creep Characteristic of Nickel-Base Single Crystal Alloy Double Wall Cooling Specimen', 2018, p. 7.

[61] R. S. Bunker and T. T. Wallace, 'Turbine airfoil with double shell outer wall', US Patent 5,328,331, Jul-1994.

[62] M. R. Jackson, D. W. Skelly, R. G. Rowe, D. G. LaChapelle, and P. S. Wilson, 'Method for making a double-wall airfoil', US Patent 5,640,767, Jun-1997.

[63] M. R. Jackson, D. W. Skelly, R. G. Rowe, D. G. LaChapelle, and P. S. Wilson, 'Double wall turbine parts', US Patent 5,820,337, Oct-1998.

[64] W. S. Kvasnak, R. S. LaFleur, F. O. Soechting, C. R. Joe, J. Moroso, and D. A. Hayes, 'Method and Apparatus for Cooling a Wall Within a Gas Turbine Engine', US 6,514,042 B2, 04-Feb-2003.

[65] G. Liang, 'Cooling system for a turbine blade having a double outer wall', US Patent 6,808,367 B1, 26-Oct-2004.

[66] R. P. Moore, 'Cooled Airfoils for a Gas Turbine Engine', 5702232, Dec-1997.

[67] J. F. Rhodes, 'Cooled Airfoil', 6,213,714 B1, 10-Apr-2001.

[68] J.-C. Han and A. P. Rallabandi, 'Turbine Blade Film Cooling Using PSP Technique', *Front. Heat Mass Transf.*, vol. 1, no. 1, Jun. 2010.

[69] M. K. Quinn, L. Yang, and K. Kontis, 'Pressure-Sensitive Paint: Effect of Substrate', *Sensors*, vol. 11, no. 12, pp. 11649–11663, Dec. 2011.

[70] S. Mhetras, J.-C. Han, and R. Rudolph, 'Effect of Flow Parameter Variations on Full Coverage Film-Cooling Effectiveness for a Gas Turbine Blade', p. 11, 2007.

[71] T. H. Wong, P. T. Ireland, and K. P. Self, 'Film Cooling Effectiveness Measurements on Trailing Edge Cutback Surface and Lands Following Novel Cross Corrugated Slot Geometry', in *ASME Turbo Expo 2016: Turbomachinery Technical Conference and Exposition*, 2016, p. V05CT19A024–V05CT19A024.

[72] T. H. Wong, 'Novel Cooling Design for Blade or Vane Trailing Edges', Doctor of Philosophy (DPhil) Thesis, University of Oxford, Oxford Thermofluids Institute, 2019.

[73] T. V. Jones, 'Theory for the use of foreign gas in simulating film cooling', p. 6, 1999.

[74] R. J. Moffat, 'Describing the uncertainties in experimental results', *Exp. Therm. Fluid Sci.*, vol. 1, no. 1, pp. 3–17, 1988.

[75] B. Kirollos and T. Povey, 'An Energy-Based Method for Predicting the Additive Effect of Multiple Film Cooling Rows', *J. Eng. Gas Turbines Power*, vol. 137, no. 12, p. 122607, 2015.

[76] M. Thomas and T. Povey, 'A novel scalar tracking method for optimising film cooling systems', *Proc. Inst. Mech. Eng. Part J. Power Energy*, vol. 230, no. 1, pp. 3–15, Feb. 2016.

[77] M. Thomas, 'Optimization of Endwall Film-Cooling in Axial Turbines', University of Oxford, Oxford, 2014.

[78] J. P. Sellers, 'Gaseous Film Cooling With Multiple Injection Stations', *AIAA J.*, vol. 1, no. 9, pp. 2154–2156, Sep. 1963.

[79] J. C. Ling, P. T. Ireland, and L. Turner, 'Full coverage film cooling for combustor transition sections', in *ASME Turbo Expo 2002: Power for Land, Sea, and Air*, 2002, pp. 1011–1021.

[80] Y. Jiang, A. V. Murray, P. T. Ireland, and L. di Mare, 'Jets Interaction in Effusion Cooling, Part I: Experimental and Numerical Study', in *ASME Turbo Expo 2019: Turbomachinery Technical Conference and Exposition*, Phoenix, Arizona, USA, 2019.

[81] ANSYS, *Fluent User Guide (Release 16.2)*. ANSYS, 2015.

[82] A. Lewark, 'Technical report: Investigation of Double-Wall Turbine Blade Cooling Possibilities', Rolls-Royce PLC, Feb. 2008.

[83] A. Bradley, 'Prediction of vane film cooling in gas turbines: Correlations and Parameters', Linkoping University, Institute of Technology, Linkoping, Sweden, 2009.

[84] R. J. Goldstein, 'Film Cooling', in *Advances in Heat Transfer*, vol. 7, Academic Press, 1971, pp. 321–379.

[85] A. V. Murray, P. T. Ireland, T. H. Wong, S. W. Tang, and A. J. Rawlinson, 'High Resolution Experimental and Computational Methods for Modelling Multiple Row Effusion Cooling Performance', *Int. J. Turbomach. Propuls. Power*, vol. 3, no. 1, p. 4, Jan. 2018.

[86] A. R. Byerley, 'Heat Transfer Near the Entrance to a Film Cooling Hole in a Gas Turbine Blade', Doctor of Philosophy (DPhil) Thesis, University of Oxford, Oxford, 1989.

[87] A. V. Murray, P. T. Ireland, and A. J. Rawlinson, 'An Integrated Conjugate Computational Approach for Evaluating the Aerothermal and Thermomechanical Performance of Double-Wall Effusion Cooled Systems', in *ASME Turbo Expo 2017: Turbomachinery Technical Conference and Exposition*, 2017, p. V05BT22A015–V05BT22A015.

[88] N. Gascoin, 'High temperature and pressure reactive flows through porous media', *Int. J. Multiph. Flow*, vol. 37, no. 1, pp. 24–35, Jan. 2011.

[89] H. S. Ifti, T. Hermann, and M. McGilvray, 'Flow Characterisation of Transpiring Porous Media for Hypersonic Vehicles', in *22nd AIAA International Space Planes and Hypersonics Systems and Technologies Conference*, Orlando, FL, 2018.

[90] A. V. Murray, 'Double-Skin Systems in Turbine NGV/Blade Applications', Master of Research Dissertation, University of Cambridge, Whittle Laboratory, 2015.

[91] A. V. Murray, 'Double-Skin Turbine Cooling Technologies - A Report of the Conjugate Computational Fluid Dynamics and Thermomechanical Finite Element Analyses Conducted at the Osney Southwell Thermo-Fluids Laboratory', University of Oxford, Osney Thermo-Fluids Laboratory, Oct. 2015.

[92] J. E. Pope, *Rules of Thumb for Mechanical Engineers: A Manual of Quick Accurate Solutions to Everyday Mechanical Engineering Problems*. Gulf Professional Publishing, 1997.

[93] D. Zhu and R. A. Miller, 'Thermal Conductivity and Elastic Modulus Evolution of Thermal Barrier Coatings under High Heat Flux Conditions', *J. Therm. Spray Technol.*, vol. 9, no. 2, pp. 175–180, Jun. 2000.

[94] A. M. Howatson, P. G. Lund, and J. D. Todd, *Engineering Tables and Data*, 3rd ed. Department of Engineering Science, University of Oxford, 2009.

[95] D. R. H. Gillespie, 'Intricate Internal Cooling Systems for Gas Turbine Blading', Doctor of Philosophy (DPhil) Thesis, University of Oxford, Osney Thermo-Fluids Laboratory, 1996.

[96] P. T. Ireland, A. J. Neely, D. R. Gillespie, and A. J. Robertson, 'Turbulent heat transfer measurements using liquid crystals', *Int. J. Heat Fluid Flow*, vol. 20, no. 4, pp. 355–367, 1999.

[97] D. R. H. Gillespie, A. R. Byerley, P. T. Ireland, Z. Wang, T. V. Jones, and S. T. Kohler, 'Detailed Measurements of Local Heat Transfer Coefficient in the Entrance to Normal and Inclined Film Cooling Holes', *J. Turbomach.*, vol. 118, no. 2, pp. 285–290, Apr. 1996.

[98] S. Luque, J. Batstone, D. R. H. Gillespie, T. Povey, and E. Romero, 'Full Thermal Experimental Assessment of a Dendritic Turbine Vane Cooling Scheme', *J. Turbomach.*, vol. 136, no. 2, p. 021011, 2014.

[99] C. Son, G. Dailey, P. Ireland, and D. Gillespie, 'An Investigation of the Application of Roughness Elements to Enhance Heat Transfer in an Impingement Cooling System', 2005, pp. 465–479.

[100] C. L. P. Tsang, D. R. H. Gillespie, P. T. Ireland, and G. M. Dailey, 'Analysis of Transient Heat Transfer Experiments', in *Proceedings of the 8th International Symposium on Transport Phenomena and Dynamics of Rotating Machinery*, Honolulu, Hawaii, USA, 2000, vol. 2, pp. 714–721.

[101] F.-M. Fang, 'A Design Method for Contractions With Square End Sections', *J. Fluids Eng.*, vol. 119, no. 2, p. 454, 1997.

[102] Promat GmbH, 'Promat: High Temperature Microporous Insulation'. Promat GmbH, 2015.

[103] BS EN ISO, 'BS EN ISO 9300:2005 - Measurement of Gas Flow by Means of Critical Flow Venturi Nozzles'. BSI, 21-Oct-2005.

[104] D. Martin, 'Effects of High Intensity, Large-Scale Free-Stream Turbulence on Combustor Effusion Cooling', Doctor of Philosophy Thesis, Loughborough University, School of Aeronautical and Automotive Engineering, 2013.

[105] Z. Wang, P. T. Ireland, and S. T. Kohler, 'Gas Temperature Measurement in Internal Cooling Passages', in *Volume 4: Heat Transfer; Electric Power; Industrial and Cogeneration*, Birmingham, UK, 1996, p. V004T09A059.

[106] B. Kirollos, 'Aerothermal Optimisation of Novel Cooling Schemes for High Pressure Components using Combined Theoretical, Numerial and Experimental Techniques', Doctor of Philosophy (DPhil) Thesis, University of Oxford, Oxford, 2015.

[107] N. E. Holgate, 'Novel Leading Edge Film Cooling Experiments and Geometries', Doctor of Philosophy (DPhil) Thesis, University of Oxford, Oxford, 2019.

[108] FLIR, 'LWIR Science-Grade Camera: FLIR A655sc: 17-1683-INS-A655sc Datasheet'. FLIR, 20-Apr-2018.

[109] FLIR, 'The Ultimate Infrared Handbook for R&D Professionals (T559243)'. FLIR, 2012.

[110] N. E. Holgate, P. T. Ireland, and E. Romero, 'The Effects of Combustor Cooling Features on Nozzle Guide Vane Film Cooling Experiments', 2018, p. 13.

[111] A. V. Murray, P. T. Ireland, and E. Romero, 'Development of a Steady-State Experimental Facility for the Analysis of Double-Wall Effusion Cooling Geometries', *J. Turbomach.*, vol. 141, Apr. 2019.

[112] Omega® Engineering, 'ANSI and IEC Color Codes† for Thermocouples, Wire and Connectors', Omega® Engineering, 2019.

[113] Honeywell, 'TruStability® Board Mount Pressure Sensors, HSC Series—High Accuracy, Compensated/Amplified, ±1.6 mbar to ±10 bar | ±160 Pa to ±1 MPa | ±0.5 inH2O to ±150 psi, Digital or Analog Output'. Honeywell, 2017.

[114] T. J. Carter, 'Common failures in gas turbine blades', *Eng. Fail. Anal.*, vol. 12, no. 2, pp. 237–247, Apr. 2005.

[115] G. S. Azad, J.-C. Han, S. Tend, and R. J. Boyle, 'Heat Transfer and Pressure Distributions on a Gas Turbine Blade Tip', *J. Turbomach.*, vol. 122, p. 8, Oct. 2000.

[116] V. U. Kakade, S. J. Thorpe, and M. Gerendás, 'Effusion-Cooling Performance at Gas Turbine Combustor Representative Flow Conditions', in *Volume 4: Heat Transfer, Parts A and B*, Copenhagen, Denmark, 2012, p. 857.

[117] N. E. Holgate, P. T. Ireland, and E. Romero, 'The Effects of Combustor Cooling Features on Nozzle Guide Vane Film Cooling Experiments', *J. Turbomach.*, vol. 141, no. 1, p. 011005, Oct. 2018.

[118] M. J. Holland and T. F. Thake, 'Rotor blade cooling in high pressure turbines', *J. Aircr.*, vol. 17, no. 6, pp. 412–418, Jun. 1980.

[119] G. B. Kelly and D. G. Bogard, 'An Investigation of the Heat Transfer for Full Coverage Film Cooling', in *Volume 5: Turbo Expo 2003, Parts A and B*, Atlanta, Georgia, USA, 2003, pp. 581–590.

[120] F. E. Ames, 'Aspects of Vane Film Cooling With High Turbulence: Part I - Heat Transfer', *J. Turbomach.*, vol. 120, pp. 768–776, Oct. 1998.

[121] J. Dittmar, A. Schulz, and S. Wittig, 'Adiabatic Effectiveness and Heat Transfer Coefficient of Shaped Film Cooling Holes on a Scaled Guide Vane Pressure Side Model', *Int. J. Rotating Mach.*, vol. 10, no. 5, pp. 345–354, Jan. 2004.

[122] R. J. Goldstein, A. I. Behbahani, and K. K. Heppelmann, 'Streamwise distribution of the recovery factor and the local heat transfer coefficient to an impinging circular air jet', *Int. J. Heat Mass Transf.*, vol. 29, no. 8, pp. 1227–1235, Aug. 1986.

[123] E. Elmukashfi, A. V. Murray, P. T. Ireland, and A. C. F. Cocks, 'Analysis of the Thermomechanical Stresses in Double-Wall Effusion Cooled Systems', *Rev. J. Turbomach.*, 2019.

[124] D. Dye, K. T. Conlon, P. D. Lee, R. B. Rogge, and R. C. Reed, 'Welding of Single Crystal Superalloy CMSX-4: Experiments and Modeling', in *Superalloys 2004 (Tenth International Symposium)*, 2004, pp. 485–491.

[125] K. W. Van Treuren, 'Impingement flow heat transfer measurements of turbine blades using a jet array', DTIC Document, 1994.

[126] Evonik Industries AG, 'Rohacell® for the Automotive Industry: Technical Information'. Evonik Industries AG, Jan-2017.

[127] G. Natsui *et al.*, 'Experimental Evaluation of Large Spacing Compound Angle Full-Coverage Film Cooling Arrays: Adiabatic Film Cooling Effectiveness', *J. Turbomach.*, vol. 138, no. 7, p. 071001, Feb. 2016.

[128] M. Thomas, B. Kirollos, D. Jackson, and T. Povey, 'Experimental and CFD Studies of NGV Endwall Cooling', in *Volume 3B: Heat Transfer*, San Antonio, Texas, USA, 2013, p. V03BT13A056.

[129] D. M. Jacobson and G. Humpston, *Principles of Brazing*. Ohio, United States of America: ASM International, 2005.

Appendix A: Simple Cooling Analysis of an Isothermal Blade

For an isothermal blade exposed to a uniform external temperature field and cooled by internal convection only (i.e. excluding external film cooling), a simplified thermal analysis can be performed which relates the non-dimensional coolant mass flow (*m**), convective efficiency of the blade coolant passage (η_c), and overall cooling effectiveness achieved (ε_o).

The heat flow to the blade due to the external hot gas field is equated to the enthalpy rise of the coolant flow due to convective heat pick-up as per equation A.1. To further simplify the analysis, an area-averaged external heat transfer coefficient is assumed.

$$Q \;=\; m_c c_p (T_{c,e} - T_{c,i}) \;=\; \int_0^A h_{ext}(T_\infty - T_m)dA \;=\; \bar{h}_{ext} A (T_\infty - T_m) \qquad \textit{(A.1)}$$

Rearranging equation A.1 and dividing through by the difference in metal temperature and coolant inlet temperature gives the result in A.2.

$$\frac{(T_\infty - T_m)}{(T_m - T_{c,i})} = \eta_c \frac{m_c c_p}{\bar{h}_{ext} A} = \eta_c m^* \qquad \textit{(A.2)}$$

The result can be rearranged to be defined in terms of overall cooling effectiveness as per equation A.3.

$$\varepsilon_o = \frac{(T_\infty - T_m)}{(T_\infty - T_{c,i})} = \frac{\eta_c m^*}{1 + \eta_c m^*} \qquad \textit{(A.3)}$$

Appendix B: Double-Wall Geometrical Investigation Range

Below follows the basic range of double-wall geometric parameters used in creating the diamond pedestal geometries and used as the basis for the circular pedestal geometries. It is noted that across all investigated geometries, wall thicknesses $L_{w,f}$ and $L_{w,i}$ were kept constant at unity to reduce the design space.

$L_{w,f} = L_{w,i}$ = 0.5 – 1.5 mm (Film and Impingement Wall Thickness)

L_p = 0.5 – 1.5 mm (Passage/Pedestal Height)

L_1 = 0.5 – 1.5 mm (Square/Diamond Pedestal Edge Length – Equates to Hydraulic Diameter)

L_2 = 0.5 – 1.5 mm (Spacing Between Pedestals)

$D_f = D_i$ = 0.5 – 1.0 mm (Film and Impingement Wall Diameters)

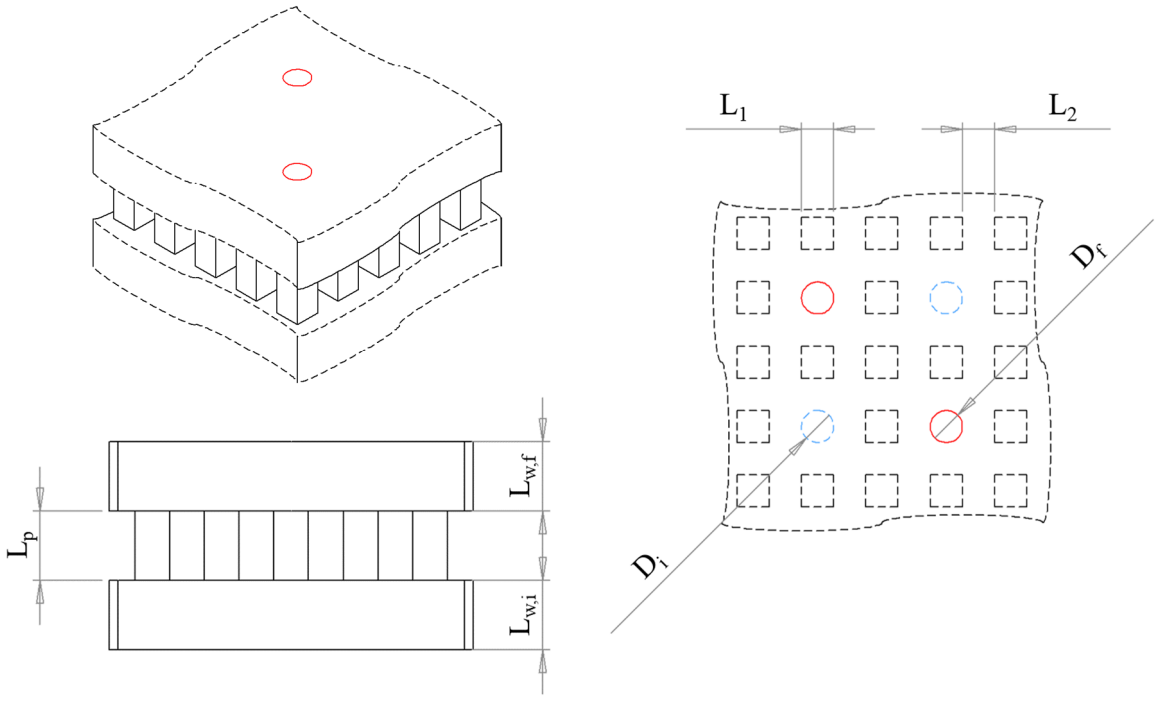


Figure B.1 – Example double-wall geometry with range of feature sizes used in the study

Appendix C: Axisymmetric Double-Wall Thermomechanical Analyses

To further understand the effect of the double-wall geometric parameters on the thermomechanical stress field, a second study was performed to complement that presented in Chapter 6. This work was conducted in collaboration with the University of Oxford's Solid Mechanics group (namely Dr Elsiddig Elmukashfi and Prof Alan Cocks) and resulted in a joint publication. The present author was responsible for the development of the thermal model, along with helping to process and understand the thermomechanical results.

In the study, an idealised model of a double-wall system is assumed. A unit cell element is considered as identified in Figure C.1 (left) where it is shown as part of an infinite repeating structure (noting the omission of the impingement and film holes). A three-dimensional representation of this unit cell is demonstrated in Figure C.1 (right). In the following analysis the temperature fields are assumed to be independent of the circumferential (θ) direction. Additionally, periodic boundary conditions are imposed at the edges of the unit cell. Consequently, the model is assumed to be axisymmetric.

Figure C.1 also demonstrates the geometrical nomenclature for the study. Across the simulations, the thickness of both the internal impingement and external film walls were constant (i.e. $L_{w,f} = L_{w,i} = L_w = 1$ mm). The effect of varying other geometric parameters on the thermal stress field was investigated across the study. These included varying ratios of:

- Pedestal height – L_p/L_w
- Pedestal diameter – D_p/L_w
- Pedestal spacing – L_b/L_w
- Fillet size – R_p/L_w

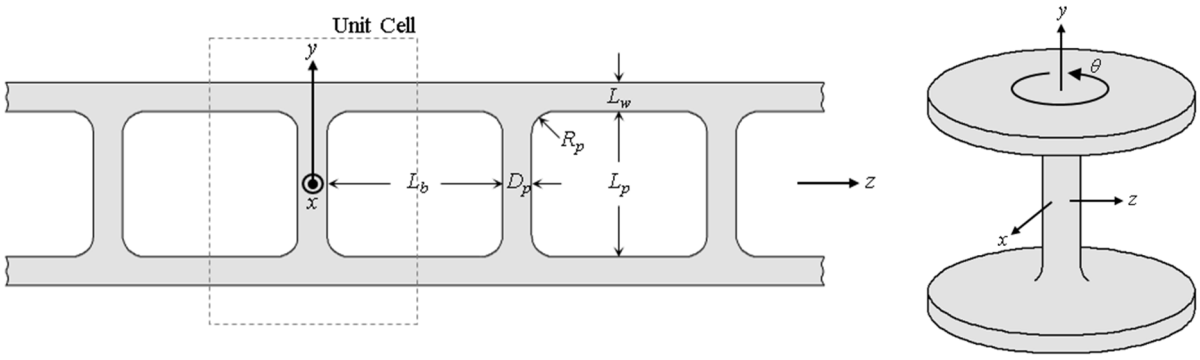


Figure C.1 - Left) Infinite repeating double-wall structure identifying the repeating unit cell. Right) Three-dimensional representation of the unit cell

C.1 Two-Dimensional Thermal Model

The literature on the cooling of gas turbines is rife with empirical correlations to predict the Nusselt number for various cooling features, for example impingement cooling incorporating various forms at differing Reynolds numbers and wall spacings, or pin-fin/pedestal cooling with different geometrical features and Reynolds numbers. However, correlations are unavailable (at least in the open literature) for systems such as the double-wall geometry considered here, where the system is an amalgamation of various cooling features which closely effect the performance of one another.

To create a temperature distribution in the two-dimensional unit cell section representative of that which would be expected during operation, a thermal model was developed that utilised a combination of empirical correlations and observations informed by computational simulations. The output of this model is a Nusselt number (and consequently heat transfer coefficient) distribution over the internal surface of the representative geometry, and varying temperature over the external surface of the film wall, thereby modelling the effect of film cooling. Through knowledge of the heat transfer coefficient and driving temperature distribution over the surfaces of the double-wall geometry, a temperature distribution can be developed throughout the solid via an FEA Fourier law conduction analysis. The section below gives a more detailed description of the thermal model that was developed by the author.

C.1.1 Internal Surface of the Film Wall

High levels of local heat transfer coefficient can be achieved by impingement cooling [6] where the high velocity coolant jet impacts the surface resulting in very high stagnation point heat transfer coefficients. General flow mixing is also increased through mixing of the jet flow after impingement. CFD typically struggles to accurately predict impingement jet heat transfer using lower fidelity turbulence models [19], and, whilst large eddy simulations (*LES*) provide reasonable accuracy, the computational resource requirements are high. Therefore, empirical correlations are used in design to predict the area-averaged or stagnation point Nusselt number based on flow characteristics such as the impingement jet Reynolds number, as well as geometric parameters such as dimensionless target plate from impingement hole distance (y/D_i). In the current model, three correlations were used to predict impingement zone local Nusselt number. These are as follows:

$35200 \leq Re_i \leq 121000$ $y/D_i = 6$ [15]	$\overline{Nu}_i = \frac{{Re_i}^{0.6}}{3.329 + 0.273(z/D_i)^{1.3}}$	*(C.1)*
$35200 \leq Re_i \leq 121000$ $y/D_i = 12$ [15]	$\overline{Nu}_i = \frac{{Re_i}^{0.6}}{4.577 + 0.4357(z/D_i)^{1.14}}$	*(C.2)*
$Re_i \geq 61000$ $y/D_i \geq 6$ [122]	$\overline{Nu}_i = \frac{\left(24 - \left\lvert y/D_i - 7.75 \right\rvert\right) {Re_i}^{0.76}}{533 + 44(z/D_i)^{1.285}}$	*(C.3)*

It is noted that equations C.1 – C.3 pertain to the area-averaged Nusselt number as a function of radial distance for the target surface considered (here based on the *z* direction) and are obtained via correlated experimental data [15], [122]. However, of particular interest here is the variation in local Nusselt number across the target surface (again in the *z* direction). Consequently, the results of the area-averaged Nu_i at a range of distances from the stagnation

point were used to determine the local Nusselt number. Note that equations C.1 – C.3 each have a range of target plate spacings (y/D_i) and Re_i over which they are valid. As there are gaps between these, the correlations were used slightly off their specified range in some cases. For example, equation C.1 was used for $6 \leq y/D_i \leq 9$, and equation C.2 for $9 \leq y/D_i \leq 12$. Outside of the specified ranges of y/D_i and Re_i, the correlation in equation C.3 was used as the results were deemed to be acceptable for the current application – although it is noted for the present work, minimum values of y/D_i of 6 were specified thus predominantly staying within the ranges advised by the correlations. At very low values of z/D_i (i.e. less than 2), a secondary peak is frequently observed in the Nusselt number outside of the stagnation point (often displaying higher *Nu* than at the stagnation point) which is thought to result from heat transfer enhancement from vortex rings in the shear layer [122]. These are disregarded in these correlations, however, the overall effect of this on the temperature profile and resulting stress field is deemed a small one.

Figure C.2 demonstrates the performance of the correlations at varying impingement jet Reynolds numbers and target plate spacings.

C.1.2 Impingement and Film Holes

The convective cooling effect within the impingement and film holes was modelled using the Dittus-Boelter correlation, a widely used correlation for predicting average heat transfer within a conduit. The correlation is repeated below in equation C.4.

$$\overline{Nu} = 0.023\ {Re_D}^{0.8}\ Pr^{0.4} \qquad \textit{(C.4)}$$

For holes perpendicular to the surface, as was the case for the current study, the correlation demonstrated satisfactory performance against experimental observations (see for example [95], [97]) over the majority of the hole area. The results also compared favourably to those from the decoupled simulations presented in Chapter 5.

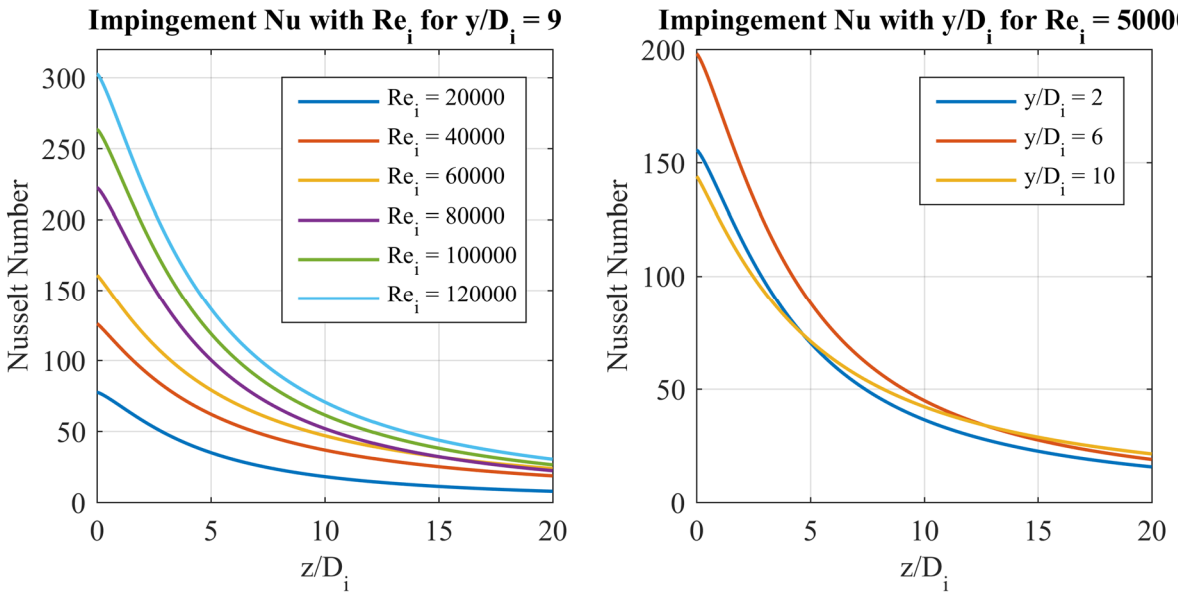


Figure C.2 – Variation in local impingement zone Nusselt number moving radial outwards from the stagnation point at (left) various impingement jet Reynolds numbers and (right) various target plate spacings

C.1.3 Film Cooling Model

The author's model for the external film cooling performance was based on the modified Goldstein correlation [84] combined with the superposition method [78] presented in Chapter 5. Distinct from the other surfaces, the heat transfer driving gas temperature, was based upon the adiabatic film temperature and was combined with a uniform heat transfer coefficient.

C.1.4 Pedestals and Other Internal Surfaces

The Nusselt number on all the other surfaces were derived from the decoupled conjugate heat transfer CFD simulations discussed in Chapter 5. For the surfaces of interest, heat transfer coefficients were calculated for several double-wall geometries using the decoupled method. The data were then rendered dimensionless yielding least squared approximations for the Nusselt number to be predicted in geometries not explicitly simulated. The Nusselt numbers predicted via this regression procedure were scaled in the differing geometries based upon the impingement zone data (for example the relationship observed in the decoupled conjugate method for stagnation point h_i and peak h_{ped} at varying pedestal spacings) obtained using the

aforementioned correlations. Figure C.3 demonstrates one such curve which shows the distribution for Nusselt number along the length of the pedestal (the side facing the impingement zone). The figure demonstrates the relatively high heat transfer occurring at the end of the pedestal connected to the impingement jet target wall, a result of a secondary impact from the wall jet, produced by the impinging jet, as it strikes this section of the pedestal. This behaviour is very similar to that observed experimentally by Son et al. [99] for pimples connected to the surface of the impingement target wall. As the distance between the impingement stagnation point and the pedestal increases, the high levels of heat transfer progressively diminish. At spacings commonly associated with the double-wall type cooling geometries researched in this thesis, this correlation for *Nu* distribution is appropriate.

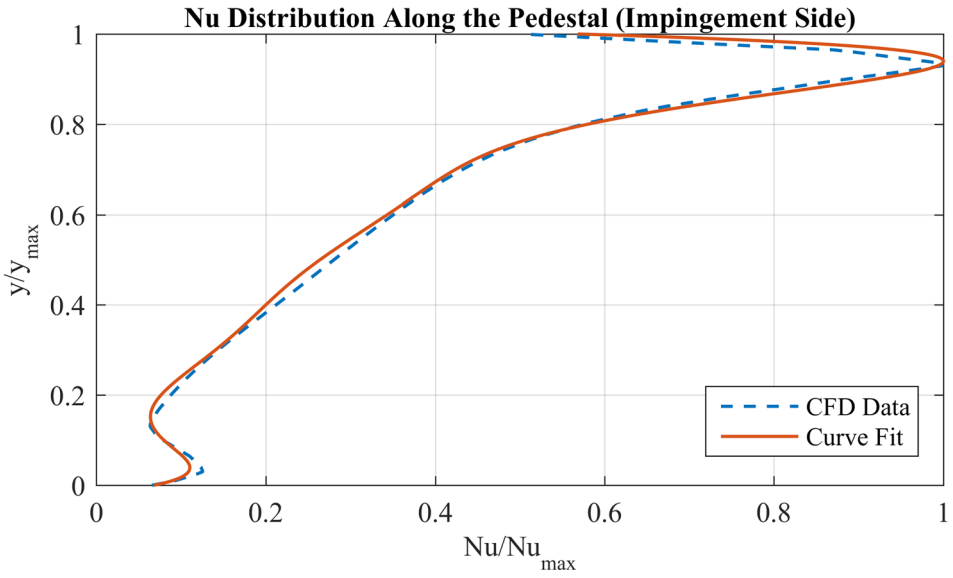


Figure C.3 – Variation in Nusselt number along the length of the pedestal (side facing the impingement hole) with fitted curve used in the two-dimensional thermal model

C.1.5 Thermal Model Example

An example of the resulting *Nu* distribution over the surface of the two-dimensional geometry is shown on the left-hand side of Figure C.4 where Re_i was set to be 80,000 for a pedestal height giving y/D_i equal to 6. Note that, in this example, there is no external film

cooling modelled – in other words, a uniform external heat transfer coefficient and uniform mainstream driving gas temperature are modelled.

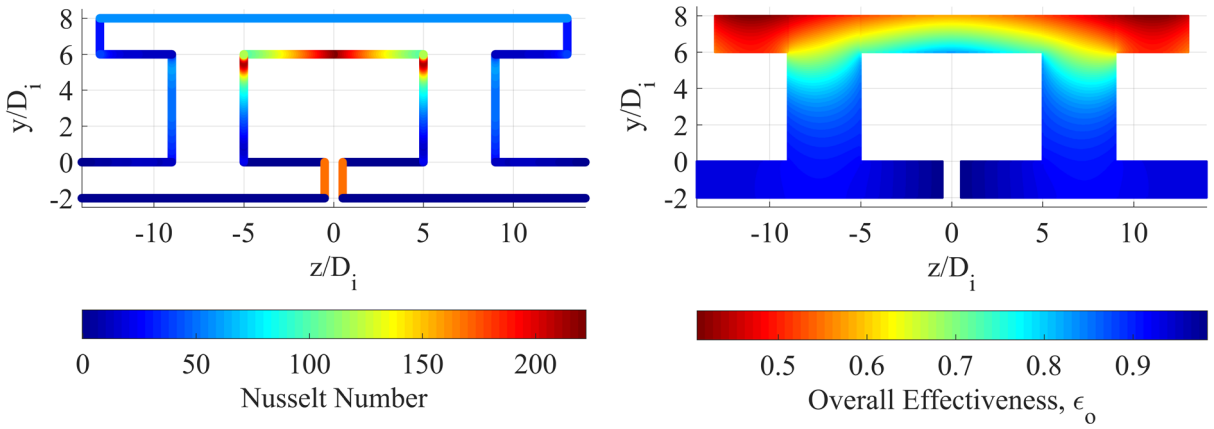


Figure C.4 – Example of (left) the Nusselt number profile developed via the thermal model and (right) the corresponding overall effectiveness temperature profile that results from the model, for the case of Re_i = 80000 and pedestal height of y/D_i = 6

C.1.6 Simplification of the Thermal Model

In the present study, the temperature field model discussed in sections C.1.1 – C.1.4 was further simplified. For the internal convective cooling, this simplification entailed specifying area-averaged heat transfer coefficients ($\bar{h}$) on each of the internal surfaces as obtained using the developed thermal model. For the external, film cooled wall, however, the heat transfer driving gas temperature (the adiabatic film temperature), was decomposed into first and higher order components, the latter of which represented the spatial variation. For each of these components, separate mechanical simulations can be performed, and the overall stress solution evaluated by superimposing the individual components. In this way, the significance of each order representing the temperature field was ascertained. The general form of the decomposed temperature field is shown in equation C.5 where the first order approximation is denoted by a bar over the symbol and a tilde denotes the amplitude of the higher order approximations. The shape functions of the higher order approximations are denoted by *f(z)*. The local stress field can subsequently be calculated as the superposition of the stresses arising from the various orders of approximation as per equation C.6.

$$T = \bar{T} + \tilde{T} f(z) \tag{C.5}$$

$$\sigma_{ij} = \bar{\sigma}_{ij} + \sum \tilde{\sigma}_{ij} \tag{C.6}$$

The following analysis predominantly focuses on the mechanical effects arising due to the first order temperature field approximation, which, in general, captures the effect of changing the various geometric ratios on the developed stress field. Figure C.5 demonstrates the area-averaged heat transfer coefficients for the three internal surfaces (the internal surfaces of both the impingement and film walls, and the pedestal wall) as impingement Reynolds number and geometric ratio L_p/L_w are varied. As discussed in the development of the thermal model, heat transfer coefficients on these internal surfaces are related to Re_i and consequently peak Nusselt numbers observed at the impingement zone stagnation point based on the correlations in equations C.1 – C.3. Maximum Nu_0 for these correlations occurred at impingement hole to target wall spacings (y/D_i) of around 6 – 8 before a general decrease in heat transfer coefficients were observed. Thus, in the figure, the maximum heat transfer coefficients are observed for L_p/L_w of 4 (corresponding to a y/D_i of 8 given D_i = *0.5* mm) on all three surfaces.

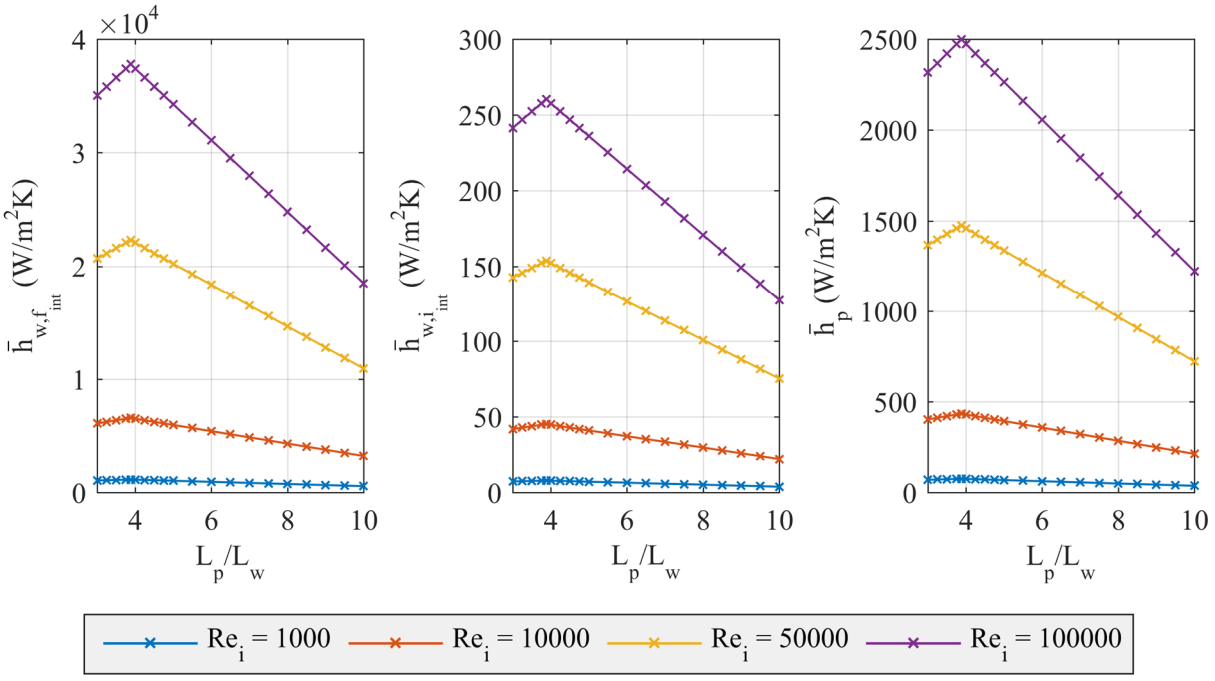


Figure C.5 - Heat transfer coefficient based on the first order approximation of the thermal field, for the three internal surfaces of the unit cell at various impingement Reynolds numbers (where D_i/L_w = 0.5)

C.2 Effect of Geometric Features on Thermomechanical Stresses

The following section discusses how varying the different geometric dimensions affects the thermal stresses developed based on the first order temperature field approximations. The numerical simulations were performed by the Solid Mechanics group [123] using *ABAQUS*. The meshes were structured in nature with a mesh sensitivity study performed. Material properties were based upon the *ABAQUS* built-in carbon steel specification which was deemed close enough to an aerofoil material to allow the relevant trends to be captured.

A theoretical bending analysis was performed by the Solid Mechanics group [123]. The model demonstrates that the peak radial and circumferential stresses occur at the fillet between the pedestal and film cooled wall for systems in which internal cooling performance is high. The maximum principal stress also occurs at the fillet and is in the radial direction (due to the radial stress concentration being greater than the circumferential concentration). A nominal stress was defined ($\bar{\sigma}$) as the value of the radial and circumferential stresses, far from the fillet (at a location $z = 0.5(D_p + L_b)$) where the radial and circumferential stresses match. This nominal stress has a maximum value on the internal surface of the film cooled wall. Indeed, the theoretical bending analysis performed by the Solid Mechanics group showed that this nominal stress takes a maximum value for an infinitely long pedestal with maximum internal cooling where the temperature gradient is largely confined to the outer wall. The value of the maximum nominal stress for this case is repeated in equation C.7, where $E'=E/(1-\nu)$. Consequently, in presenting maximum nominal stress data for each geometry, the data is presented as being non-dimensionalised by $\beta\Delta\bar{T}E'$. The maximum principal stress at the fillet can be obtained by multiplying this nominal stress by the radial stress concentration.

$$\bar{\sigma}_{max} \approx \frac{1}{2}\beta\Delta\bar{T}E' \qquad (C.7)$$

For the initial analyses, a very high internal heat transfer coefficient was specified in order that the dominant temperature gradient occurred in the film wall, and the pedestal and impingement wall temperatures were close to the coolant temperature. In order to achieve this, the impingement jet Reynolds number was set to 10^6 for each geometric iteration investigated.

Figure C.6 (left) demonstrates the variation in maximum nominal stress with varying pedestal height ratio L_p/L_w, for four values of pedestal spacing ratio L_b/L_w. The results support the theoretical model which indicated that nominal and maximum principal stresses increase with increasing pedestal height. This is expected as an increasing pedestal height reduces the heat conducted to the inner wall. Consequently, the magnitude of the temperature difference between the walls – which directly effects the relative expansion of the walls – increases. This causes the corresponding rise in stress. For L_p/L_w greater than approximately 10, there is little further increase in maximum nominal stress. The figure also demonstrates a considerable increase in the maximum nominal stresses for low values of L_b/L_w. This is almost certainly a consequence of the nominal stress being influenced by the fillet stress concentrations as the pedestal spacing is reduced. However, the figure indicates that, above a L_b/L_w of unity, there is little further thermomechanical benefit to increasing the pedestal spacing ratio.

Figure C.6 (right) shows how the fillet radial and circumferential stress concentration factors ($K_\sigma = \sigma_{max}/\bar{\sigma}_{max}$) vary with the pedestal radius ratio R_p/L_w for four values of pedestal diameter ratio D_p/L_w. It is noted that these stress concentrations were insensitive to pedestal spacing ratio L_b/L_w. The figure clearly demonstrates the radial stress concentrations exceed those of the circumferential components, which confirms that the maximum principal stresses occur in the radial direction at the fillet. The benefit of increasing the pedestal fillet radius is also evident with stress concentrations quickly dropping off as the fillet radius is initially increased. The stress concentration also appears to decrease with reducing pedestal size. This is expected as the fillet radius becomes larger, in proportion to the size of the pedestal, as the pedestal diameter reduces.

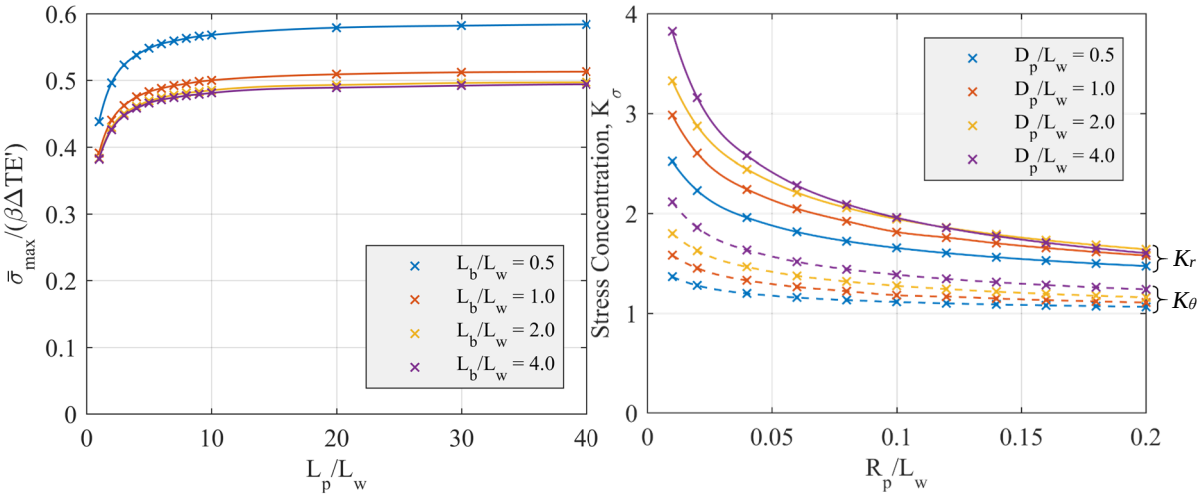


Figure C.6 – Left) Variation in maximum nominal stress with geometrical ratio L_p/L_w at four values of pedestal spacing L_b/L_w where the temperature gradient is concentrated in the film wall due to the very high internal cooling ($Re_i = 10^6$). Note $D_p/L_w = 1$ and $R_p/L_w = 0.1$.
Right) Variation in fillet radial and circumferential stress concentration factors with geometrical ratio R_p/L_w at four values of pedestal diameter D_p/L_w where the temperature gradient is concentrated in the film wall due to the very high internal cooling ($Re_i = 10^6$). Note $L_b/L_w = 1$ and $L_p/L_w = 1$.

C.3 Effect of Internal Convective Cooling Performance on Thermomechanical Stresses

The analysis reported in section C.2 ascertained the sensitivity of the stress field to the various geometric ratios for a system with very high internal convective cooling performance, such that it could be assumed that all the temperature gradient occurred in the outer wall. In this section the effect of varying the internal convective cooling performance was investigated using the area-averaged thermal field approximations. In the present investigation, the heat transfer coefficient was varied by changing the impingement Reynolds numbers to values of 10^4, 10^5 and 10^6. The ratio L_p/L_w was also varied which changed the impingement zone Nusselt numbers (as based on equation C.1 – C.3). Other geometric ratios were kept at the following values: $L_i/L_w = 0.5$; $L_b/L_w = 1$; $D_p/L_w = 1$ and $R_p/L_w = 0.1$.

Figure C.7 demonstrates the variation in the maximum nominal stress at varying pedestal height ratio (L_p/L_w) as Re_i is varied. The figure clearly demonstrates the significant reduction in stresses that occurs as internal convective cooling is reduced. This result aligns well with the three-dimensional simulations discussed in section Chapter 6 and is indicative of thermal conduction becoming more significant relative to convection, with a corresponding decrease in

the Biot number. At reduced Re_i, the temperature gradient is smaller and the tendency to be focussed in the film wall reduces. As a result, the impingement wall exhibits increased thermal expansion at lower coolant flow rates reducing the mismatch in thermal expansion between the impingement and film cooled walls thereby reducing the magnitude of the stresses. The figure also demonstrates that peak stresses occur for the lower Reynolds number flows at L_p/L_w of around 4. This is explained with reference to Figure C.5 which shows the variation in heat transfer coefficient on the various internal surfaces as L_p/L_w is varied. A peak in heat transfer coefficient is observed to occur at an L_p/L_w of 4, which, for the ratio of D_i/L_w in this study of 0.5, corresponds to an impingement hole to target plate spacing of 8. Based on the correlations in equations C.1 – C.3, this is approximately where maximum impingement zone heat transfer coefficients would be expected. Consequently, for a particular value of Re_i, the maximum temperature gradients occur for this peak value of $\overline{Nu}_{w,f_{int}}$ due to greater internal cooling effects. The results of the analysis therefore suggest that over-cooling of the system can have negative thermomechanical consequences.

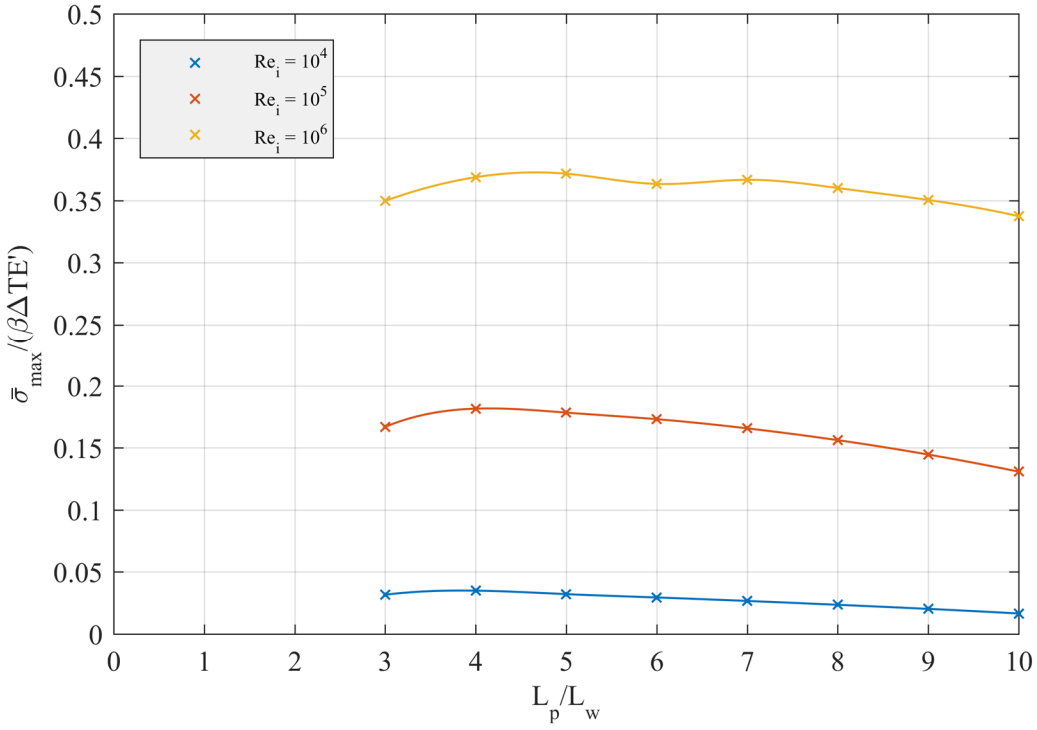


Figure C.7 - Effect of varying internal convection (through varying Re_i and L_p/L_w) on the maximum nominal stress. Note L_b/L_w = 1, D_p/L_w = 1 and R_p/L_w = 0.1

For the reader's benefit it is useful to note typical values of Re_i, ΔT, β, E, ν, E', and σ_y for an engine material such as CMSX-4 and these are provided in Table C.1. Consequently, for a known temperature difference, the above trends can be used to infer an approximate maximum nominal stress in a CMSX-4 double-wall geometry.

Table C.1 – Approximate material properties for CMSX-4 at 1300 K [124] along with an approximate range of impingement jet Reynolds numbers for engine conditions [125] and change in metal temperature (from the coolant inlet temperature, based on the results of Chapter 5)

$Re_i = 0.5 - 40 \times 10^4$	$\Delta T \approx 0 - 400$ K	$\beta = 20.1 \times 10^{-6}$ K^{-1}
$E = 82.7$ GPa	$\nu = 0.42 \therefore E' = 142.6$ GPa	$\sigma_y = 269.0$ MPa

To demonstrate this, the thermal model developed was used to produce a temperature profile for a geometry in which Re_i was set to 10^4 with a pedestal height for which maximum nominal stresses were exhibited (i.e. $L_p/L_w = 4$) as shown in Figure C.7. Other geometric ratios were set as per those for which the figure was produced ($L_b/L_w = 1$, $D_p/L_w = 1$ and $R_p/L_w = 0.1$). The temperature rise of the metal over that of the coolant (ΔT) at the location of the maximum nominal stress $\bar{\sigma}_{max}$ was 375 K. Using the data in Table C.1, the maximum nominal stress based on Figure C.7, was calculated to be 51.1 MPa. Based on the stress concentrations presented in Figure C.6b), an approximate stress concentration at the fillet of 1.8 would be expected resulting in a maximum principal stress of 92.9 MPa (i.e. $1.8 \times \bar{\sigma}_{max}$). One yield criterion, the *maximum principal stress theory*, predicts that the material yields when the maximum principal stress exceeds the yield stress, which for the present example is not the case.

It is noted that, for the above example, the stress concentration factor was calculated for a shorter pedestal length ($L_p/L_w = 1$); this is deemed acceptable as the pedestal spacing is maintained and is thought to be the more significant contribution to the fillet stress concentration. Additionally, the material properties at 1375 K will be slightly lower than those presented for temperature in Table C.1 which were for a temperature of 1300 K (although based on [124] the difference is small).

C.4 Second Order Film Cooling Thermal Model

In the above analyses, a first order, uniform external heat transfer driving gas temperature was assumed and thus the thermomechanical effect of distinct cooling films was not considered. Here, a second order approximation for the external gas temperature field is superimposed. The spanwise variation in film cooling effectiveness is based upon the correlation/superposition method discussed in Chapter 5, where the spanwise shape function of the film is considered to be a sine wave and takes the form shown in equation C.8. In this equation ψ_f is the phase angle and dimensionless local coordinate given by z/λ_f, where λ_f is the wavelength (i.e. the distance between film holes). The number of film holes per unit cell can therefore be determined from $(L_b+L_p)/\lambda_f$.

$$f_f = \sin(2\pi\frac{z}{\lambda_f} + \psi_f) \qquad (C.8)$$

In the following analysis, the phase angle was set to $\pi/2$, which, for which a value of $z/\lambda_f = 1$ would result in a single film cooling hole positioned midway between adjacent pedestals. In the following analyses, the internal heat transfer coefficients were set to a very high level (by setting Re_i to 10^6). Simulations were performed in which the ratio $\lambda_f/(L_b+L_p)$ was varied between 0.1 – 10. In analysing the stress, the nominal stress occurring midway between pedestals on the internal side of the film cooled wall, termed $\bar{\sigma}_A$, was plotted in the following figure with the location indicated in Figure C.8. Additionally, the nominal stress occurring midway between pedestals on the external surface of the film wall is presented and is termed $\bar{\sigma}_B$ (also shown in Figure C.8). The variation in these nominal stresses, along with the minimum

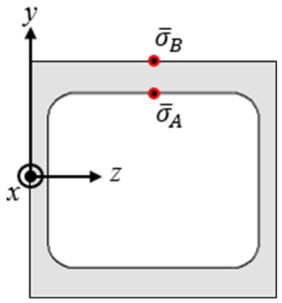


Figure C.8 - Diagram of a double-wall cell showing the location of nominal stresses used in the assessment of the stresses arising from film cooling

and maximum 1st principal stresses, are presented for varying film hole wavelength in Figure C.9.

For the case of sparse film holes, where the wavelength of the films is large, the external surface of the film cooled wall is hotter than the internal surface of the film cooled wall. Consequently, the hotter external surface attempts to expand more than the internal surface of the film wall and experiences predominantly compressive stresses. Meanwhile, the internal surface goes into tension as shown in Figure C.9. However, as the wavelength is reduced, and the regularity of films increased, the external surface of the film wall experiences significantly improved cooling. Indeed, for $\lambda_f/(L_b+L_p) \approx 3.5$, minimum stresses are observed and for closer film cooling holes, the external surface of the film wall becomes predominantly tensile due to the large cooling effect from the films. This analysis shows that, from a thermomechanical perspective, an optimal film arrangement can be obtained to reduce the stresses developed.

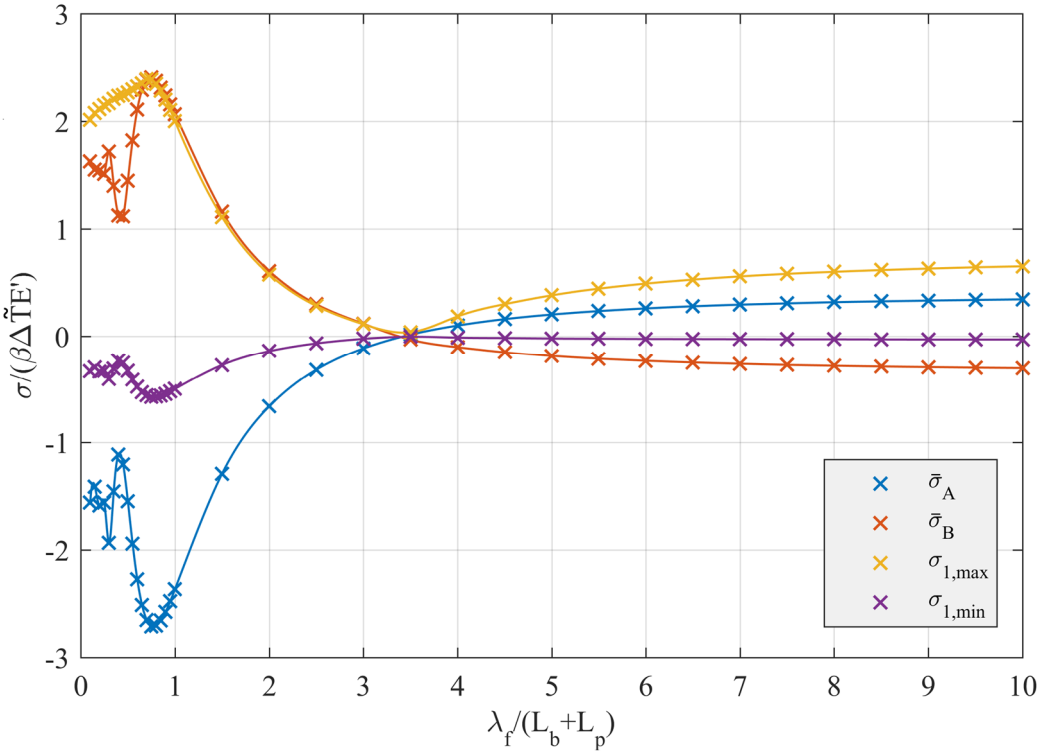


Figure C.9 - Relationship between the stress field and film hole dimensionless wavelength, $\lambda_f/(L_b+L_p)$, where L_b/L_w = 1, L_p/L_w = 1, D_p/L_w = 1 and R_p/L_w = 0.1

It is noted that in the above analyses, the effect of stress concentrations arising from the film holes themselves were negated, with only the cooling effect of the films assessed. Further analyses could consider the effect of stress exacerbation arising from film holes positioned in close proximity to one another (or other stress concentration features such as the pedestal fillets). Additionally, the phase angle in the above analysis was set to $\pi/2$. Further analyses may consider the effect of varying phase angle on the stresses developed. It is anticipated that the more significant effect of varying phase angle will be the potential interaction between stress concentrations arising from the film holes and other geometric features such as the fillets.

C.5 Summary

The work presented in this Appendix further investigated the thermomechanical stresses developed in double-wall systems during operation. The study – which was conducted in collaboration with the University of Oxford's Solid Mechanics group – took a more fundamental approach to double-wall system analysis whilst also complementing the thermomechanical work presented in Chapter 6. The contributions of the work in this Appendix are summarised below:

- The study investigated a simple axisymmetric model featuring periodic boundary conditions at the edges of the unit cell.
- A simple thermal model was developed based on a combination of correlations for Nusselt number and CFD data which allowed a realistic temperature distribution to be developed in the geometry for a specified impingement jet Reynolds number. The external temperature field variation was decomposed into first and higher order approximations.
- Area-averaged heat transfer coefficients on each internal surface were used to assess the effect of varying several geometric ratios on the nominal and maximum stresses for

high internal convection cooled systems where the temperature gradient was largely confined to the film wall.

- The geometric parameters that were investigated included pedestal diameter, pedestal spacing, pedestal height and fillet size.
- The effect of varying impingement jet Reynolds number (and thereby coolant mass flow) was then investigated with the potentially negative effect of over-cooling by internal convection identified.
- Finally, a second order temperature field approximation was introduced for the external surface of the film wall modelling the effect of varying film hole pitch with an optimal value identified from a thermomechanical perspective.

Appendix D: Manufacturing Methods

D.1 Experimental Test Piece Manufacturing Methods

The following section outlines the manufacturing methods for the double-wall geometries tested in the commissioned experimental facility. It is reiterated that test geometries for the facility were at ×10 scale with a flat plate surface area of 248 × 178 mm, and a thickness dependent on the specific double-wall geometry (namely pedestal layer height and wall thicknesses).

D.1.1 Overall Effectiveness Test Pieces

As discussed in Chapter 7 which outlined the development of the experimental facility, the relatively low thermal conductivity of stainless steel 316 (SS-316) provided a close match on Biot number to those seen at engine conditions (within around 25%). A manufacturing methodology was necessary that would ensure the test geometries were manufactured to within a suitable tolerance ensuring good thermal contact between the pedestals and the two walls.

Initially, laser sintering of the component as a single piece was considered. However, the cost was prohibitively expensive given both the physical size and the number of geometries to be manufactured. Furthermore, laser sintered components have a relatively large surface roughness which would require additional processing steps, further increasing the cost of manufacture. Small variations in solid thermal conductivity could also be introduced dependent on the laser sintering technology used which are very difficult to quantify adding an extra source of uncertainty in the overall effectiveness measurements. Consequently, an alternate method of manufacturing was sought.

The manufacturing method settled upon entailed a combination of CNC and conventional machining, along with a high temperature vacuum brazing process. Due to the proximity of the inclined film holes to the pedestals in some geometries, the impingement wall (with normally inclined impingement holes) and the pedestals were CNC machined from a single block of SS-316. The film wall with the inclined film holes was manufactured from a separate block of SS-316. The two manufactured parts were vacuum brazed to form the final double-wall test geometry. The brazing process entailed the placement of a wafer thin, nickel alloy brazing foil on the interface between the pedestals and film wall. The two parts where then placed in a brazing furnace and the temperature increased to approximately 1375 K with a weight positioned on top of the two components. To ensure successful brazing, the gap between the two parts was required to be less than 0.075 mm. This was achieved using either a slab cutter prior to machining or grinding of the surfaces after machining. Whilst it is noted that the nickel alloy brazing foil may have some very localised effect on solid thermal conductivity, the extremely thin nature of the foil means this effect is assumed negligible. Figure D.1 demonstrates some of the manufactured parts prior to brazing (namely *D3* and *G1*).

D.1.2 Film Effectiveness Test Pieces

To obtain steady-state, adiabatic film effectiveness measurements from the facility using IR thermography, test pieces were required which could be assumed to be adiabatic - a result of very low material conductivity. To achieve this low conductivity a hybrid manufacturing method was developed. As with the overall effectiveness SS-316 test geometries, the film effectiveness geometries were manufactured in two parts. The impingement wall and pedestal were manufactured from PLA using additive manufacturing. Whilst the PLA thermal conductivity value of 0.13 W/m.K is relatively low, to further reduce the effect of conduction, these 3-D printed components were manufactured using a sparse crosshatch infill pattern and

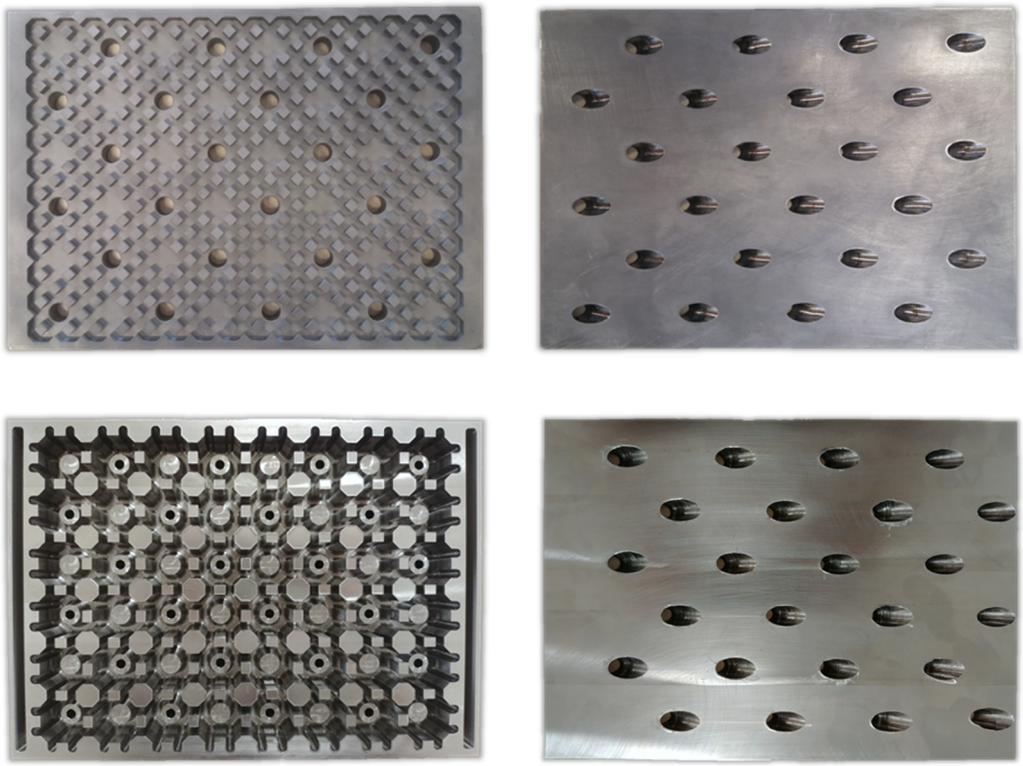


Figure D.1 – The manufactured SS-316 impingement/pedestal wall and film wall for geometries D3 (top) and G1 (bottom) prior to brazing

an example of this internal structure is shown in Figure D.2. PLA has a plastic transition temperature of approximately 335 K. However, conditions in the experimental facility were designed to exceed this to reduce both experimental uncertainties and provide a closer match on mainstream-to-coolant density ratio. Consequently, the film wall which was subjected to the hotter mainstream gas was manufactured from Rohacell®. Rohacell® is a dense foam with high temperature capabilities and a low thermal conductivity of around 0.03 W/m.K [126], [127]. It has found widespread use in obtaining adiabatic effectiveness measurements (see for example [117], [127], [128]). As demonstrated in Chapter 9, the low conductivity of the Rohacell® and assumption the test piece is adiabatic appeared to be valid across the experiments with impingement wall temperatures remaining at those of the coolant.

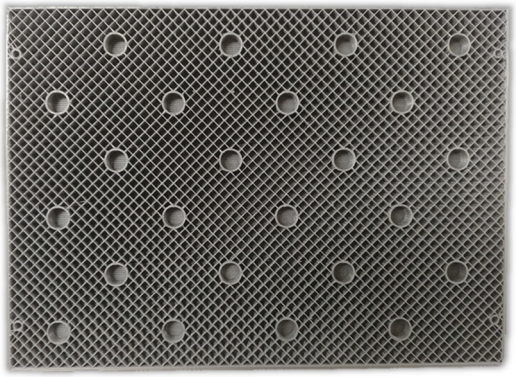


Figure D.2 - Internal structure of the PLA printed impingement wall and pedestals for film effectiveness measurements

D.1.3 Experimental Test Piece Diagrams

Diagrams of the five manufactured test geometries are shown on the following pages. Top down views are demonstrated where walls have been made transparent so the relative placement of respective features in each layer of the double-wall structure are visible. A cutaway three-dimensional render is also provided to clarify the specific structure. Note, in all cases the length of the flat plate was 248 mm, and the width 178 mm. The thickness varied between different geometries. Also identified in the figures is the presence of the flange surrounding the pedestal layer, a by-product of the manufacturing process where during designing of the test pieces, effort was made to try and minimise its effect on the internal flow features. This flange was the same size in the three diamond pedestal geometries (D3, D6 and D8), although the conduction area is more significant in D8 which features a sparser array of pedestals. The size of the flange was larger for the circular pedestal geometry C5. The crenulation concept geometry, G1, was manufactured later than the other geometries and the conductive effect of the flange minimised via machining of a pocket. Consequently, the effect of the flange is expected to be lower in this geometry. Further comment on the effect of the flange is made in Chapters 8 and 10.

D3 Test Piece

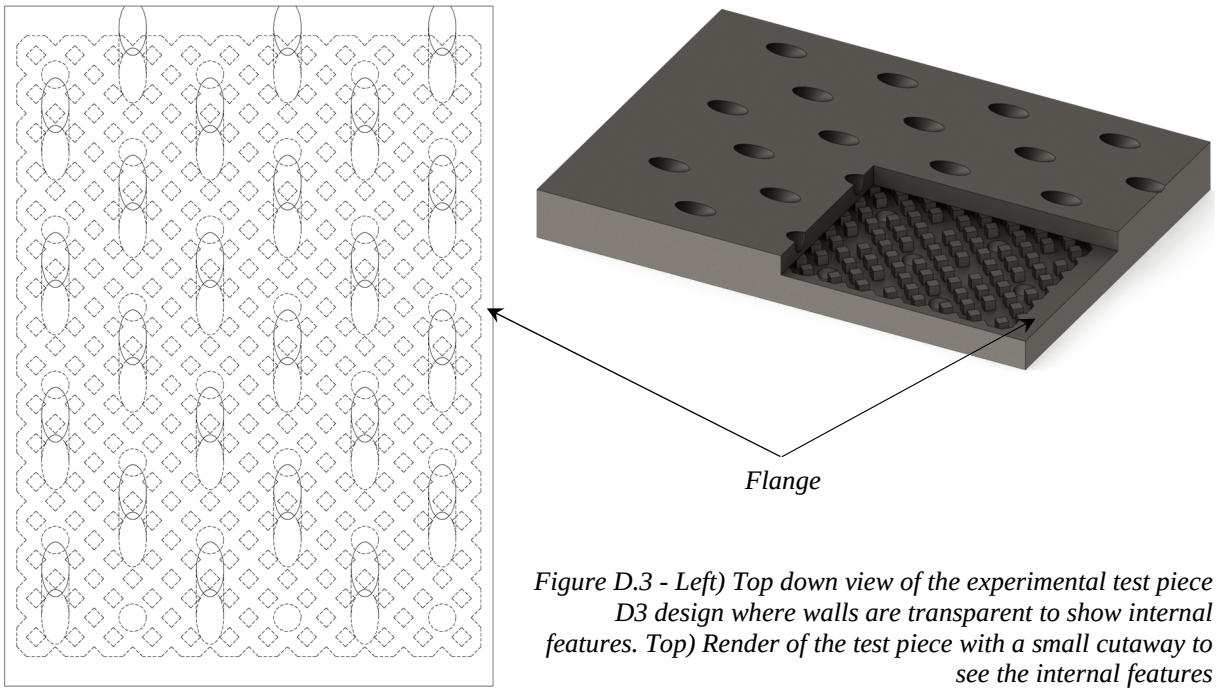


Figure D.3 - Left) Top down view of the experimental test piece D3 design where walls are transparent to show internal features. Top) Render of the test piece with a small cutaway to see the internal features

D6 Test Piece

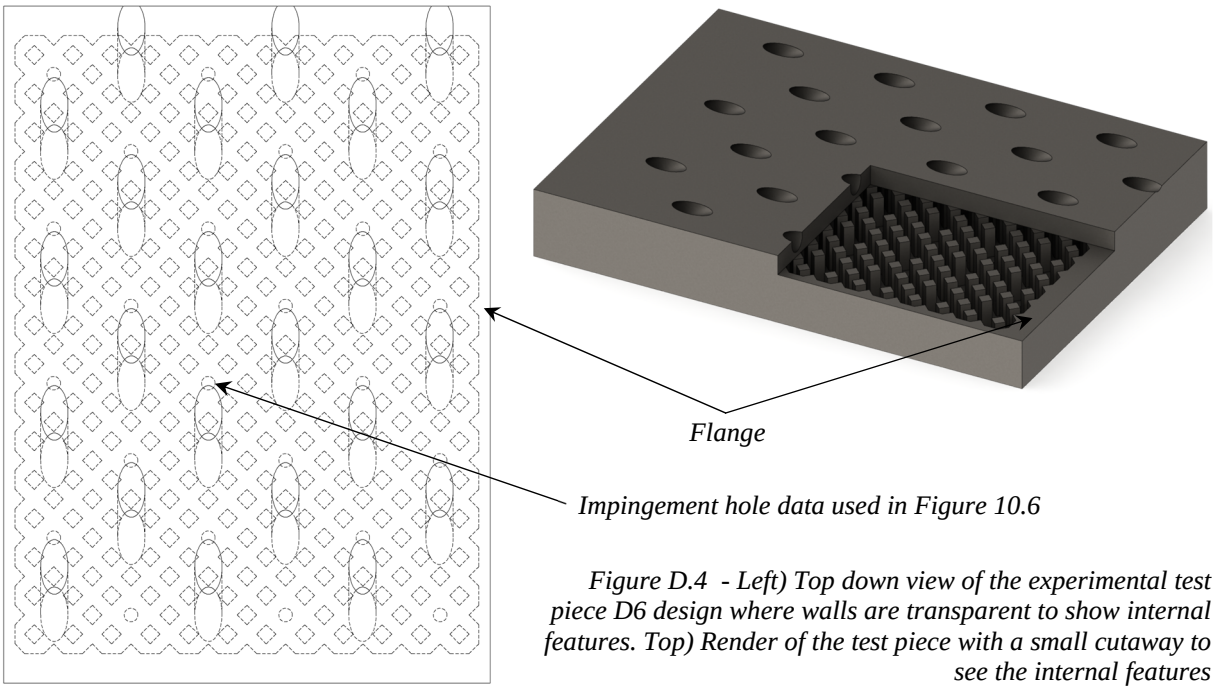


Figure D.4 - Left) Top down view of the experimental test piece D6 design where walls are transparent to show internal features. Top) Render of the test piece with a small cutaway to see the internal features

D8 Test Piece

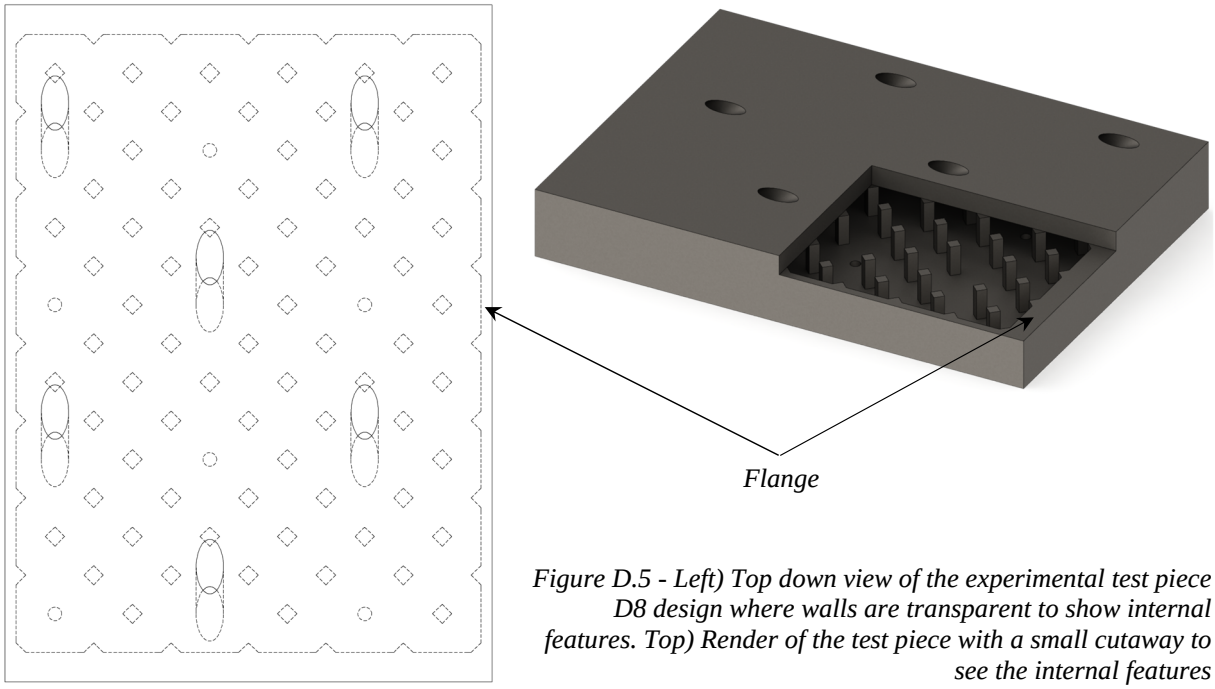


Figure D.5 - Left) Top down view of the experimental test piece D8 design where walls are transparent to show internal features. Top) Render of the test piece with a small cutaway to see the internal features

C5 Test Piece

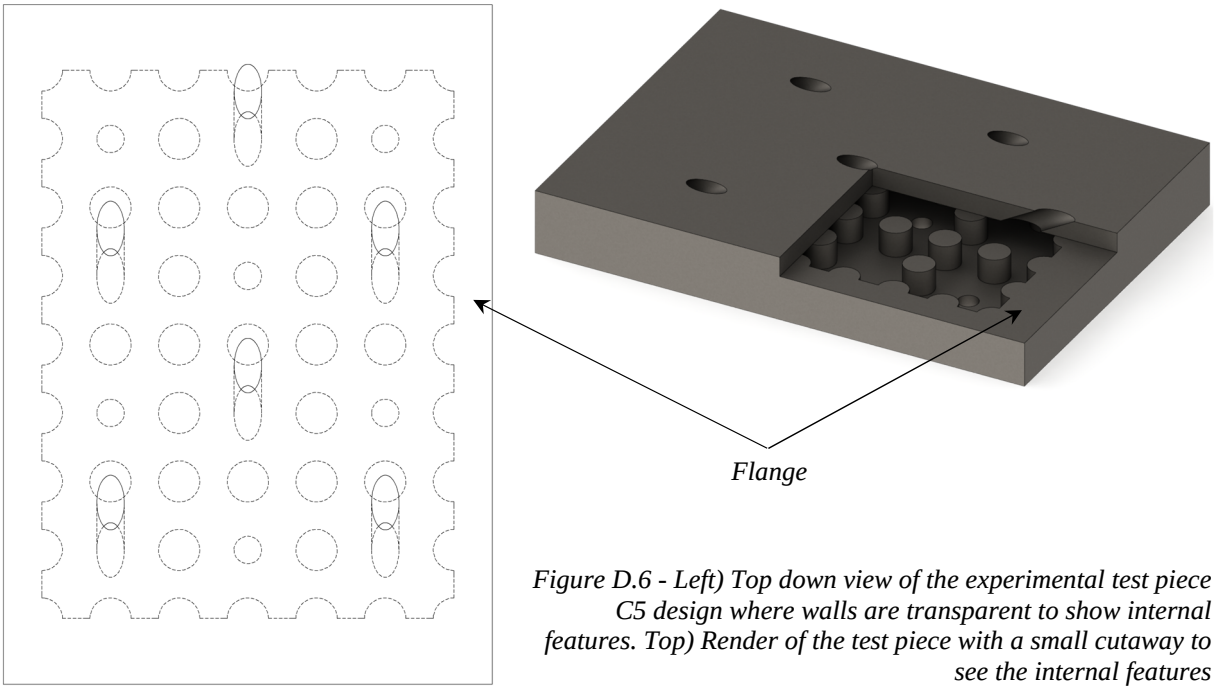


Figure D.6 - Left) Top down view of the experimental test piece C5 design where walls are transparent to show internal features. Top) Render of the test piece with a small cutaway to see the internal features

G1 Test Piece

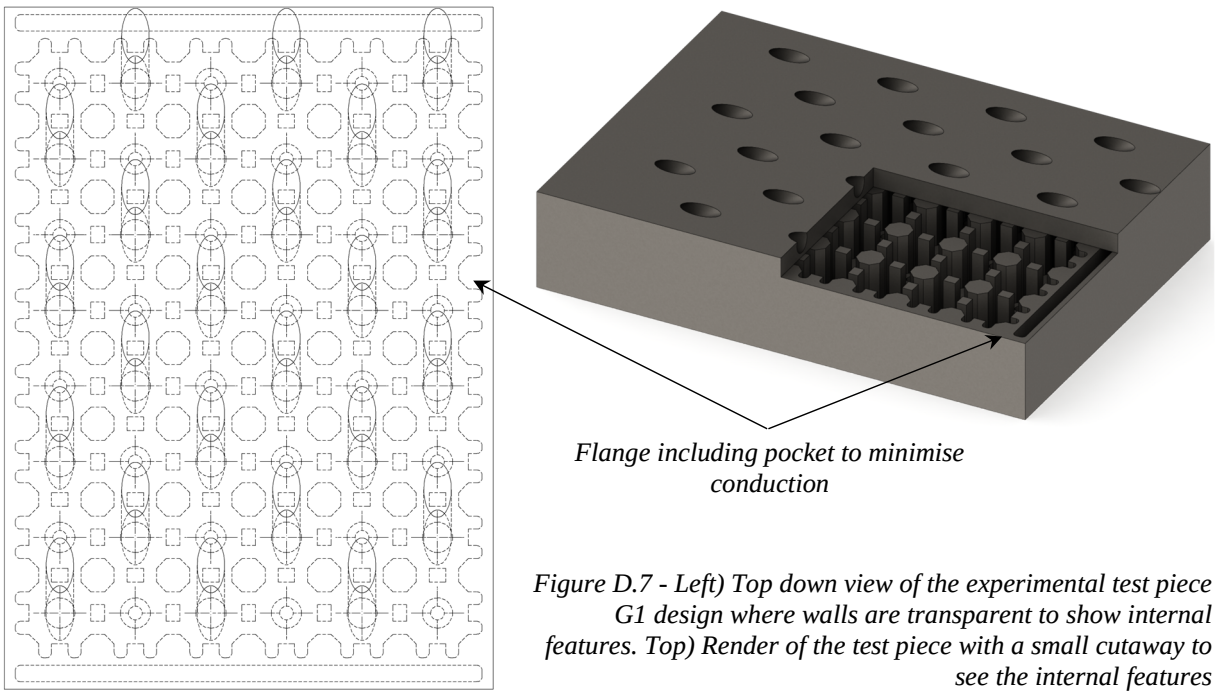


Figure D.7 - Left) Top down view of the experimental test piece G1 design where walls are transparent to show internal features. Top) Render of the test piece with a small cutaway to see the internal features

D.2 Investigation of Manufacturing Methods for Turbine Applications

In addition to investigating manufacturing methods for the ×10 scale geometries for the experimental facility, work was undertaken in collaboration with the High Temperature Research Centre (*HTRC*) at the University of Birmingham into methods that might be employed for manufacturing double-wall geometries at engine scale from materials typically employed in turbine NGVs and blades.

The work investigated the manufacturing and bonding of a ×2.3 scale, flat plate double-wall geometry featuring the basic geometrical design of D6. The turbine nickel superalloy CMSX-4 was selected as the material from which to manufacture the component. The manufacturing procedure shared many similarities with that employed for the ×10 scale, SS-316 experimental test pieces. Once again, the impingement wall and pedestals were formed together from a single piece of CMSX-4, with the film wall manufactured from a separate piece.

The two parts were then joined together through brazing. However, the specifics of the process differed significantly.

Whilst for the SS-316 test pieces, a more conventional vacuum brazing process was used, for the smaller scale CMSX-4 part, a diffusion brazing process was employed. Diffusion brazing more closely resembles diffusion bonding. In the case of diffusion bonding, no filler metal foil is required and instead the components to be bonded are raised to very high temperatures for extended durations and under high load ensuring adequate contact across the interface. The advantage of the process is the significant reduction in the formation of intermetallic phases when compared to conventional brazing that can affect the material properties, as well as the high temperature capabilities of the formed component. However, the cost and length of the process along with the lack of fillets formed at the bond greatly limit the application of diffusion bonding [129]. Diffusion brazing, however, requires a thin metal filler, typically with a thickness of less than 50 μm which is much reduced when compared to conventional brazing methods. A compressive force is applied to the parts which is less than that required for diffusion bonding, but a little greater than those applied during regular brazing. As with conventional brazing methods, the metal filler is melted. However, rather than then cooling the joint – which would result in a more typical braze in terms of the joint properties – it is held at an elevated temperature for an extended period (in terms of the current research, 8 hours at 1350 K). During this time the filler composition changes with the filler slowly diffusing into the metals being joined. This results in the temperature of the filler increasing and solidifying naturally whilst at the elevated temperature [129]. The product of this is a homogenised joint between the two parts being brazed which demonstrates both high temperature capabilities and good mechanical properties.

For the current work, it was desirable that, rather than applying a blanket foil over the joint which would result in overflow of the filler reducing control over the surface finish of the interface and potential misalignment, a preform be created. However, due to the large number

of independent pedestals, a conventional preform would be impossible to manufacture with a preform being required for each pedestal instead – clearly an extremely time consuming and expensive process. Instead, a method was proposed by the HTRC where the surface of the pedestals would be tinned with the brazing filler prior to machining, after which the pedestals would be created via fine electrical discharge machining (*EDM*). The material used for the filler was Ni-Cr-B due to both good wetting characteristics on CMSX-4 and the high resulting interface integrity. The process is demonstrated in Figure D.8.

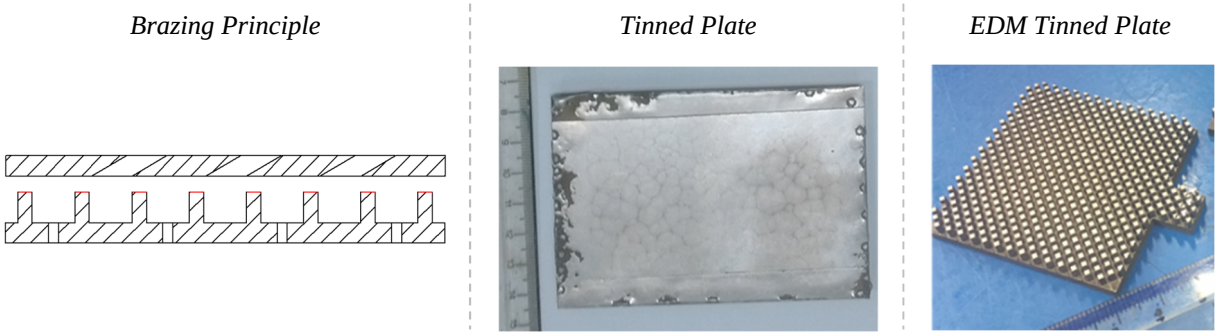


Figure D.8 – Left) Brazing principle where brazing preform only covers the pedestal surface to be bonded. Middle) Ni-Cr-B tinned CMSX-4 plate prior to machining. Right) CMSX-4 tinned plate after pedestals have been formed via an EDM process

The EDM machined impingement wall and pedestals can be seen on the right of Figure D.8. Additional pedestals were then removed, and the impingement holes machined. Prior to brazing of the two parts, the machining accuracy was ascertained via the use of a 3-D laser scanner (*GOM ATOS ScanBox Series 4*). The results of this are shown in Table D.1 where the specified geometry dimensions are provided, along with those obtained using the GOM scanner as well as verification using calipers where possible. Due to the finite radius of the wire used in the EDM machining process, a small fillet was formed at the pedestal/impingement wall interface. Additionally, an excess of material was removed at the start of each EDM cut resulting in a slight taper at the top of the pedestals. It is also noted that the impingement wall thickness deviates significantly from the specified geometry. This was a by-product of the thickness of the CMSX-4 plate available rather than a result of the machining process. Figure D.9

demonstrates several images obtained from the scanner demonstrating some of the resulting geometrical features with enlargements showing the fillets and pedestal taper resulting from the EDM process, along with two pedestals that were clipped by the milling tool when the impingement holes were being created.

Table D.1 – Specified geometry dimensions along with those measured from the manufactured component using both the GOM laser scanner and calipers (where possible)

Design Feature	Specification	GOM Scanner	Caliper
Film Wall Thickness (mm)	2.3	1.966	2.02
Impingement Wall Thickness (mm)	2.3	2.878	2.92
Pedestal Passage Height (mm)	3.45	3.125	3.17
Film Hole Angle (deg)	30	30.172	-
Radius at Pedestal Base (mm)	None specified	0.255	-
Maximum Pedestal Taper (mm)	None specified	0.383	-

One limitation of the laser scanner is the inability to obtain geometrical data for sections of the geometry not optically accessible. Consequently, after brazing of the parts an alternate method was sought for assessing the success of the braze. Due to the relative thinness of the brazed component, computerised x-ray tomography could be used to assess the internal, non-optically accessible regions of the geometry. The method relies upon the emission of x-rays which pass through the component and are detected at the opposite side. In this case,

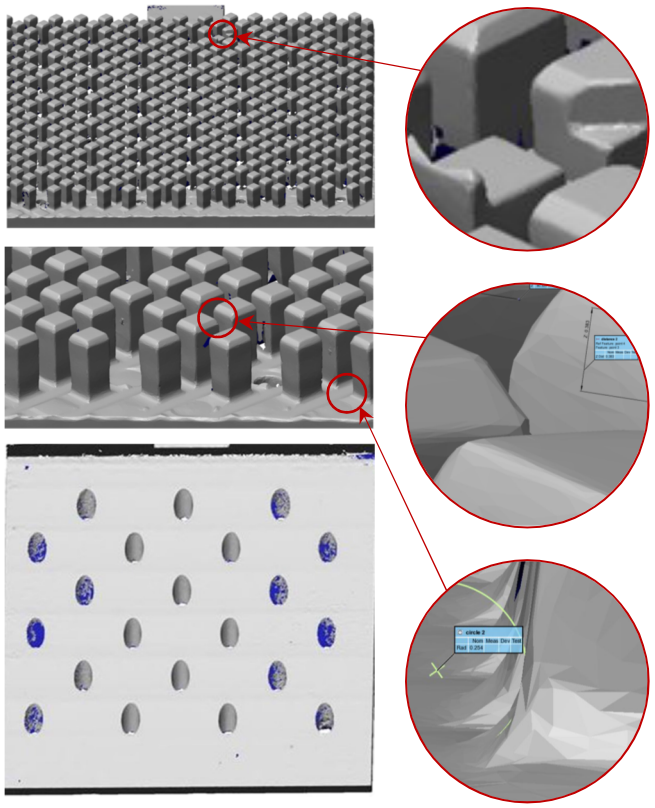


Figure D.9 – Images obtained from the GOM laser scanner highlighting several geometrical features that result from the manufacturing process

scans were taken in two directions: along the long axis of the pedestals, and in the direction of the streamwise mainstream flow field. A selection of images obtained from the scans are demonstrated in Figure D.10. The images show the success of the brazing process with all but the clipped pedestals demonstrating bonding with the film wall. The images also demonstrate the successful alignment of the two walls.

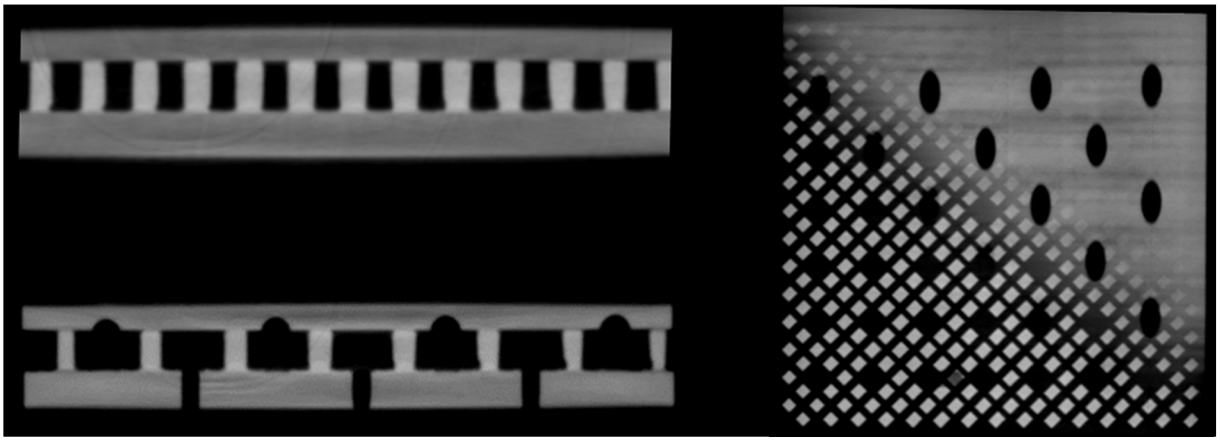


Figure D.10 - CT images of the brazed CMSX-4 double-wall geometry